ATOMICALLY THIN LAYERS AT HETEROEPITAXIAL INTERFACES

MULTISCALE ELECTRON MICROSCOPY IMAGING AND SPECTROSCOPY OF ATOMICALLY THIN LAYERS AT HETEROEPITAXIAL INTERFACES

By

HESHAM EL-SHERIF, B.Sc., M.Sc.

A Thesis Submitted to the School of Graduate Studies
in Partial Fulfilment of the Requirements for the degree of
Doctor of Philosophy

McMaster University © Copyright by Hesham El-Sherif, August 2021

Descriptive note

DEGREE	Doctor of Philosophy (2021) Materials Science and Engineering McMaster University Hamilton, Ontario, Canada
TITLE:	Multiscale Electron Microscopy Imaging and Spectroscopy of Atomically Thin Layers at Heteroepitaxial Interfaces
AUTHOR:	Hesham El-Sherif
SUPERVISOR:	Nabil D. Bassim
NUMBER OF PAGES:	xx, 220

Lay abstract

Sandwich-like materials with atomic thicknesses are recently fabricated. The interface between these sandwich-like materials has physical and structural changes that affect their bulk behavior. In this thesis, advanced microscopy techniques are developed and employed to investigate two new categories of interfaces with atomically thin metallic layers. First, a tellurium layer is realized in a 3D/3D system of cadmium telluride on a sapphire substrate, like a paper between two books. The tellurium layer is found to have a key role in producing a high-quality thin film that easily delaminates from the substrate. Second, an atomically thin gallium is introduced via confinement heteroepitaxy. This technique intercalates metallic gallium between the 2D/3D interface of graphene on silicon carbide, like inserting a paper under the hard cover of a book. Both interfaces are candidates for many next-generation electronic, optical, and infrared devices operating at the atomic scale.

Abstract

Two-dimensional (2D) materials have properties that are often different from their three-dimensional (3D) bulk form. Many of these materials are stable at ambient conditions, which allows them to be integrated with other 2D- or 3D-materials to form heterostructures. Integration of various dimensional materials attains unique electrical and optical properties that aid in developing novel electronic devices. The interface of the heterogeneous integration of these films can exhibit a weak van der Waals-like bonding.

In this thesis, an advanced characterization (from atomic to millimeter resolution) of various dimensional materials with weakly bonded interfaces is developed and employed to understand their behavior at scale. First, a large-area single-crystal cadmium telluride thin film is grown incommensurately and strain-free to a sapphire substrate despite a significant 3.7% lattice mismatch. The film remarkably delaminates as a bulk single crystal film due to an atomically thin tellurium that spontaneously forms at the interface. Aberration-corrected electron microscopy and spectroscopy reveal both the van der Waals-like structure and bonding at the film/substrate interface. Second, a large-area atomically thin gallium is intercalated at the interface of epitaxial graphene. Correlative microscopy workflows are applied to understand the thickness uniformity and area coverage of the 2D–gallium over few millimeters of the sample. Utilizing multiple correlative methods, SEM image contrast is found to be directly related to the presence of the intercalated gallium. The origin of the SEM contrast is investigated as a function of the surface potential. Then, the heterostructure characterization is scaled up over a few square millimeter areas by segmenting SEM images, each acquired with nanometer-scale resolution. Additionally, transmission electron microscopy is applied to investigate the interface of gallium–SiC, the gallium air–stability, and the role of the substrate on the heteroepitaxial growth of 2D–gallium, which charts a path for further development of these materials.

Acknowledgments

The accomplishment of this dissertation has been possible thanks to many people in academic life and beyond, in addition to many funding agencies.

First, I would like to thank my advisor, Professor Nabil D. Bassim, for all his advice, edits, supervision, meetings, and financial support throughout my McMaster journey. Working for Nabil, I acquired rare and valuable electron microscopy skills across different disciplines, which is my future career capital. I am thankful to him for giving me the opportunity to explore and exploit many ideas and research problems using electron microscopes, despite the high microscopy bills. Also, this research would not be possible without the cooperation of many research labs within my advisor's network.

With this, I would thank all the staff of the Canadian Center for Electron Microscopy (CCEM) for their training and organizing the microscopy facilities. I would here mention the names: Natalie Hamada, Carmen Andrei, Andreas Korinek, Brian Langelier, Chris Butcher, Jhoynner Martinez, Hui Yuan, Samantha Stambula, and Marcia Reid. A special thank you goes to Travis Casagrande, who trained me on two major techniques in my works (FIB and AES), and has answered many of my technical questions. I will miss all of you and all the joyful 1850+ microscopy hours I had over the last four years working on all 10 electron microscopes at the CCEM.

I thank our collaborators, Professor John Preston and Dr. Stephen Jovanovic, from the engineering physics department at McMaster University, who have fabricated the CdTe samples. I will always remember numerous discussions that we had together at Preston's office to explain the plasmons and structure of the CdTe/sapphire, prepare the manuscript, and answer the reviewer comments. This successful cooperation would not have been possible without other thoughtful and enriching discussions I had with Stephen about semiconductor and crystallography literature. I wish Stephen all the best in his new role in the United States, and I wish to meet him there in California.

I would also like to thank our collaborators in the US, Professor Joshua A. Robinson, and his group from The Pennsylvania State University. I have been

doing STEM and EELS characterizations for his group through the first year of my grad school – as one of my side projects – before focusing on the 2D gallium work for this thesis. I will never forget the bi-weekly meetings that gather the theoretical, fabrication, and characterization groups to discuss these new 2D layered materials, each from their perspective. For the 2D gallium work in this thesis, I would thank Dr. Natalie Briggs for preparing a high-quality sample that comes after so many bad samples. I would also like to thank our collaborators at North Carolina State University, Professor Ki Wook Kim, and his student Minghao Pan for calculating the DFT results, as well as our collaborators at the University of Toronto, Professor Tobin Filleter, and his former postdoc Dr. Mahdi Hamidinejad. I would finally acknowledge the funds for this project (Award FA9550-19-1-0239) from the Air Force Office of Scientific Research (AFOSR) from the US side in addition to both the Natural Sciences and Engineering Research Council (NSERC) and the Discovery Grant program from the Canadian side.

I would also like to express my gratitude to all my thesis committee members, and a special thank you goes to Professor Adam Hitchcock for accepting serving this role on my last year in this journey. I cannot be more thankful for his fast replies to my questions and edits to documents that surprisingly arrived in my inbox within two days. Here, I would thank my former group member, Weiwei Zhang, for his advice to engage Professor Hitchcock in my committee. Also, I would thank all my current and former groupmates in the Bassim research group for their support and encouragement throughout my Ph.D. experience. I will always remember the outings and the life and academic discussions I had with Longxing Chi, Weiwei Zhang, Chen Gu, Caleb Whittier, Nasim Khoonkari, and many coffee-breaks with Peng Dong.

Last but not least, I would thank my beloved wife, Karima Abdelmaaboud, for being a constant, unwavering source of support, encouragement, and motivation throughout my graduate school journey and beyond. I cannot imagine this journey without our synchronization and management of all daily tasks for our two children (Moatz and Mazan) while I was studying and she had a part-time job. Finally, thanks to all my beloved family back home in Egypt for their prayers and support.

Dedication

To
my family
and
the soul of my father

"I have gone to inspect, and I have returned to tell. Let me pass that I may report my mission."

"I did not dispute except with reason."
One of the negative confessions of ma'at

Hieroglyphic Texts are from the Book Of The Dead
(Papyrus of Ani ~1300–1250 B.C.)[1]

[1] Translated by Mohsen Lotfy Elsayed, Ketab Almawta (2009), ark:/13960/t6j16f139, page 359, and 439

Table of contents

Descriptive note ii
Lay abstract iii
Abstract iv
Acknowledgments v
Dedication vii
Table of contents viii
List of figures xii
List of tables xv
List of abbreviations and symbols xvi
Declaration of academic achievements xviii

Chapter 1 : Preface 1

1.1. Thesis story 1
1.2. Thesis outline 4

Chapter 2 Background 7

2.1. 2D materials and heterostructures 7
2.1.1. Why 2D materials? 7
2.1.2. Graphene 8
2.1.3. 2D materials beyond graphene 9
2.1.4. 2D van der Waals heterostructure 10
2.1.5. Application challenges of 2D materials 11
2.2. Heteroepitaxial interfaces 12
2.2.1. Epitaxial growth 12
2.2.2. Heteroepitaxial interface bonding 13
2.2.3. Heteroepitaxial interface mismatch 15
2.2.4. Surface reconstructions 17
2.2.5. Growth of heteroepitaxial materials 19
2.2.5.1. Mechanical stacking of 2D materials 19
2.2.5.2. Thermal methods 20
2.2.6. Remote and spontaneous van der Waal epitaxy 22
2.2.6.1. Remote epitaxy 22
2.2.6.2. 2D Materials transfer 23

2.2.6.3. Spontaneous vdW epitaxy on chalcogenide-terminated sapphire 24
2.2.7. Confinement heteroepitaxy 25
2.2.7.1. Silicon carbide 25
2.2.7.2. Epitaxial graphene (EG) 26
2.2.7.3. Nucleation of the epitaxial graphene at the step edges....28
2.2.7.4. Intercalation of epitaxial graphene 29
2.2.7.5. Confinement heteroepitaxy (Chet) growth....30
2.2.7.6. Second-harmonic generation (SHG) from 2D CHet metal....31
2.2.7.7. Possible SiC-metal interactions during the intercalation process....33
2.3. Electron microscopy....34
2.3.1. Electron microscopy versus light microscopy.... 34
2.3.2. Electron-matter interaction.... 36
2.3.3. Scanning transmission electron microscopy.... 40
2.3.4. Electron energy-loss spectroscopy 43
2.3.5. Auger electron spectroscopy 46
2.3.6. SEM for characterizing 2D materials 48
2.3.7. Correlative microscopy workflow for 2D materials.... 49
2.4. Cadmium telluride....52
2.4.1. Applications of cadmium telluride 53
2.4.1.1. CdTe-based solar cells 53
2.4.1.2. Alloying of CdTe for radiation detection....54
2.4.2. Growth of cadmium telluride.... 55
2.4.2.1. CdTe film growth at a high substrate temperature....55
2.4.2.2. CdTe film growth at a low substrate temperature....56
2.4.3. CdTe growth on a sapphire substrate.... 56
2.5. Summary....57
Chapter 3 Atomically Thin Tellurium at CdTe/Sapphire Interface....59
3.1. Introduction....59
3.2. Material fabrication....60
3.2.1. Pulsed laser deposition fabrication system 60
3.2.1.1. Process description 61
3.2.1.2. Set up description 62
3.2.2. Growth parameters of CdTe thin film 63
3.3. CdTe film delamination....64
3.4. Cross-section preparation of CdTe/sapphire interface 65
3.5. CdTe/sapphire interface characterization 67
3.5.1. STEM and core-loss EELS experimental conditions 67
3.5.2. Interface structure 68

3.5.3. Interface bonding 72
3.6. Reconstructed topmost sapphire layer 78
3.7. Misfit dislocation-free interface 82
3.7.1. Geometric phase analysis (GPA) 83
3.7.2. STEM-Moiré imaging 86
3.7.3. Laminar twin CdTe layer 88
3.8. Tellurium buffer thickness versions 91
3.9. CdTe film characterization 93
3.9.1. CdTe film polarity 93
3.9.2. CdTe surface quality 95
3.10. Summary 97

Chapter 4 Atomically Thin Gallium at Epitaxial Graphene Interface 99

4.1. Introduction 99
4.2. Material fabrication 100
4.2.1. Epitaxial graphene (EG) 100
4.2.2. EG plasma cleaning 101
4.2.3. Gallium intercalation 102
4.3. Cross-section preparation of EG and 2D-Ga samples 103
4.3.1. Process workflow 103
4.3.2. Preparation parameters 104
4.4. Epitaxial relationship before and after intercalation 105
4.4.1. SiC-EG epitaxial interface 105
4.4.2. SiC-Ga epitaxial interface 106
4.4.3. Ga-EG interface 107
4.5. Air stable 2D-Ga under the EG confinement 109
4.5.1. Delaminating the EG 109
4.5.2. Cross-section near the peeled edge 111
4.5.3. STEM and EELS investigation across the peeled edge 111
4.6. Sensitivity of SEM contrast to the gallium locations 115
4.6.1. Tracking SEM contrast over the steps of 2D-Ga synthesis 115
4.6.2. Correlative characterization with SEM contrast 120
4.6.2.1. SEM correlation with Auger electron spectroscopy 120
4.6.2.2. SEM correlation with cross-section STEM images 125
4.7. Thickness uniformity of 2D-Ga. 128
4.7.1. Atomic-scale STEM montage of the cross-section 128
4.7.2. Analysis of STEM montage 130

4.8. Origin of SEM contrast 133
4.8.1. Trapped electrons inside potential barriers 133
4.8.2. Surface potential calculations by DFT 136
4.8.3. Surface potential measurements by KPFM 138
4.8.3.1. KPFM-SEM correlation for EG surface 138
4.8.3.2. KPFM-AES-SEM correlation for 2D-Ga surface 140
4.9. Significance of SEM contrast for characterizing 2D-Ga 143
4.9.1. Calculating the bulk coverage percentage of the 2D-Ga 143
4.9.1.1. SEM image acquisition parameters 144
4.9.1.2. SEM image segmentation methods 144
4.9.1.3. Calculating gallium coverage over 2 × 1.5 mm area 146
4.9.1.4. How SEM contrast analysis pushes the microscopy limits 147
4.9.1.5. Automation of the segmentation process. 151
4.9.2. Optimizing the electron transport 152
4.9.3. Optimizing the CHet fabrication 154
4.10. Si-Ga interface challenge 155
4.10.1. SiC-EG interface prior intercalation 156
4.10.2. Existence of Si-vacancies prior to intercalation 157
4.10.3. The reconstructed interface of the as-prepared EG 160
4.10.4. Gallium-filling of Si-vacancies 163
4.10.5. Gallium-discontinuity at 3C-6H stacking order 166
4.10.5.1. 6H-SiC versus 3C-SiC stacking order 166
4.10.5.2. Relation of 3C-stacking with the EG growth mechanism 166
4.10.5.3. Growth of 2D-Ga across 3C-6H stacking order 169
4.11. Summary 171

Chapter 5 Conclusions and Outlook 173

5.1. Multiscale characterization of CdTe/sapphire interface 173
5.2. Multiscale characterization of 2D-Ga 174
5.3. Common properties 176
Appendixes 179
Microscopy art 196
Bibliography 197

List of figures

Figure 1. 2D materials vdW heterostructure. 11
Figure 2. Schematic illustration of epitaxial growth. 14
Figure 3. Heteroepitaxial interfaces to overcome lattice mismatch. 17
Figure 4. Schematic cross-sectional view of solid and reconstructed surface. 19
Figure 5. Remote Epitaxy. 23
Figure 6. Schematic of the SiC polytypes. 27
Figure 7. Schematic of the SiC miscut angle. 28
Figure 8. Nucleation of EG on SiC step bunch. 29
Figure 9. Cartoon of the Confinement Heteroepitaxy (CHet) growth. 32
Figure 10. Second harmonic generation (SHG) from 2D CHet metals. 33
Figure 11. Electron microscopes compared to a light microscope. 36
Figure 12. Electron beam-sample interaction model. 39
Figure 13. Fast electron interaction with an atom. 39
Figure 14. STEM imaging. 41
Figure 15. STEM-EELS technique. 44
Figure 16. Detection of electrons. 45
Figure 17. Auger electron spectroscopy map of 2D Gallium intercalated EG. 48
Figure 18. SEM detection of graphene number of layers. 49
Figure 19. Crystallography of cadmium telluride (CdTe). 53
Figure 20. A schematic of the pulsed laser deposition growth system. 63
Figure 21. CdTe layer transfer to flexible polysulfone (PSU) film. 65
Figure 22. Consideration of cross-section attachment to the FIB needle. 66
Figure 23. Preparation of CdTe cross-section sample for TEM investigation. 67

Figure 24. STEM imaging of the CdTe/sapphire interface. 69
Figure 25. Core-loss EELS of CdTe/sapphire interface. 70
Figure 26. Denoised core-loss EELS map of CdTe/sapphire interface. 72
Figure 27. Monochromator alignment of Low-loss EELS. 73
Figure 28. Reference low-loss EELS spectra of CdTe, Sapphire, and Te. 74
Figure 29. Analysis of low-loss EELS experiments at CdTe/sapphire interface....76
Figure 30. Structure correlated to CdTe/sapphire interface bonding.....................77
Figure 31. Reconstruction evidence at the topmost sapphire layer........................79
Figure 32. GPA strain mapping at the CdTe/sapphire interface. 85
Figure 33. STEM-Moiré imaging at the CdTe/sapphire interface...........................87
Figure 34. Strain relaxation mechanisms of CdTe/sapphire interface....................90
Figure 35. Tellurium thickness variations. 92
Figure 36. CdTe thin film polarity..94
Figure 37. CdTe surface quality..96
Figure 38. Graphical conclusion of the CdTe/sapphire system. 98
Figure 39. Cartoon of the tube furnace growth of 2D CHet metals......................103
Figure 40. Photograph of a 1 × 1 cm EG after gallium intercalation.....................103
Figure 41. Coordinating FIB cross-sections for STEM investigations. 104
Figure 42. The epitaxial interface of EG and 2D-Ga. 108
Figure 43. Atomic spacing of 2D-Ga heterostructure. 108
Figure 44. Scratching of the 2D-Ga surface. 110
Figure 45. STEM imaging across the peeled EG edge. 113
Figure 46. EELS investigation across the peeled EG edge....................................114
Figure 47. Evolution of SEM contrast during the CHet growth. 117
Figure 48. SEM imaging instability of SiC substrate. 119

Figure 49. Morphology of epitaxial graphene. 119
Figure 50. SEM correlation with AES surface chemical maps. 121
Figure 51. Scaling correction between SEM and AES techniques. 122
Figure 52. Working distance (WD) sensitivity to SEM detector. 122
Figure 53. Effect of stage tilt in visualizing particles. 124
Figure 54. SEM correlation with atomic layer thicknesses. 126
Figure 55. Stitching atomic-resolution STEM images. 129
Figure 56. A stitched atomic-resolution STEM montage. 129
Figure 57. Stitched STEM montage. 132
Figure 58. Schematic of electron emission from SiC, EG, and 2D-Ga. 135
Figure 59. Surface potential calculation by DFT. 137
Figure 60. Correlation of SEM contrast with KPFM of EG surface. 140
Figure 61. SEM contrast correlation with KPFM and AES for 2D-Ga. 142
Figure 62. SEM montage covers a scalable area of 1.5 × 2 mm^2 area. 145
Figure 63. SEM segmentation from the image histogram. 145
Figure 64. Segmentation of a large field dense-pixelated SEM frame. 149
Figure 65. Scaled-up characterization of the 2D-Ga over 1.5 × 2 mm^2 areas. 150
Figure 66. Superconductivity measurement of a 2D-Ga heterostructure. 153
Figure 67. Tracking the successful Ga intercalation using the SEM contrast. 155
Figure 68. Reconstruction appears on the EG interface before intercalation. 158
Figure 69. Electron beam damage study of the topmost SiC of EG sample. 159
Figure 70. Core-loss EELS of EG shows the reconstructed topmost SiC layer. 162
Figure 71. STEM imaging and spectroscopy of gallium filling Si-vacancies. 165
Figure 72. Topmost SiC transformation from 6H to 3C stacking order. 168
Figure 73. Gallium-discontinuity at 3C-6H stacking order transformation. 170

Figure 74. Summary of the multi-scale characterization of 2D Gallium. 172

List of tables

Table 1. Description of SEM contrast of the 2D-Ga surface. 118

List of abbreviations and symbols

2D	Two-dimensional
2D-Ga	Two-dimensional gallium
6PP	Six point probe devices
ABF	Annular bright field
AC-TEM	Aberration-corrected transmission electron microscopy
ADF	Annular dark field
AES	Auger electron spectroscopy
AFM	Atomic force microscopy
BF	Bright field
BL	Buffer layer
BN	Boron nitride
CdTe	Cadmium telluride
CL	Camera length
CPD	Contact potential difference
C_s	Spherical aberration coefficient value
C-TEM	Conventional transmission electron microscopy
DB	Dangling bonds
DP	Diffraction pattern
DFT	Density functional theory
EDS	Energy-dispersive X-ray spectrometry
EELS	Electron energy loss spectroscopy
EG	Epitaxial graphene
ETD	Everhart-Thornley detector
ELNES	Energy-loss near-edge structure
eV	Electron volt
FIB	Focused ion beam
FWHM	Full-width half-maximum
GPA	Geometric phase analysis
HAADF	High angle annular dark field
KPFM	Kelvin probe force microscopy
LAADF	Low-angle annular dark field
LEED	Low energy electron diffraction
LEEM	Low energy electron microscope
NBED	Nanobeam electron diffraction

NLO	Non-linear optical
PCA	Principal Component Analysis
PPMS	Physical property measurement system
PL	Photoluminescence
QFEG	Quasi-freestanding epitaxial graphene
SAED	Selected area electron diffraction
SE	Secondary electrons (emission)
SEM	Scanning electron microscopy
SERS	Surface-enhanced Raman scattering
STEM	Scanning transmission electron microscopy
SHG	Second harmonic generation
STM	Scanning tunneling microscopy
TEM	Transmission electron Microscopy
TLD	Through-lens detector
TMD	Transition metal dichalcogenide
THz	terahertz
vdW	van der Waals
h-vdW	*half*-van der Waals
WD	Working distance
Z	Atomic number
ZLP	Zero loss Peak
α	Convergence angle of the STEM probe
β	Collection angle of the scattered STEM probe
ε_{xx}	Normal strain along the x-axis
ε_{yy}	Normal strain along the y-axis
ns	nano second

Declaration of academic achievements

This thesis is written coherently based on the electron microscopy characterization work by *Hesham El-Sherif* for two material systems that exhibit confined layers at epitaxial interfaces. However, this thesis does not fully reflect the diversity of the work performed by the author during his graduate studies that may not fit into the monographed story of this thesis. To declare academic achievements – below is a categorized list of *El-Sherif*'s publications achieved with his supervisor, *Professor Nabil Bassim*, as of August 2021.

(A) Journal publications contributed to parts of the story of this thesis and were accomplished during the graduate school period (2017–2021):

1. *El-Sherif, H.*, N. Briggs, B. Bersch, M. Pan, M. Hamidinejad, S. Rajabpour, T. Filleter, K. Kim, J. Robinson, and *N. Bassim*. "Scalable Characterization of 2D Gallium Intercalated Epitaxial Graphene." ***Submitted*** (2021).
2. Jovanovic, M., *H. El-Sherif (co-first author)*, *N. Bassim*, and J. Preston. "Spontaneous Relaxation of Heteroepitaxial Thin Films by van der Waals-Like Bonding on Te-Terminated Sapphire Substrates." ***Small*** 16, no. 45 (2020): 2004437. DOI:10.1002/smll.202004437.

(B) Journal publications accomplished beyond this thesis, as side projects during the graduate school period (2017–2021):

3. Nisi, K., S. Subramanian, W. He, K. Ulman, *H. El-Sherif*, F. Sigger, M. Lassaunière, M. Wetherington, N. Briggs, J. Gray, A. W. Holleitner, *N. Bassim*, S. Quek, J. Robinson, and U. Wurstbauer. "Light–Matter Interaction in Quantum Confined 2D Polar Metals." ***Advanced Functional Materials*** 31, no. 4 (2021): 2005977. DOI:10.1002/adfm.202005977.
4. Steves, M., Y. Wang, N. Briggs, T. Zhao, *H. El-Sherif*, B. Bersch, S. Subramanian, C. Dong, T. Bowen, A. Fuente Duran, K. Nisi, M. Lassauniere, U. Wurstbauer, *N. Bassim*, J. Fonseca, J. T. Robinson, V. Crespi, J. A. Robinson, and K. Knappenberger, Jr. "Unexpected Near-Infrared to Visible Nonlinear Optical Properties from 2-D Polar Metals." ***Nano Letters*** 20, no. 11 (2020): 8312-8318. DOI:10.1021/acs.nanolett.0c03481.
5. Kozhakhmetov, A., B. Schuler, A. Tan, K. Cochrane, J. Nasr, *H. El-Sherif*, A. Bansal, A. Vera, V. Bojan, J. Redwing, *N. Bassim*, S. Das, R. Hennig, A. Weber-Bargioni, and J. Robinson. "Scalable Substitutional Re-Doping and

its Impact on the Optical and Electronic Properties of Tungsten Diselenide." ***Advanced Materials*** 32, no. 50 (2020): 2005159. DOI:10.1002/adma.202005159.
6. Rajabpour, S., A. Vera, W. He, B. Katz, R. Koch, M. Lassaunière, X. Chen, C. Li, K. Nisi, *H. El-Sherif*, M. Wetherington, C. Dong, A. Bostwick, C. Jozwiak, A. van Duin, *N. Bassim*, J. Zhu, G. Wang, U. Wurstbauer, E. Rotenberg, V. Crespi, S. Quek, and J. Robinson. "Tunable Two-Dimensional Group-III Metal Alloys." ***Submitted*** (2021). arXiv:2106.00117.
7. Whittier, C., R. Anthony, *H. El-Sherif*, A. Knights, and *N. Bassim*. "Transmission Electron Microscopy study of SiGe fabricated via Ge+ ion implantation and preferential Si oxidation." ***submitted*** (2021).
8. Al-Atabi, H., *H. El-Sherif*, *N. Bassim*, C. Jones, J. Edgar. "Compositional and structural analysis of single crystal Scandium Nitride." ***In preparation*** (2021).
9. Mohamed, A., O. Taha, *H. El-Sherif (co-second author)*, L. Connerton, P. Hooton, *N. Bassim,* I. Connerton, A. El-Shibiny. "Bacteriophage ZCSE2 is a Potent Antimicrobial Against Salmonella enterica Serovars: Ultrastructure, Genomics and Efficacy." ***Viruses*** 12, no. 4 (2020): 424. DOI:10.3390/v12040424.

(C) Conference publications from this thesis and beyond (2017–2021):

- *El-Sherif, H.*, et al." ***MSC Bulletin*** 47, no. 1 (2021).
- *El-Sherif, H.*, et al. ***Microscopy and Microanalysis*** 27, no. S1 (2021). DOI:10.1017/S1431927621002671.
- *El-Sherif, H.*, et al. ***Microscopy and Microanalysis*** 26, no. S2 (2020): 3116–3118. DOI:10.1017/s1431927620023867.
- *El-Sherif, H.*, et al. ***ECS Meeting Abstracts***, IOP Publishing, no. 23 (2020): 1342. DOI:10.1149/MA2020-01231342mtgabs.
- *El-Sherif, H.*, ***Microscopy and Microanalysis*** 24, no. S1 (2018): 470–471. DOI:10.1017/s1431927618002842.

(D) Conference presentations from this thesis and beyond (2017–2021):

- Oral conference presentations as a first author (**3** national, **5** international).
- Poster conference presentations as a first author (**4** national, **2** international).
- Invited conferences (**1** international at ECS 2020 conference)
- Invited seminars (**1** national at Simon Fraser University)

Chapter 1 : Preface

1.1. Thesis story

How does a material behave in bulk form? This question could be a mysterious observational question until this behavior can be explained microscopically or/and spectroscopically down to the smallest building block of the material, which is the atom. Understanding materials at the atomic scale is the key factor for material fabrication, design, and selection for many applications. In recent decades, characterization near and at the atomic scale helped the needs of the industrial sector of electronic materials for the development of novel and efficient devices. These devices, such as transistors, are now manifested in our daily life as part of smartphones, laptops, satellites, televisions, and more.

The electronics industry depends mainly on silicon as a substrate, in addition to other solid-state crystalline materials, mainly in the form of thin films or recently two-dimensional materials stacked on top of each other. The stack of these layers is the actual electronic device that could perform differently at certain thicknesses and with specific quality of the layers. Characterization of this material stack in cross-section view by electron microscopy is facilitated by the preparation of cross-sections with methods such as mechanical polishing or, recently, by focused ion beam systems. Characterization of cross-sectional electronic materials near-atomic scale is lately expanded by the development of the aberration-corrected scanning transmission electron microscopy (AC-STEM) equipped with analytical tools such as electron energy-loss spectroscopy (EELS).

In this thesis, advanced aberration-corrected STEM and EELS characterizations in the cross-section view are developed and employed for characterizing novel electronic material stacks. This characterization is applied to understand the **bulk behavior** of two material system stacks that exhibit atomically thin layers at their interfaces. The first bulk behavior is the *delamination* of a thin film of cadmium telluride (CdTe) from its sapphire substrate and its high-quality heteroepitaxial growth. Second is the wafer-scale *coverage percentage* of the two-dimensional gallium (2D-Ga) -intercalated epitaxial graphene interface. Although CdTe/sapphire and 2D-Ga are two different material systems fabricated with different techniques, the *atomically thin layers* at both interfaces are found to affect the material in bulk, and are influenced by the substrate surface reconstructions upon which the layers grow.

Delamination of CdTe after growth on the sapphire substrate provides an opportunity to transfer the CdTe film to arbitrary substrates, such as crystalline, non-crystalline, and flexible substrates. This transferring process may be used to build heterostacks that function as devices for optoelectronic devices. Recently, our work presented a low-temperature growth of CdTe on a sapphire substrate using pulsed laser deposition.[1] In this work, the CdTe is grown strain-free, incommensurately to the substrate, and remarkably delaminated in bulk due to an atomically thin layer of tellurium present at the interface.[1, 2] Here, the root cause of this delamination can be explained by the basic understanding of the CdTe/sapphire interface at the atomic scale. Atomic structure, chemical composition, and bonding at this interface complexion are revealed by STEM and EELS with aberration-corrected electron microscopy. The understanding of this interface is related to the growth temperature and the substrate termination.

Coverage percentage calculation of two-dimensional materials over millimeter bulk scale is an extremely challenging scaling-up task. Unlike CdTe, which has a uniform coverage with a few hundred nanometers thickness, a 2D material can be messy, contaminated, and disconnected at the nano- and micro-scale because of the challenges of growing 2D materials. Film thickness and quality determination at the lateral–bulk scale of 2D materials may be estimated with spectroscopic photon-based techniques (XPS mapping, Raman mapping, and ellipsometry), but these techniques provide only a holistic indication limited by the spectroscopic beam size, which is a few to hundreds of micrometers. This resolution limit can be far exceeded with electron microscopy techniques capable of resolving the atomic scale. Nevertheless, the span length of a typical electron microscopy image covers only a few tens of nanometers in the case of using AC-STEM techniques. Here, correlative electron microscopy protocols can bridge both the span-length limit and the resolution limit by correlating signals from different techniques. An example of this is our multiscale characterization of 2D-Ga heterostructures to calculate the coverage percentage of the intercalated gallium over a millimeters span length and with enough resolution in secondary electron contrast to resolve the number of atomic layers of the heterostructure.[3] The characterization of 2D-Ga utilizes scanning electron microscopy image contrast that is affected by the local surface potential of a 2D-Ga heterostructure. After applying multiscale correlative microscopy workflows, changes in local potentials can be categorized with its secondary electron emission and used to identify the existence of intercalated gallium regions and the thicknesses of the heterostructure.

On another thread, the work from this thesis raises the importance of material characterization *beyond the atomic scale*. The STEM and EELS characterization of

these two systems revealed the subtleties of substrate **surface reconstruction** for heteroepitaxy with sub-atomic scale distortions that could affect material growth. In the case of the CdTe/sapphire interface, the topmost layer of sapphire has a surface reconstruction to minimize the surface energy. This reconstruction is prevalent after the low-temperature growth of the CdTe film, in which a tellurium monolayer terminates the sapphire with weak bonding. In the case of the 2D-Ga, the silicon carbide substrate has highly energetic silicon dangling bonds at the SiC-buffer layer interface, which are passivated by the Ga atoms. However, our work reveals a surface reconstruction at the topmost SiC layer that exists prior to the intercalation process. This surface reconstruction may be responsible for the observed structural changes in the 2D-Ga to accommodate strain at the interface.

1.2. Thesis outline

Chapter 1 summarizes the thesis story and provides an outline of the thesis chapters.

Chapter 2 provides background information on three main topics. First, the chapter covers the two-dimensional materials and heterostructures and the associated applications challenges. Then, the fundamentals of heteroepitaxy interfaces and surface reconstruction are discussed, focusing on the spontaneous van der Waal growth, which is the fabrication of the material used in chapter 3. Subsequently, the chapter focuses on confinement heteroepitaxy and the intercalation of epitaxial graphene/SiC interfaces, which is the fabrication method for the material used in chapter 4. Furthermore, the chapter demonstrates background on the basics and techniques of electron microscopy characterization

used throughout this thesis. Finally, the chapter discusses the motivations for using advanced STEM and EELS techniques to characterize heteroepitaxial systems with weakly bonded interfaces.

Chapter 3 focuses on the electron microscopy characterization of the CdTe/sapphire interface, the CdTe film, and the sapphire substrate. First, the chapter covers the conditions and the setup used to fabricate the CdTe thin film. Then, atomic-scale STEM and EELS characterization is discussed to explain the structure and bonding at the interface to reveal an atomically thin tellurium layer that terminates the sapphire substrate. Also, the quality of the CdTe film, the delamination of the film, and strain analysis at the interface are studied. The chapter discusses the surface reconstruction of the topmost sapphire layer and the thin tellurium layer thickness variation, including the possible formation of a tellurene (i.e., 2-D tellurium) structure.

Chapter 4 concentrates on the characterization of atomically thin gallium (2D-Ga) intercalated at the epitaxial graphene interface. First, the chapter explains the sensitivity of SEM image contrast to the peculiar details of the 2D-Ga heterostructure. The SEM contrast is discussed extensively concerning the heterostructure thicknesses and the location of gallium. Then, the thickness and location of the 2D-Ga are quantitatively analyzed by STEM image-stitching and segmentation methods to scale up the characterization of the 2D-Ga to cover a few millimeters squared area. Following this, the significance of SEM contrast (and hence local material structure) on electron transport and optimizing the 2D-Ga fabrication is discussed. Then, STEM imaging and spectroscopic techniques are deployed to understand the air stability of the 2D-Ga structure and SiC-Ga

interface instability, revealing possible surface reconstruction effects at the topmost layer of the SiC substrate.

Chapter 5 delivers conclusions and contributions to the field from the characterization work done for the two materials systems in this thesis, followed by the similarities of the two systems and their potential applications. The chapter ends with a list of possible future works.

Finally, appendices are added to support some claims in chapters 3 and chapter 4.

Chapter 2 Background

2.1. 2D materials and heterostructures

2.1.1. Why 2D materials?

Two-dimensional (2D) materials are planar materials that are often one or few atoms thick with a large lateral extent. Two-dimensional materials are in-plane confined layers that give properties that are often very different from their 3D bulk form because the surface states, in the case of 2D materials, are a larger proportion of the total bonds. Many of these materials are stable at ambient conditions, which allows them to be integrated into many applications. They tend to have covalent or metallic bonds in-plane and van der Waals bonds in the out-of-plane direction. Depending on the number of 2-D layers in a stack of layers, as well as electronic coupling with the substrate, the electronic and optical properties of 2-D structures can be changed quite dramatically.[4] 2D materials offer opportunities for the creation of 2D heterostructures with a variety of properties and the invention of novel devices in the field of electronics, energy harvesting, biosensing, and environmental monitoring.[5]

In this thesis, scalable electronic devices of 2D materials and heterostructures, such as transistors, are the main concern for the wide and rapidly expanding 2D materials field. Motivation towards understanding the growth of scalable 2D electronics is necessary because achieving transistors or other switches at the atomic level (1~5 atomic layers) could theoretically finish Moore's law. In addition, 2D semiconductors may go beyond Moore's law limit by fitting 2D devices on top

of each other to form hierarchical vertical structures. With this motivation, 2D electronics may achieve much higher communication speeds.[6, 7] Besides the atomic size factor, 2D semiconductors have a higher electrostatic gating control – because of atomic-scale thickness – than silicon, which could overcome the issues related to short-channel effects. That is because of their atomic-scale thickness and lower dielectric constant.[8]

2.1.2. Graphene

Bulk graphite has been recognized for centuries as an attractive, delaminated material. The first known 2D material, Graphene, was discovered by A. Geim and K. Novoselov in 2004 by mechanically exfoliating graphite using scotch tape.[9] The discovery of graphene was awarded the 2010 Nobel prize, and since then, it opened the door for hundreds of thousands of research publications in this area. Nowadays, graphene flakes are commercialized in many daily-life applications, such as flexible printed-electronic inks[10] and in the improvement of batteries.[11] In the field of scalable electronics, graphene, with its zero value bandgap, is applied in many research devices as a conductor or semiconductor after doping. The scalability of graphene for electronic devices is achieved through two main fabrication processes: an additive process with the chemical vapor deposition of cracked methane on copper or nickel substrates[12] and the subtractive process of silicon sublimation from silicon carbide (SiC) substrate, which leaves behind a graphene film.[13, 14] The first method results in centimeter-wide, or higher, graphene on copper foils, which needs to be transferred to dielectric substrates for electronic applications. The second fabrication method does not require further transfer processing because SiC is a

dielectric substrate, and while it results in graphene grown within SiC micro-terraces, it covers all of a SiC substrate surface – that may be a few centimeters wide.

2.1.3. 2D materials beyond graphene

Instead of doping graphene to open a bandgap, the 2D confinement can be found in many other 2D materials with a variety of bandgaps. First-principles studies suggest the applicability and performance of hundreds of new 2D materials. In a recent study[15], computational calculations are conducted for 258 two-dimensional materials in which only a few tens of them are already tested experimentally. It requires extensive experimental research to fabricate and apply 2D materials beyond graphene in a real-life product, especially for electronic-grade applications. There are a variety of 2D semiconducting materials – such as transition metal dichalcogenides (TMDs), hexagonal boron nitride (hBN),[16, 17] Phosphorene,[18, 19], and Tellurene.[20, 21]

For example, tungsten diselenide or molybdenum disulfide offers opportunities for fabricating low-power electronics because of their nonzero bandgap in contrast to graphene. Two-dimensional electronics can achieve the minimum size possible electronic devices on a chip which may change the semiconductor industry that has been based on silicon substrates historically.[22] Another category of confined 2D materials was introduced recently via the confinement heteroepitaxy technique, which is typically a method for intercalation of atomic layers between deliberately defect-filled epitaxial graphene and a silicon carbide substrate.[23, 24] This method offers a new route to designing 2D metal, 2D nitride, and 2D oxide heterostructures protected with a graphene capping layer.

2.1.4. 2D van der Waals heterostructure

The integration of multiple 2D materials in heterostructure form is a way of making devices for a real-life application. This integration can be customized by mechanically stacking different 2D materials to make heterostructures.[25, 26] Different 2D layered structures can be used to build functional 2D heterostructure devices with countless combinations.[27] That functionality is because every 2D layer has its own potential and electronic properties. The stack of 2D materials has a different electron structure as a result of the assembly of quantum wells. Assuming we have 10 different 2D materials, the possible alternatives to stack the 10 layers are 10 to the power of 10 (=10^{10}) probabilistic alternatives. This gives the opportunity for designing heterostructures with different electron band alignments that function for specific devices at certain conditions in voltage and current of a gate-source-drain design. Figure 1 shows a schematic diagram of 2D vdW heterostructures made of graphene, h-BN, and TMDs. These heterointerfaces can offer completely different types of 2D electronic systems by changing the Fermi levels and the bandgap structure. However, the synthesis of high-quality heterostructures is limited by a variety of materials growth factors, including the mismatch of crystal structures, the orientation of the substrate, and the proposed 2D material needed to be grown. Moreover, the growth and electronic properties of materials are affected by the lattice constants of the materials and their thermal expansion coefficients.[28, 29]

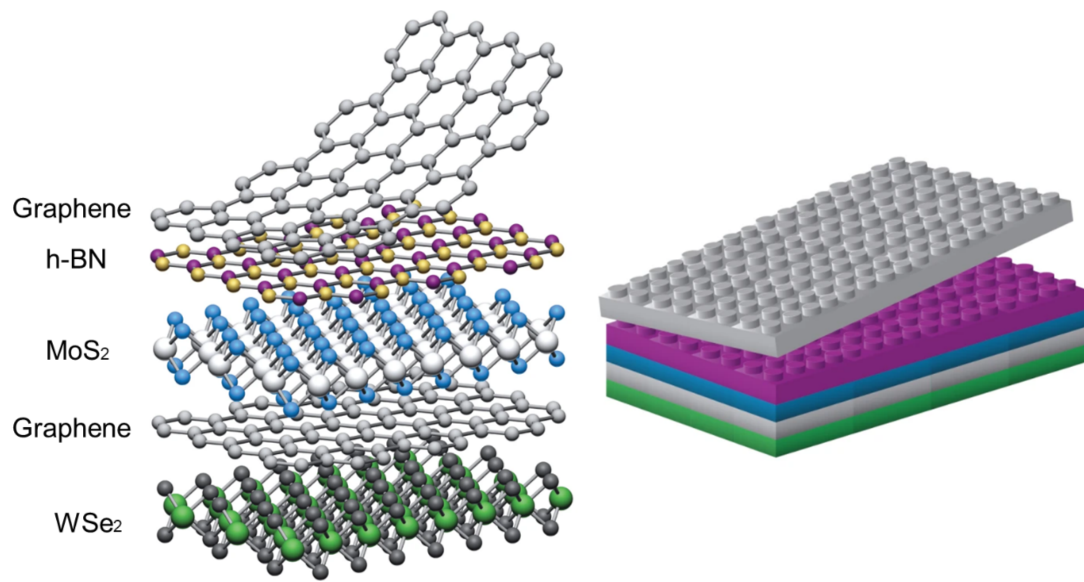

Figure 1. 2D materials vdW heterostructure. Schematic diagram, reproduced from [30], of 2D vdW heterostructures composed of graphene, h-BN, MoS_2, and WSe_2. The stacking process of the heterostructure is similar to the stacking of building blocks.

2.1.5. Application challenges of 2D materials

Desirable properties of 2D materials make them candidates for integration in many real-life applications, which is currently a common research question posed to many theoretical and experimental research communities. Integration challenges are mainly related to implementing a scalable fabrication method and the environmental stability of 2D layers or heterostructures. Optimization of the geometry and performance of a 2D material device are crucial factors for end-use applications.[31] The performance of these devices can be constrained by the advances in wafer-scale fabrication, bonding or interconnection, the associated contact resistance, and generally how to function/scale-up an atomic-scale device in a macro-scale system.[32] In addition, grain boundaries and other defects will lower the quality of the 2D materials.[33, 34]

In this thesis, the scalable fabrication and characterization of 2D materials is the main challenge to solve. Other non-scalable preparation methods, such as mechanical exfoliation or liquid-based exfoliation, resulting in small size 2D flakes, which limit the properties and performance over a large area in a wafer with one or more centimeters size. For graphene, CVD synthesis on copper provides large-scale fabrication. Many other successful trials have also been pursued to fabricate TMDs on sapphire substrates [35-37] at wafer-scale for electronic-grade applications.[8, 38-42] One of the considerations for a large-area CVD growth is the matching size of the lattice spacing between two layers in a heterostructure or between a 2D material and the substrate. For example, graphene and h-BN have a ~1.8% lattice spacing difference, which is called lattice mismatch percentage.[43] This can be controlled by a careful choice of fabrication methods and their processing parameters to achieve different phases of the same 2D materials.[36] In addition, it is important to understand the dynamics of atoms on the surface during the nucleation process.[44]

2.2. Heteroepitaxial interfaces

2.2.1. Epitaxial growth

Epitaxy is a word from the Greek root *epi*, which means above, and *taxis* which means an ordered manner. Epitaxy has been the dominant technology for developing a variety of modern optoelectronic devices. The epitaxy process is a growth of deposited atoms on a typically single-crystal substrate that templates the crystallographic orientation to form a crystalline thin film of the deposited atoms.[45] Epitaxy can be classified into two main processes.

First, *homoepitaxy* is the growth of the same material as the substrate, as illustrated in Figure 2a. The motivation for growing this same material as the substrate is to obtain a single-crystal thin film with higher quality than the bulk substrate, which can be fabricated under certain conditions. In addition, homoepitaxy growth allows the incorporation of dopant atoms that subtly alter the electronic structure of the material with few defects introduced into the system.

Second, *heteroepitaxy* is the growth of a dissimilar material to the substrate, as seen in Figure 2b-c. Because of this dissimilarity, the heteroepitaxial layer shares a congruent crystal structure but is not identical to the substrate, resulting in an interface with a unique structure, composition, and bonding. Beyond the interface, the heteroepitaxy growth of the thin film can be structurally relaxed after a few layers away from the interface, as seen in Figure 2b. This strain relaxation occurs through the development of misfit dislocations, surface roughness, or other crystallographic defects. To decrease the interface-related dislocations, the orientation of the growth direction between film and substrate is an essential factor because, in specific directions, a lattice mismatch can be accommodated, as seen in Figure 2c. Another option is to grow epitaxial layers below a certain critical thickness to suppress dislocation nucleation.

2.2.2. Heteroepitaxial interface bonding

Transferring an epitaxial relationship to the thin film from the substrate can occur with multiple interface bonding scenarios. This relative bond strength can be varied from weak vdW bonds, covalent bonds, metallic bonds, and ionic bonding, depending on the substrate, the deposited film, and the growth conditions. For example, a metamorphic growth (Figure 3a) has a buffer of compositionally

graded material that is covalently bonded to the atoms of the substrate and the film. This metamorphic interface prevents the film delamination but gradually changes the lattice constant from that of the substrate to the lattice of the film to accommodate strain and lattice mismatch at a certain critical thickness of the film. In some cases, a weak interface bonding occurs at the interface while transferring the substrate information to the film's adatoms that are locked in place by vdW forces. This is called a van der Waal epitaxy which mainly happens when a substrate does not have dangling bonds, and thus no chemical bonding has occurred.[46] For example, the growth of epitaxial gallium nitride thin films on an epitaxial graphene layer attached to a silicon carbide substrate.[47] In this case, the thin film can be delaminated after the growth, and it has no misfit dislocations because of the weak bonding.

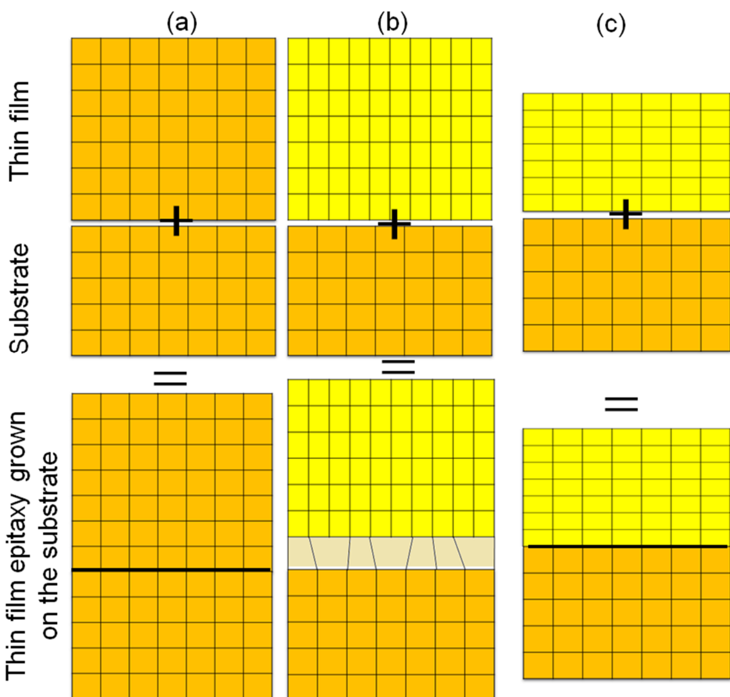

Figure 2. Schematic illustration of epitaxial growth. (a) homoepitaxy growth. (b) heteroepitaxy growth between lattice-mismatched desired-film (yellow)

and substrate (orange) with a relaxed interface. (c) heteroepitaxy growth between lattice-matched film and substrate. Lines represent atomic planes in this schematic.

Understanding the bonding at the atomic level at the interface determines the understanding of the thin film bulk behavior such as delamination from the substrate, crystallography of the film, and the film quality. One of the main goals to improve thin film quality is to reduce the dislocation density inside the film because lower dislocation density corresponds to higher carrier mobility when applying this thin film in electronic applications. For this purpose, misfit dislocation suppression at the interface is one of the factors that can be controlled when fabricating thin films.

2.2.3. Heteroepitaxial interface mismatch

A mismatch means that there is a difference between the lattice constant of the heteroepitaxial thin film (or 2D material) and the corresponding substrate. Lattice mismatch is a significant concern for fabricating wafer-scale of thin films or 2D materials. Larger mismatch values lead to loss of symmetry in one lattice direction or more. This mismatch introduces linear defects that accommodate the mismatch strain. As a result, the crystal will have tensile and compressive strains near the interface.

Figure 3 illustrates strategies for accommodating strain at the interface by engineering the atomic bonding at the interface. Compositionally graded interface, as illustrated in Figure 3a, accommodates the strain by providing an interface zone with different compositions. This compositionally graded interface changes the lattice constant gradually between the substrate and the thin film. This interface is

called metamorphic, and accommodates strain from the lattice mismatch between the substrate and film. However, this interface exhibits higher density dislocations associated with the high-temperature growth of this metamorphic interface, such as threading dislocations.[48] As a result of both the dislocations and metamorphic interface, the performance of the thin film for electronic applications can be degraded significantly. This problem motivates research communities to introduce new fabrication methods without a compositionally graded interface.

Sharp transitions in composition from the substrate to the thin film is achieved for both thin film and 2D material systems. For example, a mechanical transfer of a 2D material over another 2D material (such as graphene on boron nitride) has interfaces with weak interaction and no or minimal composition changes, as illustrated in Figure 3b. This 2D/2D interface is also achieved using metal-organic chemical vapor deposition (MOCVD) methods to grow Tungsten diselenide (WSe_2) on graphene.[49]

The same sharp transitions behavior can also be achieved using a modified buffer layer at the interface for 2D/3D and 3D/3D systems, as illustrated in Figure 3c-d. This buffer layer may be transferred mechanically or grown epitaxial to provide weak interaction at the interface for growing the thin film or the 2D material. The grown layers can be easily delaminated away from the substrate due to the presence of weak interactions at the interface. Furthermore, the substrate with the buffer layer can be used for further growth of the 2D layer or thin film after the first delamination, similar to a copying machine.[50] Here, the weak interface bonding is the key point to obtain a sharp composition transition interface over a

wafer-scale fabrication. This weak bonding mitigates the interface strain while still transferring the epitaxial relationship to the grown film.[51]

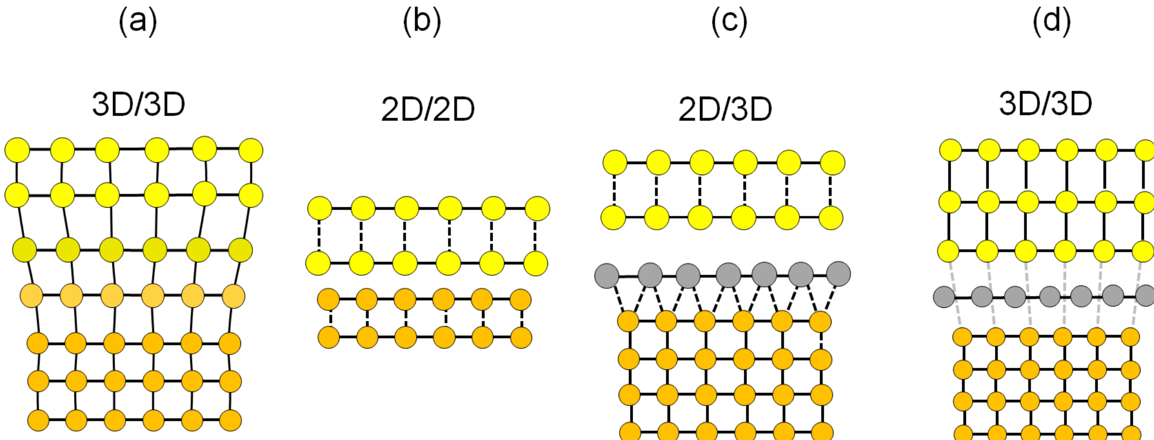

Figure 3. Heteroepitaxial interfaces to overcome lattice mismatch. (a) Illustration of metamorphic 3D/3D growth, for which the substrate (orange) and epitaxial film (yellow) have different lattice constants. (b) Illustration of vdW epitaxy of a 2D material on a 2D substrate (2D/2D). Strong bonding is in-plane, as indicated by the solid lines on the substrate and film. Weak vdW-bonding occurs out-of-plane, indicated by the hashed lines, to accommodate the lattice mismatch. (c) 2D/3D material system where a thin layer (gray color) is deposited to passivate the surface. (d) An illustration of remote epitaxy of a 3D film on a 3D substrate (3D/3D). The substrate surface is modified by a mechanically transferred 2D material (gray color), such as graphene, which allows for weak interaction at the interface.

2.2.4. Surface reconstructions

Surface reconstruction is a minimization of the overall electronic and bonding energies of the topmost layer or a few layers of a crystal. The reconstructed layers are also known as the "***selvedge***" layer, which causes crystallography changes within a scale of sub-Angstrom displacements, as seen in Figure 4. These tiny changes in the atomic spacing at the top layers differ from those of the bulk interior crystal. Surface reconstruction is a significant factor associated with substrates

used for growing thin films. Reconstruction may occur just after the cleavage of a bulk crystal to obtain a substrate for growth. Other reconstructions may be induced at a higher temperature. The reconstruction forms a new surface lattice constant with a corrugated shape, which is described by its in-plane periodicity and out-of-plane rotation relative to the original bulk crystal.[52]

Annotation of the surface reconstruction is usually described by the in-plan periodicity relative to the original bulk periodicity. For example, in Figure 4d the original lattice of the 6H-SiC hexagonal lattice has an in-plan structural unit cell of 1×1 periodicity. After the reconstruction, the unit cell will become larger due to an out-of-plane corrugation of the topmost layer. The size of the first possible new "*in-plane structural unit cell*" reconstruction (occurs around 800 °C) is √3 larger than the original 1×1 periodicity. In addition, this new reconstruction is twisted out-of-plane by 30° relative to the original periodicity. Thus, the reconstruction of the 6H-SiC that happens around 800 °C is called "(√3 × √3) R30°" surface reconstruction, which represents only the in-plane deformation at the topmost layer. On the other hand, the out-of-plane deformation is simply described by the selvedge distance "*d*" in Figure 4b-c, which is the spacing between the reconstructed layer (or layers) surface and the original bulk interior crystal surface.[14, 53, 54]

In a heteroepitaxial interface, surface reconstructions are essential to understand because they can affect the growth behavior and the thin film quality. Growing a thin film on an energy-minimized surface could lead to weak interactions at the interface, which can accommodate the subsequent epitaxial growth. An example of this is the (6√3 × 6√3) R30° reconstruction on hexagonal 6H-SiC, which is called the *carbon buffer layer* because it is richer in carbon than silicon. This reconstructed

layer is attached to the SiC and allows epitaxial growth of thin films relative to the SiC substrate.[55]

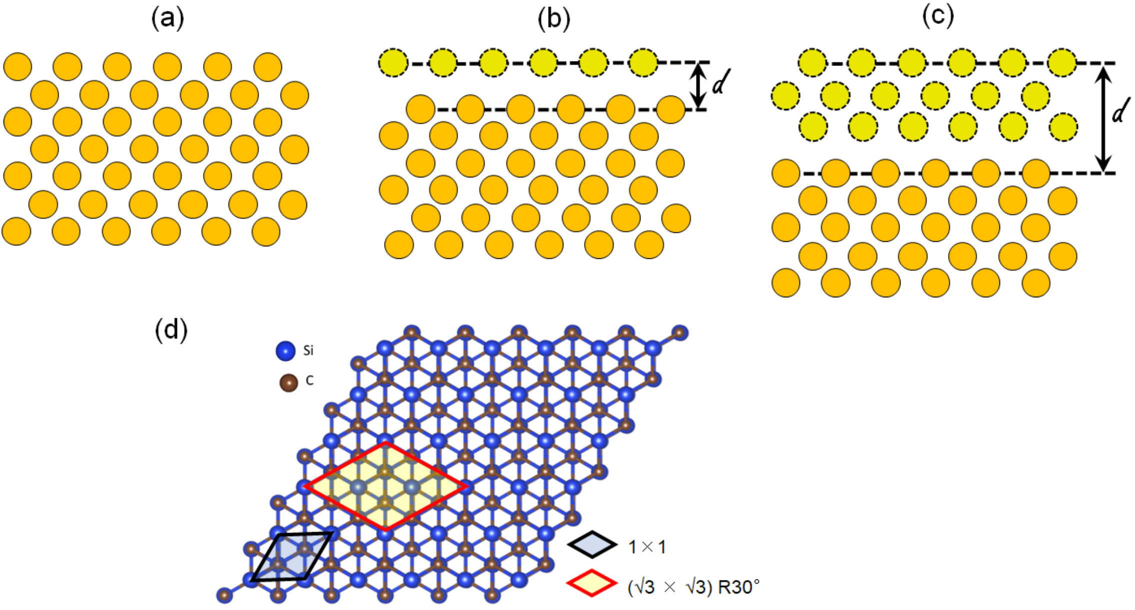

Figure 4. Schematic cross-sectional view of solid and reconstructed surface. (a) Bulk exposed plane. (b) Outward atomic relaxation. (c) Reconstruction of outer layers. The ***d-spacing*** represents the selvedge distance due to the surface reconstruction. The distance *d* represents the spacing between the reconstructed layer (or layers) surface and the original bulk interior crystal surface. (d) in-plan view of the 1×1 periodicity and (√3 × √3) R30° surface reconstruction on the surface of SiC.

2.2.5. Growth of heteroepitaxial materials

2.2.5.1. Mechanical stacking of 2D materials

Heteroepitaxial interfaces may be prepared by mechanical stacking of exfoliated flakes in the air atmosphere. The goal of mechanical stacking is the placement of a crystal (2D material or thin film) in a specific desired location, which could be on a substrate or directly on another crystal. Heterostructure interfaces prepared by mechanical stacking are generally limited to the size of *micrometer* flakes, which

disadvantages the growth capability of scalable electronics and hence the practical application. However, the recent development of mechanical stacking methods in a vacuum enables the transfer of a large area of 2D materials over a few millimeters to centimeter sizes.[56, 57]

2.2.5.2. Thermal methods

In this thesis, epitaxial growth is meant to be a thermal method that provides *scalable* fabrication of films with millimeter size or higher. Thermal fabrication of heteroepitaxial interfaces and structures is categorized into two main methods: chemical vapor deposition or physical vapor deposition. The following paragraphs provide a brief overview of these methods.

Chemical vapor deposition (CVD) is the most applicable and promising technique for the fabrication of wafer-scale heterostructures, thin films, and many semiconductors. There are many types of CVD processes categorized depending on the growth temperature, precursor compositions, and level of vacuum. A chemical interaction occurs between precursors near the substrate, which results in the deposition of atoms on the substrate. The growth temperature activates the substrate surface to adsorb and diffuse vapor heteroatoms and build a thin film in the bottom-up direction inside a furnace atmosphere. Typically, the CVD process is performed inside a vacuum-environment reactor (as simple as a tube furnace) at high temperatures ranges, such as 800–1200 °C, enables the chemical interaction between the precursor and the substrate. Due to the high temperature, the interface could have a mixture of gradual compositional changes between the substrate and the film, which is called a metamorphic or pseudomorphic interface. This is because the surface often reconstructs, and there is a reaction at the growth

interface. Relaxation of the metamorphic interfaces results in high dislocation density that is created at a minimum critical thickness of the metamorphic layer.[58-60]

Physical vapor deposition (PVD) does not require chemical interaction prior to the deposition process. Instead, the atoms of the thin film substance are evaporated or sputtered at low vacuum pressure, then deposited on a substrate at low temperature. The evaporation process may be applied by a laser beam or a thermal heater, far from the substrate. Then, the evaporated atoms may be transferred to the substrate region with the help of an inert or reactive gas flow (or simply their mean free path in a vacuum environment), depending on the desired film composition. This allows lower temperature growth needed at the substrate region.

Both CVD and PVD produce scalable films. The quality of these films is controlled by the growth parameters such as temperature, material deposition rate, and degree of vacuum. The behavior of the surface reconstruction of the substrate at specific growth conditions is also a critical factor. In addition, the surface roughness of the substrate and step edges at the atomic scale is also a significant factor to be considered for high-quality growth.

Nowadays, the holy grail in research efforts related to 2-D materials is to achieve scalable and high-quality films with affordable synthesis and characterization routines. The following two sections discuss two epitaxial growth methods that are recently developed for scalable and high-quality 3D/3D and 2D/3D material systems.

2.2.6. Remote and spontaneous van der Waal epitaxy

In this section, a background of growing incommensurate and transferable thin films by the remote epitaxy method is discussed. Growing large-scale films with this method is limited by the associated 2D layer transfer process. This may be overcome by using sapphire (Al_2O_3) as a substrate for the synthesis of chalcogenide-based thin films.

2.2.6.1. Remote epitaxy

Remote epitaxy is a current strategy to overcome heteroepitaxial lattice mismatch by introducing a 2D material interlayer (such as graphene) on a substrate before depositing a film using a metalorganic chemical vapor deposition (MOCVD) or pulsed laser deposition (PLD), typically at 600-900 °C.[50] Remote epitaxy can be either homoepitaxy or heteroepitaxy. For example, graphene-coated substrates allow remote epitaxy growth of highly lattice-mismatched single-crystalline films with a reduced dislocation density.[61] This allows the growth of transferable films that are incommensurate to their substrates. At a particular type and number of 2D layers, the epitaxial registry can be preserved between the film and substrate without the direct formation of rigid bonds, which act as a transparent layer to intermolecular interactions. [46, 62] For example, the quality of a homoremote epitaxy of a gallium nitride (GaN) thin film is optimized for one layer of graphene terminating the interface of a GaN substrate, as illustrated in Figure 5a. The quality of the GaN is assisted by the electron back scattering diffraction (EBSD) mapping over a few micrometers to look at the crystallinity of the grown film. But for a homoremote epitaxy of gallium arsenide (GaAs), three layers of hexagonal boron nitride (h-BN) are found to produce high-quality GaAs film rather than a

monolayer h-BN, as illustrated in Figure 5d-f. The variation of the 2D layer thickness originates from the ionicity of a substrate to the penetration distance of the electrostatic forces for a given 2D material. The ionicity mass and penetration distance can be theoretically calculated for a combination of substrate and 2D materials to optimize the 2D layer thickness required for transferring the charge from the substrate to the film and consequently produces a high-quality film.[50, 63]

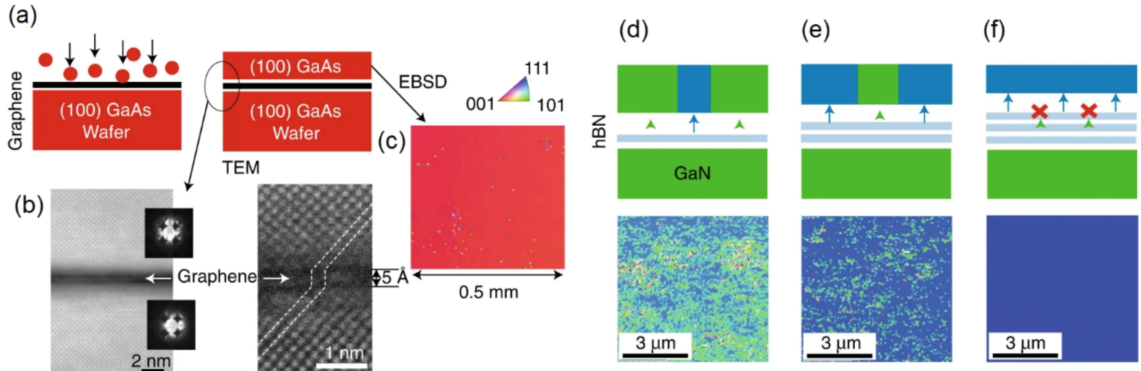

Figure 5. Remote Epitaxy. (a) illustration of the remote epitaxy interface. (b) cross-sectional TEM at GaAs/graphene/GaAs interface showing the atomic interaction of GaAs through graphene. (c) electron back scattering diffraction (EBSD) of remote epitaxial GaAs showing one single domain of the GaAs (001). (d-f) Schematic (top) and EBSD (bottom) of the exfoliated surface of GaN on 1, 2, and 3 hexagonal boron nitride (hBN) transferred on the GaN substrate. The highest quality of the remote epitaxy GaN is found in (f), where the hBN is 3 layers, which is different from the optimized number of the layer in the case of graphene in (b).[46]

2.2.6.2. 2D Materials transfer

Introducing 2D materials on a substrate can be applied by transferring layers with the assistance of a wet chemical etching method or by using a thermal release tape in a dry process. The wet process starts with fabricating a 2D layer foil which is a

2D material grown on a foil substrate such as graphene on copper foil or hexagonal boron nitride on platinum foil. Then, the foil is coated with a polymer film (such as Polymethyl methacrylate, PMMA) on the 2D layer face using a spin coater. Using an acid, the metallic foil can be dissolved. This makes the 2D layer attached only to the polymer film floating on the acid surface tension. This floating layer can be transferred to another substrate and cleaned from the polymer by acetone.[64] The dry method directly attaches the 2D layer with thermal tape (Kapton tape) at room temperature, then released it at the desired substrate at a higher temperature. The thermal expansion of the tape and the 2D layer is different. Hence, the 2D layer can be detached from the tape when slightly heated. The substrate should be very clean to enable the 2D layer to be attached firmly to the substrate after the detachment from the thermal releasing tape[65]

The quality of the transferred 2D layer is affected by the transfer method in which traces of polymer in the wet method, or the glue in the thermal tape, are still attached to the 2D materials. This motivates much research to minimize the density of the polymer contamination, which improves the quality of the transferred 2D layers for applications. However, no perfect polymer removal can be achieved down to the atomic level. These contaminations, as well as defects in the 2D layers, are usually seen in high-resolution TEM.[66] This transfer quality limits and controls the large-scale fabrication of scalable remote epitaxy layers, which motivates other research communities to find alternatives.

2.2.6.3. Spontaneous vdW epitaxy on chalcogenide-terminated sapphire

Recently, sapphire has been used as a substrate to achieve remote epitaxy of chalcogenide-based thin films, but *without* the use of 2D material transfer. This

allows a new route to remote vdW epitaxy that produces high-quality transferable single crystal of films such as cadmium telluride or indium antimonide. Jae-Yeol Hwang et al. studied the growth of $Bi_{0.5}Sb_{1.5}Te_3$ (BST) on an α-sapphire substrate as an example of a 2D/3D system growth of vdW epitaxy.[67] They found that monolayer tellurium is bonded to the sapphire substrate at the oxygen sites. The authors interpreted the sapphire-Te formation as a result of a surface reconstruction driven by the formation of a pseudomorphic tellurium monolayer during the PLD process, which promotes the spontaneous vdW epitaxy. The growth of the film was via a pulsed laser deposition at low substrate temperature, 200–230 °C. This unique interface was introduced as a new concept for promising spontaneous vdW epitaxial growth.

2.2.7. Confinement heteroepitaxy

2.2.7.1. Silicon carbide

Silicon carbide is a wide bandgap semiconductor, which is commercially implemented on an industrial scale for high quality and high-performance power electronics.[68] The silicon atoms are bonded covalently with four carbon atoms and vice versa. The growth of SiC single crystals can be achieved by a vapor growth method named the Lely method.[69] In this method, the Si and C power sources are evaporated at high temperature (~2500 °C), and inert (Argon) gas environment, in which the vapors sublimate through a porous graphitic crucible towards a seed of SiC placed in the middle of the crucible. The structure of the SiC lattice may vary depending on the Si and C atomic arrangement, which can be controlled during the SiC single crystal growth. Three main SiC structures (known as polytypes) are called 3C, 4H, and 6H in either the Si-face or the C-face direction,

as illustrated in Figure 6. Both the 4H and 6H polytypes have zigzag crystallography in the $(11\bar{2}0)$ direction but with 4 and 6 atomic planes of the unit cell size, respectively. The atomic planes for the 6H unit cell called B^*, A^*, C^*, A, B, and C in which every two layers with the same letter have the exact vertical alignment of the Si atoms but with different carbon polarity. The 3C-SiC polytype has planes without zigzag shape in the $(11\bar{2}0)$ direction, as illustrated in Figure 6**a**. While the 6H-SiC is a semiconductor with a wide bandgap, the 4H- and 3C-SiC structures are considered conductors because they have almost double the electron mobility compared with the 6H polytype. SiC can be Si-face, where the Si atoms face up in the $(000\bar{1})$ direction, or C-face if it is in the (0001) direction. The miscut angle of the SiC single crystal (Figure 7) controls the surface morphology. This miscut results in a step edge and terrace structure in the SiC wafers. The terrace width can be controlled by engineering the miscut angle.[70]

2.2.7.2. Epitaxial graphene (EG)

Due to the terrace-and-step SiC morphology, the thermal heating of SiC at high temperatures (~1300 °C) and vacuum results in silicon sublimation from the SiC surface that starts at the step edges [71-73] because the terrace step edges are a low-energy site for graphene nucleation. The carbon atoms remain on the surface due to their high thermal stability to form graphene layers. Graphene thickness can be controlled by the pressure, time, and temperature of the sublimation process. A buffer layer (BL) of carbon can exist between the SiC and the epitaxial graphene (EG), which allows dangling bonds in the Si atoms. This buffer layer of carbon is bonded covalently to the SiC with a nonsymmetric bonding distribution that allows the existence of dangling bonds at the Si-termination. The BL is

associated with a surface reconstruction that appears around 1000 °C temperature of the Si-sublimation process.[74] The low energy electron microscopy diffraction (LEED) is used to track the surface reconstruction over the growth time to ensure the successful growth at the position of the LEED beam interaction with the sample. In this case, these dangling bonds between the silicon carbide substrate and the graphene limit the electronic properties of the graphene, such as electron mobility, because the graphene out-of-plane bonding is not homogenous.

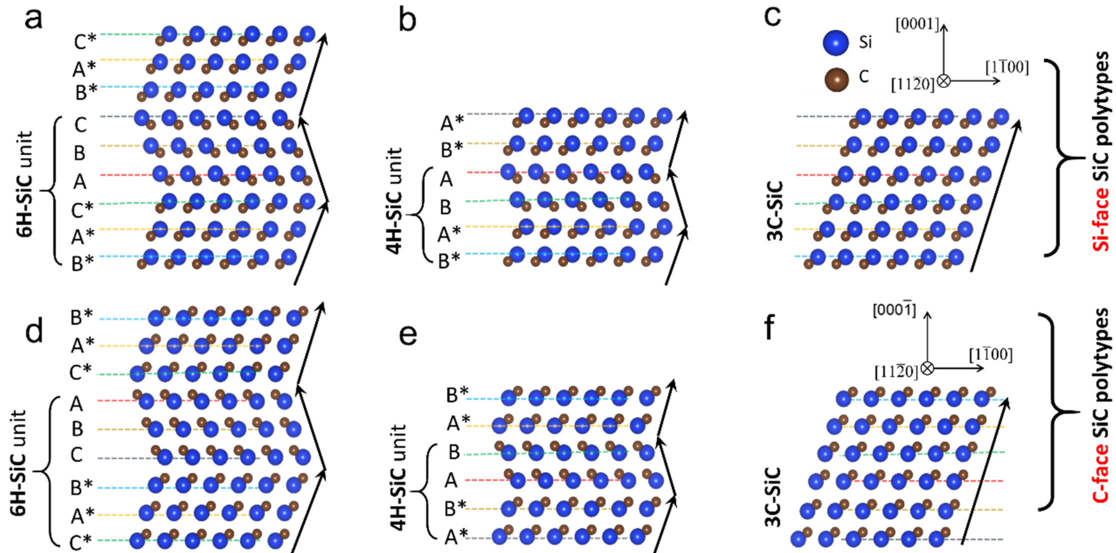

Figure 6. Schematic of the SiC polytypes. (a-c) the stacking order of 6H-, 4H-, and 3C-SiC at the Si-face (0001) direction. (d-f) stacking order of 6H-, 4H-, and 3C-SiC at the Si-face (000$\bar{1}$) direction. The stacking order in (a) is the one used in the experimental work in this thesis.

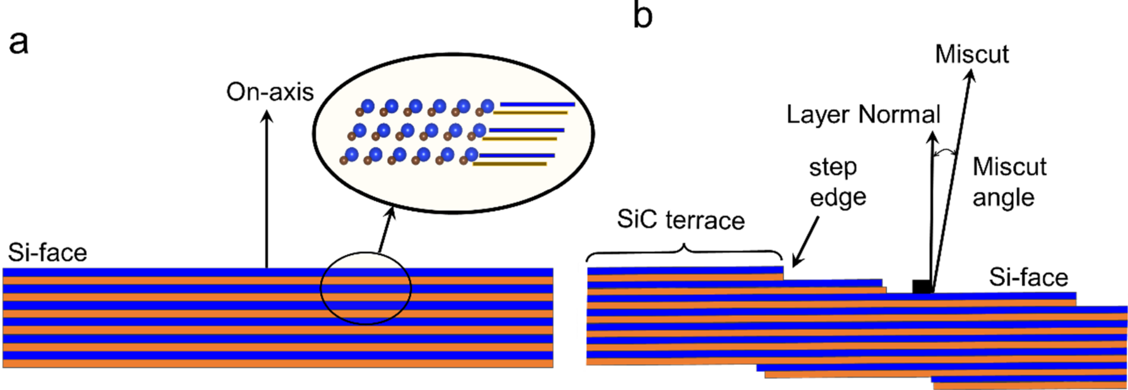

Figure 7. Schematic of the SiC miscut angle. (a) on-axis Si-face SiC substrate. (b) off-axis Si-face SiC substrate. The miscut ends up in a morphology that contains terraces and edges of atomically thick step edges.

2.2.7.3. Nucleation of the epitaxial graphene at the step edges

Faster growth of graphene at SiC step bunches than the terrace middles was reported in [71], and it is presumed to start at the SiC step bunches because these sites have the lowest energy site for graphene nucleation. Figure 8 shows cross-sectional TEM images of a SiC step bunch in the $(11\bar{2}0)$ direction in which the graphene at the step bunches is much thicker than the terraces themselves. These TEM images suggest that the low bonding coordination of the step bunches plane may prevent the required surface reconstruction identified for the formation of graphene on the Si-face (0001) plane.[71, 75] Besides, the SiC surface defects on the terrace step may disturb graphene nucleation and prevent the formation of continuous graphene layers. Understanding EG nucleation and the fact that it initially grows at the SiC step edges have helped to design graphene nanoribbons that can be applied as high electron mobility connectors between devices built on the SiC substrate.[76]

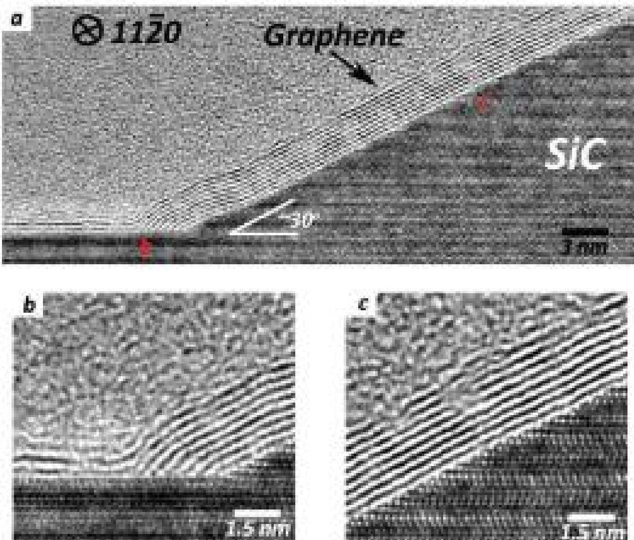

Figure 8. Nucleation of EG on SiC step bunch. (a) multi-layer graphene grown at the SiC step bunch compared with the lower number of layers at the terrace. (b and c) zoom in at the terrace and the step bunch. (d) a schematic diagram shows the noted orientations of the SiC terrace and step bunch.[71]

2.2.7.4. Intercalation of epitaxial graphene

Intercalation of atoms is the process of insertion of atoms or molecules under or in between layered materials such as graphite to modify their chemical or electronic properties. Intercalation of graphite was first reported in 1859 by B. Brodie et al. [77] for the benefit of catalysis. Since then, much work was performed in intercalating graphite and a few graphene layers with gas or liquid molecules or metallic atoms [78] for various applications such as lubrication, catalysis, and electrochemistry. Intercalation of atoms, such as boron [74], at the EG-SiC interface, is possible to increase electron mobility. In the field of epitaxial graphene, it is essential to delaminate the buffer graphene layer that can be attached to the Si-face SiC after sublimation of the Si atoms at high vacuum and high temperature (1000-1300 °C).

The intercalation of epitaxial graphene can be done with hydrogen atoms, *hydrogenation*, or *hydrogen passivation*, to separate the buffer layer from the SiC substrate and to make weak and stable vdW bonds instead of having active dangling bonds.[79, 80] The vdW bonds are a result of the passivated SiC termination, which improves the electron mobility of the graphene because the electron traps will be lowered.[81] This passivation process is considered an electronic-grade and wafer-scale process, and the resulting graphene, called quasi-freestanding epitaxial graphene (QFEG), has many implementations for electronic applications. The QFEG layer resulting from the hydrogen intercalation helps to improve the unique graphene electron transport and mobility for electronic devices in contrast to the as-prepared epitaxial graphene with the buffer layer.[82, 83] The QFEG layer was then used as a platform for building large-scale 2D heterostructures on the SiC terraces.[84, 85]

2.2.7.5. Confinement heteroepitaxy (Chet) growth

Recent work has shown that the previously mentioned hydrogen intercalation of 6H-SiC could be replaced with metallic atoms to form, for the first time, 2D metallic layers confined between the SiC substrate and the top graphene layer. The fabrication process utilizes a simple tube furnace operating between 600–800 ℃, where a 1 cm^2 of Si-polar SiC substrate is faced down on a crucible with a few pieces of metal.[23] Before the intercalation process, the EG is subjected to an oxygen plasma treatment to deliberately damage the top graphene layer to help intercalate the metal atoms. This process is illustrated based on reference [23] in the schematic in Figure 9. Liquid metals are the best-desired intercalants for this process, such as gallium, indium, and tin, because their lower evaporation

temperature that assists in transporting the atoms from the liquid metal source to the SiC substrate that is typically ~2-4 cm away from the metal flake. Non-liquid metals can also be intercalated with the same method but have a relatively limited coverage percentage than liquid metals. Furthermore, the process of intercalating metals can be extended to intercalate two types of metals to form 2D alloys, such as an indium/gallium alloy[86] or a gallium/tellurium alloy. The 2D metals realized from the CHet intercalation opened various investigations into the fundamental physics of superconductivity [87, 88] and non-linear optics (NLO) fields.[89]

2.2.7.6. Second-harmonic generation (SHG) from 2D CHet metal

In recent years, non-linear optical (NLO) materials have been recognized as promising candidates for many photonic applications such as high-speed optical modulators, ultra-fast optical switches, and high-density optical data storage based on the fact that photons are capable of processing information at the speed of light. Such emerging applications help in pushing quantum computing innovation forward to replace ordinary electronic-based computers. Second-harmonic generation (SHG) is an exciting property in the field of NLO, which is mainly associated with non-centrosymmetric crystal structures because of the loss of symmetry in these point groups.

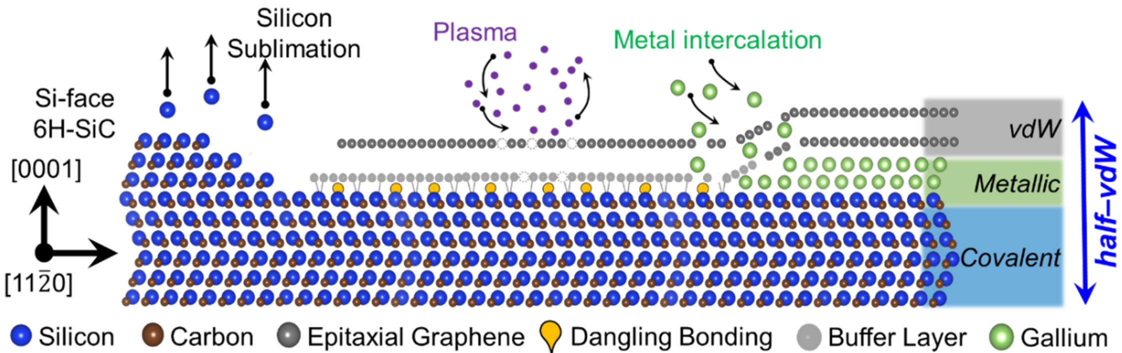

Figure 9. Schematic of the Confinement Heteroepitaxy (CHet) growth. Cartoon image showing the CHet fabrication steps. The heterostructure is called half-van der Waal due to the bonding variation from covalent to metallic to van der Waal across the vertical dimension.

Figure 10a shows the basic understanding of the generation of a second harmonic where an SHG-active surface interacts with two photons with equivalent energies to result in only one photon with twice the frequency and half the wavelength. Recent research shows that the 2D metals (Gallium and indium) realized through CHet synthesis are SHG active and claims that the 2D metals have the largest known second-order nonlinear susceptibility values (Figure 10b) compared with other 2D materials such as TMDs and commercialized substrates such as gold and gold-coated-graphene.[89] The claim of having considerable SHG intensity from 2D metals compared with other materials will open the doors for applying the 2D CHet metals as for surface-enhanced Raman scattering (SERS) for detecting biological samples like viruses or bacteriophages. The 2D CHet metal SERS has the advantage of being a flat surface (Graphene) that searches for a bio-organism in the substrate much more conveniently than the currently commercialized SERS substrates.

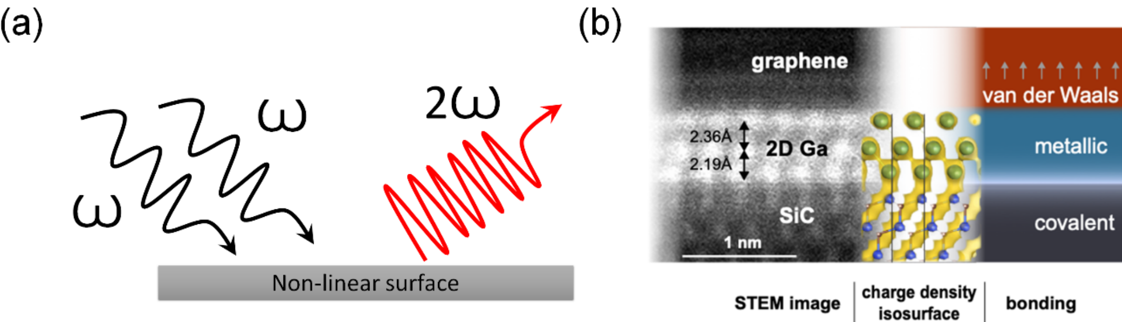

Figure 10. Second harmonic generation (SHG) from 2D CHet metals. (a) cartoon image of the SHG generation. When two photons interact with a non-linear non-centrosymmetric surface, the resultant wave is the summation of the two input waves. (b) STEM images reveal the layers of the SiC substrate/2D Ga/bilayer graphene structure (left). The bonding transits from covalent to metallic at Ga layers and then to van der Waals at the Ga-graphene interface, resulting in an electrostatic gradient.[89]

2.2.7.7. Possible SiC-metal interactions during the intercalation process

Liquid metals as the intercalant in the CHet layers may be favorable due to their low melting point, but it raises the risk of the dissolution of the SiC substrates. It was reported in 2012 that gallium has the ability to dissolve a few layers of the SiC surface at temperatures between 600 and 1200 ℃ to form graphene on the SiC substrate, utilizing the gallium as a catalyst. In this process, the dissolution of Si and C atoms occurs on the gallium flux/SiC surface. During cooling, the carbon atoms segregate on the gallium surface as well as the SiC surface to form graphene only at the area where the gallium exists.[90] The same idea was also reproduced for Si substrates by utilizing a CVD furnace and a carbonaceous flow gas to form graphene on gallium drops on a Si wafer.[91]

Recent work has demonstrated that many Mg-Si stoichiometries can exist after the intercalation of Magnesium into 6H-SiC with monolayer epitaxial graphene.[92] In this work, the intercalation of Mg breaks the buffer layer SiC covalent bonding

to form a second freestanding quasi-free epitaxial graphene that decreases the overall graphene work function. However, the Mg-Si bonding information that was extracted from fitting X-ray photospectrosocpy (XPS) shows unique intercalant chemical compounds that are thought to arise from differing Mg-Si stoichiometry. This suggests that a few Mg atoms may be diffused inside the SiC or replaced Si or C atoms from the first SiC layer. Studying the 2D CHet metals should investigate the possible interface instabilities that may exhibit at this atomic scale.

2.3. Electron microscopy

In this section, a brief overview of the main electron microscopy methods is described. Bridging the resolution gap between different techniques becomes essential to understand materials' properties. Ultimately, correlative microscopy workflow (across techniques in both plan and cross-section views) provides a comprehensive look at 2D materials and thin films at the wafer scale.

In the following chapters, we will utilize multiple electron microscopy characterization to investigate the interface. Moreover, the surface quality and their bulk behavior will be discussed in terms of electron imaging and spectroscopy at different length scales, from the atomic resolution to the bulk size.

2.3.1. Electron microscopy versus light microscopy

Since its development in the earlier nineteen-thirties, electron microscopy (EM) has achieved significant contributions in imaging materials and structures with a spatial resolution that surpasses the conventional optical microscope.[93, 94]

Nowadays, scanning (SEM) and transmission (TEM) electron microscopes provide high imaging capabilities with sub-nanometer[95] to sub-angstrom resolution.[96] With this spatial resolution, very fine structural details can be captured from the atomistic scale to hundreds of micrometers, making the EM the most viable imaging technique that fills this imaging length-scale range.

The operational mechanism of an electron microscope and light microscopy are quite similar. Figure 11 shows the similarities and differences of the primary device components between a typical light microscope, TEM, and SEM from the source to the detector levels. Both start with a source of the probing emission (light vs. electrons), and then a condenser the lens to focus the emission into a small fine probe with a cone shape. In both light and electron microscopes, there is an objective lens just after the sample, followed by a projector lens(es) to control the magnification. The focusing unit in electron microscopes is an electromagnetic lens compared with a glass lens in the case of a light microscope. That is because the electrons are difficult to focus, and it usually needs sets of magnetic sub-lens to perform the focusing purpose, which explains why an electron microscope is taller than an ordinary optical microscope. In the light microscope, the detection can be done by the human eye through the eyepiece lens. However, in electron microscopes, the detection should be through an electron-sensitive detector – such as a fluorescent screen in TEM or an SE detector in SEM.[97] In Transmission Electron Microscopy (TEM), the electron probe may interrogate the sample by the broad beam in a parallel illumination sample (similar to the optical microscope), which is called "TEM" mode, or it may be focused on toa tiny probe that scans the sample (similar to the SEM) surface pixel by pixel which called the Scanning TEM (or STEM) mode.

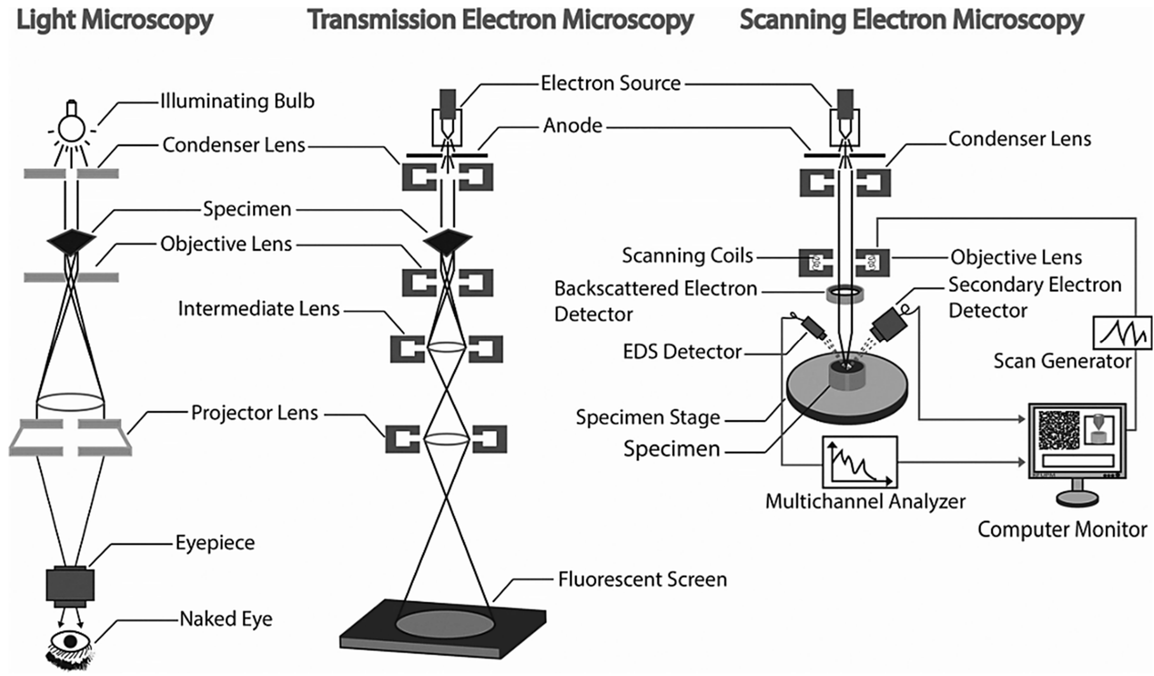

Figure 11. Electron microscopes compared to a light microscope. A schematic illustrates the basic similarities and differences of light (left), TEM (middle), and SEM (right) microscope components. Electrons are accelerated by a high tension at the electron source. [97]

2.3.2. Electron-matter interaction

Electrons are one type of ionizing radiation that interacts with the inner-shell electrons of a substance atom. Initially, the electron beam is accelerated by a high-tension voltage applied at the extraction point of the electron source, usually from 1 to 30 keV in SEMs or 40 to 300 keV in TEMs. When these fast electrons hit the sample, the electrons interact with the sample atoms within a specific range called the interaction volume. This interaction produces a wide range of secondary signals from the localized position of the beam-specimen interaction. The signals from a typical electron beam interaction with a sample are illustrated in Figure 12. These signals can provide local chemical, bonding, and structural information

about the specimens. The following are definitions of the incident and the resultant signals from electron–matter interaction:

***Incident beam*:** To get the best signal out of any specimen, we have to generate the best source signal. The incident beam can be generated from different electron sources, such as a tungsten filament or a cold field emission gun (FEG). The main characteristics of the electron source are its voltage and current, and energy spread. Moreover, it is essential to generate a beam with a narrow convergence angle from the source before focusing it on using magnetic lenses. Therefore a small source with high brightness is essential.

Secondary electrons (SE): This radiation comes from a ~10 nm deep position from the sample surface. They contain information about the topology and morphology of the surface. The SEs emission has much less energy (<50 eV) than the initial electron beam because they result from the incident (or backscatter) interaction of the swift electrons with the valence electrons in the sample. An SE detector is a basic unit in any SEM microscope. However, it can also be found in some TEM microscopes to check the cleanliness of a FIB prepared sample.

Back scattered electrons (BSE): They come from a deeper position than SE and are scattered back elastically from the surface where the BSE detector is there to collect them. Back scattered electrons have approximately the same energy as the initial electron beam because they are bent around the atomic nucleus without interaction with the atomic shells. BSE gives a chemical contrast image in the SEM microscope by strong nuclear scattering, changing the image (i.e., higher numbers of protons scatter the electrons more strongly) grey level concerning the change of

the chemical composition of the surface. Typically, the BSE detectors are employed in SEM microscopes.

Characteristic X-rays: these are the X-rays that are generated from a deeper position than the BSE of the surface. It is the X-ray radiation that is generated when an electron moves from a higher energy orbital (such as L) to a lower orbital (such as K). This transition in an atom is a process that follows the fast electron beam collision with the atom. The generated X-rays give an identified elemental composition of the elements in the X-ray generation position based on the quantized nature of the energy transitions in atoms. These x-rays are measured using X-ray detectors in a technique called energy dispersive spectroscopy (EDS).

Continuous X-Rays: or it is called *bremsstrahlung* radiation. It results when some electrons lose their energy during passing through the sample atoms without knocking any other electrons from the sample atoms. They are a source of noise in the EDS analysis.

Auger electrons: these electrons come from a 0.3 to 3 nm (i.e., ~ 1 to 10 thick atomic layers) deep position from the surface. Auger electrons are helpful in characterizing the elemental composition of an atomically thin surface, such as 2D materials. The Auger process is related to three electrons occurred at two different levels, as illustrated in Figure 13b. The Auger effect from the atomic shell level is a chain of radiationless transitions in an atom in which one of its inner shell electrons is ionized. This process ends with the ejection of an electron, which is known as an Auger electron, and it has a specific kinetic energy, which may be analyzed as a fingerprint of the composition at that point.

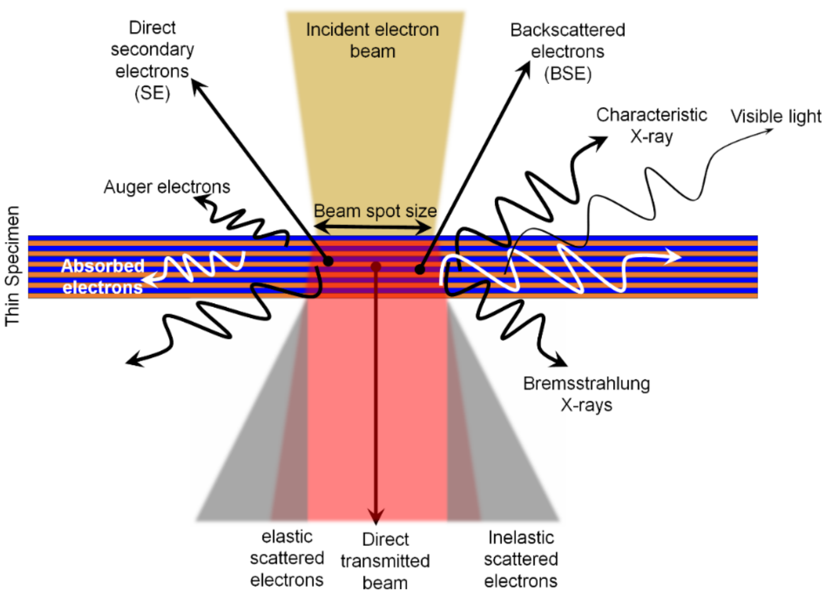

Figure 12. Electron beam-sample interaction model. Illustration figure showing electron beam interactions with a sample and the possible secondary signals generated by the incident beam-sample interaction.

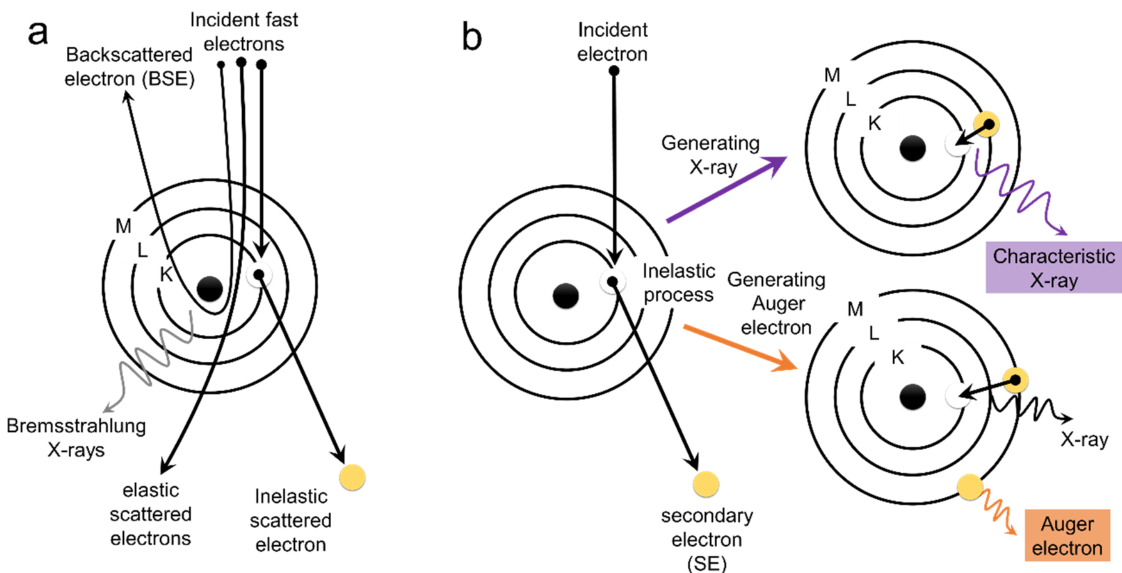

Figure 13. Fast electron interaction with an atom. (a) elastic and inelastic radiation. (b) generation of X-rays (top) and Auger electrons (bottom) processes.

2.3.3. Scanning transmission electron microscopy

Scanning transmission electron microscope (STEM) is considered the ultimate characterization technique at the nanometer and the atomic scales because of its uniqueness in both imaging and spectroscopy measurements. In STEM, the probe is focused on forming a conical electron tip. This beam with its sharp focus point interacts with the same at its focal point, which can be reached a sub-angstrom size in the case of using an aberration-corrected microscope. With sub-angstrom, atomic columns and individual atoms can be easily resolved in STEM images. The process of STEM imaging of a sample is by rastering the sample pixel-by-pixel, similar to the SEM rastering mechanism. As a result of passing this cone-shaped probe through the sample at each pixel, discs of the beam are diffracted and overlapped within a broader range of angles than the incident convergence beam (α) angle, as illustrated in Figure 14a. To collect imaging information from this wide range of scattering, we need to define a range of the inner and outer collection angles in the scattering cross-section.[98] Figure 14b-d shows how STEM imaging for a biological feature (a bacteriophage stained by Uranyl acetate from [99] – *performed by the author of this thesis for a side project)* can be significantly different based on the range of the collection angles. In Figure 14b-d, while the STEM-BF and STEM-HAADF contrast appear to be the negative complements of each other, the ADF emphasizes the Uranium nanoparticles attached to the outer phage wall as part of the staining exhibiting its trademark bright contrast for materials of high atomic number (Z).

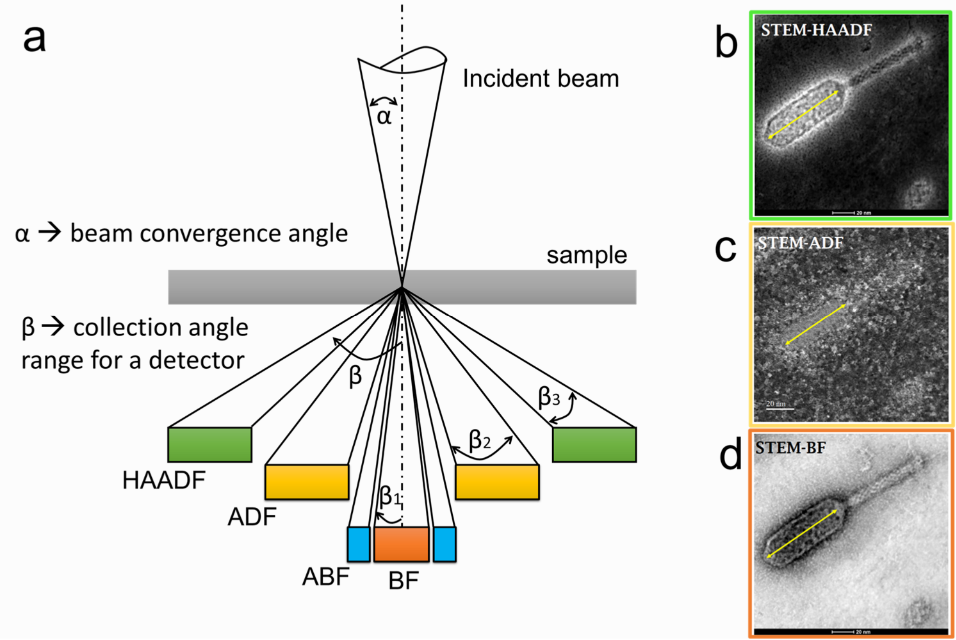

Figure 14. STEM imaging. (a) Schematic diagram of the STEM probe interaction with a sample. The type of images (BF, ADF, or HAADF) is based on the range of collection angle from the scattered beam from the sample. (a-c) Example of STEM imaging with different detectors. The images show the same site taken by STEM-BF, STEM-ADF, and STEM-HAADF for a ZCSE2 bacteriophage. The yellow line in a-c represents the same feature location in the three images. The STEM images are reproduced from [99], which is conducted by the author of this thesis as a side project.

STEM bright-field (STEM-BF) imaging can be performed using a solid detector (red color in Figure 14a) that collects the signal from the central diffracted disk that contains primarily the coherent scattering, which makes it an analogy of the HR-TEM imaging technique. Typically, the STEM-BF is collected approximately from 0 to 10 mrad. STEM Annular bright-field (STEM-ABF) imaging can be performed using an annular detector (blue color in Figure 14a) that collects a narrow range of scattering angles (approximately within 10-20 mrad) near the central diffracted beam. This is the most suitable imaging technique for light elements, such as Li or O or N, in complex oxide crystals and ceramic materials that contain heavy

elements as well. Furthermore, the STEM annular dark-field (STEM-ADF) detector (orange color in Figure 14a) collects mainly the elastically scattered electrons at much higher angles than the BF and ABF detector ranges.

The most significant ADF imaging range (~50-200 mrad at camera length around 100 mm) is the high angle annular dark-field (HAADF) because it is directly related to the atomic number (Z). The HAADF imaging (green color in Figure 14a) represents atomic mass-contrast in the image due to Rutherford nuclear scattering, similar to backscattered electrons, but instead forward scattered in a transmission orientation. In high-resolution STEM images, a cross-section sample is assumed to have the same thickness within a few nm span length window of the HAADF imaging. This assumption makes the HAADF image only depends on the Z number, which gives a direct interpretation of the atomic columns from the micrograph intensities.

The Camera length (CL) has an effect on all angular ranges of collection. Instead of using multiple detectors, only one detector still be able to get all the possible types of images (BF, ABF, ADF, and HAADF) by adjusting the CL to spread the diffracted beam at a different angle of convergence. In other words, the CL changes the position of the scattering cross-section on the detector. Additionally, the probe convergence angle (α) also affects the imaging collection angle of a detector because of changing the diffracted scattering angle. For sharp probes (α=1), the CBED disks become almost separated, which means higher divergence of the exit wave from the sample. The sharp STEM probes can be utilized to perform Nanobeam electron diffraction (NBED), which probes the sample with the beam size that can be sub-angstrom for an aberration-corrected electron beam.

2.3.4. Electron energy-loss spectroscopy

The STEM technique provides unique information about the chemical and structural properties of the sample because it collects co-located and simultaneous signals while rastering the sample pixel-by-pixel. One of these signals is the transmitted beam itself. While most of the beam transmits through a thin sample without losing any energy (termed elastic scattering and which forms the zero-loss peak (ZLP)), a small proportion of the passing electrons lose energy by interacting with the specimen atoms and their electronic structure termed *inelastic scattering*, and which is interesting here. This process is called electron energy-loss (EEL). To analyze the transmitted beam, a magnetic prism is placed after the fluorescent screen level to bend the beam into a drift tube and then project the EEL on a camera to form an EEL spectrum (or EELS), as illustrated in Figure 15a. This setup is called the EELS spectrometer filter or the Gatan Imaging Filter (GIF) if it is provided by the Gatan company. Acquiring an EELS spectrum image can be performed simultaneously during acquiring an ADF or HAADF image, pixel-by-pixel because electrons counts for EELS are different from the diffracted electrons that count for ADF imaging, as shown in Figure 15b-c. Besides the ZLP, the EELS have two main regions, which scale as a function of energy: (1) low-loss and (2) core-loss.

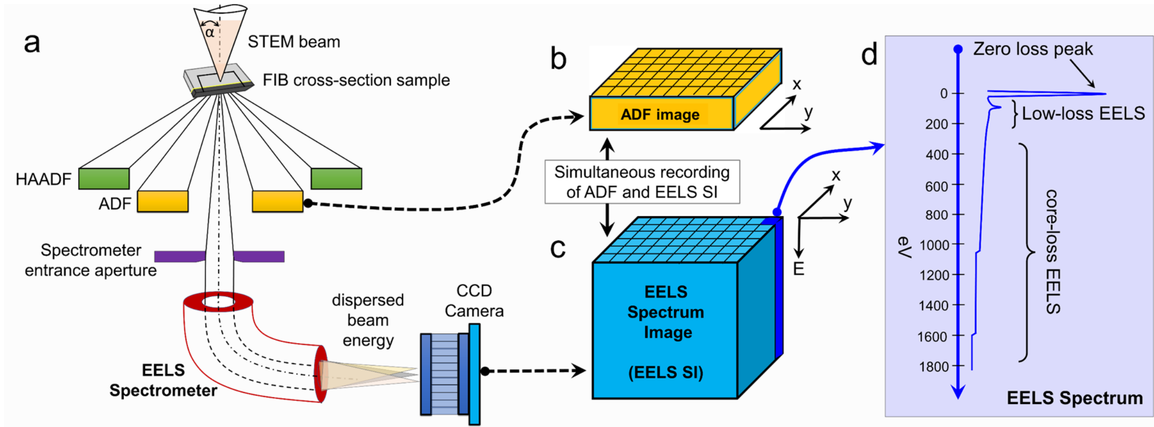

Figure 15. STEM-EELS technique. (a) schematic diagram of the EELS spectrometer set-up. (b and c) schematic cartoons of ADF image and EELS spectrum image acquired simultaneously using the ADF detector and a CCD camera shown in a. (d) an EELS spectrum extracted from one column of the EELS spectrum image at a given pixel location (x,y) in the ADF image. The spectrum shows the zero loss peak, low-loss EELS, and the core-loss EELS regions.

The low-loss EELS region in Figure 15d represents the electrons that lose a small amount of energy because of their interaction with the surface and thickness of the sample, as well as electronic interactions, including the collective oscillations of the electron cloud (plasmonic), the nuclear oscillations of the lattice (phonons) and the electronic structure of the sample (such as the band structure). This region is attractive in studying the localized electronic and optical properties of nanostructures as well as estimating the sample thickness and density.

On the other hand, the core-loss EELS region in Figure 15d represents the electrons that lose energy due to *inelastic* scattering from their inner shell orbitals. The core-loss gives information on the chemical composition for each pixel during rastering the sample. These energy transitions are the inverse of the emitted secondary signals (i.e., the x-ray emission transition has a corresponding energy loss of equal magnitude). Moreover, studying the energy-loss near-edge structure (ELNES)

provides unique experimental information about the nature of the bonding at the atomic scale. For more information about EELS, consult Egerton's book.[100]

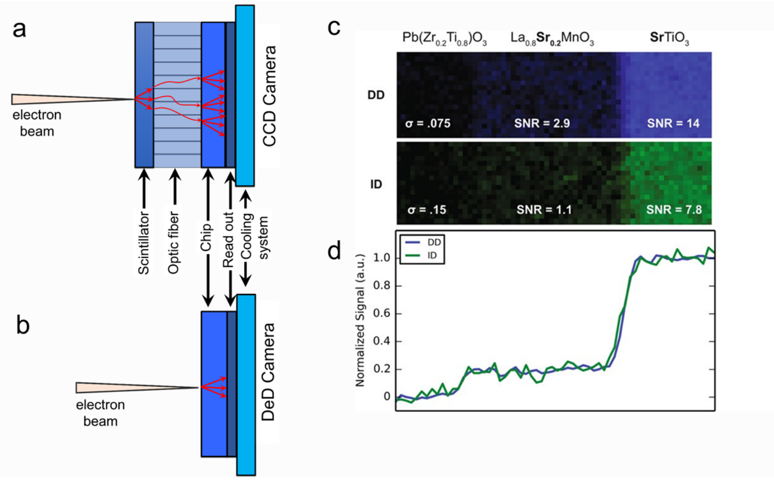

Figure 16. Detection of electrons. Schematic diagram of the charge-coupled device (CCD) camera. (b) Schematic diagram of direct electron detector (DeD) camera. (c) core-loss EELS mapping for the Sr element in a PZT/LSMO/STO heterostructure, using DeD and CCD camera. (d) line profiles were integrated across the interface showing that the DeD has less noise than the CCD.[101]

One of the main factors affecting an EELS analysis for an atomically thin layer is the type of detector used to collect the EELS signal. Ordinarily, a charge-coupled device (CCD) camera is used to record the scattered electrons at the end of the EELS spectrometer. In the case of using a CCD camera, the electrons hit a scintillator that generates photons from the interaction. Then the photons pass through a set of optic fibers into the CCD chip that converts the photons into electrons. Then the read-out system measures an amplified signal, as illustrated in Figure 16a. The main drawback of the CCD camera is the possibility of scattering the entering electron into the scintillator on two or more electrons into the CCD

chip, which affects the spatial resolution and significantly decreases the signal-to-noise ratio (SNR).

Alternatively, a recent advance in the detector industry introduces a direct electron detector (DeD) that directly measures the incident electron on a complementary metal-oxide-semiconductor (CMOS) chip, as illustrated in Figure 16b. The use of DeD improves both the spatial and energy resolutions in addition to decreasing the SNR of imaging and the EELS spectrum. For example, in Figure 16c-d, from [101], the SNR of the strontium (Sr) map showed an improvement by a factor of ~2-3 when using the DeD compared with the scintillator base detector.

2.3.5. Auger electron spectroscopy

The Auger process is, similar to EELS, an inelastic scattering event. The ejection of Auger electron results from a de-excitation process when an electron from a higher orbital move back to a lower orbital. This de-excitation process comes after the first inelastic scattering event of the fast electron collision with an inner shell electron that results in an ionized atom, as illustrated previously in Figure 13b. Therefore, the Auger radiation is associated with 3 electron events, where the 3rd event is the Auger electron ejection. That is why the Auger electron peak is labeled with 3 atomic shells (Such as KLL) that represent the transitional event that happens at these shells.

The Auger electrons have low ejection energy; that is why they are sensitive to detection from the few nm depths (typically from 0.3 to 3 nm) of the surface. Auger electrons that may be generated from deeper depth will be consumed in the sample.[102] The characteristic Auger peaks intensities are identifiers for the

surface elements and compositions. The relative intensities of the Auger peaks can be used in quantifying the compositional percentages.

Auger quantification is usually performed through a comparison of the experimental signal with a reference signal from the same or similar elemental system. The quantification process is affected by the possible overlapping between present elemental peaks as well as the chosen reference and the quality of the experimental signal. In general, Auger quantification can give rough percentages that help when one compares it with other quantification results from large interaction areas such as XPS or local areas such as EELS quantification.[102] Since AES is probed by an electron SEM beam with a size of 5-10 nm, the AES quantified maps have better in-plane resolution compared with XPS maps, which are usually probed by a several hundred micrometer X-ray beam. Here, the AES comes in between the XPS and STEM-EELS in terms of spatial resolution. Besides, the AES has the advantage as a nondestructive test in contrast to the STEM-EELS of cross-section samples, which requires a destructive process to prepare. Figure 17 shows an example of AES mapping of a 2D Gallium intercalated between silicon carbide and epitaxial graphene. .[23] The total heterostructure is about 4 atomic layers on top of the silicon carbide, which is well identified in the AES maps.

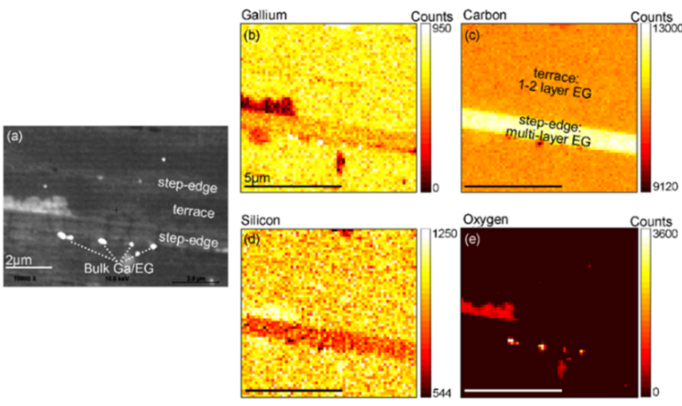

Figure 17. Auger electron spectroscopy map of 2D Gallium intercalated EG. Auger electron spectroscopy map of 2D gallium grown by the CHet method. (a) SEM of Auger image. (b), (c), (d and e) are the elemental AES mapping for Gallium, Carbon, Silicon, and Oxygen.[23]

2.3.6. SEM for characterizing 2D materials

Secondary electron (SE) emission from a beam-sample interaction is a primary detected signal in SEM to produce micrographs. In SEM, the SE emissions are low-energy electrons generated as a result of inelastic scattering of the incident beam and backscattered electrons as well and their interactions with the valence electrons of the sample atoms. The SE energies are 1-50 eV with the vast majority under 5 eV and are generated from the 1-10 nm depth from a bulk sample surface.[103]

Unlike bulk samples, low-dimensional materials placed on a uniform dielectric substrate are found to generate sufficient SE emission to be recognizable in SEM images regardless of the material's size relative to the larger beam-sample interaction volume.[104] This high SE signal has been explained as owing to local surface potential differences in the example of imaging carbon nanotubes on the SiO_2 surface.[105]

Unlike one-dimensional materials, the SE emission from two-dimensional (2D) materials gains more interest because it could distinguish the number of the 2D layers, as seen in Figure 18. This non-invasive identification method has been widely applied to graphene flakes in the last decade.[106, 107] In the case of graphene, a suppression of electron emission explains the differential SEM contrast of flakes with different thicknesses.[107] The suppressed emission is

found to depend physically on the local work function (surface potential) of the 2D material, which is primarily controlled by the number of graphene layers.[108]

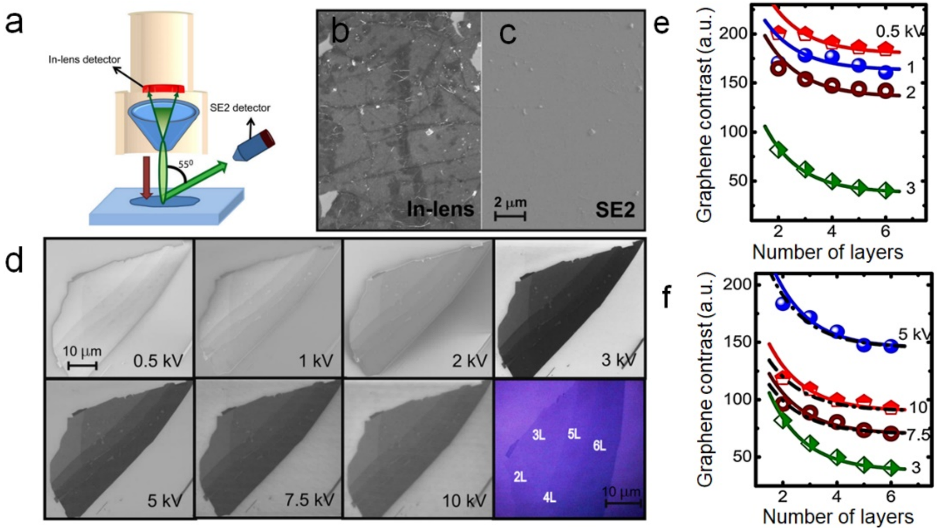

Figure 18. SEM detection of graphene number of layers. Reproduced from [107]. (a) illustration figure of the SEM detectors' position relative to the sample. (b and c) are SEM images taken from the same sample site with in-lens and Everhard-Thornley detectors, respectively, for transferred graphene on Si/SiO_2 substrate. (d) SEM images were taken by the in-lens detector for a graphene flake with a various number of layers near the flake edges. The colorful right-bottom image is an optical microscope image of the same flake. (e and f) The intensity of the secondary electron emission from different graphene number of layers as a function of the primary electron energy. The contrast relation with the number of layers shows that the highest graphene contrast is achieved at 5 keV (f) for a high voltage range.

2.3.7. Correlative microscopy workflow for 2D materials

Other methods may be employed in determining 2D material thickness – such as Raman spectroscopy[109] optical microscopy,[110] and atomic force microscopy[111] – but the electron microscopy-based techniques remain the highest of the spatial resolution imaging in the 2D materials field. This improved

resolution merits more attention to correlate non-electron-based and lower-resolution methods with SEM or TEM acquired from the same sample's site.[112-115] Commonly, the concept of correlative characterization across multiple techniques bridges the resolution gap as well as explains the properties of the material as a function of co-located spectroscopic signals with in-plane imaging.[116-120]

Beyond the correlation with in-plane images, EM is used to examine 2D materials in cross-section view by using the focused ion beam (FIB) microscope to prepare a site-specific lift-out from 2D flakes.[121, 122] Moreover, SEM and scanning-TEM (STEM) techniques are ultimately correlative microscopy methods in themselves. That is due to the multi-signal emissions that are related to the material's electronic structure, chemical bonding, and chemical composition, in addition to the structural information.

Applying correlative microscopy is essential in determining the thickness of 2D materials because assuming that the highest SE emission in SEM images results from a monolayer may be debatable.[106, 107] Hence, the correlative methods could be applied on the same flake to confirm the direct relationship between the different SEM contrast and the number of 2D layers. No direct correlative electron microscopy between SEM and cross-sectional TEM has been applied to identify and confirm the number of 2D layers of SEM contrast to the best of our knowledge. Also, only flakes of single 2D materials are widely explored in the literature using the SEM thickness determination method. Besides flakes, few reports studied epitaxial 2D layers in SEM images with a few micrometer sizes.[114, 123] However, applying a facile SEM contrast method has not been established on a

large scale that covers a wafer of a 2D material. The SEM method also is not well-explored for a stack of different 2D materials in the van der Waal heterostructure form.

Generally, correlative microscopy is getting exciting in the last few years due to its impact on understanding structure and chemistry in various fields. For example, the correlation between the contact potential differences (CPD) and the AFM maps revealed new information about the graphene thicknesses and structures in the out-of-plane direction, which is not possible if we look at the height map individually.[124, 125] The AFM is also used to correlate characterization with Raman signals in the 2D materials field.[126, 127] The AFM/Raman correlation is enhanced in the instrument known as the "tip-enhanced Raman microscope," where the laser from the Raman microscope is reflected and localized on a small area on the sample from a conductive AFM tip. This method allows the mapping of local Raman experiments with a nanoscale probe compared with the original Raman that has a probe of typically ~1 micrometer. In addition to measuring the Raman scattering, the same correlative idea can be utilized for measuring infrared absorption. Interestingly, the correlative microscopy concept is not limited only to be done with the same apparatus, such as the AFM/CPD or AFM/Raman. The same position from an AFM map can be navigated using SEM or TEM microscope for performing, for example, EDS mapping. Here, the information on the surface heights from AFM in addition to the chemical composition from the EDS map.[128] In the field of biology, it is getting viral to correlate the optical microscope with TEM-EDS and SEM-EDS to understand the chemical composition of interactive biological organisms.[129, 130] The biological research communities call this technique

correlative light electron microscopy (CLEM) which is based on navigating a specific position from a light microscope inside SEM or TEM.

STEM characterization is also considered as correlative electron microscopy because it can provide different images (HAADF, ABF, BF, LAADF, and MAADF) at different collection angles, as well as spectroscopic measurements. When the STEM is equipped with aberration-corrected lenses for the spherical aberration, the power of the STEM is getting interesting because the STEM images can reveal the crystal structure in real space with the simultaneous EDS, EELS, and photoluminescence signals. The ultimate advantage in the probe-corrected STEM is that the EDS or core-loss EELS can provide the chemical composition while near-edge fine structure EELS can provide information about the bonding in the system. Low-loss EELS and photoluminescence signals may be utilized for electronic structure information for specific samples. Although the probe-corrected STEM is considered as the ultimate characterization technique – because it can provide structure, chemical, bonding, and electronic information in localized and simultaneous attributes – it has a significant limitation. The limitation of STEM is the *sample size* and the *span length* of the typical atomic resolution images. A cross-section sample is typically a few micrometers wide which is prepared by FIB lift-out process, as summarized in Appendix 1. This micrometer size window is hard to give a complete picture of a sample that is non-homogeneous in plan view.

2.4. Cadmium telluride

Cadmium telluride (CdTe) is a chemically and thermally stable semiconductor with a cubic zincblende structure, as illustrated in Figure 19a. Both Cd and Te are

less thermally stable than the CdTe, which has a melting point of ~1040 C. In addition, CdTe is less toxic than both Cd and Te, which have biohazard considerations for recycling and fabrication. At room temperature, a single crystal CdTe has a band gap of 1.5 eV. This band gap value makes CdTe a candidate for photovoltaic and radiation detection applications.

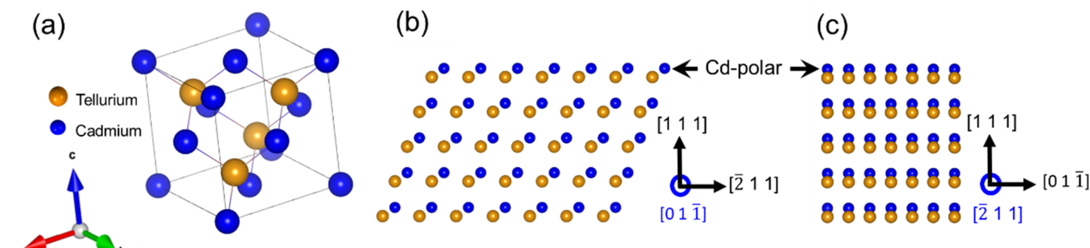

Figure 19. Crystallography of cadmium telluride (CdTe). (a) Isometric view of the CdTe unit cell. (b and c) Projection views of the CdTe in the (01$\bar{1}$) and ($\bar{2}$11) directions, respectively. The CdTe lattice in b and c show a Cd-polar film in the (111) upward direction.

2.4.1. Applications of cadmium telluride

2.4.1.1. CdTe-based solar cells

The key application for CdTe is the solar cell. Materials optimally collect the solar energy with a band gap of 1.34 eV, called the Shockley-Queisser limit, and can reach a theoretical efficiency limit of ~33%.[131] Many semiconductors match this limit, such as GaAs or InSb, but these materials are expensive to fabricate compared to the solid CdTe and silicon thin films.[132]

Cadmium telluride has a band gap of 1.45 eV, which is very close to the desired limit. Furthermore, Fabrication of CdTe solar cells is affordable and comparable to silicon-based cells. Cadmium telluride solar cells have strong absorption of sunlight compared to silicon which means few micrometers thick CdTe films are

sufficient to absorb the same energy by a silicon-based solar cell with few hundreds of micrometers. This advantage of the size reduction is because of the direct band gap nature of the CdTe compared with the indirect band gap in the case of silicon. Besides the economic advantages, CdTe thermal stability is higher than silicon, making CdTe-based solar cells perform better than silicon in devices operating at higher temperatures.

The primary CdTe solar cells in the market – by First Solar Inc. – have a lower efficiency than silicon solar cells. However, recent research has achieved efficiencies up to 22.1% so far, significantly higher than the typical 14.3% efficiency of the silicon.[133] The economic and thermal stability advantages make CdTe solar cells a competitor in the market and attractive materials for research.

2.4.1.2. Alloying of CdTe for radiation detection

Tuning the CdTe band gap can be achieved by different alloying elements such as mercury, zinc, chlorine, and magnesium. Mercury cadmium telluride (HgCdTe) thin film can be deposited on a Cadmium zinc telluride (CdZnTe) substrate to form a heterostructure known as a detector material for infrared tera-hertz radiation.[134, 135] Doping CdTe with minor chlorine or magnesium concentrations adds hole/electron and the possibility of controlling the single-crystal film polarity, named Te-polar in reference [136] or Cd-polar in Figure 19c-d. In addition, experimental investigation of doped CdTe shows that chlorine or magnesium atoms are more likely to be segregated at the grain boundaries of the polycrystalline CdTe film.[137] This segregation improves the performance of the CdTe in detecting X-ray and gamma-ray.

2.4.2. Growth of cadmium telluride

2.4.2.1. CdTe film growth at a high substrate temperature

The growth of CdTe films at temperatures above 450 °C is considered a high-temperature growth. One of the high-temperature growth methods of CdTe is close space sublimation, where CdTe is sublimed from powders at high temperatures. In this process, an inert gas (such as argon) is used to transport the Cd/Te vapors towards the substrate, where a film starts to grow. The progress of this fabrication results in a large-area growth of polycrystalline CdTe films with a high density of dislocations, twinned domains, and grain boundaries.

Dislocation nucleation and mitigation in CdTe films is a widely explored research area since mid of the last century. Cadmium telluride films are usually fabricated with high dislocation density. Many reports discussed threading dislocations accompanied by dislocation clusters and networks as a result of the high-temperature growth.[138, 139] Other reports studied the density of micro-twins [136, 140, 141] and mismatch dislocations at the interface with the substrate.[140, 142]

Besides the dislocations, grain boundaries are significantly present in the grown CdTe film because of the polycrystalline nature of the film grown at this high temperature. Grain boundaries may reduce the CdTe mechanical properties such as strength and flexibility. However, many reports suggested that the grain boundaries in the CdTe act as sources for enhancing the carrier collection, which may increase the electron mobility, and not negatively reduce its electronic performance.[143, 144]

2.4.2.2. CdTe film growth at a low substrate temperature

Substrate temperature below 450 °C is considered a low-temperature growth of a CdTe film. Generally, CdTe is fabricated using vacuum evaporation via molecular beam epitaxy or pulsed laser deposition at temperatures well below 450 °C and pressures around 10^{-6} mbar.[145, 146] Extremely low substrate temperature (70 °C) is also applicable to fabricate CdTe using electro-deposition methods, which results in a commercial polycrystalline structure with a good Cd:Te stoichiometry ratio.[147]

The advantages of such growth temperatures are to minimize the energy consumption of the fabrication, and consequently, the cost of the film. In addition, lower temperature enables lower stress between the CdTe film and the substrate. This lower stress manifests in lower dislocation densities at the film and the interface. Low observed dislocation densities were reported for low-temperature growth of HgCdTe and CdZnTe on silicon substrates at 300–360 °C through evaporation in molecular beam epitaxy.[135] Also, low dislocation density was reported for low-temperature growth of CdTe on InSb substrate at 230 °C using molecular beam epitaxy.[142]

2.4.3. CdTe growth on a sapphire substrate

Sapphire is a desirable substrate for many semiconductors because of its thermal stability during the growth of the film. Sapphire also has high thermal conductivity with coefficient of thermal expansion that matches the CdTe. Moreover, sapphire is an insulator with a very high band gap well-suited for

building devices on a wafer surface. In addition, sapphire can be affordable commercially in the form of silicon-on-sapphire (SOS) substrates.

The lattice mismatch between the c-plane of the sapphire (0001) and the CdTe (111) plane is 3.7%, which is suitable for epitaxial growth under the possible presence of mismatch dislocations.[148] A metal (titanium) buffer layer may be deposited on the sapphire to modify the surface to accommodate lattice mismatch.[149] Many papers reported micro-twins of the CdTe/sapphire system, a widely common defect type in CdTe thin film. Twinning results from the coalescence of two CdTe islands (grains), which both grown epitaxially in the (111) direction. This coalescence results in a twin boundary in the (111) up-ward direction, similar to the two grains but rotated in-plane.[136] After the coalescence event, the CdTe may mitigate the twin at a higher thickness (few micrometers) of the film; hence, micro-twins are likely to be concentrated near the interface.[136, 141, 150]

2.5. Summary

As mentioned in Chapter 1, the motivation of this thesis is to use aberration-corrected STEM imaging and EELS techniques in correlation with other characterization methods to understand weakly-bonded heteroepitaxial interface systems. With advanced STEM techniques and sensitive detectors, a single atomic plane can be characterized in the cross-section view for understanding the bonding, structure, chemical composition, and quality of that particular layer and its neighbors. Combining STEM with other correlative microscopy workflows establishes an opportunity to scale up the atomic scale understanding to a

universal behavior in micrometer and millimeter scales of these confined atomically thin layers in heteroepitaxial systems.

Two recently developed interfaces are included in this thesis for this motivation: the chalcogenide-terminated sapphire substrate and the confinement heteroepitaxy intercalation of epitaxial graphene. Both material systems provide heterogeneous integration of various 2D and 3D layers, which is a critical factor for their deployment in the electronics industry. First, tellurium-termination (as a chalcogenide) of a sapphire substrate offered vdW epitaxy of 2D/3D system ($Bi_{0.5}Sb_{1.5}Te_3$)[67]; however, it is not investigated for a 3D/3D system. The Tellurium behavior in terminating sapphire may also be available for Cadmium telluride (CdTe) thin film on sapphire.[1] Therefore, the CdTe/sapphire (as a 3D/3D system) may be grown using pulsed laser deposition at low substrate temperature. Here, the CdTe/sapphire is an attractive heteroepitaxial interface because the atomically thin tellurium termination controls the growth of the CdTe film and should resolve a polar CdTe film. Second, confinement heteroepitaxy of metal (such as gallium) intercalation of epitaxial graphene is a 2D/3D system with a unique interface that contains a variety of bonding from covalent (SiC) to metallic (gallium) to vdW (graphene) across a 2 nanometer interface height.[23] This is interesting, and challenging, interface for STEM imaging and EELS techniques to understand the metal-SiC epitaxial relationship and the role of graphene in providing air-stability for the layer.

Chapter 3 Atomically Thin Tellurium at CdTe/Sapphire Interface

3.1. Introduction

High-quality single-crystalline thin films are a significant enabler in achieving substantial electrical and optical properties of *various dimensional materials*. Heterogeneous integration of these films may be achieved by in-situ fabrication or lift-off technologies from compliant substrates with remote and van der Waals epitaxy growth of semiconductors.[61] However, the quality of transferred semiconductor films depends on the quality and actual size of manually transferred two-dimensional (2D) materials, limiting the size of direct large-area single-crystal films.

In this chapter, a one-step growth method is introduced to fabricate thin films that are incommensurate to their substrate through a *spontaneous van der Waals-like epitaxy*.[1] In this low-temperature growth, a buffer layer of chalcogenide is spontaneously attached to the interface with a weak chemical interaction between a surface-reconstructed substrate and a 3D film. The chapter will focus on the fundamental understanding of the cadmium telluride (CdTe) on a sapphire interface fabricated via pulsed laser deposition at approximately 300 °C.[1, 2] A monolayer of chalcogenide (tellurium) at the interface is examined by various spectroscopic scanning transmission electron microscopy (STEM) techniques, including low-loss and core loss electron energy-loss spectroscopy (EELS) to reveal both the bonding and chemical composition at the interface.

The CdTe film is investigated at the atomic scale using STEM imaging of the interfacial and CdTe film regions. The strain at the CdTe-sapphire interface is examined using both geometric phase analysis (GPA) and the STEM-moiré analysis. Microscopic investigations provide evidence that misfit dislocation-free CdTe films grow with high quality on the tellurium-terminated sapphire surface. The relatively low growth temperature maintains the top-most sapphire layer in the single aluminum reconstruction, as confirmed by core-loss EELS. Tellurium is more kinetically favorable to nucleate above oxygen sites in sapphire than Cadmium at these growth and interface conditions. This is followed by the CdTe film, with its first tellurium layer oriented toward the pseudomorphic tellurium layer on the sapphire, forming van der Waal-like bonds. This interface complexion allows for a unique incommensurate van der Waals heteroepitaxial growth.

The chapter also demonstrates the realization of a monolayer of *tellurene*, a 2D form of tellurium with 3-atomic-thickness, if more tellurium is deposited at the film/substrate interface. The growth progress of this interface complexion could lead to the fabrication of various dimensional (3D/2D/3D) high-quality heterostructures via one-step growth using a pulsed laser deposition system.

3.2. Material fabrication

3.2.1. Pulsed laser deposition fabrication system

Pulsed laser deposition (PLD) is a physical vapor deposition method. The energetic pulses of an excimer laser focus on a target material to form a plasma of the target in a vacuum environment, which then travels to the substrate in the form of a “plume.”[151] One of the significant advantages of the PLD technique is the

capability of achieving a high-quality thin film with a stoichiometry ratio similar to the target materials used to produce the plasma, particularly for arriving cations. This advantage allows the synthesis of various thin film materials, including thin films with vdW epitaxial interfaces grown at relatively low temperatures.[152] The following sections present a description of the process and the actual setup achieved at McMaster University at Professor Preston's research laboratory.

3.2.1.1. Process description

The PLD process starts with focusing a laser on the target material. Here, the laser creates a depth of penetration depending on the pulse wavelength and the specific heat of the sample. After a few laser pulses, the energy absorption at the surface of the target material becomes sufficient to evaporate the target material, which forms a cloud-like plasma or plume near the target surface. The generated plasma travels towards the substrate with the help of an inert gas flow at low pressure of a mTorr range. Typically, inert gases such as Helium or argon are used for depositing metals or chalcogenides. However, the inert gas may be replaced by oxygen or nitrogen to fabricate oxides and nitrides thin film.

The evaporated atoms condense on the substrate and nucleated in a favorable local position on the substrate based on the energetics of the process. The nucleation benefits from the high kinetic energy of the arrived atoms as well as additional controllable heating at the substrate. The substrate heating promotes the surface diffusion of adatoms to their lattice sites and enhances nucleation, which provides a high-quality thin film. Finally, the thin film is grown layer-by-layer until it

reaches its desired thickness. The thickness of the PLD process can be controlled down to tens of atomically thin layers up to a few micrometers.

3.2.1.2. Set up description

Figure 20 shows a schematic representation of the PLD system used in this study to fabricate cadmium telluride (CdTe) thin films. First, a laser system with a vibration-isolation optical table (3) is activated and focused into the growth chamber from the input site (4). The focused laser interacts with the target (1), which can be positioned or rotated using the orbital (10) and carousel (11) knobs outside the chamber. The growth chamber of the PLD system maintains a vacuum during the growth with the ability to introduce inert gas from the valve in (12) to help in transferring the plasma from the target site to the substrate position. The ablated material plume that contains atoms from the target materials is subjected towards the substrate (2), which can be heated using a furnace (7) while monitoring the substrate temperature with a thermocouple (6). Once the substrate reaches the desired temperature, a shutter (8) can be opened to allow the reflected laser and atoms from the target to reach the hot substrate.

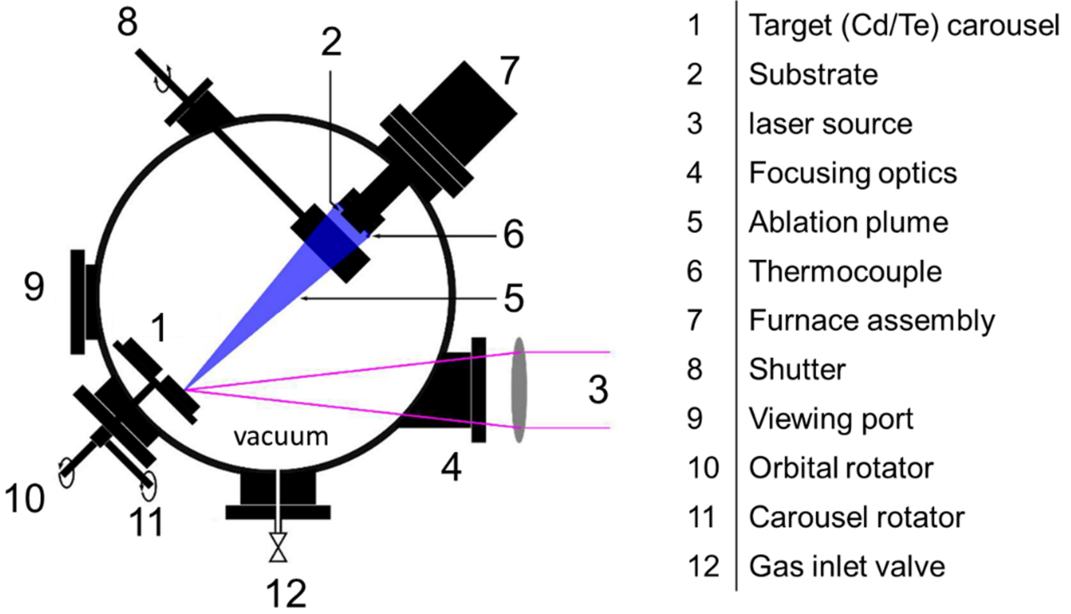

Figure 20. A schematic of the pulsed laser deposition growth system.

3.2.2. Growth parameters of CdTe thin film

A Light Machinery IPEX-848 excimer laser source is used to ablate cadmium and tellurium targets for the growth of CdTe films and heterostructures on a sapphire substrate. The laser source uses a mixture of krypton and fluorine in a buffer of neon in its laser head, producing laser light with a wavelength of 248 nm. The laser source produces pulses with an average duration of 12–20 ns with a beam size of 12 mm by 26 mm. The energy can be varied between 100–450 mJ per pulse. The frequency of the laser pulses reaches a rate of 200 Hz. A Granville Philips 275 Convectron gauge is used to measure the growth chamber pressure. Most depositions occurred in vacuum at the system base pressure ~2×10^{-7} Torr. During growth, substrates were held at a nominal temperature of ~300 °C with a target-to-substrate spacing of 8 cm. Before deposition, the sapphire substrates were

cleaned by solvent and then degassed for 1 hour under vacuum a temperature of 450 °C. Targets have 99.999% purity.

3.3. CdTe film delamination

Large-area CdTe films exhibit the remarkable properties of delaminating in single crystal form at large dimensions (1 × 1 cm) and can be transferred to flexible polysulfone (PSU) films. The film may be patterned by standard lithography to form long stripes of CdTe similar to Figure 21a. In both cases, the layer transfer should be done for clean sample surfaces. To start transferring, a thin layer of chromium (5 nm to 10 nm) is deposited in order to increase the adhesion to the CdTe film, followed by a thin platinum layer as a metal contact for device testing purposes. Then, a 10% w/w solution polysulfone (PSU) film (25-150μm) is placed on top of the CdTe/Cr/Pt heterostructure and uniformly spun at 230-270 °C. The heating purpose is to melt the PSU polymer, making it adhere better to the CdTe film. Upon cooling to room temperature, the PSU polymer solidifies and adds positive strain, which helps in the delamination of the CdTe film from the sapphire and helps prevent film wrinkling and buckling, as seen in Figure 21b. Then, after delamination, the CdTe/Cr/Pt heterostructure can be used for testing as a film on the flexible substrate, as seen in Figure 21c. The next step toward device functionality is to transfer other thin films on top of the CdTe film. Achieving this heterostructure on a flexible substrate can be implemented in *wearable devices*. The mechanical behavior of these transferred films is beyond the scope of this dissertation but represents an exciting topic for future study.

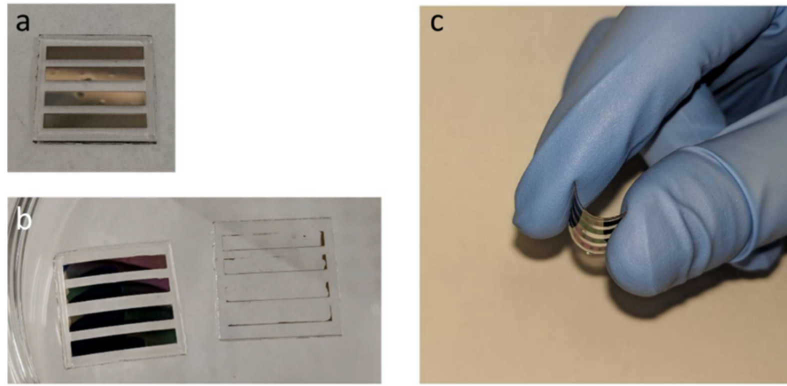

Figure 21. CdTe layer transfer to flexible polysulfone (PSU) film. (a) As-grown CdTe on a sapphire substrate coated with PSU 10% w/w solution. To improve the CdTe-PSU adhesion, chromium and platinum layers are sputtered at the interface. (b) delaminated CdTe on PSU film (*left*), leaving the sapphire substrate (*right*) with few residuals. (c) The exfoliated CdTe film may be bent elastically on the PSU.

3.4. Cross-section preparation of CdTe/sapphire interface

Approximately 280 nm thick CdTe film on sapphire is grown on the sapphire substrate. SEM may be used to image the film and substrate as seen in Figure 23a, where the SEM stage was adjusted at high tilt ~56° to reveal a 3D-like image of the CdTe film on the sapphire. The lift-out of the CdTe/sapphire interface is a painstaking surgical preparation process because of the weak interaction at the interface. The risk of causing unintentional delamination of the film during the preparation process is high. To prevent delamination of the CdTe film, the FIB needle should be attached to the cross-section away from the interface, as seen in Figure 22.

An NVision 40 (Carl Zeiss, Germany) scanning electron microscope equipped with gallium focused ion beam (FIB) system is used to extract and prepare cross-section lift outs from the CdTe/sapphire surface. Two cross-sections are prepared from

two perpendicular zone axes. First, a cross-section having sapphire ($11\bar{2}0$) and CdTe ($01\bar{1}$) zone axis. Second, a cross-section perpendicular to the previous direction: sapphire ($1\bar{1}00$) and CdTe ($\bar{2}11$). Since sapphire has a hexagonal structure, the two perpendicular cross-sections present a view in two perpendicular views. Before sectioning, a 100 nm amorphous carbon and 3 μm tungsten protective layer was deposited on the regions of interest in Figure 23b-c. More details about the standard FIB cross-section preparation are summarized in Appendix 1.

Two samples were prepared by performing a standard lift-out procedure, bonding to the side of the cross-section, and attached to TEM half grids using tungsten deposition. Samples were thinned in multiple steps by lowering the ion beam voltage gradually from 30 kV to 5 kV until they appear transparent in the electron beam image at 5 keV. The cross-section thickness, measured later in the TEM by low-loss EELS, was found to be less than 100 nm for the CdTe film.

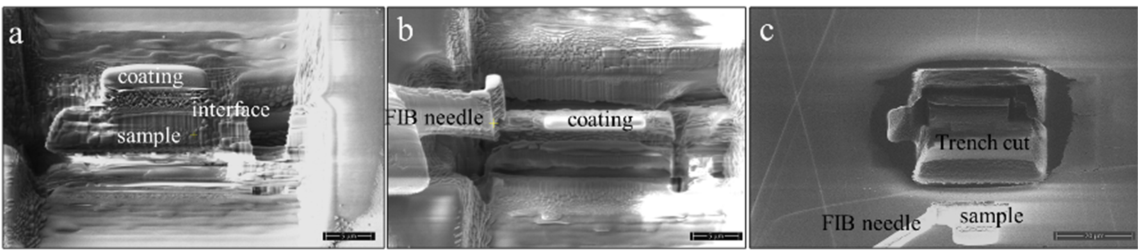

Figure 22. Consideration of cross-section attachment to the FIB needle. (a) SEM image of the sample after trench milling, (b) SEM image of the FIB needle attached away from the coating and the interface. (c) ion-beam image of lift-out of the sample from the trench. The scale bar is 5 μm in (a and b) and 20 μm in (c).

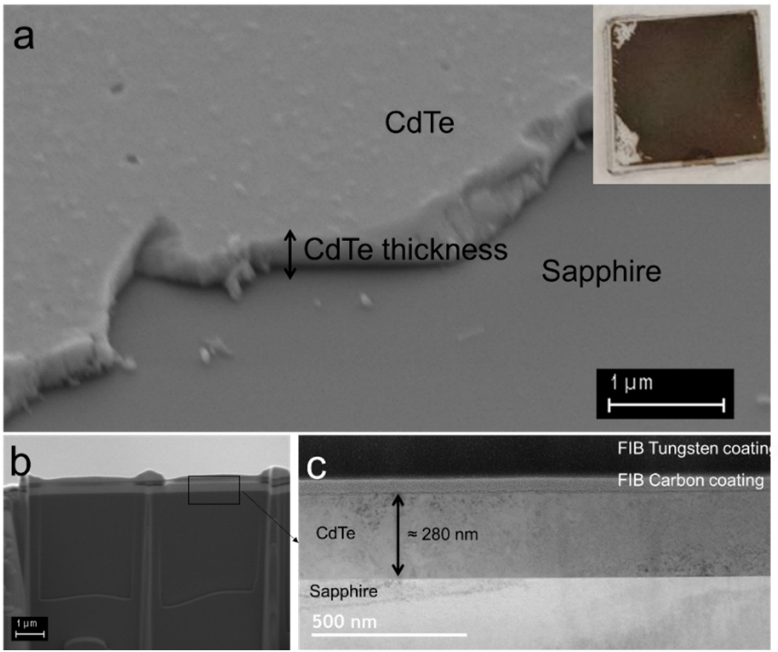

Figure 23. Preparation of CdTe cross-section sample for TEM investigation. (a) SEM image (taken at a tilted SEM stage) of the CdTe film on sapphire taken at a region with scratched CdTe. The right insert is a photo of 1 × 1 cm sapphire substrate with a CdTe film. (b) SEM image of a FIB cross-section with 2 windows prepared in the (120) zone axis of sapphire. (c) TEM image of the cross-section shows an approximately 280 nm thick CdTe film on sapphire. The carbon and tungsten layers above the CdTe are deposited during the FIB preparation to protect the CdTe film from ion-beam damage.

3.5. CdTe/sapphire interface characterization

3.5.1. STEM and core-loss EELS experimental conditions

The prepared cross-sections are imaged using a high-resolution STEM imaging and core-loss EELS mapping provided in (FEI Titan 80–300 cubed) transmission electron microscope. The Titan microscope is equipped with a high-brightness cold field emission gun (XFEG) and two spherical aberration correctors in both the image and probe-forming planes. Several STEM images were collected at 200 keV

with around 100 electrons/Å^2/second dose rate using an in-column Fischione HAADF detector (model 3000) at 19.1 mrad beam convergence angle, 50.5-200 mrad collection angles at 91–115 mm camera length, and 50 μm C2 aperture.

The core-loss EELS maps at the interface were acquired at a lower camera length (37 mm) to increase the signal counts using a direct electron detector (Gatan K2) at 0.32 Å pixel size 0.0025 s pixel time and 0.5 eV/channel electron dispersion, and 4 eV FWHM energy resolution. The core-loss EELS spectrum image is denoised using the weighted principle component analysis plugin in the Digital Micrograph software package. EELS measurements were performed at the atomic scale to map the interface elements at the following edges: cadmium (Cd-M edge at 404 eV), oxygen (O-K edge at 532 eV), tellurium (Te-M edge at 572 eV), and aluminum (Al-K edge at 1560 eV). The 40 eV energy gap between O-K and Te-M is wide enough to resolve the two edges (O-K is a sharp onset peak, while Te-M is a delayed edge) using the built-in multiple linear least squares (MLLS) fitting with standard Hartree-Slater cross-section models in the Digital Micrograph software. The EELS map has a pixel size of 0.32 Å to sufficiently resolve the atomic columns and to confirm that the monolayer at the interface is tellurium, not cadmium.

3.5.2. Interface structure

The STEM-HAADF images in Figure 24 reveal a monolayer at the CdTe/sapphire interface with weaker HAADF intensity. Since HAADF intensity is related to the atomic number, the monolayer is assumed to be a non-CdTe plane. Figure 24a shows the interface at the CdTe $(01\bar{1})$ zone axis, while Figure 24b shows the interface when CdTe $(\bar{2}11)$. Zone axis from a different cross-section sample. An atomic model of the epitaxial interface with a monolayer is overlaid in both

figures. The spacing between the monolayer tellurium and the first layer of the CdTe film (Te-Te) is about ~3.17 Å from the STEM image, which agrees with the simulated model. The accuracy of the spacing measurement depends on the pixel size of the image on the detector (2048 × 2048) and the magnification. The domain preference is found to be a cubic CdTe (111) parallel to hexagonal sapphire (0001) and a [111]/[0001] orientation relationship.[1]Figure 25b shows core-loss EELS mapping at the interface in which the tellurium map shows more tellurium than the cadmium at the interface. Moreover, the monolayer tellurium can also be detected through an EELS line scan in Figure 25c that shows a sharp tellurium peak at the interface with no significant cadmium. The resolution of these EELS results is sufficient to reveal the monolayer because the pixel size is adjusted to 0.32 Å, and the sample is thinned to less than 100 nm thick to minimize the plural scattering.

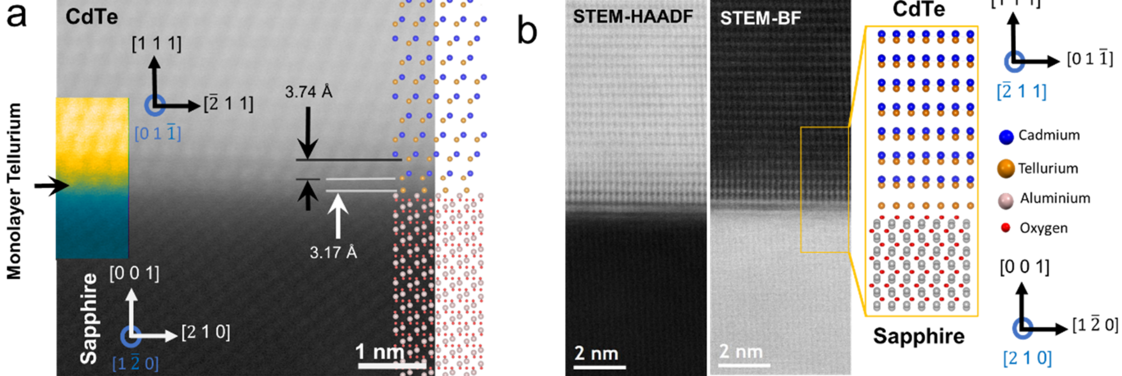

Figure 24. STEM imaging of the CdTe/sapphire interface. (a) STEM-HAADF image shows the interface of the CdTe (011) zone axis. The left insert is a false-colored region emphasizing the tellurium at the interface. The right insert is an atomic model overlayed on the STEM-HAADF image that shows the measurements of the Te-Te distance at the interface. (b) STEM-HAADF (left) and STEM-BF (right) image shows the interface of the CdTe (112) zone axis. A monolayer of tellurium terminated the CdTe/sapphire

interface. (a and b) are STEM images taken from two different FIB samples prepared in perpendicular directions to show the interface in different zone axes.

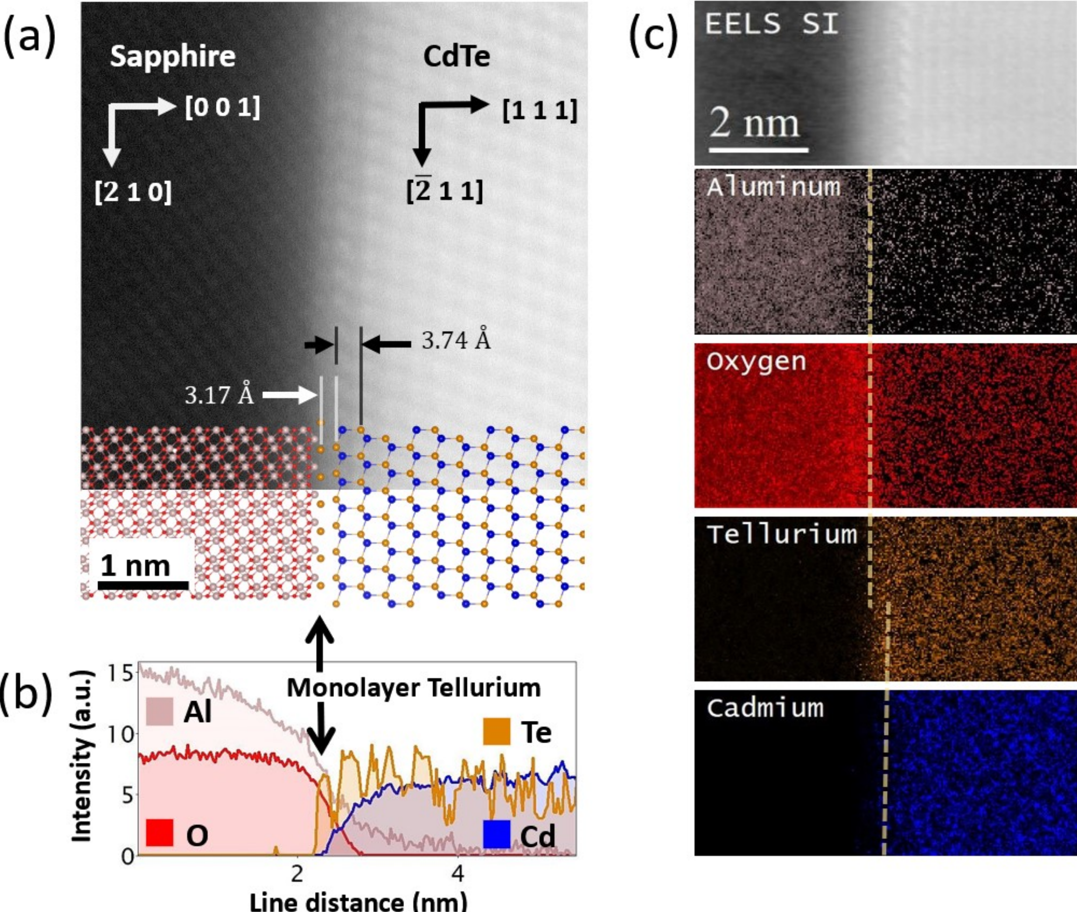

Figure 25. Core-loss EELS of CdTe/sapphire interface. (a) STEM-HAADF image at the CdTe/sapphire interface shows a monolayer terminating the sapphire topmost layer. The bottom overlay is an atomic model overlayed on the structure with the same color code in Figure 24. (b) a line scan EELS map was taken crossing one of the tellurium atoms at the interface showing Al-L, O-K, Te-M, and Cd-M edge profiles across the interface. The EELS spectrum image (SI) shows resolution near the atomic fringes. The CdTe region shows a tellurium layer preceding the CdTe film. (c) STEM-HAADF image indicating the EELS line scan results on the right. The EELS line scan shows monolayer tellurium at the interface.

More postprocessing analysis on the EELS mapping may be applied to denoise the mapping of tellurium and cadmium, as seen in Figure 26. The denoising process is applied by decomposing the EELS spectrum image, then reconstructing a new spectrum image from the first 10 principal components. The choice of 10 components is safe to maintain the main core loss signal because the interface contains only 4 edges (Cd-M, Te-M, Al-L, and O-K) that are well separated in the spectrum. After denoising, clearer maps show the atomic positions of tellurium and cadmium in addition to the position of the monolayer tellurium (Figure 26c) at the interface. Moreover, the denoised Cd/Te EELS profiles in (Figure 26c) shows an incremental increase of the Cd:Te stoichiometric ratio at the first two CdTe layer (~0.85, and ~0.95) before reaching the expected 1.00 Cd:Te ratio at the third layer. This may mean that the tellurium (as a chalcogenide) has preferential deposition (due to lowered vapor pressure) or a higher probability of attachment than cadmium on the sapphire substrate at the growth temperature. This scenario may be correlated with a previous density functional theory (DFT) modeling of adatoms on the single aluminum terminated surface of sapphire, which indicates a chemical binding energy preference for tellurium.[153] In addition, it is more likely for Te to nucleate rather before Cd because tellurium has lower vapor pressure (269 μTorr)[154] than cadmium (50.4 mTorr)[155] at the substrate temperature (300 °C), which means that Te will condense on the substrate before the Cd at certain PLD vacuum conditions.

The phenomenon of tellurium-terminated sapphire at CdTe/sapphire interface is comparable to a previous study of the spontaneous Te-termination of α-sapphire following the deposition of the van der Waals Bi_2Te_3 2D layered, as a 2D/3D interface system.[67] However, our observation of this phenomenon in the

CdTe/sapphire interface system is the first reported for a 3D/3D system[1], which has important implications for thin film growth.

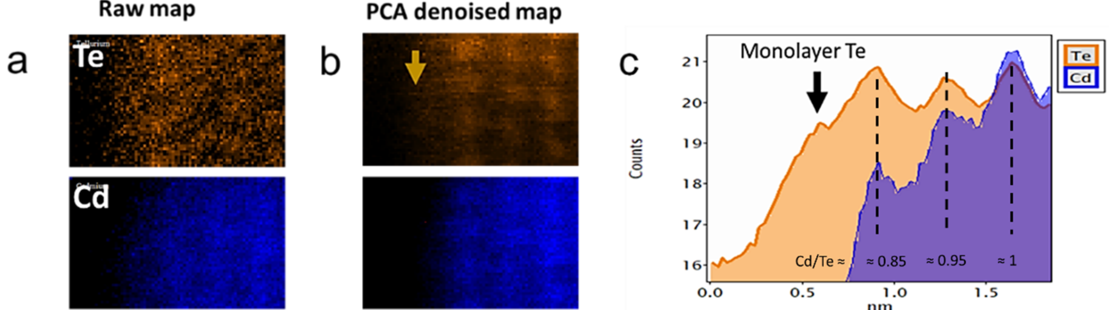

Figure 26. Denoised core-loss EELS map of CdTe/sapphire interface. (a) Row data elemental composition mapping of tellurium (top) and cadmium (down) M-edges. (b) Denoised maps of the data in (a) after applying principal component analysis (PCA) to the first 10 components. (c) intensity profile of the denoised maps in (b) showing a monolayer tellurium peak before the CdTe starts. The first layer of the CdTe thin film also shows a higher tellurium concentration.

3.5.3. Interface bonding

Low-loss EELS experiments were performed in (FEI Titan 80–300 cubed) transmission electron microscope at monochromated conditions to achieve high energy resolution. Low-loss EELS maps at the interface were acquired at 300 keV with a monochromated electron beam of 0.14 eV FWHM energy resolution (Figure 27a) achieved at 0.05 eV/channel electron dispersion. The microscope is also aligned to achieve a high spatial resolution to resolve atomic columns (Figure 27b) with the help of the two spherical aberration correctors in both the image and probe-forming planes. The low-loss spectrum image is acquired at 37 mm camera length, less than 50 pA screen current, 1.6 Å pixel size, and 0.1 Second/pixel time using a Gatan US1000FTXP CCD camera. The STEM images were collected using the in-column Fischione HAADF detector (model 3000) and a 50 μm C2 aperture.

Figure 27c shows a cascade of low-loss EELS spectra acquired across the interface from the sapphire region (green) to the interface (blue) then to the CdTe region (red). The insert image is the EELS spectrum image which resolves the atomic fringes, and where the spectra are collected with the same color code as indicated. Low-loss EELS usually contain a bulk plasmon peak around 25 eV, which changes its position depending on the type of the material and the temperature of the sample. Since EELS are collected at room temperature, we neglect the effects of temperature. In addition to the bulk plasmons, another plasmon peak may be found in the case of 2D materials around 5 eV, which is an indication of vdW or weak bonding in the sample.[156, 157]

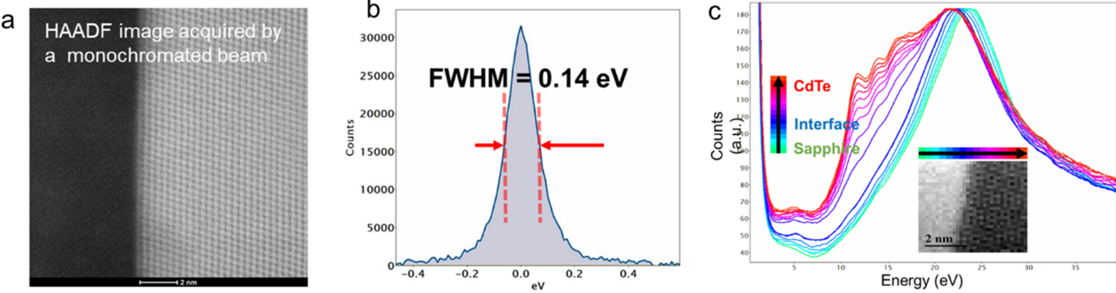

Figure 27. Monochromator alignment of Low-loss EELS. (a) STEM-HAADF image of CdTe/sapphire interface acquired with a monochromated beam. (b) FWHM measurement of the energy resolution at 0.05 eV per channel dispersion of the monochromated beam used in imaging (a). (a and b) provide evidence of achieving both high energy resolution (0.14 eV FWHM of the zero-loss peak (ZLP)) and spatial resolution (< 2 Å) to resolve fringes of the CdTe layers and the possible tellurium terminated-sapphire layer. (c) Successive low-loss STEM-EELS spectra cover both the surface and bulk plasmon ranges. Each colored spectrum is extracted from a 2x30 pixel size window starting from the sapphire (green), through the interface (blue), and finally to the CdTe region (red). The spectra are normalized to have equivalent ZLP integrals. The insert in (c) is the EELS spectrum image.

The purpose of the low-loss EELS experiment is to study the bonding at the interface and to examine the bonding signature in both plasmon peaks related to the bulk (strong bonding) and weak bonding. In addition, the bonding information should be spatially resolved to be correlated to the atomic scale arrangement of the interface. To achieve this purpose, the data in Figure 27c should be compared to the reference profiles of spectrum contents. Figure 28 illustrates how the reference profiles are collected. References of the CdTe and sapphire are collected from the FIB cross-section sample, away from the interface, at the same conditions after acquiring the interface spectrum image in Figure 27c. To acquire a reference EELS for the Te-Te bond, a new sample of pure tellurium is sonicated in deionized water and dropped onto a quanti-foil TEM grid. The pure tellurium bulk sample was the same sample used as a target in the PLD fabrication. Then, STEM mode is adjusted at the same monochromated conditions as those used for acquiring Figure 27c, and a thin tellurium layer is selected to acquire the reference signal as seen in Figure 28c, f.

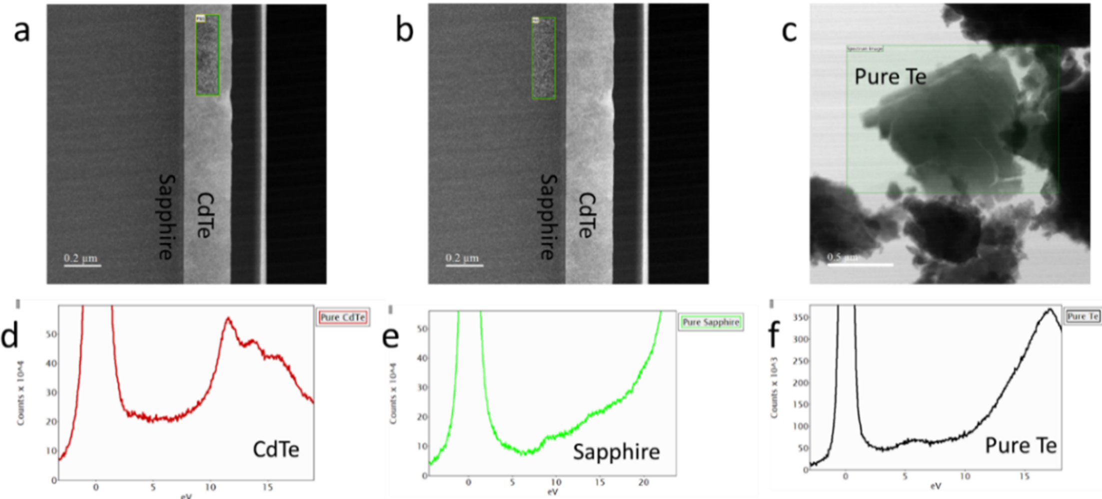

Figure 28. Reference low-loss EELS spectra of CdTe, Sapphire, and Te. (a-c) STEM-HAADF images showing a green box where the EELS signal is

collected for CdTe, Sapphire, and Te references, respectively. (d-f) low-loss EELS signal from the positions indicated in (a-c). CdTe and sapphire signals are collected from the FIB cross-section ~50 nm away from the interface. A reference tellurium signal is collected from pure Te flakes that are used as the source for the PLD growth. The tellurium signal is collected from a thin flake to reduce the effect of plural scattering.

Now, EELS data from the interface and references are ready to be compared, as can be seen in Figure 29. At the interface, a unique high-intensity peak at ~ 5.6 eV can be seen in the cascade plot of the spectra in Figure 29c, which also can be mapped to illustrate that the high plasmon intensity comes from the interface (Figure 29b). The interface spectrum with high intensity is then extracted and compared to the reference spectra, as illustrated in Figure 29d. Here, the interface peak at ~ 5.6 eV is correlated only to the plasmon peak from the tellurium reference, which indicates a weak bonding at the interface. Further verification may be applied to the original EELS data at the interface by decomposing the spectrum image to its main principal components. Figure 29e shows the first six principal components, where the fifth component reveals a unique peak between 4-8 eV, in good agreement with the reference comparison done in Figure 29d.

To investigate the origin of the weak bonding of the tellurium reference, the structure of pure tellurium from the D_3 point group (or $P3_121$ space group) with trigonal structural[158], similar to the $\gamma-\mathbf{Se}$ structure, is assumed as seen in Figure 30a-c. This structure consists of helix rods of tellurium atoms bonding strongly with covalent bonds. However, the bonds between the rods are weak vdW π-bonding. This assumed structure contains both σ and π bonds along and between the Te-rods, respectively. In Figure 30e-f, mapping of both the weak bonding (π) and the covalent bonding (π+σ) can be obtained from the EELS spectrum image at

the interface. These two maps are in correlation with the (π) and (π+ σ) peaks found in the tellurium reference in Figure 30d or Figure 28c, f.

In summary, the low-loss EELS analysis concludes that the monolayer tellurium that is revealed from imaging and core-loss EELS (Figure 24 to Figure 26) is actually has a Te-Te vdW or weak bonding. The Te-Te bond is between the Te-terminated layer and the Te atomic plane of the first CdTe crystal. This implies that the CdTe film grows in a Cd-polar direction where Cd is up, and Te is facing down to make the vdW bonding with the Te-terminated layer.

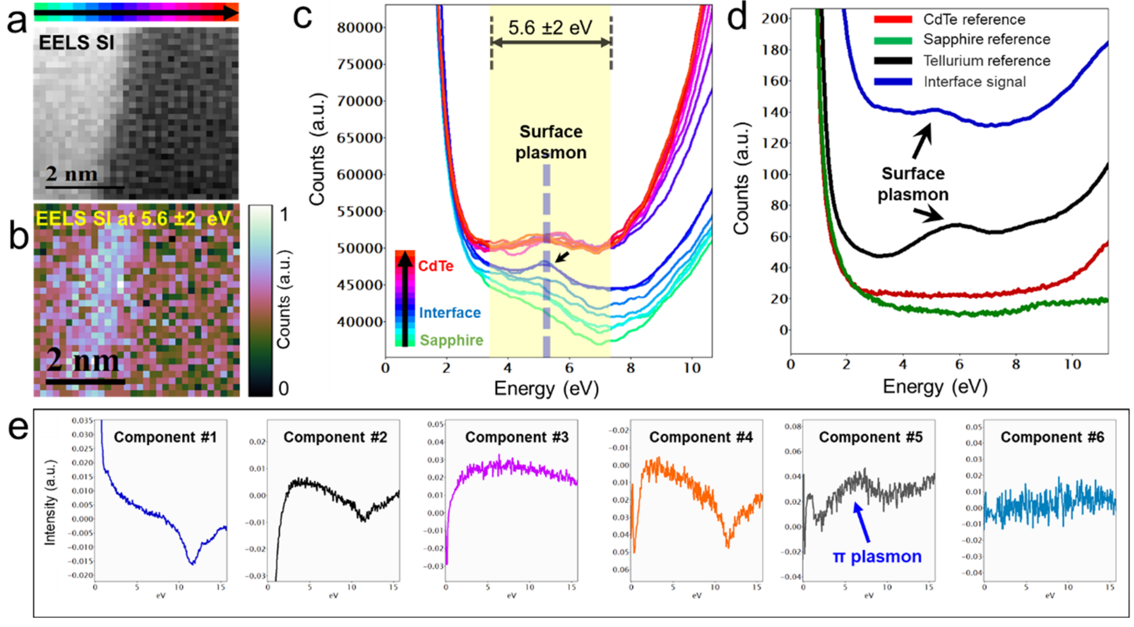

Figure 29. Analysis of low-loss EELS experiments at CdTe/sapphire interface. (a) EELS spectrum image acquired by the monochromated beam in Figure 27 at the interface. The color bar and arrows indicate the transition from the sapphire substrate (green) to CdTe film (red). (b) EELS spectrum image of (a) showing the signal integrated within the 5.6 ± 2 eV region. The false-color indicates that the highest intensities in that energy range are concentrated at the CdTe/sapphire interface. (c) Low-loss EELS spectra correspond to the transition of the EELS signal across the interface. The

spectra evolve from sapphire to the interface (blue) and then to the CdTe, indicating a unique plasmon feature at the interface with a peak intensity at approximately ~5.6 eV. Spectra are normalized to have equivalent ZLP integrals. (d) Low-loss EELS representative spectra for CdTe, sapphire, the film-substrate interface, and a pure Te sample are compared by the same normalization. The plasmon feature at the interface is not seen in the substrate or the film but corresponds to the π plasmon in pure Te. (e) Multivariate statistical analysis of the EELS spectrum image in Figure 18a showing the principal components of the spectrum image. The CdTe bulk plasmon peak starting at 11.5 eV appears in components 1, 2, and 5. Component 5 also shows a peak between 4 and 8 eV, which matches the weak bonding plasmon found at the interface. Components 3 and 6 are interpreted to be related to the sapphire noise. Note that the negative intensities present in the spectrum components do not have a physical meaning but rather are generated by lowering the dimensionality during the denoising process.

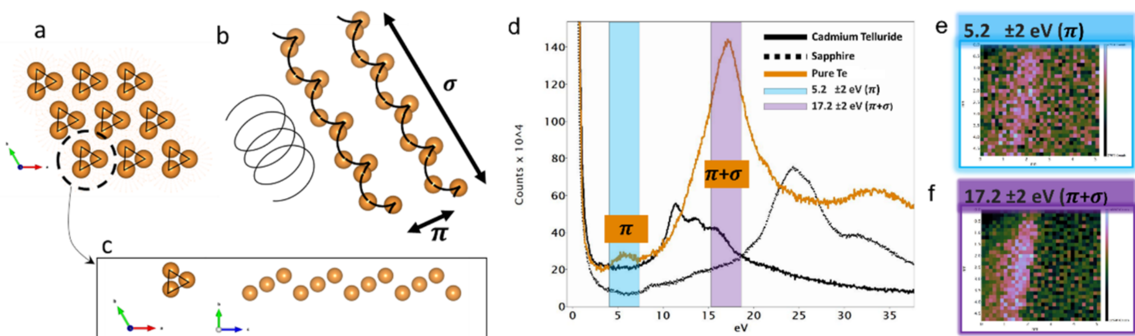

Figure 30. Structure correlated to CdTe/sapphire interface bonding. (a) c-plan top view of the tellurium structure in which contains groups of triangles. (b) schematic representation of two Te-triangles which are weakly bonded to each other. What is considered triangles in the c-plane is a helix chain-like of strongly covalent-bonded tellurium atom. (c) representation of top-view (left) and side-view (right) of a helix chain-like tellurium rod. (d) Low-loss EELS spectra of CdTe, sapphire, and pure tellurium references aligned with the integration of the zero-loss peak. The cyan and purple colors in (d) represent the energy window for the π and (π + σ) bonding of the tellurium reference collected in Figure 28. It is noticed that the π and (π + σ) peaks are not overlapping with the peaks for CdTe and sapphire. (e and f) low-loss EELS spectrum image on the interface (same in Figure 29a) at the π and (π

+ σ) energy windows (5.2±2, and 17.2±2 eV) for the pure tellurium reference indicated in (d). The low-loss maps in (e and f) show higher intensity only at the interface, which means the interface contains a tellurium layer that has a plasmon response similar to the pure tellurium behavior.

3.6. Reconstructed topmost sapphire layer

The investigation of the sapphire surface reconstruction is based on experimental EELS data and comparison with literature evidence. First, as a tool, the core-loss EELS may indicate a surface reconstruction possibility at the topmost layer of the sapphire substrate. Figure 31a-f shows the EELS maps and the corresponding profile of both O-K and Al-K edges. The EELS map shows the intensity change of the oxygen and aluminum edges at the topmost sapphire position compared with the deeper bulk sapphire EELS signal. By looking at the fine structure EELS signal (Figure 31g), the O-K edge at the topmost layer is found to shift to higher energy and has lower counts. This spectrum change may be explained as a result of **(i)** different compositional ratios or **(ii)** different bonding at the top layer or as **(iii)** a distorted bond length of oxygen and aluminum due to surface reconstruction, or **(iv)** a combination of the previous possibilities. Below is a discussion of these possibilities.

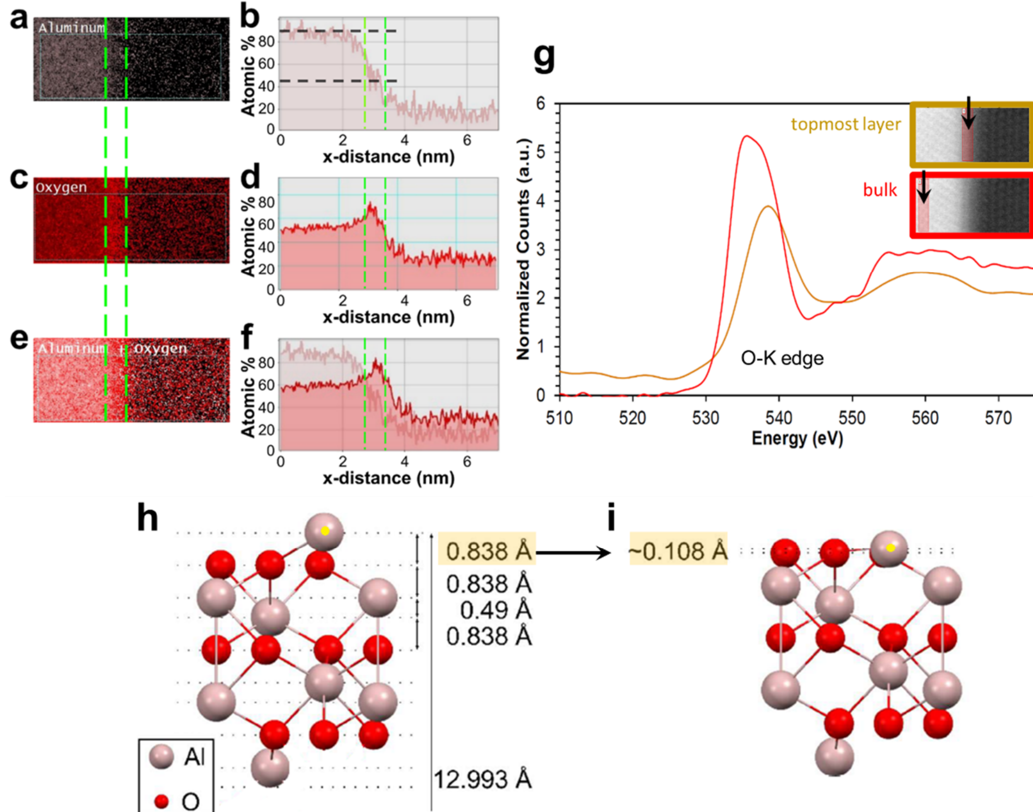

Figure 31. Reconstruction evidence at the topmost sapphire layer. (a, c) Core-loss EELS elemental compositional maps for Al-K and O-K edges, respectively. (b, d) the corresponding profile generated by compressing the maps in (a,c) into a profile in the horizontal direction. (e, f) Composite chemical map for aluminum and oxygen maps and the corresponding compositional profile, respectively. The noise level in (b,d, and f) is increased because of the compression of the area maps in (a,c, and e). The area between the two green lines in (a-f) indicates the topmost layer of the sapphire. The atomic percentage of the Al-K edge at the topmost layer is about half of the bulk value, which indicates that the topmost layer has less Al than the bulk as a single layer Al termination. Generally, the noise level in the O-K map is higher than the Al-K because O-K is overlapping with the Te-M edge. However, the increase in the O-K signal count at the topmost layer may be because of different bonding or concentration. (g) O-K EELS edge comparison of the bulk (bottom insert SI) and the topmost layer of sapphire (upper insert SI). The spectra show ~2eV shift right in energy at the topmost layer. This means that the oxygen at the topmost layer is not bonded in the same way as the bulk sapphire. This indicates a surface

reconstruction that may be induced during the growth because the monolayer tellurium is bonded to the oxygen sites. Curves are also smoothed by a low-pass filter and aligned vertically by integral. (h) structure model of sapphire with single Al-atom termination. (i) reconstructed topmost layer of sapphire where the top Al layer is moving towards the bulk.

(i) different compositional ratios

A much simpler reconstruction, and a wide plateau of reconstruction stability, occurs for sapphire (0001) by the movement of aluminum surface atoms from their bulk position into the oxygen layer below, as seen in Figure 31h. This can be seen in the Al-K edge map Figure 31b, where the topmost layer has lower Al-K counts compared with the bulk sapphire. This means the sapphire substrate may have a one-aluminum atom termination before the growth of the CdTe film. The oxygen signal at the topmost layer (in Figure 31d) is a compositional ratio between the elements at this layer, which are only oxygen and aluminum. Since the aluminum number of atoms is only one (compared with 3 aluminum atoms/layer in bulk), the oxygen to aluminum ratio becomes higher at the topmost layer. This can be a reason for the higher counts in the oxygen signal.

(ii) different bonding at the topmost oxygen

The c-plane sapphire is expected to provide dangling bonds, unshielded charge, surface polarity, and to break bonds by deposited adatoms, easily at growth temperatures at 1400 °C, and above.[159, 160] However, in the CdTe/sapphire system, the substrate growth temperature is about 300 °C which is well below the 1400 °C limit of changes in the c-plane sapphire. Consequently, the tellurium adatoms can only interact with local weak chemical bonds within the sapphire or

satisfy any random unbalanced charges or dangling bonds at the step edges. Therefore, it is expected that the tellurium monolayer is weakly-bonded at the topmost sapphire layer at the growth temperature. These weak bonds may introduce changes to the local surface structure at the topmost layer of the substrate, as discussed in the following paragraph.

(iii) Distored O-Al or O-O bond length induces a surface reconstruction,

The most energetically favorable c-plane reconstruction of sapphire is a single Al-terminated surface, as seen in Figure 31h. This surface is nonpolar and expected to be stable and lacking dangling bonds below 1400 °C in a vacuum.[159, 160] This surface is believed to be the natural reconstruction of the sapphire after cleavage for minimizing the total surface energy by bending the dangling bonds towards the bulk surface. This stability allows the sapphire surface to form atomically flat terraces for subsequent thin film growth.[161]

However, the interaction of molecules[162, 163] or atoms [164] with substrates can introduce new surface reconstructions. Previous work suggests that the tellurium introduces surface reconstructions of the c-plane sapphire at 500 °C growth temperature.[67] Similar behavior may occur at a temperature of 300 °C t, which is the growth temperature of the CdTe system. When new tellurium adatoms arrive, the surface reconstruction can become dynamic to minimize the system energy in the presence of new layers at the interface, but the low-temperature growth maintains general weak bonds between the tellurium and sapphire. Examples of how sapphires may reconstruct at the growth are provided in Figure 31i, where the topmost aluminum atom is bent towards the bulk surface. This reconstruction can be associated with multiple changes in the O-O and Al-O bond

length in the real space. Unfortunately, the distance changes between atoms are beyond the electron microscopy spatial resolution limit. However, fortunately, the fine structure EELS may indicate the changes in bond length in the energy space. Therefore, the structural change in the O-K edge (Figure 31g) is more likely because of the surface reconstruction at the topmost sapphire layer.

(iv) multiple reasons.

In summary, the core-loss EELS analysis of the O-K edge and the discussed literature in (i, ii, and iii) implies that the sapphire is reconstructed prior to the growth of a single aluminum layer (Figure 31h). During the growth, further reconstruction (Figure 31i) may be introduced as part of the system relaxation but with weak chemical interaction due to the low-temperature growth. This combination implies changes in the bond lengths and subsequently introduces structural changes in the O-K edge (in Figure 31g), but these length changes are beyond the resolution limit of a standard STEM experiment.

3.7. Misfit dislocation-free interface

In this section, analytical electron microscopy techniques are employed to examine the strain at the CdTe/sapphire interface. Also, STEM images are studied to understand possible relaxation mechanisms through laminar twins at the atomic scale. Geometric phase analysis (GPA) or STEM-Moiré imaging are effective techniques to map the strain in the lattice and the interface. The previous structural and bonding analysis of the interface results in a tellurium monolayer at the interface with vdW-like bonding. This heterostructure system (sapphire/Te/CdTe) makes the analogy of the remote epitaxy growth of 3D/3D systems. In remote

epitaxy, a 3D system remotes the epitaxial registration of the substrate through a 2D material (graphene or boron nitride) with accommodating misfit strain at the interface, which results in a high-quality interface and thin film.

3.7.1. Geometric phase analysis (GPA)

First, GPA is employed for STEM image (Figure 32a) showing a CdTe in the ($\bar{2}11$) zone axis. This zone axis (similar to Figure 24b) is selected for GPA because it shows both CdTe and sapphire without satellite diffraction peaks, which helps to choose two perpendicular FFT spots, instead of 60° spots as in the ($01\bar{1}$) zone axis. The perpendicular reflections help to increase the GPA mask size, which increases the accuracy of the map. In addition, the ($\bar{2}11$) zone axis shows recognizable differences of the atomic spacing, as can be seen in the selected area electron diffraction (SAED) pattern with about ~3.7% lattice mismatch. Although the SAED can provide the lattice mismatch information, it cannot describe this mismatch at the interface because it represents the diffraction from a large field of view of ~1-micrometer spot size that covers both CdTe and sapphire regions. The GPA analysis is conducted using Strain++ software[165] (open source) by applying two masks (in red and blue in Figure 32b), with the size shown. An area of the CdTe lattice near the interface is selected to be the reference in which strain is relatively referenced to the CdTe lattice. Figure 32c shows the strain mapping at the interface where no periodic stress at the interface, which means no periodic misfit strain at the CdTe/sapphire interface. The phase image comes from the reflection spot representing the growth direction (Figure 32d) shows a separated interface with a gap correlated to the monolayer tellurium. This indicates that the CdTe grows with mismatch-free dislocations at the interface. A GPA analysis of a different

material system is added in Appendix 2 to understand how a surface with mismatch dislocation appears in GPA analysis,

The GPA of the CdTe/sapphire interface shows stressed lattice far from the interface, which implies lattice incoherency during the growth. This incoherency may be released by carbon contamination inside the PLD chamber or impurities from the target materials. These growth defects are localized inside small positions inside the CdTe film and do not affect the overall growth orientation of the film but may affect the film performance as a device.

The GPA results emphasize the unique compliant interface of the CdTe/sapphire interface, which allows for spontaneous relaxation of the misfit strain. Subsequently, higher quality CdTe films on sapphire are possible due to this compliant interface. However, the field of view of the GPA is limited to the span length of the atomic resolution TEM image (~30 nm in this work) at a given magnification. To further expand the field of view of the interface, other techniques may be used, such as dark field electron holography or STEM-Moiré imaging.

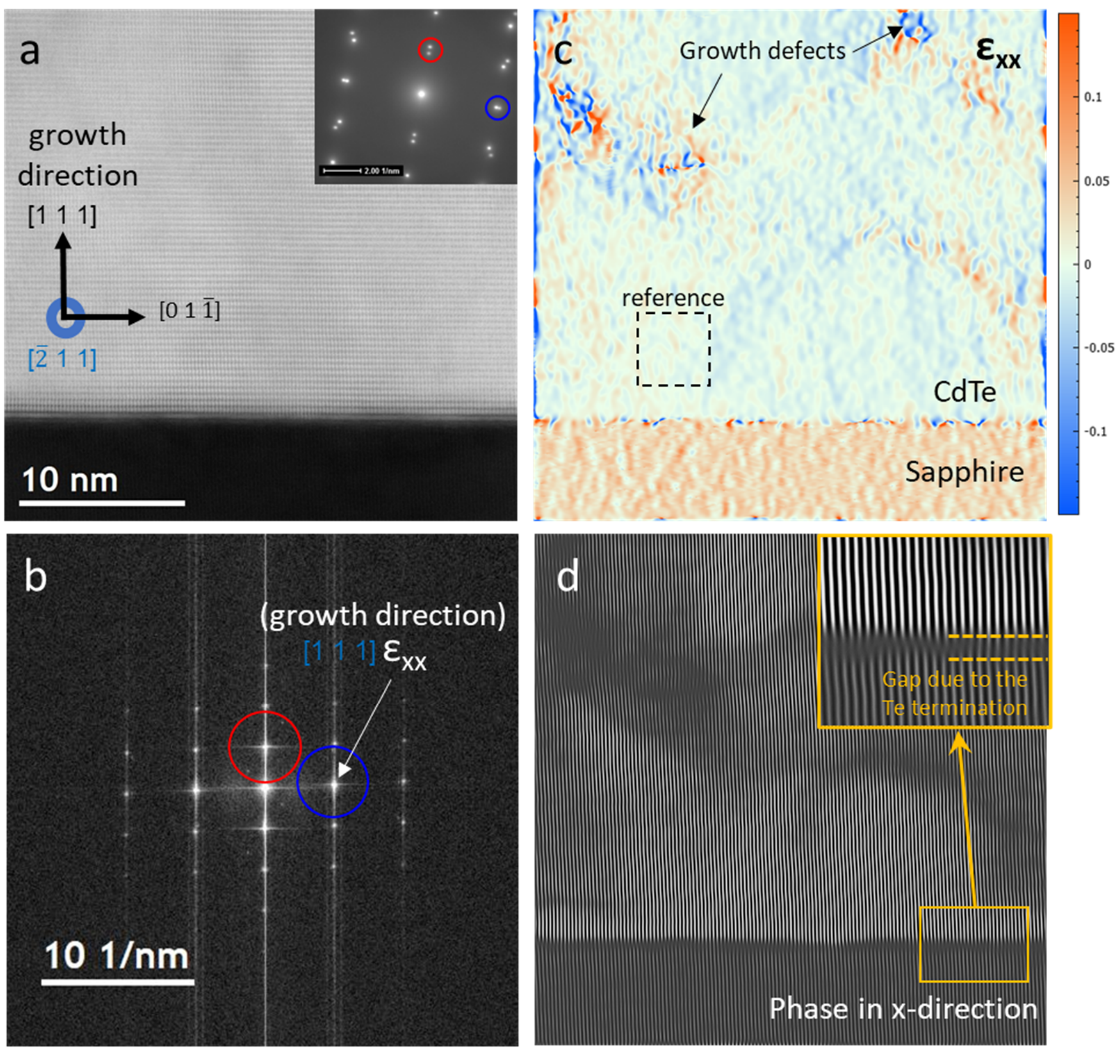

Figure 32. GPA strain mapping at the CdTe/sapphire interface. (a) STEM-HAADF image showing CdTe in the ($\bar{2}$11) zone axis. The insert is a selected area electron diffraction (SAED) taken in TEM mode at the same zone axis. (b) FFT indicates the two refection spots used for the strain mapping. (c) geometric phase analysis of in the x-direction (growth direction) showing about ~4% lattice spacing variation cross the interface. CdTe lattice is used as the reference for the GPA. No periodic stress points at the interface are found, which means no mismatch dislocation. The stress points at the CdTe middle indicate possible growth defects. (d) phase in the x-direction showing no dislocation at the interface.

3.7.2. STEM-Moiré imaging

A STEM probe is typically below an angstrom in diameter under probe correction conditions. This fine probe channels at the column of atoms that are perfectly aligned. STEM image can resolve the atomic structure when the probe scans the sample with step pitches smaller than the crystal lattice spacing at higher magnification at a given zone axis. However, at lower magnifications, Moiré fringes appear when the probe step pitches are larger than the atomic planes [166, 167] as a result of the interference between the STEM scan steps and the lattice (Figure 33a). This benefits the search for dislocations within a large field of view (at low STEM magnifications) because a single dislocation can disturb the moiré fringes, as seen in (Figure 33b). In the following analysis, STEM-moiré imaging is used to search for dislocations at the CdTe/sapphire interface with a larger field of view than the GPA.

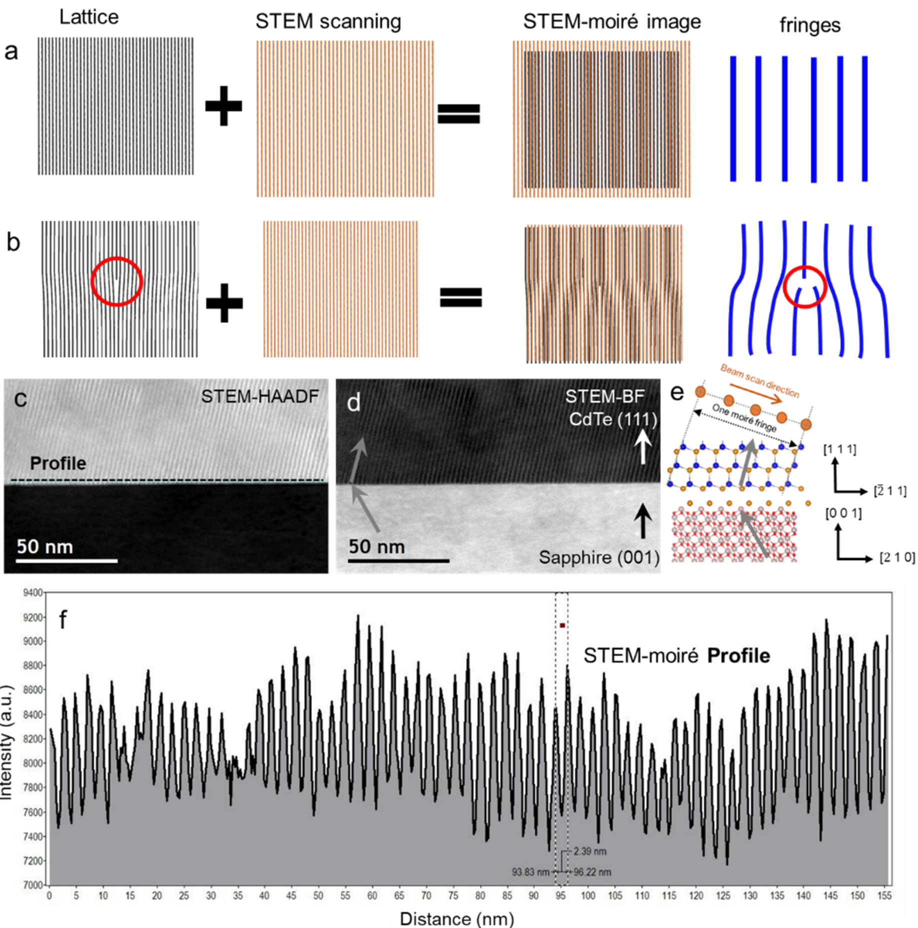

Figure 33. STEM-Moiré imaging at the CdTe/sapphire interface. (a, a and b) schematic representation of the STEM-Moiré imaging of a coherent lattice and a lattice with a dislocation, respectively. (c and d) STEM-HAADF and STEM-BF images were taken at a 9° twist angle between the period lattice and the STEM sampling. Experimentally, the electron beam is rotated at 9° relative to the interface to align the scan rastering direction perpendicular to the CdTe fringes. Dwell time is adjusted to acquire a 512 × 512 frame with 0.34 nm pixel size. (e) Atomic model showing the direction of the tilted CdTe fringes (gray color), which are perpendicular to the scanning and generates Moiré fringes in (a,b). (f) STEM-Moiré profile taken parallel to the interface, as indicated in the STEM-HAADF image. Moiré fringe width is ~2.39 nm which covers CdTe planes (7 tilted planes) similar to the width of the model in (e). The Moiré fringes appear continuous at a larger span length (~155 nm) of the image, which indicates no misfit dislocation.

Figure 33c shows a STEM-HAAF taken at 640 kX magnification where the STEM probe is adjusted to scan perpendicular to the CdTe tilted fringes (gray arrow in Figure 33e). The dwell time is adjusted to have a match between the STEM probe and a CdTe column for every CdTe fringe in the real space. The resulted STEM image (Figure 33c-d) shows moiré fringes aligned to the interface without dislocations over a length more than 155 nm. Extra STEM-Moiré images from a different material system (SiGe/Si) in added in Appendix 2 to understand how mismatch dislocation appears in STEM-Moiré imaging.

The strain analysis using GPA and STEM moiré imaging shows that the CdTe film grows free of misfit dislocations at the interface because of the monolayer decorated tellurium layer. However, the interface can have some other imperfections, such as the sapphire step edges that fundamentally exist at the atomic scale after cleavage or cutting the substrate at a miscut angle. The following section discusses strain relaxation at some of the interface imperfections which are found in the two FIB cross-sections used in this analysis.

3.7.3. Laminar twin CdTe layer

An inverted CdTe layer (Figure 34a-b) is observed as a laminar twin of the first CdTe layer. This inversion is a mechanism to relieve strain at sapphire surface sites, contains step edges, or the absence of the decorated tellurium monolayer. The HAADF intensity of this layer suggested a lower density of different Cd:Te compositions, as discussed previously in Figure 26c. Within the two prepared FIB cross-sections, a few positions of the CdTe laminar twin are observed. Two main reasons are postulated to explain the strain relaxation due to the laminar twin.

First, Figure 34c-d shows the growth of the inverted first CdTe layer across a step edge of the sapphire. The step edge may change the sapphire termination condition, and subsequently, the alignment of the tellurium monolayer can be changed or absent at some point. This discrepancy of the tellurium monolayer across the sapphire step produced an in-plane dislocation loop at the first CdTe layer when as the film continues to grow. Here, the CdTe inversion at the first layer occurred to relieve the strain of the interface at the first CdTe layer. It is also observed that even though a dislocation starts to grow from the interface (Figure 34c), it can be relaxed after a few layers of the film.

Second, the CdTe laminar twin is also observed in a flat sapphire surface without step edges, as seen in Figure 34e. In this case, the inverted first CdTe layer is postulated to accommodate a stacking fault or overgrown CdTe at some site of the sapphire substrate. This may also be because of the inhomogeneity of the monolayer tellurium layer at the interface, either because of the absence of the monolayer Te or the increased Te density, which affects the vertical alignment of the tellurium atoms across the interface.

These TEM observations uncover the fundamental strain relaxation mechanisms of the CdTe/sapphire interface that all contributes to overcoming the misfit strain. The strain relaxation at the interface seems to occur spontaneously and abruptly because of the van der Waals-like interface and the tellurium-terminated sapphire interface. The modification of the sapphire substrate by the chalcogenide (tellurium) further adds the possibility to delaminate the film and for further reuse of the substrate for other possible growth.

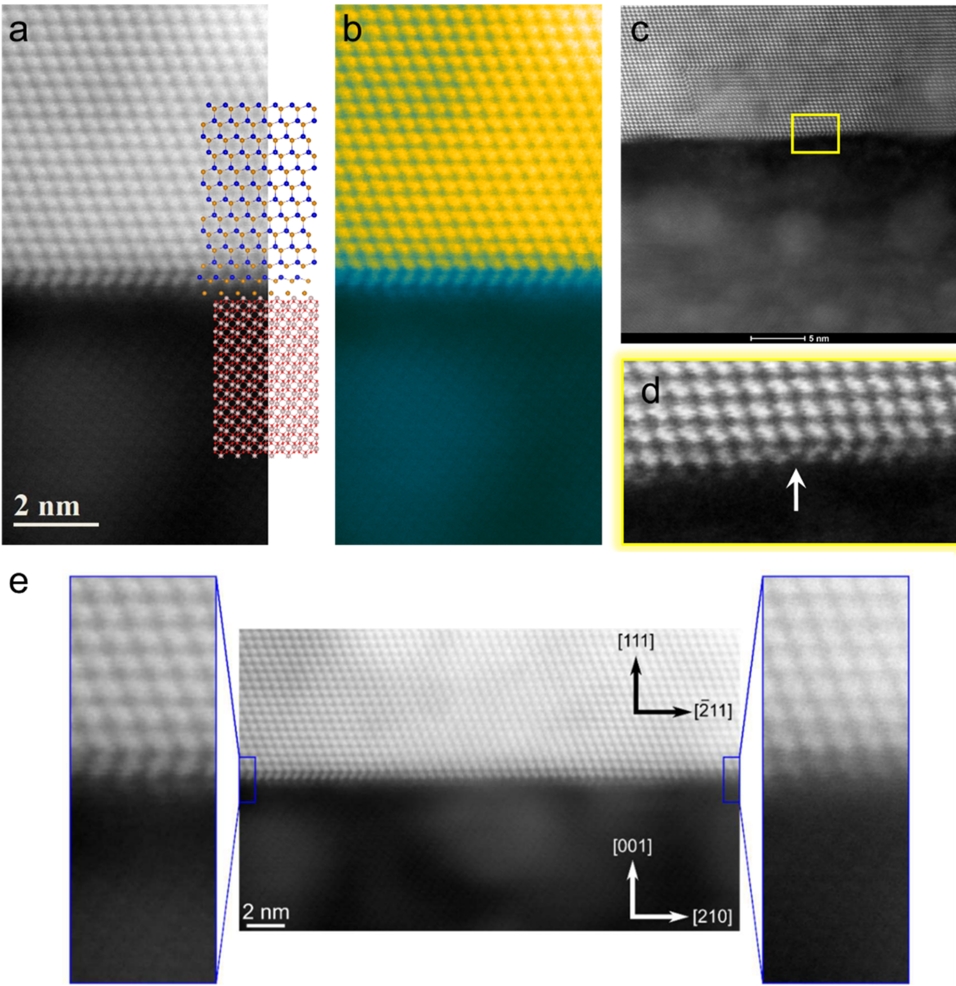

Figure 34. Strain relaxation mechanisms of CdTe/sapphire interface. (a) STEM-HAAD image at the interface showing the first CdTe plane with a laminar twin. (b) False-colored image of (a) showing better visualization on the first CdTe plane. The lower HAADF contrast of the first CdTe plane may indicate a change in the Cd/Te compositional ratio. (c) Low-magnification STEM-HAADF image at the CdTe/sapphire interface showing a dislocation appears at the interface then relaxed at the height of ~18 CdTe plane. The yellow box indicating an atomic step edge of the sapphire is illustrated in (d). The laminar twin of the first CdTe layer occurs as a relaxation of the film growth across the sapphire step edge. (c and d) indicates that even if a dislocation appears at the interface at a sapphire step edge, the CdTe film can be relaxed at a certain height of few atomic planes. (e) A laminar twin

occurs to compensate for an overgrown stacking fault at the CdTe/sapphire interface.

3.8. Tellurium buffer thickness versions

Sapphire-terminated tellurium is found mainly with a monolayer thickness within the screened FIB cross-sections, each being ~12 μm wide. However, due to the weak bonding at the interface, the tellurium registry of the sapphire may be changed. Moreover, depending on the PLD growth conditions, the local amount of tellurium atoms that reach the substrate may be changed at some sites. This may increase the thickness of the tellurium buffer, as can be seen in Figure 35a-c. The tellurium thickness variation seems not to affect the bulk exfoliation of the CdTe film, which implies the weak bonding condition is still preserved at different thicknesses of tellurium. This weak bonding can be examined using the STEM as a function of the electron beam damage. In all STEM imaging and spectroscopy, the beam current is reduced to around 50 pA to minimize beam damage. However, at more than 200 pA currents, the interface can be easily damaged in seconds even with fast dwell time scanning. Surprisingly, the tri-layer tellurium (Figure 35c) is found to be *stable* under a higher electron beam current, which implies that this tri-layer has both in-plane and out-of-plane strong bonds between the tellurium atoms.

The observation of the tri-layer tellurium can be exciting to the 2D material community because it is similar to the Tellurene structure in cross-section view.[20, 168-170] It seems that injecting more tellurium atoms to the interface not only changes the Cd:Te ratio as seen in Figure 26c but also can stabilize the epitaxial structure of tellurium with weak bonding with the sapphire. Tellurium

is believed to be sputtered from the target source in PLD as individual atoms, but recalling the structure of the target gives the possibility of sputtering tellurium rods (Figure 30a-c or Figure 35d-f). These tellurium rods may stay disconnected from the substrate or act to stabilize a form of 2D tellurium material depending on the fabrication conditions. This inhomogeneity of tellurium thicknesses at the CdTe/sapphire interface may be the reason for observing a significant skewed Photoluminescence (PL) response (see Appendix 3)of the CdTe/sapphire sample before delamination compared with the same sample after delamination.

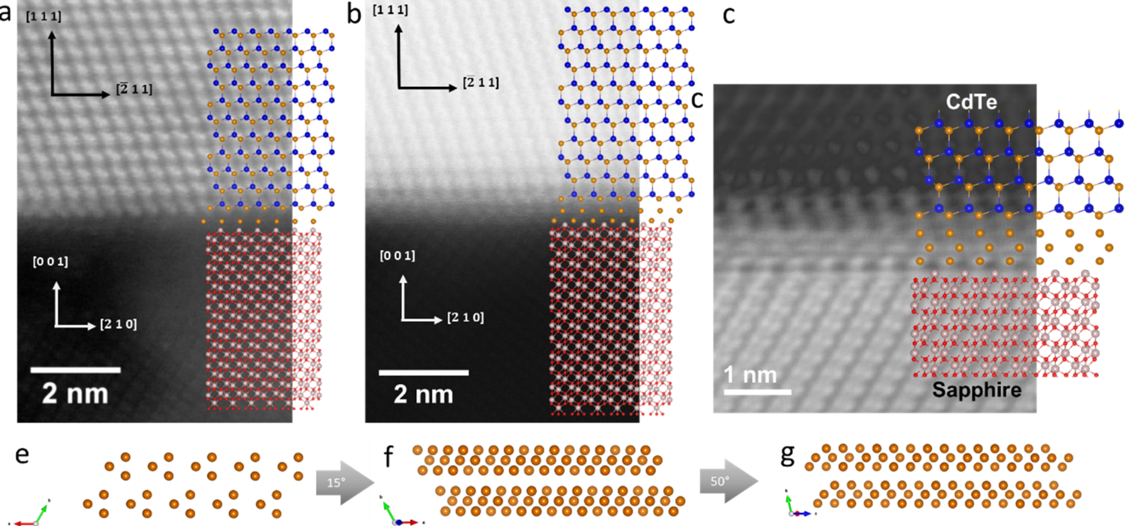

Figure 35. Tellurium thickness variations. (a) STEM-HAADF image showing monolayer tellurium buffer. (b) STEM-HAADF image (inverted contrast compared to HAADF) showing bilayer tellurium buffer. (c) STEM-ADF image showing a tri-layer of tellurium at the interface. (e-f) structure of Gamma-selenium (similar to Figure 30a-c) at different rotations along the vertical axis. The tri-layer tellurium in (c) may represent tellurium rods sputtered from the PLD target. The tellurium structure in (c) is also similar to the Tellurene structure in cross-section view[20], which may imply that extra tellurium at the interface may stabilize a 2D form of tellurium with stronger in-plane bonding.

3.9. CdTe film characterization

In this section, more characterization is presented to characterize the CdTe thin film away from the interface. First, the CdTe film polarity is examined with imaging and EELS techniques. Then, the surface homogeneity and surface roughness are characterized.

3.9.1. CdTe film polarity

The previous analysis confirms that the CdTe grows with its (111) direction perpendicular to the sapphire (0001) c-plane (Figure 36a-b). However, these growth orientations are valid for Cd-polar or Te-polar thin films. It is essential to understand the thin film polarity for device integrating and performance aspects. A STEM-HAADF image (Figure 36c) is acquired at ~100 nm far from the interface. A HAADF intensity profile is extracted from the image (Figure 36d) across 3 atomic planes of the CdTe film. Each atomic plane contains double atoms, of which one represents the Cd, and the other is the Te. Since HAADF intensity is a function of the atomic number, the Cd-polarity (up) of the thin film can be revealed from the HAADF intensity profile (Cd is 48, but Te is 52) with sufficient STEM resolution to resolve the ~1.1 Å spacing between the Cd and Te columns. It is worth mentioning that the FEI Titan microscopy resolution ranges between ~ 0.8–1 Å, experimentally, after achieving probe correction of the higher-order aberrations, which makes it possible to measure the Cd-Te spacing. EELS mapping (Figure 36e-f) of the Cd-M and Te-M singles is performed as a direct analysis to confirm the polarity of the CdTe film. This challenging EELS mapping is possible because of the very thin FIB cross-section (less than 50 nm) and the very small probe size.

Both STEM-HAADF and EELS maps confirm that the CdTe film grows with cadmium facing upward to the film surface and tellurium facing down towards the interface. This implies that the first atomic plane of the thin film should be a tellurium layer facing towards the tellurium buffer that decorates the sapphire surface. This confirms that the interface has a Te-Te bond relationship which is studied to be weak vdW-like bonding.

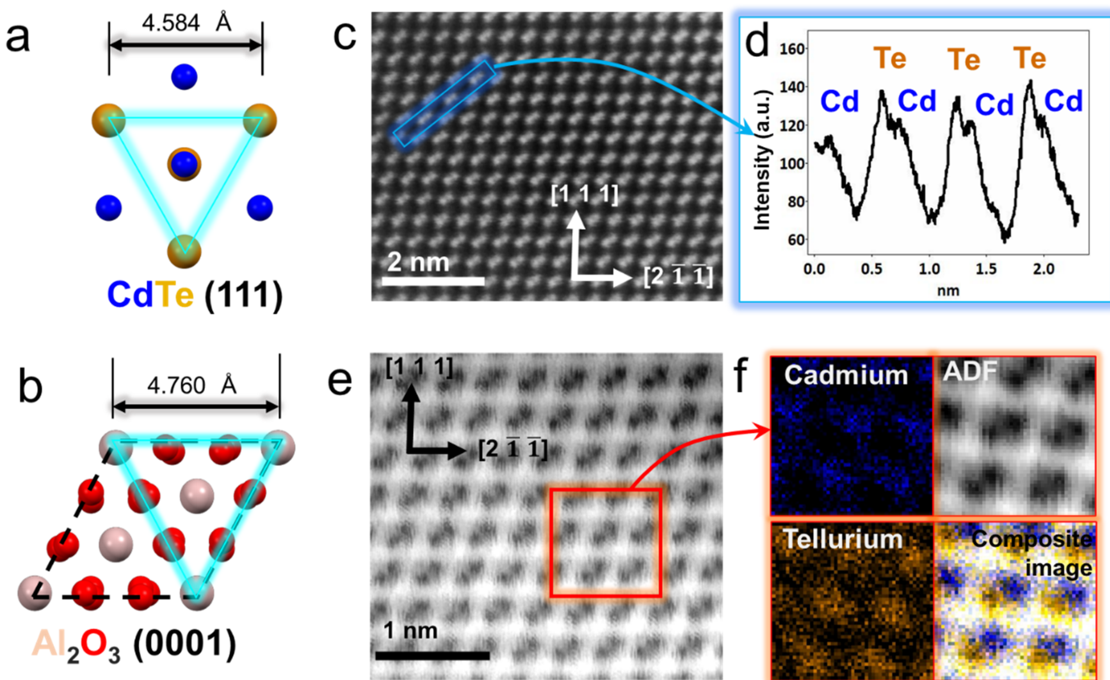

Figure 36. CdTe thin film polarity. (a and b) c-plane of CdTe (111) and sapphire (0001) with the corresponding lattice parameters. (c) STEM-HAADF image of the CdTe crystal. (d) HAADF intensity profile extracted from the indicated area in (c) showing that the film is cadmium polar. (e and f) ADF image and the corresponding core-loss STEM-EELS map achieved at the atomic scale with the direct electron detector to map the cadmium and tellurium. The EELS map confirms that the film is cadmium polar (up), and the tellurium is facing downward to the interface. This means the first atomic plane of the thin film should be tellurium facing towards the tellurium buffer that decorates the sapphire surface. This also confirms that the interface has a Te-Te bonding.

3.9.2. CdTe surface quality

Now, the assessment of the CdTe film moves from the atomic scale to a *larger length scale* to look at the film thickness using SEM techniques with few tens of micrometer span length imaging. SEM images (Figure 37a) show that the CdTe surface is not smooth compared to how it looks shiny in bulk by the naked eye. The surface contains lines at the micrometer scale. These lines are not scratches, but they are formed during film growth. These lines follow a structural origin in which some of them are parallel, and others are intersected with angles in relationship with the crystallographic orientations.

A quick electron backscattered diffraction (EBSD) map is taken at high magnification (Figure 37b-d) to investigate these surface lines further. The EBSD confirms that the CdTe grows in its (111) direction, as can be seen from the pole figure. In addition, EBSD shows that the surface lines represent a twinned area with an orientation different than the primary (111) direction of the CdTe film.

A *correlation* between STEM imaging of this twinned domain with the line seen in the SEM image is performed at the FIB sample preparation stage. A cross-section sample was extracted across one of the surface lines, thanks to the FIB's capabilities in the preparation of site-specific lift-outs samples. The STEM-HAADF image in Figure 37e shows a twinned area with a small width that was captured in the cross-section sample from a surface line.

Another *correlation* is performed using the SEM image detectors available in the microscope at a high tilted stage condition. Figure 37f-g shows two SEM images taken at 54° stage tilt with the in-lens and Everhart–Thornley detectors, respectively. The secondary electron emission from the SEM beam interaction with

the CdTe surface can be sensitive to the surface features with a nanometer scale. Depending on the tilt of the SEM stage, the secondary electron emission is subjected towards the ETD to provide more detectable signals representing the roughness of the CdTe surface (Figure 37g).

The tilted stage SEM imaging and EBSD correlation with the cite-specific FIB/STEM imaging provides a robust ***correlative characterization*** that bridges the "span length" gap between the atomic scale characterization and the bulk characterization of the CdTe film. The correlative characterization concept will be further discussed in the next chapter for the characterization of 2D heterostructures.

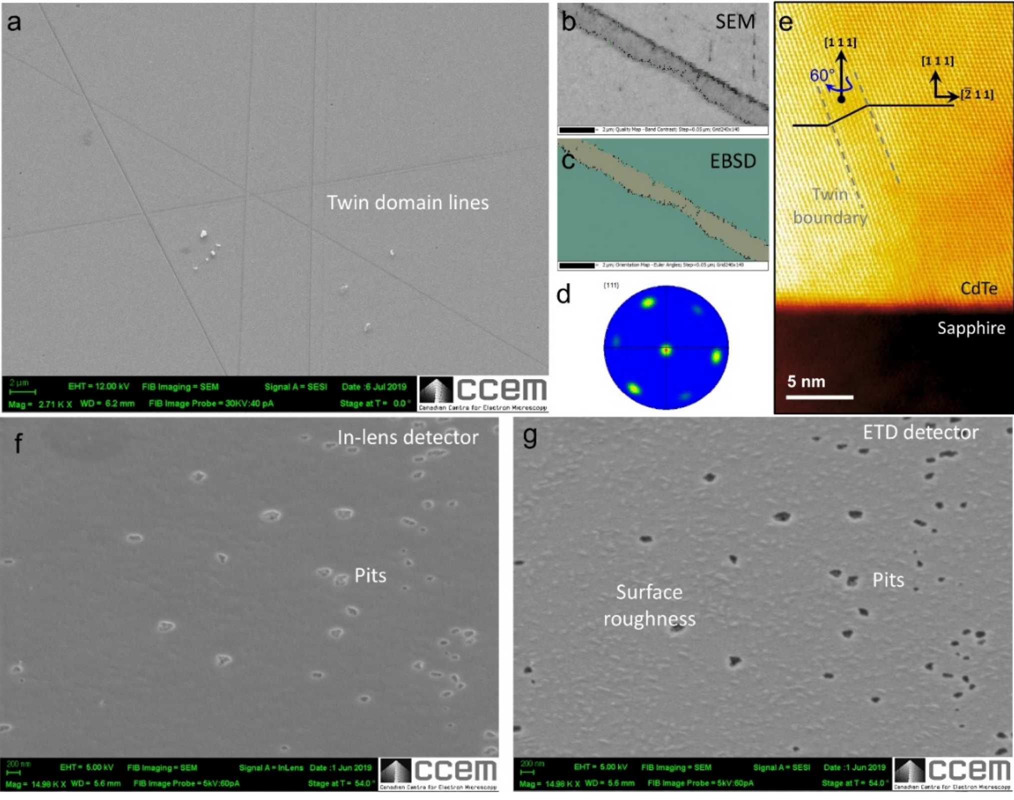

Figure 37. CdTe surface quality. (a) SEM image taken by an Everhart–Thornley detector (ETD) at zero stage tilt showing indented lines on the surface. (b

and c) high magnification SEM images of one of the surface lines and the corresponding orientation map from electron backscattered diffraction (EBSD) mapping, respectively. The turquoise color in (c) represents the (111) growth direction of the CdTe film, and the gray color represents a non-(111) orientation. The EBSD analysis confirms that the surface line contains a different domain direction in contrast to the main (111) CdTe film. (d) pole figure in the (111) direction of the area in (b and c). The pole figure shows weak twin spots represents the line region in the SEM image. (e) STEM-HAADF image (false-colored) showing a twin in the CdTe film initiated from the interface. (f and g) are SEM images taken from the same site at high stage tilt (54°) with in-lens and ET detectors, respectively. Surface roughness and features become visible in (g) rather than (f).

3.10. Summary

The demonstrated PLD one-step fabrication produces high-quality single-crystalline CdTe thin film at relatively low-temperature (300 °C). Universal delamination of the CdTe thin film is enabled by a tellurium layer that is spontaneously occurred at the given fabrication conditions and the reconstruction of the sapphire substrate. Mismatch dislocation-free interface is present at the CdTe/sapphire interface thanks to the atomically thin tellurium buffer. This is due to the vdW-like bonding between tellurium buffer and the first atomic plane of the Cd-polar CdTe film. Implications of this work may be applied in wearable devices by transferring CdTe thin films to flexible substates.

Furthermore, the sapphire substrate can be used for further growth after the delamination, like a copying machine. Other chalcogenide-based thin films (such as InSe or InSb) may be fabricated on this compliant sapphire-terminated tellurium interface. The further investigation of the thick tellurium layer at the

interface may lead to a direct growth of CdTe/Tellurene/Sapphire as a 3D/2D/3D system by a one-step growth.

Finally, the correlation between SEM/EBSD with TEM techniques enables identifying twinned regions/lines from the SEM contrast. This facilitates looking at the homogeneity and quality of the CdTe film in a scalable manner. Understanding SEM contrast through correlative microcopy can bridge both resolutions- and span length gaps between characterization techniques.

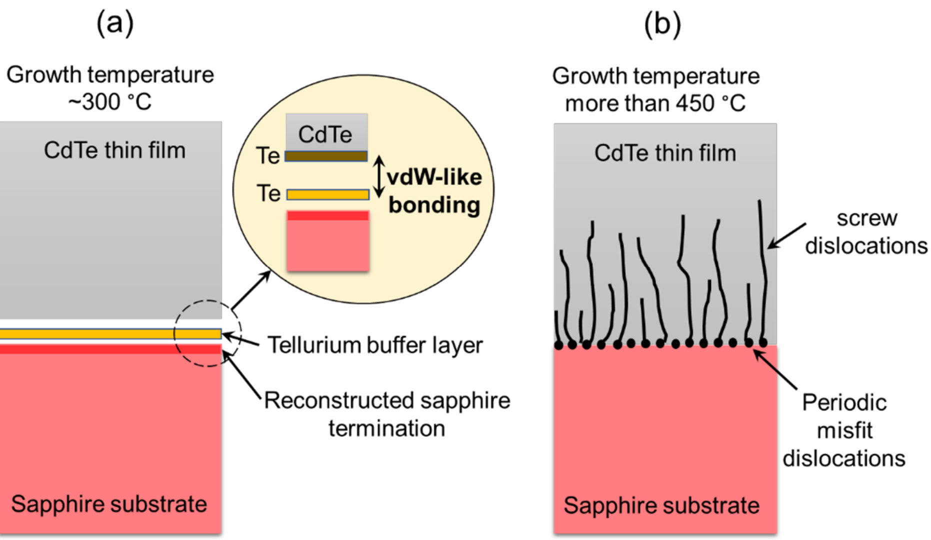

Figure 38. Graphical conclusion of the CdTe/sapphire system. (a) low-temperature growth of CdTe using PLD technique at typically ~300 °C. The relatively low growth temperature enables the topmost sapphire layer to keep a single aluminum reconstruction that allows the formation of a tellurium buffer layer with vdW-like bonds. (b) the typical interface of CdTe/sapphire interface grown at higher temperature (with techniques such as MOCVD) demonstrates misfit location because of the strong bonding at the interface. The interface also may present a pseudomorphic interface intermixing between sapphire and CdTe elements.

Chapter 4 Atomically Thin Gallium at Epitaxial Graphene Interface

4.1. Introduction

Heterogeneous integration of various 2D materials is a critical factor for their deployment in the microelectronics industry. Recently, the synthesis of various 2D materials confined at the epitaxial graphene interface has been realized through confinement heteroepitaxy (**CHet**).[23] In this technique, atoms intercalate at the interface of epitaxial graphene (EG) and silicon carbide (SiC) substrates, which facilitates large-area, environmentally air-stable 2D nitrides,[24, 171] 2D oxides,[172, 173] 2D metals,[23, 174] and 2D alloys.[175] This air-stability provided by the graphene cap is the crucial ingredient for next-generation quantum, high-frequency electronics, optical, and sensing technologies.[176] In addition, the use of EG enables superior heterostructure quality compared to graphene transferred by liquid methods.[177, 178] Furthermore, the CHet produces scalable layers, not flakes, over a 1 cm^2 of single-crystal SiC substrates in contrast to other techniques with limited area coverage.[179, 180]

One of the materials recently achieved through CHet is 2D–gallium (2D-Ga or Gallenene), which is characterized as a half-van der Waal 2D metal due to the bonding variation across the SiC/EG interface.[23] Two-dimensional Ga exhibits exotic optical and electronic properties, such as enormous non-linear optical response,[89] superconductivity,[23], and epsilon-near-zero behavior.[181] To achieve such properties across large areas of any CHet-synthesized material, the

heterostructure's thickness uniformity and area coverage should be understood quantitatively.

In this chapter, comprehensive electron microscopy characterizations of 2D-Ga layers at the epitaxial graphene interface are presented. Site-specific FIB cross-section samples are prepared for STEM characterization to understand the structure and thicknesses of 2D-Ga. Moreover, the role of the graphene confinement is examined with STEM imaging and spectroscopy to confirm the air stability of the 2D-Ga hetero-stack. The characterization work in this chapter recommends SEM as an affordable, non-destructive, easy-to-use technique for characterizing CHet surfaces. The 2D-Ga is characterized through multiple correlative characterizations in both plan-view and cross-section view to understand the uniformity and area coverage of these layers over a bulk scale using SEM contrast. The established link between SEM contrast with the thickness of EG and 2D-Ga helps to use SEM to optimize the growth conditions of the 2D-Ga and selectively design devices for better electron transport performance. Finally, the interfacial stability between gallium and the SiC substrate is investigated to reveal possible surface reconstructions at the SiC interface before and after the interaction.

4.2. Material fabrication

4.2.1. Epitaxial graphene (EG)

Epitaxial graphene is grown via silicon sublimation from the Si-face (0001) plane of the 6H-SiC structure. In this process, the high temperature decomposes the Si and C atoms at the SiC surface in a high vacuum atmosphere. The Si atoms leave

the surface, but the C remains on the surface due to the differences in vapor pressure between Si and C. A carbon-rich layer (called the buffer layer) is formed on the surface along the SiC terraces. The buffer layer (BL) is still attached to the Si-face atoms of the substrate. Progress of the Si-sublimation results in increasing the carbon content of the buffer layer up to reaching a graphene structure. At this time, the graphene layer (called epitaxial graphene (EG)) is detached from the SiC substrate, and a new buffer layer appears from Si-sublimation at the topmost layer of the SiC. The fabrication can be stopped at this time to have monolayer graphene (fully detached) with a buffer layer (still attached) at the interface. The SiC/BL/EG heterostructure is usually called a monolayer epitaxial graphene. Further progress in the Si-sublimation process results in developing new graphene from the previously mentioned BL and forming another BL to make a SiC/BL/2EG heterostructure called bilayer epitaxial graphene.

The fabrication parameters of the EG used in this study are as follows. A cleaned 6H-SiC with Si-face (0001) is annealed in an argon atmosphere containing 10% hydrogen at 1500 °C for 30 min to remove subsurface damage. Then, the sublimation process occurs at 1650-1800 °C, 700 Torr Ar, for 20 min. The fabrication is performed in a vertical silicon sublimation Furnace (located at Joshua A. Robinson laboratory at Pennsylvania State University), reaching a limit of 2400 °C and 10^{-6} Torr. [23]

4.2.2. EG plasma cleaning

To open holes through which intercalating atoms may pass, EG is plasma cleaned and etched. This process deliberately damages and cleanses the EG surface. EG layers were plasma treated (with 150/50 sccm O2/He under a pressure of 500

mTorr and 50 W power for 60 seconds) to induce defects in EG using a (Tepla M4L) plasma system.[23]

4.2.3. Gallium intercalation

Once the EG surface is intentionally damaged, it is ready for gallium atoms to be intercalated at the interface of epitaxial graphene (EG) and silicon carbide (SiC) substrates. A horizontal tube furnace (STF-1200 at Pennsylvania State University) with a 1-inch outer diameter quartz tube was used for gallium intercalation. A custom-made alumina-crucible (Figure 39) was used to hold 1 × 1 cm EG substrates – placed on the Si-face – downwards towards the inside of the crucible.[23] The crucible was then filled with (30–60 milligrams) metallic Ga (Sigma Aldrich, 99.999%) directly underneath the EG substrate. The crucible was placed into the furnace and then evacuated to a pressure of 5 mTorr. The tube was then pressurized to 300–700 Torr with Ar atmosphere. Then, the furnace was heated to 600-1100 °C under a ramp rate of 20° min–1 and an Ar flow of 50 sccm.[23] The optimized temperature for intercalation is set at around 700–800 °C. The furnace was held at the growth temperature for 30 min, then cooled to room temperature. Figure 40 shows a photograph of the final product (1 × 1 cm size) after intercalation. Scratches near the surface edges and corners may exist because of tweezers during the handling of wafers.

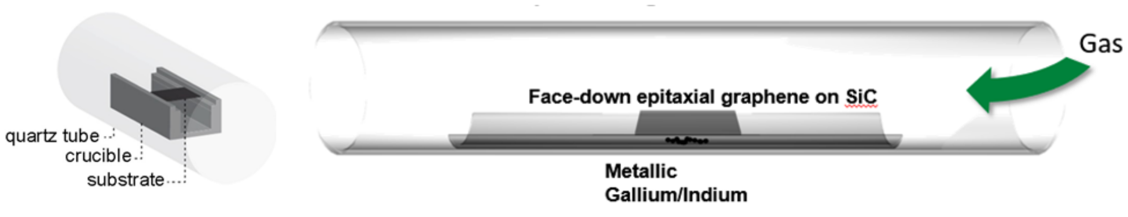

Figure 39. Cartoon of the tube furnace growth of 2D CHet metals. Confinement Heteroepitaxy technique. (left) illustration figure of a SiC substrate in a ceramic crucible. The SiC substrate is Si-face down in front of metallic flakes placed on the crucible bottom surface. (right) A schematic diagram of the tube furnace. [23, 88]

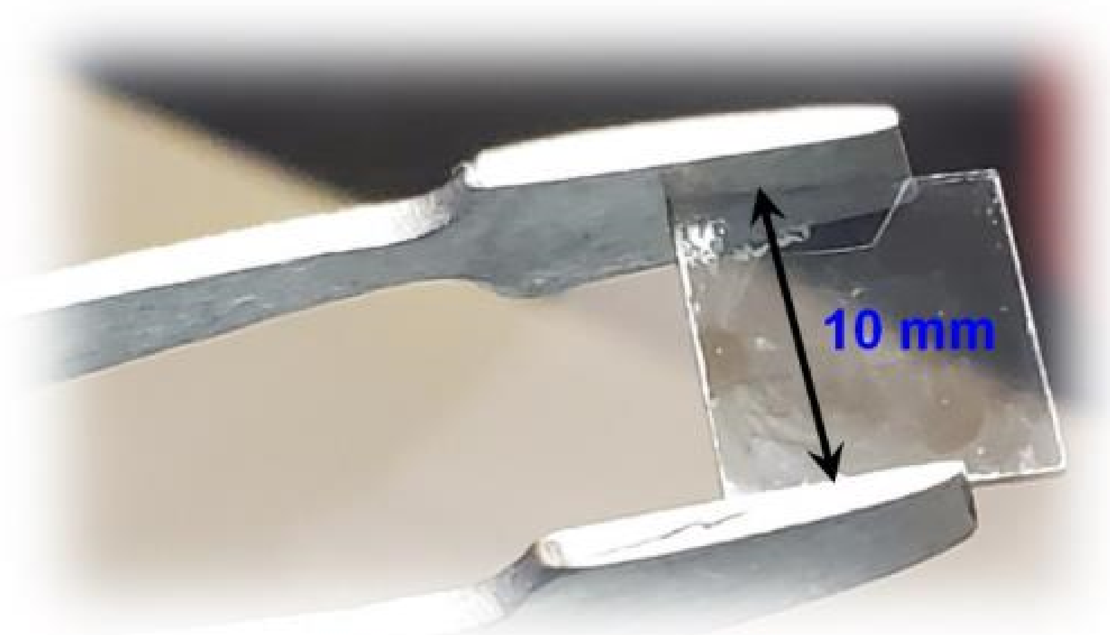

Figure 40. Photograph of a 1 × 1 cm EG after gallium intercalation. The SiC substrate is transparent to visible light before and after the intercalation process. Some surface defects, such as scratches near the edges, may be visible.

4.3. Cross-section preparation of EG and 2D-Ga samples

4.3.1. Process workflow

Imaging of the EG and 2D-Ga surfaces by SEM shows a feature-rich (contrast-rich) surface with multiple contrast, as shown in Figure 41. The focused ion microscope is equipped with an SEM column to image the surface before the FIB cross-sectioning process. This facility allows a unique ability of the FIB system to select

both the site and orientation of the cross-section. In this thesis, many FIB samples are prepared in parallel and perpendicular to the step edges of the SiC substrate. Then the cross-section samples are imaged in correlation to the position where it is extracted to link the SEM contrast with the structure from the atomic scale STEM images. For this purpose, the sites of the cross-section lines (yellow and blue colors in Figure 41) are optimized to cut through as many as possible features of differing contrast.

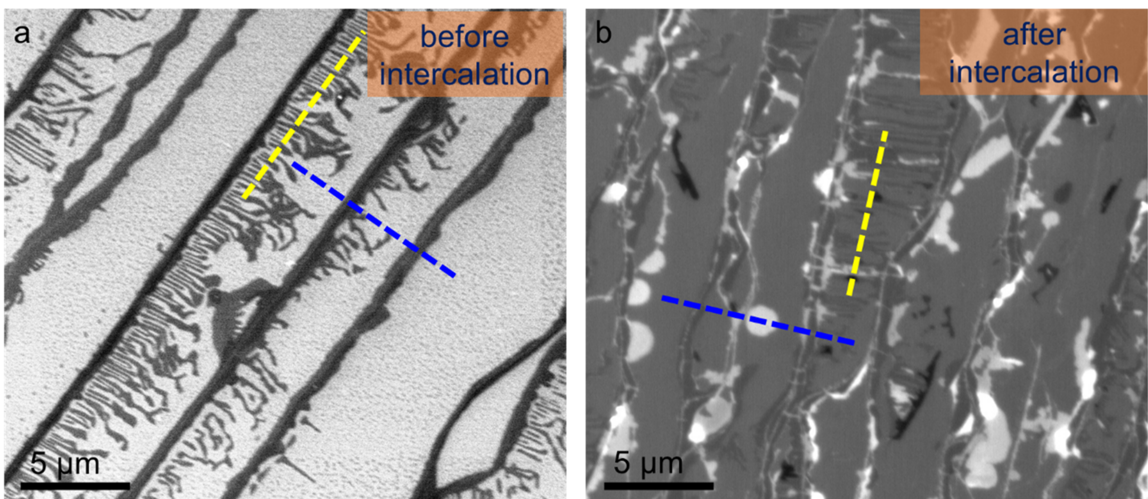

Figure 41. Coordinating FIB cross-sections for STEM investigations. (a) epitaxial graphene (EG) substrate before intercalation. (b) epitaxial graphene after intercalation of gallium to form the 2D-Ga heterostructure. Blue lines represent examples of the coordination of the FIB cross-section perpendicular to the SiC step edges. Yellow lines represent examples of a FIB cross-section designed perpendicular to the terrace fingers and parallel to the SiC step edges. The cross-section length is arranged between 10-12 µm in such a way as to cover many features within the same line.

4.3.2. Preparation parameters

To prevent contamination from standard gallium source, FIB, cross-section samples are prepared with a Xe+ plasma ion source provided by using a Helios G4

PFIB UXe DualBeam. First, the through-lens detector (TLD) of the PFIB system is used to image the surface and navigate to the site of interest. Then, a 200–500 nm carbon/platinum coating is deposited on the site of interest followed by two layers (carbon, tungsten) of ~100 nm thick each, using the electron beam at 5 keV and 6.4 nA. Then the Xe ion beam is used to deposit an additional 5 μm tungsten layer at 30 keV. Later, the samples are prepared by performing a standard lift-out procedure and attached to TEM half grids using a platinum deposition. Finally, both sides of the samples were thinned in multiple steps by gradually lowering the ion beam voltage from 30 kV to 2 kV until the cross-section window appeared transparent in the SEM at 3 keV imaging voltage. More details about the standard FIB cross-section preparation are summarized in Appendix 1.

4.4. Epitaxial relationship before and after intercalation

4.4.1. SiC-EG epitaxial interface

Graphene grown on SiC by the Si-sublimation method is called epitaxial graphene.[182] It results from sequences of surface reconstruction of the topmost SiC layer(s) that increase the carbon percentage until it becomes a fully separated graphene layer from the substrate.[13, 183, 184] The presence of a buffer layer (BL) at the interface is associated with the $(6\sqrt{3} \times 6\sqrt{3})$ R30° reconstruction of hexagonal 6H-SiC in plan view imaging with techniques like AFM or STM.[185, 186] But, using atomic-scale STEM imaging, the BL can be seen directly and identified from the HAADF intensity. Mono- (Figure 42a) and bi-layer (Figure 42b) epitaxial graphene layers show a layer at the SiC-EG interface with low HAADF intensity, called the carbon buffer layer. The BL is still attached to the silicon atoms of the Si-

face SiC topmost layer. Moreover, the BL does not entirely contain carbon, but some silicon atoms may exist; that is why it is called a carbon-rich layer.

4.4.2. SiC-Ga epitaxial interface

After the gallium intercalation, the Si-dangling bonds at the SiC-BL interface are passivated by the gallium atoms. As a result, the BL is separated to form a new free EG layer. This BL detachment is imaged in mono- and bi-layer EG, as shown in Figure 42c-d. Later analysis from a different cross-section shows the gallium intercalation of tri-layer EG to have 4 layers of graphene after intercalation. However, the intercalation may not be working for thicker EG layers than in the tri-layer case. The thickness limitation is because of possible insufficient damage from the plasma, in which it appears more challenging for the gallium atoms to intercalate beneath a thick EG. Later on, in this study, Figure 54e shows an example of non-intercalated thick graphene.

At the interface of SiC-Ga, the Si-Ga atomic spacing is measured from the STEM-HAADF image in Figure 43 to be ~2.35 Å. This spacing is similar to the atomic planar spacing of the 6H-SiC substrate, which means that the first Ga layer grows epitaxially to the SiC substrate as a result of passivating the Si dangling bonds (high energy surface) from the intercalation process. However, the spacing between the two gallium layers (Ga1-Ga2) drops to 2.24 Å. This spacing compression may be a result of accommodating the strain already induced at the first layer. Moreover, this spacing shift may be a representation of the non-centrosymmetric transition from the covalent bonds (Si-C and Si-Ga) to the relatively weaker metallic bonds (Ga-Ga) in the confined gallium.

Still, the bilayer gallium is considered to follow an epitaxial relationship to the SiC substrate. This can also be confirmed by the yellow arrows (Figure 43) that indicate the same stacking direction as the SiC substrate.

4.4.3. Ga-EG interface

The distance between the topmost gallium and the down-most EG is measured in Figure 43 to be 3.88 Å, higher than the 3.34 Å spacing between each EG representing the vdW spacing of graphene. This measurement means that the coupling between Ga and EG happens in the range of the weak interaction with vdW-like bonds, confirming that the BL is wholly separated from the interface. Moreover, the Ga-EG spacing (3.88 Å) represents another non-centrosymmetric transition from the metallic bonds (Ga-Ga) at the confined gallium to the weaker out-of-plane bonds at the EG.

Gallium is a known catalyst material for growing graphene and carbon nanotubes.[187, 188] This makes the Ga-EG interface a platform for healing the previously introduced defects to the EG by the plasma process. This healing effect was previously studied by Raman. [23] Here, in Figure 42 and Figure 43, the STEM image shows that EG still preserves its 3.34 Å spacing of the vdW fingerprint of the graphene.

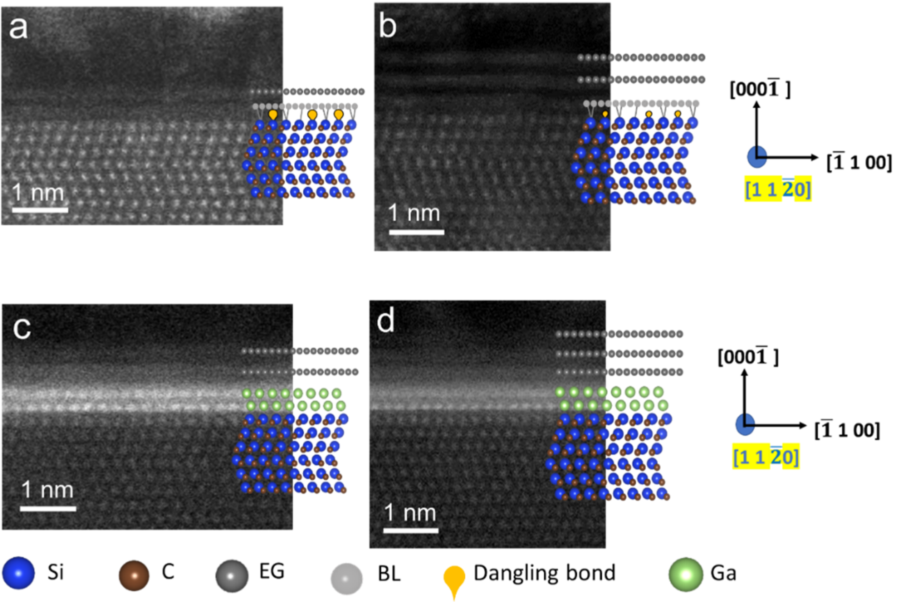

Figure 42. The epitaxial interface of EG and 2D-Ga. (a and b) SiC substrate before intercalation, with mono- and bi-layer epitaxial graphene layers, respectively. A buffer layer (BL) exists in both cases at the interface and is indicated with the light-gray color of the atomic model. (c and d) gallium intercalated mono- and bi-layer epitaxial graphene, respectively.

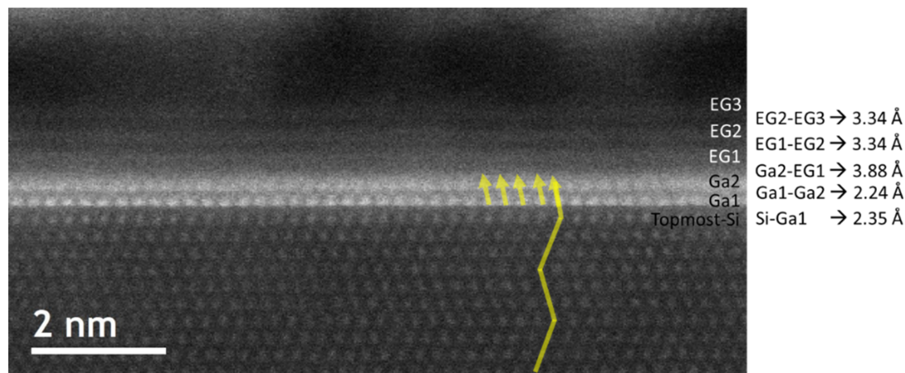

Figure 43. Atomic spacing of 2D-Ga heterostructure. The yellow zigzag at the SiC substrate indicates the atomic arrangement of the (11$\bar{2}$0) direction of the SiC. The yellow arrows in the bilayer gallium indicate the same stacking direction as the SiC substrate, which means that the bilayer gallium follows epitaxial growth at the SiC interface.

4.5. Air stable 2D-Ga under the EG confinement

Graphene encapsulation is the key factor in stabilizing 2D-Ga to form a structure with an epitaxial relationship to the SiC under the confinement and protecting the metallic layer from oxidation in air. This air stability allows the implementation of this material in the application. The air stability of 2D-Ga has been explained using X-ray photoelectron spectroscopy (XPS) techniques in the original work by N. Briggs et al.[23] In this previous work, XPS spectra show the oxygen signal, which is interpreted to be due to gallium oxide particles on the sample's surface. However, no atomic-resolution EELS investigations show the role of graphene in the air protecting 2D metallic layer. In this section, STEM and EELS techniques are employed to investigate the role of graphene in protecting the 2D-Ga.

4.5.1. Delaminating the EG

Epitaxial graphene is peeled off from a micrometer area, as illustrated in Figure 44a. The peeling of graphene is performed by a sharp tweezer similar to the many scratches on the surface that can be introduced during the handling of the wafer. Then the sample is exposed to air for ~3 weeks before extracting a cross-section from the same scratch site. The SEM imaging of the surface shows wrinkled graphene (marked with the arrow in Figure 44e) on the edge of the scratch, which indicates the boundaries of the peeled regions. Interestingly, the area without graphene shows two SEM contrast levels; one is very bright, which means a changing surface. This charging surface should be the SiC substrate (wide band gap) without any EG or Ga on top. The other contrast in the peeling area is less charging which may be gallium on top of the SiC but without EG. Figure 44c shows a model of how the scratching may occur in such a way that removes the metal

(gallium) from the middle of the scratch but peels off the graphene near the edge, which keeps an area of 2D-Ga without EG. This area (between the green and orange lines in Figure 44a-b) is assumed to have a peel action only, without damage from the scratching process. The weak bonding length between Ga and EG (3.88 Å in Figure 43) between Ga and EG is a reasonable explanation of the EG peeling off near the scratch edge. This becomes an interesting position to lift out a sample for analysis.

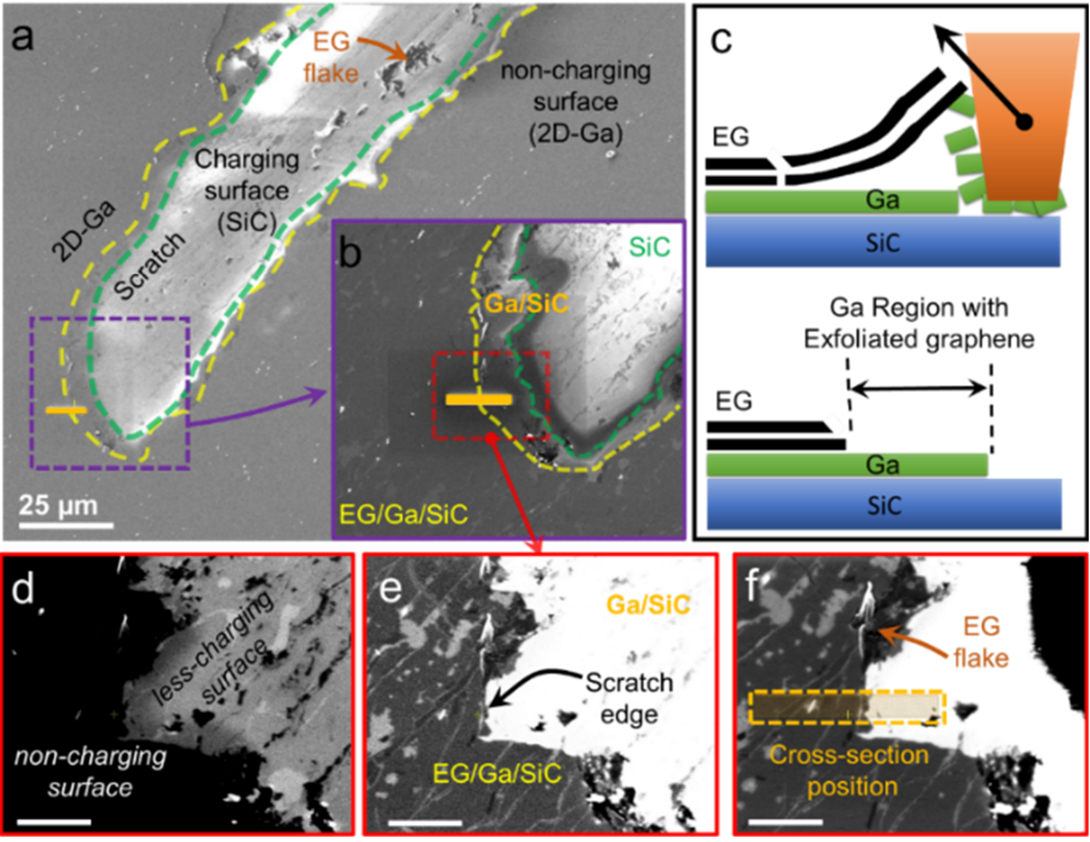

Figure 44. Scratching of the 2D-Ga surface.(a) low-magnification SEM image shows a scratch (bright contrast) on the surface. (b) zoom-in SEM image at the scratch end where a FIB sample is prepared. SEM images in (a and b) are taken by the Everhart-Thornley detector (ETD). The scratch region with SiC surface is charging due to the wide bandgap of the SiC. The area between the green and yellow lines is believed to have pristine Ga without

graphene cap because it is not charged in SEM. (c) An illustration figure shows the scratching mechanism and the possibility of having peeled graphene from a micrometer region near the scratch edge. (d-f) SEM images (scale bar = 5 µm) taken at different contrast – by the in-lens SEM detector – to emphasize the scratched area with Ga on top (d), or the unscratched region with EG on top (e), as well as the position (f) where the FIB cross-section is prepared from after days of air exposure.

4.5.2. Cross-section near the peeled edge

Figure 44d-f shows the specific site where a FIB cross-section was prepared from both regions with and without the graphene cap. Since the sample was exposed to air prior to the FIB preparation, this cross-section allows studying the air-exposure effect on the structure and chemical composition of Ga layers. The cross-section was designed to have about a 12 µm length in which half of this length covers the peeled region, and the other half covers the unpeeled region. More details about the standard FIB cross-section preparation are summarized in Appendix 1.

4.5.3. STEM and EELS investigation across the peeled edge

Spatial correlation between the SEM image of the cross-section position and STEM imaging of the FIB lift-out lamella is performed as seen in Figure 45a-b. The first step to establishing the correlation is to find the scratch edge at the middle of the cross-section. Figure 45c and d show STEM-BF and HAADF images from the scratch edge site. Now, the correlation between SEM and STEM images can be performed because all FIB cross-sectioning steps are recorded. For example, the direction of the cross-section can directly be identified when the welded edge of the FIB lamella to the TEM grid is recorded.

Figure 45e-f shows confined bilayer gallium under 2 or 3 EG layers at the unpeeled region. The structure of the confined gallium looks epitaxial to the SiC, similar to other investigations in Figure 42 and Figure 43. The epitaxial graphene (low atomic number) appears with better contrast in the STEM-BF image, which shows non-damaged EG at the unpeeled area. However, the STEM images in the peeled site (Figure 45g-h) show no graphene, which confirms that the EG is peeled off from this region. Moreover, the surface of the SiC has either damaged gallium layers (Figure 45g) that still preserve the structure or a completely damaged gallium with a cloud-like shape in Figure 45h. These changes in the gallium structure are assumed forms of gallium oxide because of the prior exposure to the air.

Core-loss EELS mapping at the interface (Figure 46) is applied further to explain the gallium at the peeled and unpeeled regions. The unpeeled region shows pristine, non-oxidized gallium encapsulated between the SiC and the EG layers. Only a few traces of oxygen signal are found co-located with EG location. The oxygen in the EG is more likely introduced during the oxygen plasma process that is intentionally made to open holes in the EG for intercalation. In contrast, the EG-peeled regions show a robust oxygen signal co-located with the gallium.

This comparative atomic resolution study across the peeled- and unpeeled-EG regions confirms that the EG provides both air stability and epitaxial structural stability to the gallium layers. Two-dimensional gallium does not exist in nature with a structure similar to the SiC at room temperature. Instead, the CHet synthesis templates the gallium to follow the SiC structure under graphene confinement. Moreover, the EG provides the desired protection to the gallium

layers against air, which makes this *metastable* gallium structure air-stable and accessible for device implementations.

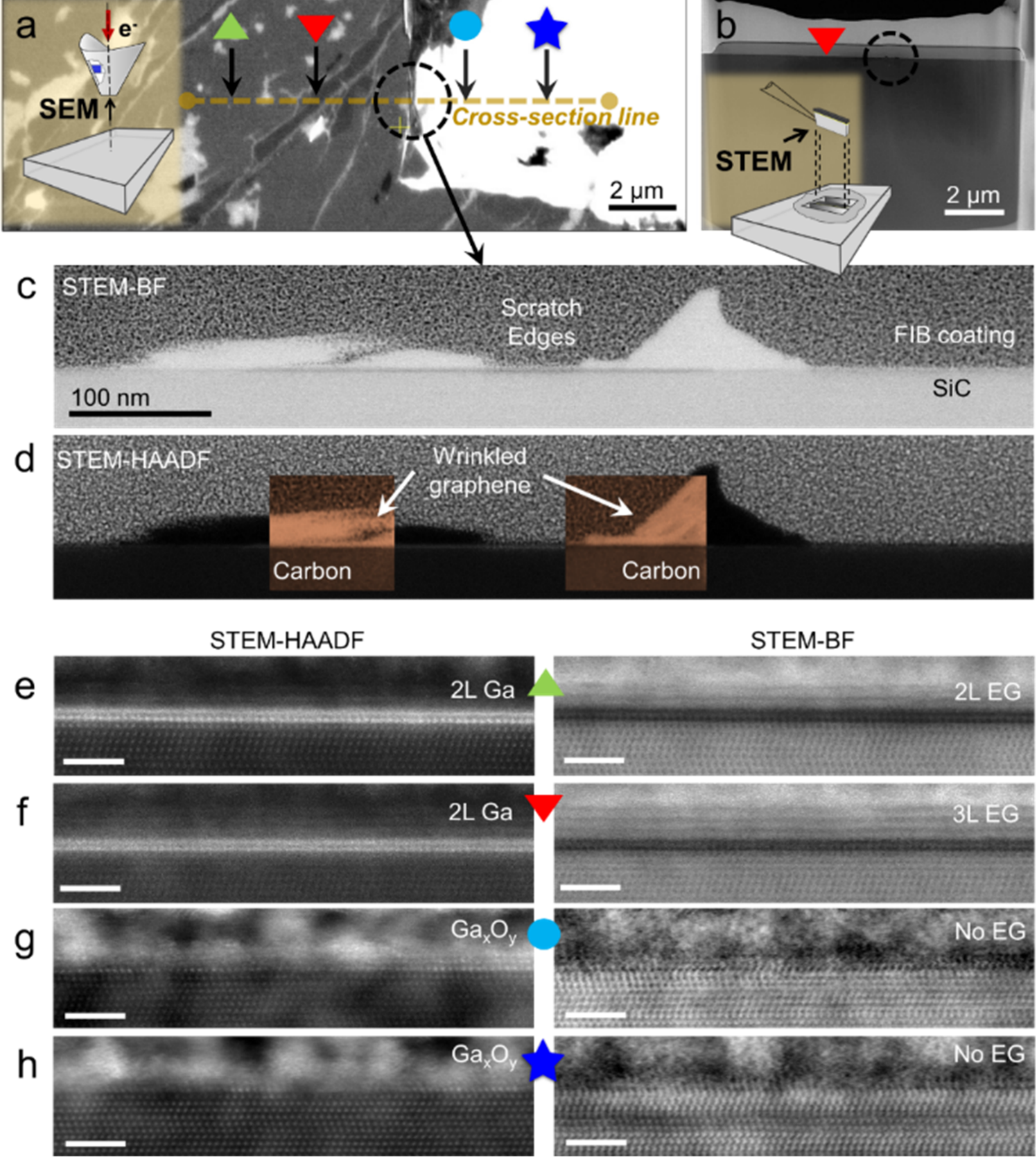

Figure 45. STEM imaging across the peeled EG edge.(a) SEM image shows the cross-section line (yellow) with 4 regions of interest indicated by the colored symbols. (b) STEM-HAADF image of the cross-section after the FIB preparation from the specific site as indicated in the SEM image in (a) and Figure 44d-f. The left inserts in (a-b) are schematics of the SEM and STEM

sample-beam coordination. (c and d) STEM-BF and STEM-HAADF images, respectively, from the scratch edge, show wrinkled graphene flakes from the exfoliation. The colored (brown) inserts in (d) are EELS C-K edge maps that show dis-continuous intensity due to the wrinkles of the peeled EG. (e-h) STEM images of the marks illustrated in (a). 2D-Ga is crystalline and epitaxial to the SiC under graphene confinement. However, the absence of EG results in a less crystalline layer in (g) or a complete amorphous Ga_xO_y layer in (f). The scale bar is 2 nm in (e-h).

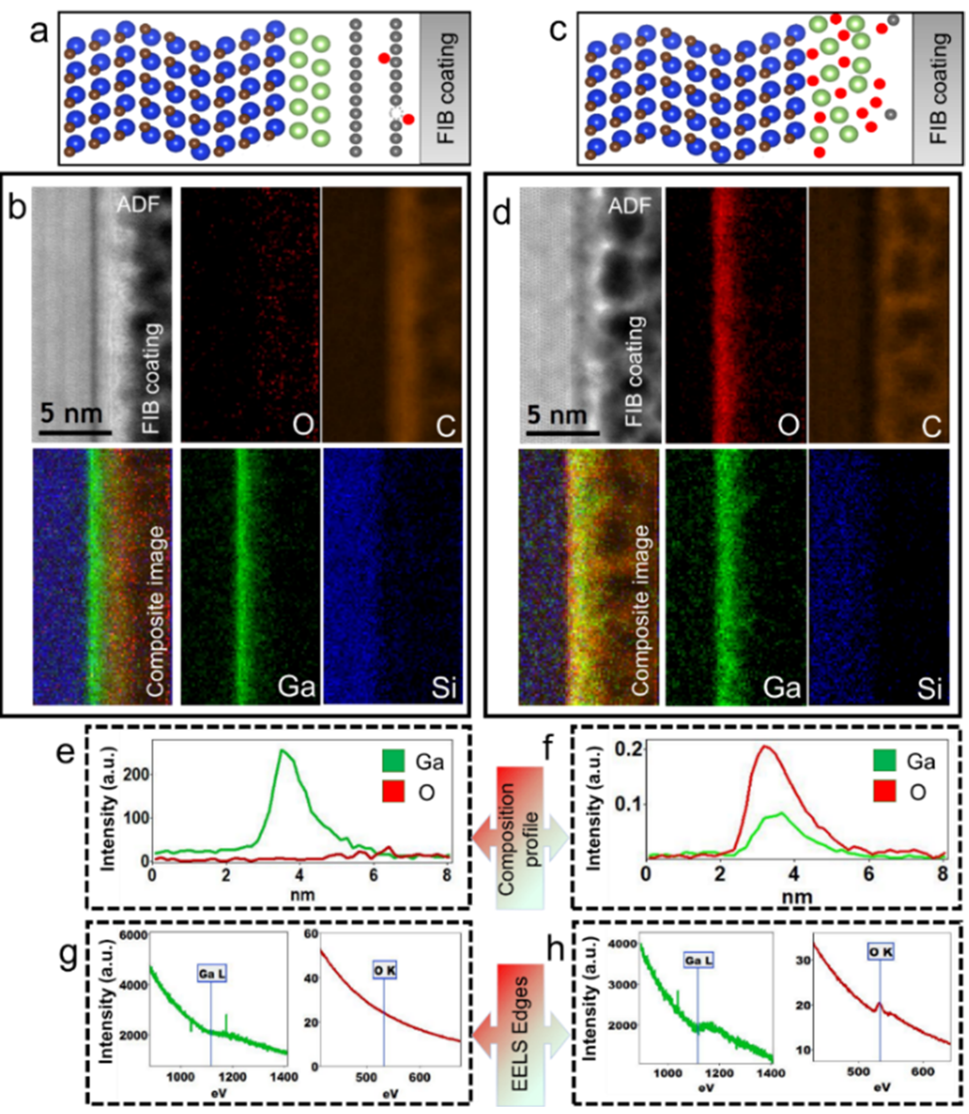

Figure 46. EELS investigation across the peeled EG edge. (a and b) ball-and-stick models of the interface with and without the EG cap, respectively. (c

and d) EELS maps for oxygen, gallium, carbon, and silicon acquired from the corresponding annual dark-field (ADF) image for both interfaces with and without the EG cap, respectively. (e – f) compositional profiles and (g – h) EELS Ga-L and O-K edges of the gallium and oxygen EELS signals acquired in (c and d), respectively, across the interface. The EELS investigation shows pristine Ga under the EG confinement without oxygen signal. This demonstrates the role of EG in shielding the metal layer against exposure to air.

4.6. Sensitivity of SEM contrast to the gallium locations

In the previous sections, SEM images of EG and 2D-Ga showed that the surface of these samples is contrast-rich. STEM images showed that the gallium has a bilayer thickness, but the graphene cap can vary from a bilayer thickness and up. This variation in the 2D-Ga thicknesses can cause variations in a device performance when using this heterostructure in applications, as will be discussed later. This raises the need for a characterization method that can identify the thicknesses of the layers with high spatial resolution without introducing damage.

In this section, an in-depth study is conducted to use SEM as a quick, easy to afford, and high spatial resolution technique to identify the gallium locations within the SiC terraces as well as the thickness of EG.

4.6.1. Tracking SEM contrast over the steps of 2D-Ga synthesis

To locate the sites that have successful gallium interaction at the SiC-EG interface, the SEM contrast is tracked through the preparation steps to understand the evolution of the surface morphology, as seen in Figure 47. Starting with the SiC substrate, the SEM imaging of the surface is challenging and unstable because of charges associated with its wide bandgap and low electric conductivity. However,

the steps from the miscut angle of the SiC wafer could be captured at some parts of the SEM images, as illustrated in Figure 47a and Figure 48.

Once the EG has been synthesized on the SiC surface, a more stable SEM imaging is possible for this surface thanks to the graphene coverage, which increases the surface conductivity. The morphology of the EG-prepared surface also shows the characteristic evolution of SiC terrace size to form flattened and larger terraces separated by surface step bunches. Because the Si sublimation starts from the SiC step edges[116], the EG surface usually exhibits thicker graphene near the step bunches, while the middle of the terraces presents a controllable graphene thickness down to a monolayer above the BL, as shown in Figure 47b,e. The SEM morphology of the EG terrace may vary depending on the sublimation process parameters. For example, a partially grown BL or a nascent EG nucleation could result in finger shapes areas of thicker EG within the terrace, as can be seen in Figure 49.[189, 190] However, the SEM contrast from the EG surface presents mainly two peaks in the image histogram related to the monolayer (at the terrace middles) versus thick EG near the SiC step edges.

Following the EG formation, Ga atoms intercalate beneath the EG surface layer through the CHet process. Besides the formation of 2D confined Ga layers, the process detaches the BL to passivate the dangling bonds (DB) of the Si-face SiC, which forms an extra free-standing EG layer. This detachment process is previously confirmed in literature by Raman measurements.[23, 191]

SEM imaging of the 2D-Ga surface is also stable, and interestingly it results in a multi-feature surface. This contrast-rich surface can be categorized by five main color-codes that appear as five successive peaks in the image histogram, as

illustrated in Figure 47c. The summary of these contrast and their meanings are presented in Table 1. At this stage, it is assumed that one (or more) of the SEM contrast that appears in the image histogram represents the location of the intercalated gallium, and the question is what material features do these contrast levels correspond to.

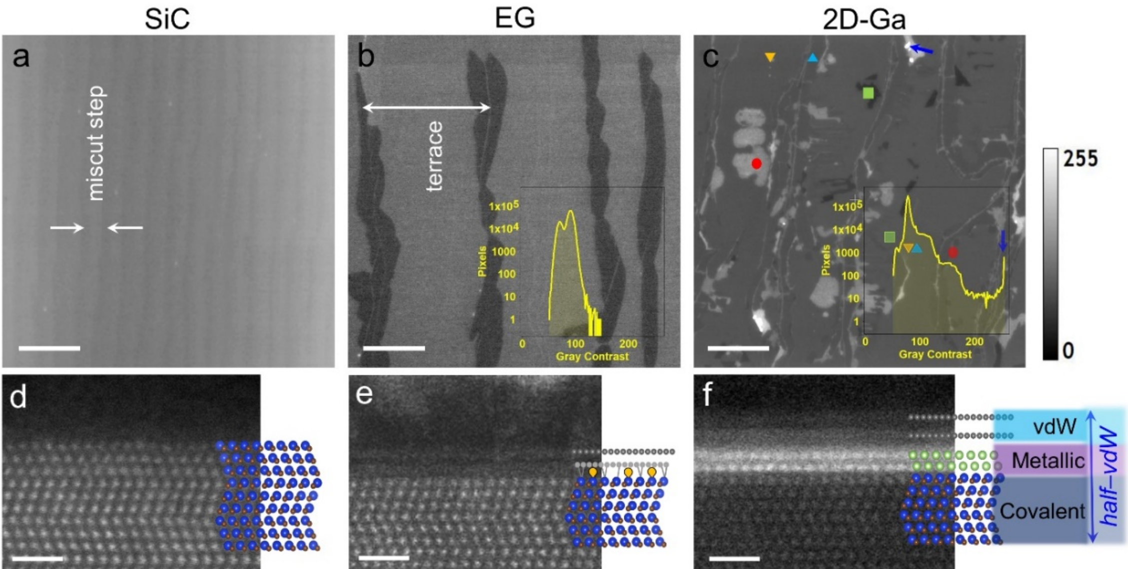

Figure 47. Evolution of SEM contrast during the CHet growth. (–c) plan-view SEM images acquired using a through-lens detector (TLD) for SiC, EG, and 2D-Ga, respectively. The contrast of all SEM images is adjusted to the same grayscale (bar on the right). The inserts are the corresponding log-scale histograms of the gray levels. The scale bar is 3 µm. (d–f) STEM-HAADF cross-section images for SiC, EG, and 2D-Ga, respectively. The inserts are ball-and-stick atomic structure models. The cross-section STEM images in (e and f) come from the middle of the terrace. The scale bar is 1 nm. A more detailed study of the SEM imaging conditions on the image histogram is added in Appendix 4.

Table 1. Description of SEM contrast of the 2D-Ga surface.

Gray scale	Color level	Peak Order	Symbol	Description
	Saturated Bright	I	blue arrow	Ga particles
	Bright	II	red circle	Non-intercalated EG or damaged layers
	Light Gray	III	orange downward triangle	2layer Ga covered by 2 layers EG (2/2 Ga/EG)
	Medium Gray	IV	blue upward triangle	2-layer Ga covered by 3+ layers EG (2/3 Ga/EG)
	Dark	V	green square	Thick EG

By comparing the EG and 2D-Ga micrographs, it is understood (see Figure 47b-c) that the secondary electron (SE) emission from the 2D-Ga is generally suppressed. This SE suppression that makes the image appear dimmer may be because of the Ga intercalation, in addition to the separation of the BL that forms an extra EG layer (Figure 47g-i). The 2D-Ga can be identified from the histogram as an extra generated peak (see peaks numbers II, III, and IV in Table 1 and their correspondences in Figure 47c) that dominate the gray levels between the bright-dark range in the image histogram. These gray colors (II, III, and IV in Table 1) have the same local structures – relative to the middle of the terraces and step bunches – similar to the EG surface before the intercalation process. The distribution of these features (II, III, and IV) suggests that the contrast evolution from EG to 2D-ga results from the Ga presence at the interface.

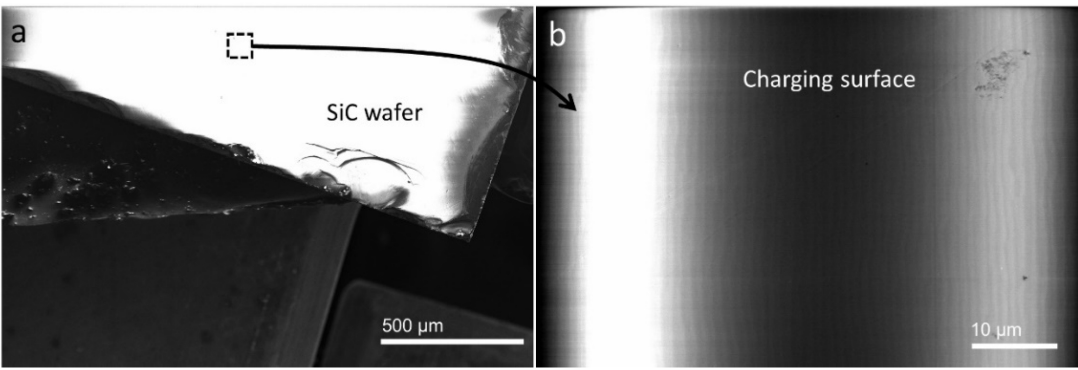

Figure 48. SEM imaging instability of SiC substrate. (a) low-magnification SEM image shows the wafer edges. (b) high-magnification SEM image shows the steps of the wafer miscut. Both images show charging effects because of low substrate conductivity. This makes imaging of the SiC surface challenging without using a surface coating layer like gold or carbon.

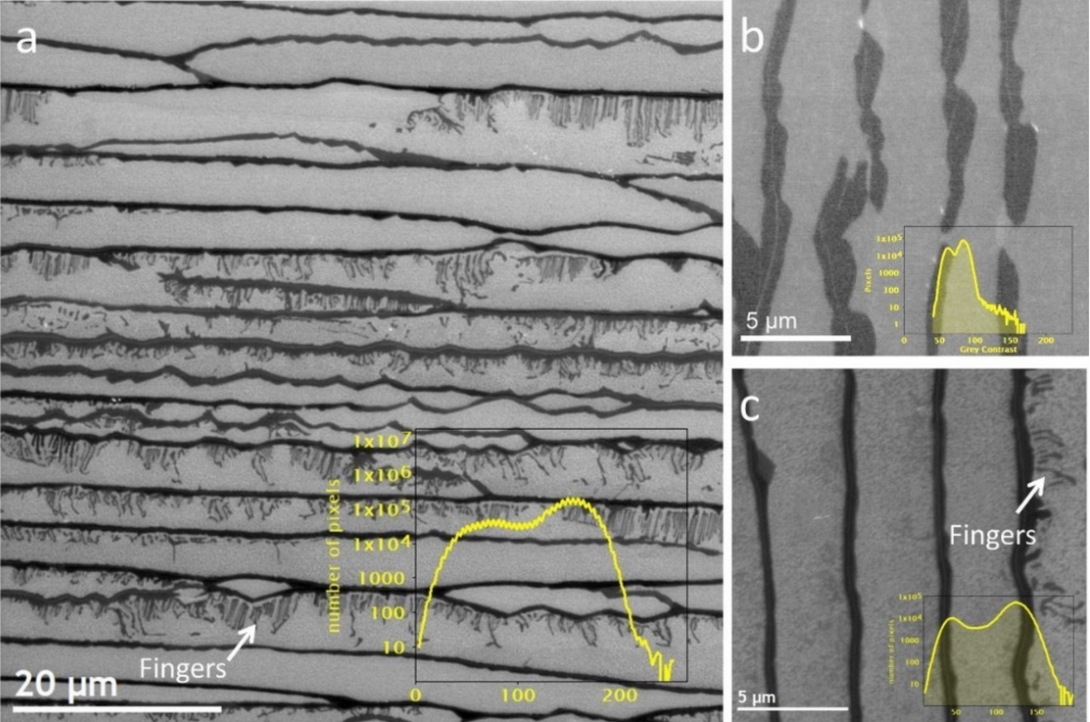

Figure 49. Morphology of epitaxial graphene.(a) low magnification SEM image acquired by a through lens detector. The surface shows thick (dark) graphene at both the step bunches and in some positions within the middle of the terraces as finger shaped growths. The histogram (taken from the whole) image shows mainly 2 peaks representing the monolayer EG (bright) and the thick graphene (dark). The higher magnification image shows areas without (b) and with (c) fingers. The fingers and dots within the middle of the terraces represent a partially grown EG layer.

4.6.2. Correlative characterization with SEM contrast

The previous SEM contrast comparison between EG and 2D-Ga surface may not be sufficient to conclude and link the contrast to the gallium presence. To identify the spatial locations of the 2D-Ga, correlative microscopy is required to determine both chemistry and the number of layers of the 2D-Ga heterostructure surface relative to the SEM contrast generated by the differential surface potentials.

To ensure that the SEM contrast is appropriately understood, we applied various correlative characterizations in both plan-view and cross-section view linked to the same site as imaged in SEM to resolve ga location and the layer thicknesses. In addition, we applied both theoretical and experimental correlative microscopy to understand the surface potential of various thicknesses of the 2D-Ga heterostructure.

4.6.2.1. SEM correlation with Auger electron spectroscopy

Auger electron spectroscopy (AES) is used to acquire maps which are then correlated with SEM images acquired using an Everhart-Thornley detector (ETD), as illustrated in (Figure 50). Because the AES is an electron-based characterization method, AES resolution is spatially compatible with SEM images at low and medium magnifications. A JEOL JAMP-9500F field emission Auger microscope with a chamber vacuum of 10^{-6} mbar was used to acquire AES maps. The Auger electrons are analyzed using a hemispherical analyzer equipped with a seven-channel detector and used to map the 2D-Ga heterostructure areas (Figure 50e-g). Typically, the Auger microscope was operated at 5 keV for SEM imaging, but 10 kV, 10–20 nA, a tilt of 30°, and a working distance of 20–25 mm were used when mapping the surface.

To accurately correlate SEM with AES maps, some considerations are necessary. First, AES maps are acquired with a tilted stage (30° or higher) to increase the signal count. This correlation requires a scaling correction of the AES maps to compensate for the stage tilt (Figure 51) to be compared with an SEM image at no tilt for the same site. Second, the working distance (WD) in SEM images has to be considered depending on the SEM detector used.[123] In our work, we validate that different SEM detectors are suitable to capture the 2D-Ga heterostructure contrast by controlling the WD (Figure 52).

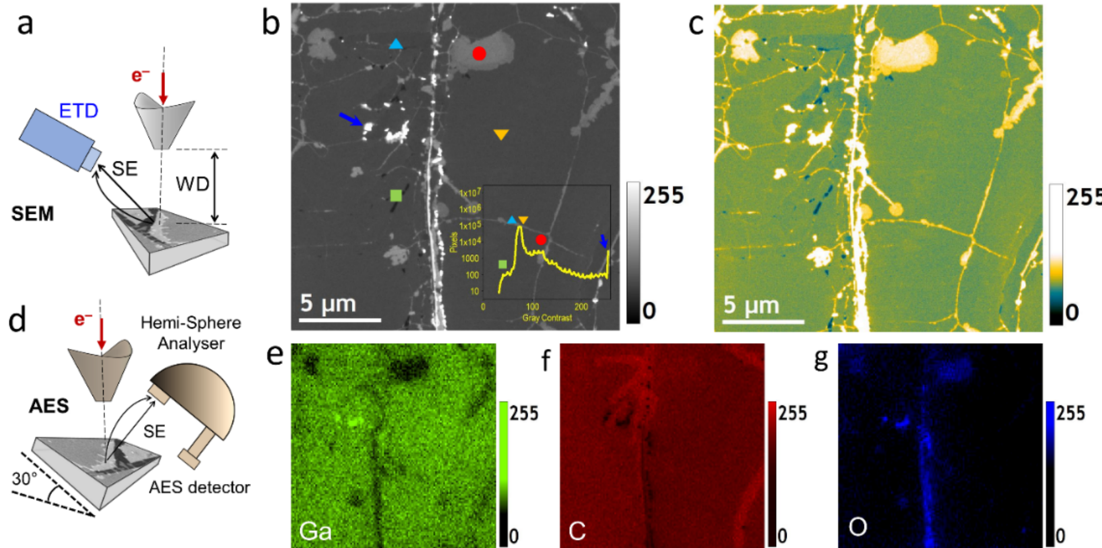

Figure 50. SEM correlation with AES surface chemical maps. (a) Schematic diagram of ETD imaging coordination at a high working distance (WD) condition. (b) The log-scale histogram of the SEM image (insert) shows the main five contrast regions. (c) False-color image of the greyscale SEM image in (b). (d) schematic diagram of the Auger electron microscopy (AES) setup. (e-g) AES maps of gallium, carbon, and oxygen from the same area in (b-c). Spatial correlation between (b) and (e-g) is corrected to compensate for stage tilt, as described in Figure 51. The SEM-AES correlation shows that the gray contrast regions in the SEM image are co-located with the Ga signal.

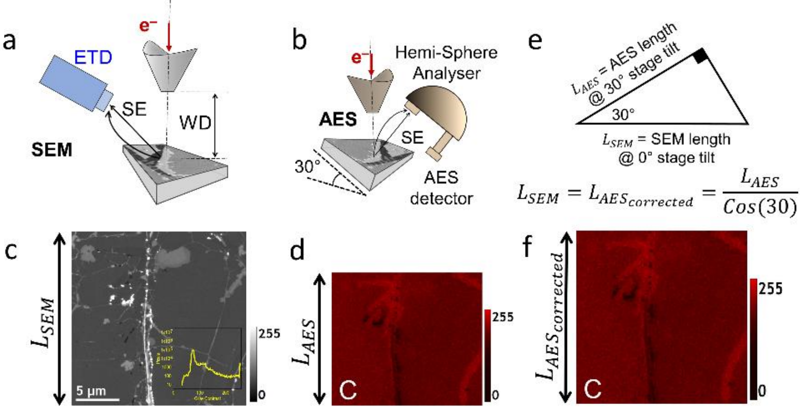

Figure 51. Scaling correction between SEM and AES techniques. (a-b) cartoons for the sample-beam coordination in SEM and AES. (c-d) are co-located SEM images and AES maps acquired for the carbon signal in the 2D ga surface. (e) shows the correction for the 30° stage-tilt in the AES used to correlate with the SEM image spatially. (f) A stretched AES map in (d). All the AES maps in the main text are spatially corrected to compensate for the AES stage tilt.

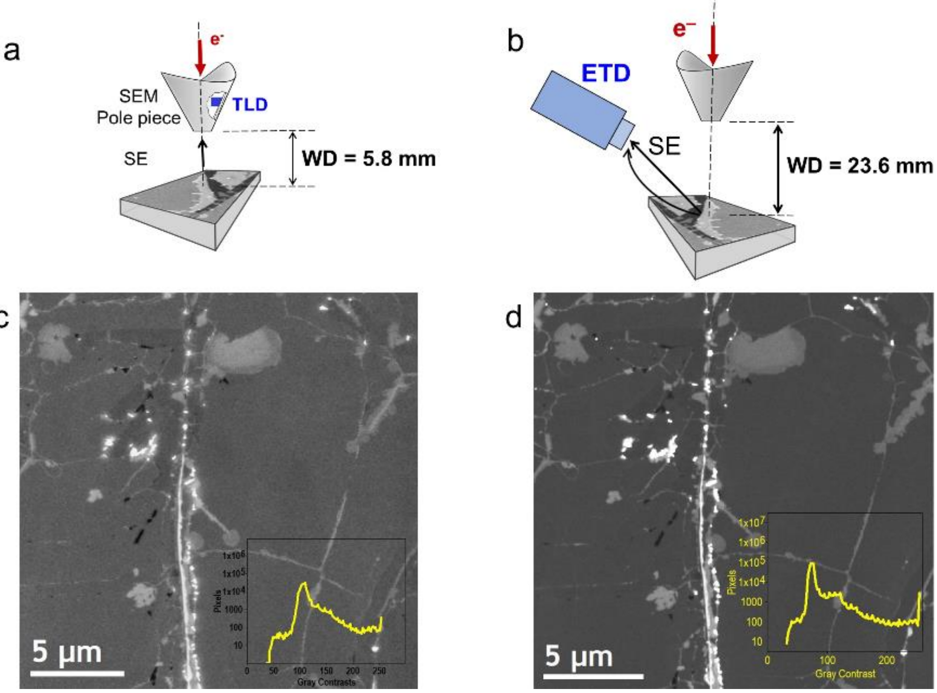

Figure 52. Working distance (WD) sensitivity to SEM detector. (a and b) illustration figures of the sample-beam coordination using the through lens

detector (TLD) and the Everhart-Thornley detector (EDT), respectively. (c-d) The corresponding SEM images were taken by the TLD and ETD for the 2D Ga surface, respectively. The SEM images are taken (taken at 23.6 mm WD, zero stage-tilt, and 3 keV) from the exact location where the AES correlation is performed in Figure 50. To achieve sufficient contrast in the SEM images, the WD should be high (20-30 mm) in the case of using the ETD but low (3-8 mm) in the case of using the TLD. The working distance effect was previously examined in the case of epitaxial graphene on SiC substrate.[123] Here, our examination of the WD provides similar results for the 2D Ga heterostructure. The TLD image was taken by Zeiss NVision40, while the EDT was acquired by JEOL JAMP-9500F.

Furthermore, the current, voltage, and contrast effect should be optimized and understood to maximize the signal sensitivity to the heterostructure (Appendix 4). In this work, we used 5 keV as the optimal electron source voltage, which is previously reported for the highest graphene contrast in SEM images.[107]

The intensity of AES maps may be carefully quantified to determine the thickness of 2D materials, as previously reported.[192, 193] However, AES is not a fast-imaging technique compared to SEM. Moreover, quantification of AES signal has its limitations regarding the edges overlaps and the way of how the detector collects the signal. Generally, AES intensities are favorable to only look at qualitative thickness comparison that implies the relative thickness relationship. In this analysis, the chemical analysis from the AES shows perfect matching between the Ga map (Figure 50e) and the gray color levels in SEM. In addition, the carbon map (Figure 50f) presents uniform intensity except for the medium-gray color in SEM, which is interpreted as thicker graphene. These AES correlations illustrate that the chemical signals of the 2D-Ga heterostructure are embedded in the SEM image, which could be visually improved by adding a false-colored scale (Figure 50c).

Interestingly, most of the surface defects (AES, oxygen signal) and the non-intercalated regions (no AES Ga signal) are associated with the bright contrast. Particles on the surface and step edges have higher contrast than the flat regions due to the edge effects of their physical height. This edge effect can be augmented at **higher tilts** of the SEM stage to better identify the particles from the flat areas (Figure 53). Moreover, the non-intercalated regions present bright contrast because of their lowered suppression of the SE emission. The most intriguing finding is that the oxygen signal correlates mainly with the defects and particles on the surface, implying a stable non-oxidized Ga layer at the pristine regions, as previously studied with XPS.[23]

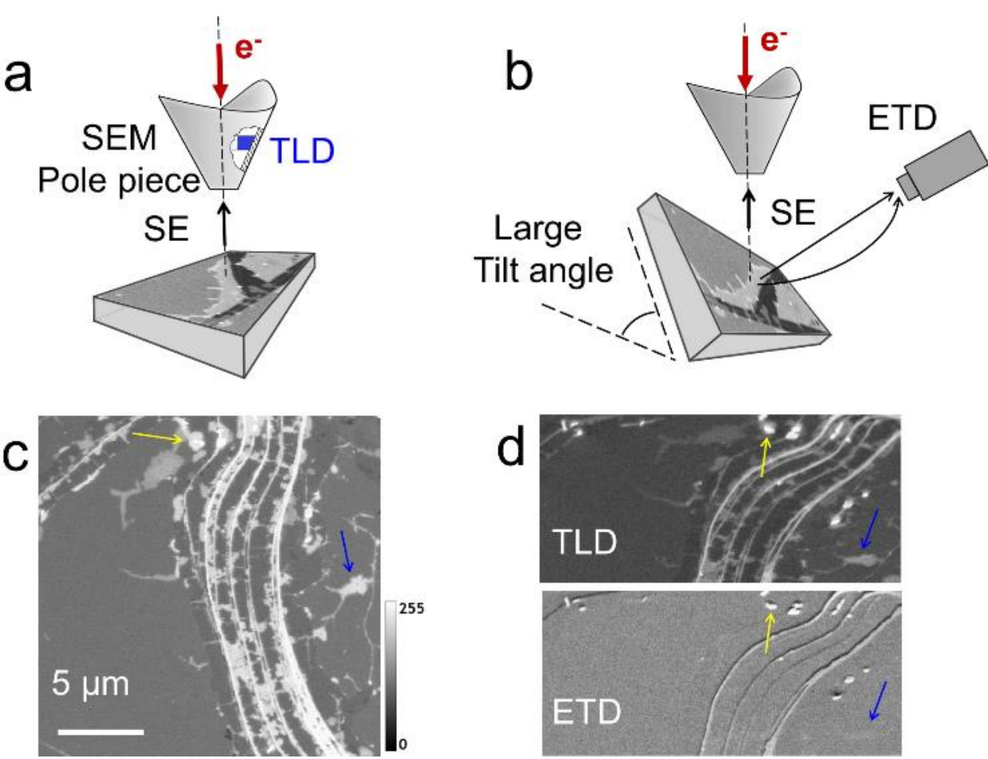

Figure 53. Effect of stage tilt in visualizing particles. (a and b) cartoons of imaging a 2D ga surface at zero- and high-tilted stage. (c) Through lens detector (TLD) image at zero-tilt. (d) Through the lens detector (TLD) and

Everhart-Thornley detector (EDT), images were taken at 54° tilt from the same position in (c). The yellow and blue arrows in (c and d) indicate a Ga particle and a non-intercalated region, respectively. Imaging on a tilted stage with different detectors helps distinguish particles and non-intercalated buffer layers that both could appear bright in SEM images at zero-tilt.

4.6.2.2. SEM correlation with cross-section STEM images

A site-specific FIB preparation was applied to lift-out samples correlated with the five main contrast in SEM, as shown in Figure 54. Our cross-section correlation confirms that the gray SEM colors represent the location of a bilayer Ga. The differences between gray colors are related to EG thickness variation. The main intercalated heterostructure in the middle of the SiC terrace is bilayer Ga covered by bilayer EG, which appears as the light-gray contrast in SEM. A secondary intercalated structure exists near the step bunches or as finger shapes across the terrace with coverage of three or more graphene layers. This variation in graphene thickness is evolved from the original EG structure before the intercalation process, as illustrated in Figure 49.

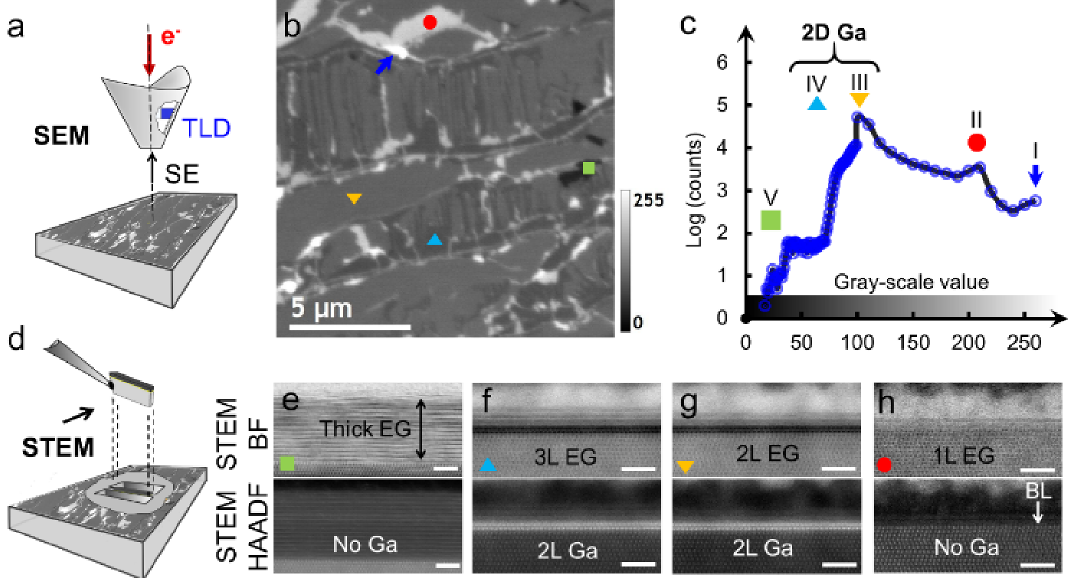

Figure 54. SEM correlation with atomic layer thicknesses. (a) schematic diagram of the through lens detector (TLD) of the SEM. (b) SEM image recorded by the TLD at low WD. (c) log-scale histogram of the SEM image in (b). (d) cartoon of coordination of the SEM and the FIB cross-section. (e-h) STEM-BF (top) and STEM-HAADF (bottom) images were taken from different FIB samples at the dominant contrast regions indicated by the same color markers in (b and c). The scale bar is 2 nm. The cross-section correlation shows that the gray contrast levels III and IV are related to a bilayer Ga intercalation covered by 2 and 3 EG layers, respectively.

All non-gray contrast show defected or non-intercalated regions, with thick or thin EG, in the cross-section view as demonstrated in Figure 54e,h. This makes only the gray colors in SEM represent the Ga intercalated regions with differential gray range varies depending on the number of EG layers with a minimum of two EG caps. This minimum EG thickness ensures no graphene contrast flipping (see Appendix A2) associated with monolayer graphene at low imaging voltages.[107] This makes the SEM imaging of the 2D-Ga surface more stable and reliable at different beam energy conditions; see Appendix A2 for a detailed work. However,

we recommend the 5 keV voltage and 1.6 nA current as the primary electron energy to achieve the best graphene contrast in SEM images.

Now, let us discuss these results. The present AES and STEM correlative microscopy unlocks the SEM contrast associated with the Ga intercalation positions and the heterostructure thicknesses. Tracking an intercalant has previously been achieved using optical microscopes; however, it depends on the optical absorption of both the 2D material and the intercalant, which both should have optical excitation that lies in the visible light range.[194] Another interesting optical characterization of 2D materials and heterostructures is the non-contact terahertz (THz) near-field spectroscopy. Although this technique is scalable and can image wafers of 2D materials with a few centimeters, it has around 300 μm spatial resolution.[195] This means THz microscopy is not a practical option to resolve the SiC terraces, which is typically around 5 μm, depending on the miscut angle. Recent work suggested that Ga intercalated EG could be realized in an optical microscope; however, the optical contrast and resolution do not differentiate heterostructure thicknesses nor confirm the confinement in cross-section imaging.[179] This invokes the powerful spatial and spectroscopic advantages of the SEM thickness determination approach compared with the optical microscope in tracking intercalants or characterizing 2D layer and heterostructures.

The previous AES and STEM correlative characterization established the necessary understanding of the SEM contrast linked to the EG thickness. Correlating SEM contrast with the cross-sectional STEM view of 2D-Ga demonstrates that the dominant light-gray contrast corresponds to bilayer ga and

EG bilayers. However, STEM imaging is typically a *narrow spatial range* of observation and may not be sufficient to link contrast and thicknesses directly.

4.7. Thickness uniformity of 2D-Ga.

In this section, a scale-up of the STEM image span length is performed by stitching hundreds of STEM images covering all the FIB cross-section lamella. A protocol is established to construct long montages of STEM images that cover >7 micrometers and still preserve atomic resolution to resolve the atomic thicknesses.

4.7.1. Atomic-scale STEM montage of the cross-section

A series of STEM images at 1.3×10^6 magnification are acquired along the 2D-Ga cross-section with a 2048×2048 resolution at 2 μs pixel time. A 10%–25% overlap between successive images is maintained to help identify mutual fiducial markers on the carbon/platinum coating. Then, for every 10 successive images, the stitching plug-in in the Digital Micrograph software is used to stitch the ten images automatically using a cross-correlation algorithm (Figure 55). The 10-images-long stitched montages (Figure 56) were calibrated and screened using ImageJ software to measure the spatial length of the 2D-Ga versus the heterostructure thicknesses across the 7 μm interface of the FIB lamella. Finally, a correlation between the spatial length of the heterostructure thicknesses and the SEM contrast was established in Figure 57.

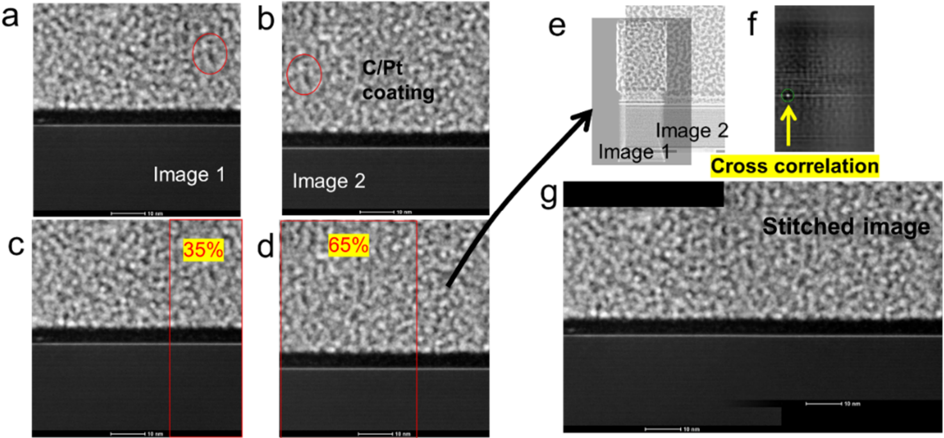

Figure 55. Stitching atomic-resolution STEM images. (a-b) two successive STEM-HAADF images. The carbon/platinum (C/Pt) coating provides fiducial marks (see red circles) for the postprocessing stitching. (c-d) are the same images in (a-b) with an identified 35% overlap. This means 35% of the right side of image No.1 to be searched for matching with the 65% of the left side of image No.2. (e) modified contrast and brightness of the overlap regions in (c-d) helps to find the cross-correlation in (f) more efficiently than using the original STEM images. (g) Seamless stitching of the two images in (a-b) using the correlation identified in (f).

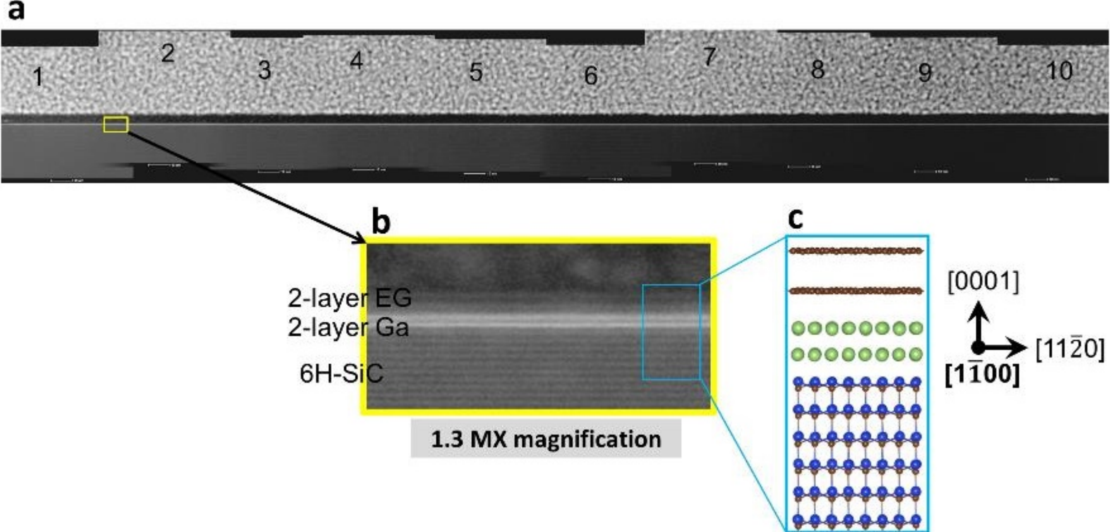

Figure 56. A stitched atomic-resolution STEM montage. (a) A montage of 10 STEM images stitched using the cross-correlation method in Figure 55. The images are acquired at the same conditions with 1.3 MX magnification. (b) a

close-up of the yellow box in (a) shows that the heterostructure is bilayer Ga covered by bilayer EG. The FIB sample used for building this montage is parallel to the $[1\bar{1}00]$ zone axis, as described in the ball-and-stick cartoon in (c). The stitched STEM montages are acquired without tilting the FIB sample in the TEM microscope to achieve a spatially correct correlation between the STEM montages (cross-section view) and the SEM images (in plan-view). Additional visualization of the whole cross-section was performed by manually stitching successive montages (10-images-long each) in Microsoft PowerPoint.

4.7.2. Analysis of STEM montage

The montage is built with hundreds of successive STEM images using the cross-correlation stitching technique thanks to a carbon/platinum coating that is intentionally deposited during the FIB preparation process (Figure 61 and Figure 56). The montage view verifies the relationship of heterostructure thicknesses and SEM contrast by directly counting the number of Ga and EG layers observed in the STEM images (Figure 57d). Figure 57 is direct evidence that 2D-Ga prefers to form a bilayer over SiC terraces. This direct spatially resolved evidence verifies conclusions previously inferred by both experimental and theoretical spectroscopic ellipsometry.[181] Unlike spectroscopy, inspecting the CHet surface using SEM contrast accurately visualizes the thickness uniformity and defect distribution of the 2D-Ga.

The SEM contrast variation is closely correlated with EG thickness variation and location of the intercalated Ga. This presents two primary sources of SE suppression for this system. First, a uniform suppression of the SE emission due to Ga intercalation occurs due to detachment of the buffer layer to form an extra graphene layer. Second, the EG thickness variation across the SiC terraces is due to the EG growth process, which is present before the CHet intercalation process.

This explains why the SEM contrast variation of the 2D-Ga surface is mainly controlled by vdW heterostructures which change with EG thickness.[107] However, understanding the *origin of the SEM* contrast requires further investigation about the surface potentials (and hence SE emission) at different hetero-stack structures.

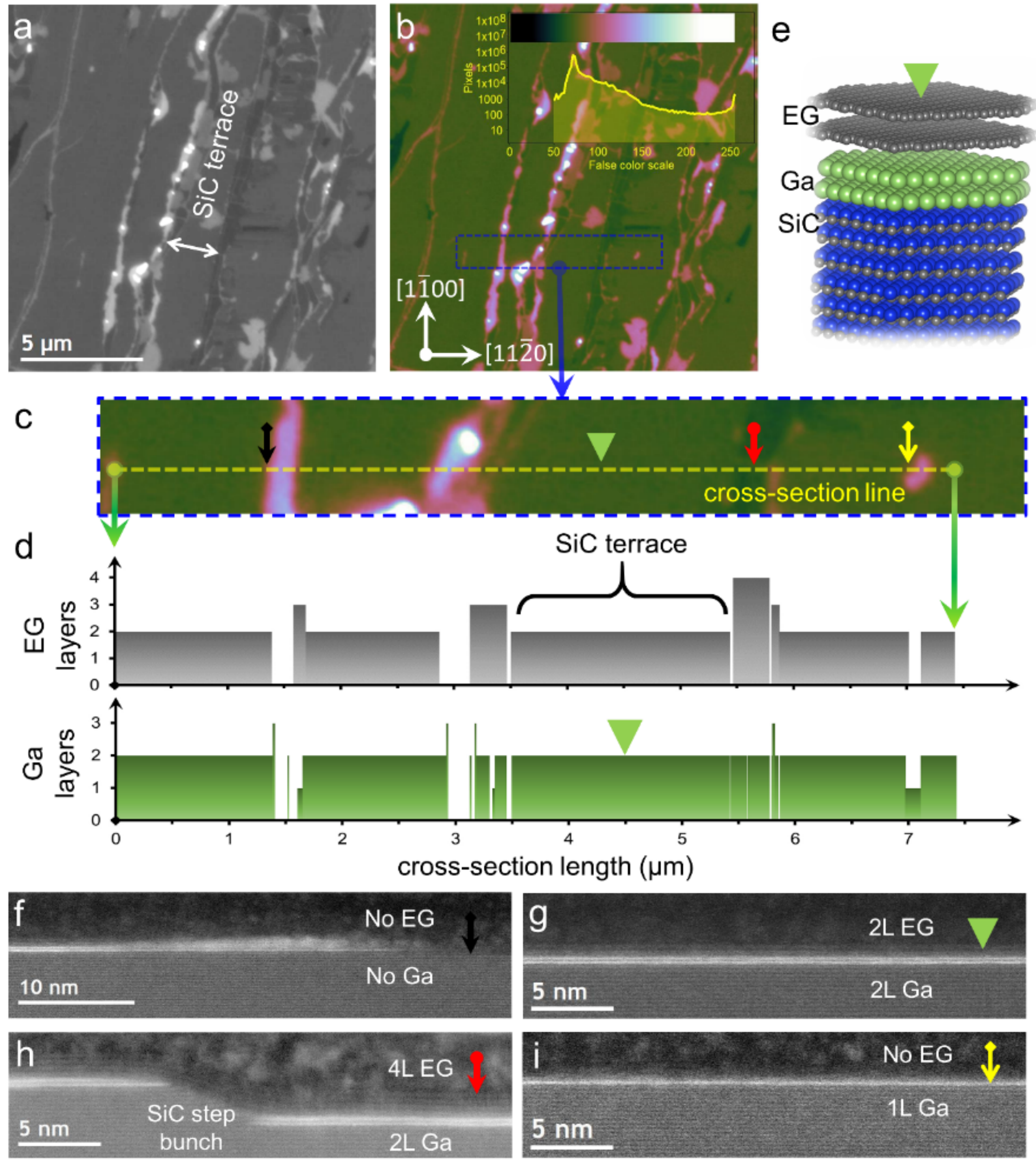

Figure 57. Stitched STEM montage. (a) SEM image showing SiC terraces with contrast variation near the step edges. (b) False-colored image of (a), which shows uniform color/contrast along the middle of the terraces. The insert is the log-scale histogram of the colored SEM image aligned with the color bar code. (c) Close up of the site where the FIB cross-section is extracted (blue rectangle in (b)). (d) Distribution of the number of layers of the EG and Ga counted from stitched montages (Figure 55 and Figure 56). The middle of

the SiC terrace has a uniform structure of bilayer Ga covered by bilayer EG, as illustrated in the 3D model in (e). (f-i) STEM-HAADF images cropped from the STEM images used to produce the stitching results in (d). Resolution of the HAADF images was intentionally reduced during the acquisition to facilitate stitching. The markers on the HAADF images indicate the exact plan-view locations in (c).

4.8. Origin of SEM contrast

4.8.1. Trapped electrons inside potential barriers

Let us assume a potential barrier is introduced in front of the emission path of electrons generated from a beam-sample interaction. In this case, there is a chance for the electrons to tunnel through this barrier as part of the electron probability cloud outside this potential barrier. Intuitively, confinement (or trapping) electrons inside an infinite potential barrier, such as 2D materials, increases when the potential of the barrier increases. However, and unexpectantly, barriers with Dirac cones, like graphene, are experimentally observed to transmit electrons even if the potential approaches infinity, called Klein tunneling.[196] The electron transmission through graphene (as a potential barrier) depends on the incident angle of the electrons to the graphene. Normal incidence angle leads to complete transmission of the electrons without reflection. In contrast, non-normal incidence angles lead to some electrons being reflected from the barrier. These reflected electrons are assumed to bounce and be trapped inside a continuous graphene sheet.[197-199]

In SEM imaging of graphene, the accelerated electrons interact with the sample at a specific interaction volume. The size of the interaction depends on the imaging conditions. This interaction results in secondary electron (SE) emission from the

sample surface. Here, the mechanism of the SE leaving the EG or the 2D-Ga surface is similar to the previously mentioned model of electrons interacting with a potential barrier.[199] In the case of 2D-Ga, the first vdW spacings exist at the Ga-EG interface. The SE may leave the Ga surface with a variety of incident angles to the bottom surface of the first EG in contact. At this point, some electrons with the non-normal incident angles have more chance of being trapped inside the graphene layer (Figure 58), resulting in a general suppression of the SE emission that reaches the detector. Other electrons have a higher probability of transmitting through the EG layer depending on the extraction bias voltage applied in the SEM chamber to accelerate the emitted electrons towards the detector. The range of SEM bias voltage (~20-500 V)[200, 201] is far higher than the potential barrier of graphene, which is reported between 36 meV[202] and 420 meV[203] depending on the graphene size and quality.

To summarize, the SE suppression found in SEM imaging of the 2D-Ga surface (Figure 47c) depends mainly on how many potential barriers are placed in front of the path of the electrons leaving the surface towards the SEM detector. Potential barriers are physically translated to the number of layers of EG. The gallium atoms are spontaneously intercalated at the SiC-buffer layer interface to passivate the silicon dangling bonds. This interface preference for the intercalation process results in detachment of the buffer layer.[23] This makes the detached buffer layer act as an extra potential barrier in front of the SE emission before leaving the surface. Thus, this SE suppression is an indication of the successful gallium intercalated position.

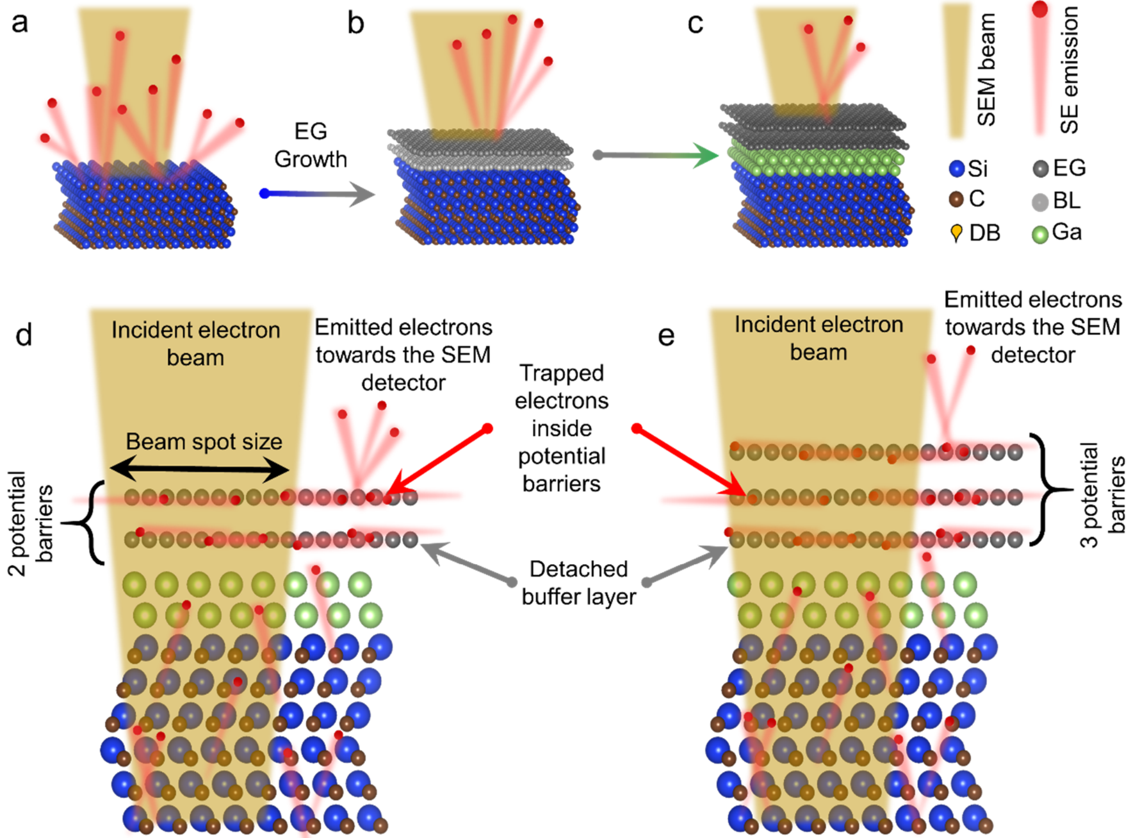

Figure 58. Schematic of electron emission from SiC, EG, and 2D-Ga. (a-c) schematic representation of the evolved suppression of the SE emission from SiC, EG, and 2D-Ga, respectively. (d, e) schematic representation of 2D-Ga covered by 2 and 3 layers of graphene, respectively. In contact with the gallium, the bottom graphene layer is the detached buffer layer resulting from the intercalation process. Depending on the number of potential barriers (graphene), the emitted electrons from the surface are higher in case of (d) than (e) because more potential barriers lead to more electrons trapped inside the graphene.

In the following sections, the surface potential for SiC, EG, and 2D-Ga at different thicknesses was calculated using density functional theory (DFT). In addition, correlative microscopy was performed between SEM with both the contact

potential differences using Kelvin probe force microscopy (KPFM) technique and the surface chemical mapping of gallium using AES from the same site.

4.8.2. Surface potential calculations by DFT

Surface potential is calculated using density functional theory (DFT) for SiC, EG, and 2D-Ga at different thicknesses of graphene coverage and substrate termination. The calculations (see Appendix 5 for details) support that increasing the number of graphene layers induces a potential increase (Figure 59), which agrees with previous experimental work of measuring the effect of the number of layers on surface potential.[204] In addition, introducing a bilayer Ga at the interface between BL and SiC results in increasing the graphene potential due to detaching the BL. This potential increase is noted in both cases of intercalating mono- and bi-layer graphene. This makes the intercalated position exhibit more suppression of the SE emission to appear dimmer in the SEM images than the EG before intercalation.

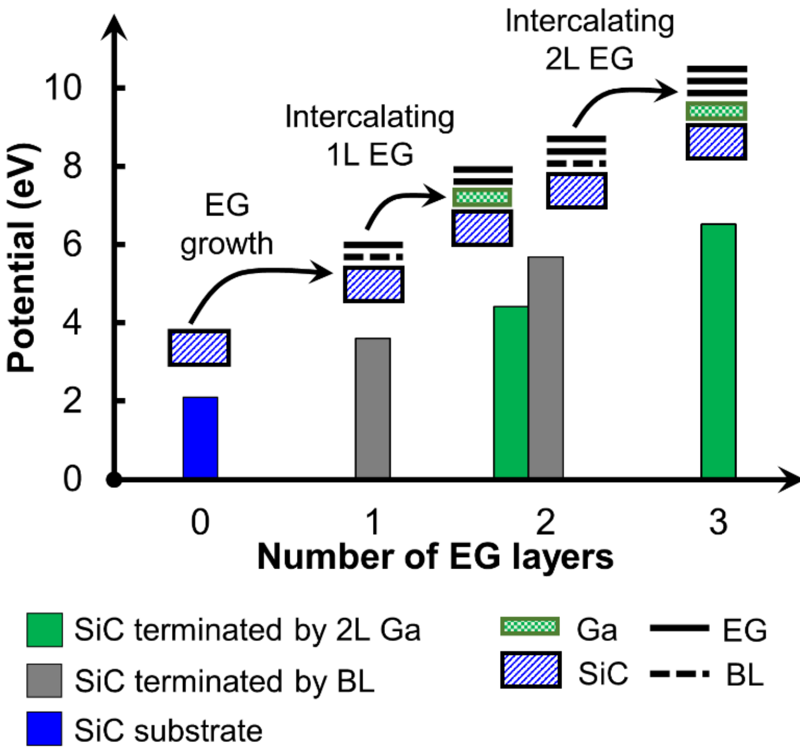

Figure 59. Surface potential calculation by DFT. DFT calculations of graphene potential (eV units) at different substrate termination and EG thicknesses.

The DFT calculations in Figure 59, the non-intercalated bilayer EG has a higher potential than the intercalated monolayer EG (see the gray and green color bar at 2 EG). It may be assumed that identifying the intercalated mono-layer EG regions can be misleading if another non-intercalated bi-layer EG is present at the same SEM image. However, understanding the local distribution of the EG thickness before the intercalation makes it easier to identify 2D-Ga regions after the intercalation. To further explain this, the local morphology of the bilayer EG (and even thicker) is always present near the step edges (see dark contrast in Figure 47d) or as a finger shape perpendicular to the step edge edges (see dark contrast in Figure 49). In contrast, the monolayer EG is at the middle of the SiC terrace, which will be the same local position after the intercalation. In addition, the

gallium is *uniformly* intercalated across different EG thicknesses and crossing the SiC step edges, as explained from the STEM stitched montage in Figure 57.

4.8.3. Surface potential measurements by KPFM

Kelvin probe force microscopy (KPFM) is employed to experimentally investigate the potential differences of the EG and 2D-Ga surface in correlation with the SEM contrast. Surface potential mapping (Figure 60c and Figure 61d) is performed using an Asylum Cypher atomic force microscope (AFM) from Oxford Instruments. A micromachined, Ti/Ir coated silicon cantilever (ASYELEC-01) is used for the measurement. The normal stiffnesses and resonance frequency (k= 2.9 N/m, f = 74 kHz) were calibrated using new Sader's method.[205] In this study, the KPFM process is performed through two-pass mapping.[206] The first pass records the topography in tapping mode. Then the second pass records the contact potential difference (CPD) – a relative measurement function of the bias voltage with voltage units – of the same site at 2 nm offset away from the surface. During the second pass, the probe oscillation is induced by an AC input bias. The DC voltage required (provided by a feedback loop to the bias) to negate these oscillations is recorded as CPD. Calculating the local surface potential in eV units from the CPD is avoided because the KPFM experiment is conducted in air, not in a vacuum. Therefore, comparing the potentials from KPFM with the DFT values can only be considered qualitatively.

4.8.3.1. KPFM-SEM correlation for EG surface

Figure 60d shows the EG surface with a monolayer (light-gray) in the middle of the SiC terrace and other thick EG at the step edges and EG-fingers inside the

terrace. The monolayer EG assumption at the terrace middle is based on the EG fabrication parameters, controlling the EG thickness. [23] The correlation between the KPFM map in Figure 60c and the corresponding SEM image from the same site demonstrates that the dark regions in SEM have the highest relative surface potential. In the following paragraphs, two *concerns* are discussed that a thicker EG at the step edges provides higher surface potential than the middle of the terrace.

First, the graphene thickness relationship with surface potential is related to the doping type of the EG samples. Doping type is reported to change the relationship between the graphene potential and the thickness of the graphene.[207, 208] The EG used in this thesis is n-doped before and after intercalation as previously measured using Angle-resolved photoemission spectroscopy.[23] Therefore, the higher potential regions in Figure 60c are characterized as thicker graphene.[208] Consequently, the light-gray regions at the middle of the terraces are the monolayer graphene. This morphology agrees with previous interpretations to address the origin of the SEM contrast for graphene flakes[107], and here we further verify this in the case of our EG samples.

Second, minor differences in potential can result from the SiC stacking order, which is recently reported in correlation with low energy electron microscopy (LEEM) images and KPFM maps.[209] However, the substrate termination effects do not appear in our SEM images of the heterostructure. That is because the contrast in SEM comes mainly from the vdW EG layers, which act as potential wells. Therefore, potential sensitivity to SiC stacking orders is more likely to be resolved by the LEEM method than SEM imaging. This makes the SEM contrast

more suitable for identifying EG thicknesses without subtler effects from the SiC substrate.

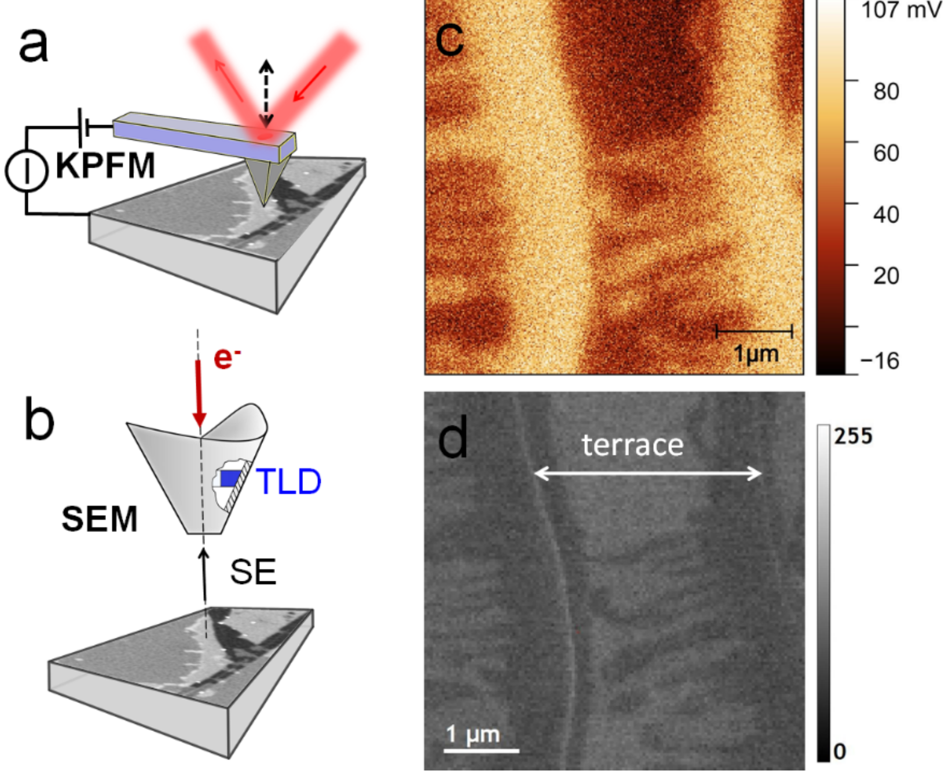

Figure 60. Correlation of SEM contrast with KPFM of EG surface. (a–b) cartoons of the Kelvin Probe Force Microscope (KPFM) and SEM experiments. (c) contact potential difference map (in mV units). (d) the corresponding co-located SEM image of an EG surface.

4.8.3.2. KPFM-AES-SEM correlation for 2D-Ga surface

Figure 61 shows a correlation between SEM, KPFM, and AES scans at the same location. Some considerations are needed to achieve such correlation across the three different techniques. KPFM map is recorded with a large frame of 10 × 10 µm size. Then, within this large KPFM frame, other smaller frames of 5 × 5 µm and 2 × 2 µm size were scanned with 512 × 512 pixels to provide higher resolution. The

large frame is correlated with an optical navigation microscope at 5–10X magnification, where the wafer edge – or fiducial Ga particles on the surface – are captured with the KPFM map location. Then, the same position is navigated to in the SEM with the help of the wafer edge or surface marks. Later, SEM images at different magnifications are acquired at zero stage tilt, 5 keV, and 1.6 nA. A window of the same site is cropped from both the KPFM maps and SEM image and presented in Figure 61d-e. Finally, the sample is transferred to the AES to acquire an AES map from the same mentioned position. Before acquiring the AES maps, SEM images from the site of interest are acquired using the AES system, which also functions as an SEM with an ETD detector. The acquired AES map is acquired near the wafer edge due to instrument limitations, which contains thick EG patches (see Appendix 6 for details) that appear darker in the image. The KPFM correlation is designed with a wide frame at low magnification; see Appendix 7 for details. Then the AES maps are spatially corrected for the tilt used (similar to the methodology in Figure 51). Finally, the site representing the area in correlation with both SEM and KPFM is cropped and presented in Figure 61f.

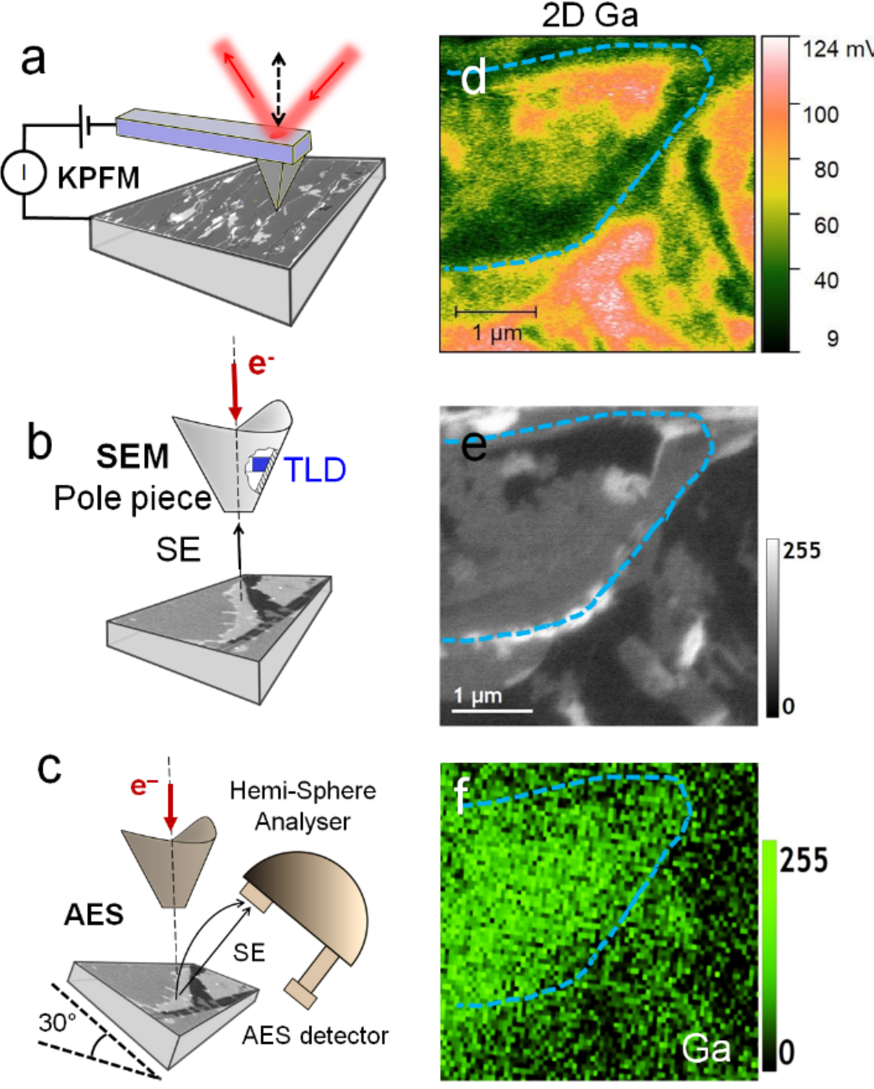

Figure 61. SEM contrast correlation with KPFM and AES for 2D-Ga. (a-c) cartoon representations of the KPFM, SEM, and AES experiments. (d) KPFM map acquired prior to the SEM image in (e). SEM image was taken by TLD at 5 keV and 1.6 nA. (f) AES maps at gallium of the same position in (d and e). The correlation between SEM, KPFM, and AES shows that intercalated Ga introduces distinguishable medium gray contrast in the SEM image that is directly related to an evolution in the contact surface potential differences in the range of ~ 30–70 mV of the KPFM map in (d).

The gray SEM contrast is found in correlation with the range of ~30-60 mV (green and yellow colors in Figure 61d) of the KPFM map from this triple-technique correlative characterization. The gray SEM contrast also agrees very well with the location of intercalated ga, as seen in the AES map. The potential range (~30-60 mV) of the KPFM map within the Ga regions may be explained as a reason for SiC stacking order across the SiC step.[209] This potential variation is expected because KPFM is sensitive to the potential of the whole heterostructure, including the substrate effects. In contrast, SEM is mainly sensitive to the vdW layers that are represented by the EG number of layers. The AES-SEM correlation is also presented in Figure 50, but here (Figure 61), it is correlated with KPFM as well.

4.9. Significance of SEM contrast for characterizing 2D-Ga

The previous three sections established the grounds for characterizing 2D-Ga with SEM utilizing the detached buffer layer. The ability to locate the intercalated regions from the SEM contrast is verified using multiple correlative microscopy approaches with different techniques as well as theoretical calculations. In this section, significant contributions using SEM in the characterization of 2D-Ga are discussed to calculate the scalable coverage, optimizing the synthesis and electron transport of the 2D-Ga.

4.9.1. Calculating the bulk coverage percentage of the 2D-Ga

Leveraging the knowledge gained from the stitched STEM montage in Figure 57 and the AES correlations in Figure 50 and Figure 61, the SEM contrast can be segmented into regions corresponding to the heterostructure thicknesses and

quality. The following methods and results describe the segmentation process of 30 dense-pixelated SEM frames that cover ~2 × 1.5 mm area.

4.9.1.1. SEM image acquisition parameters

To further explain the method, a matrix of images that covers ~2 × 1.5 mm area near the edge of a substrate (Figure 62). The minimum pixel size may be 1-10 nm in SEM, depending on the beam size. However, the pixel size is increased when acquiring densely pixelated images to reduce the acquisition time. In this study, one SEM frame of 6144 × 4096 pixels requires 2.1 minutes to acquire a pixel size of 67.4 nm. This condition makes the total time for acquiring a matrix of 30 frames about one hour. Still, this pixel size is spatially sufficient to resolve the features within the SiC terraces. An overlap of 10-15% between the SEM images is maintained in both horizontal and vertical directions.

4.9.1.2. SEM image segmentation methods

The segmentation of SEM images was performed using DragonFly Software.[210] The dense-pixelated SEM images were cropped to exclude the overlapping regions. Then, all images were leveled by mean plane subtraction. After then, all leveled images were segmented by identifying the thresholds for the bright, gray, and dark contrast from the histogram. Figure 63 shows an example of identifying the contrast and segmenting the SEM image from the histogram. The global threshold range can be determined from the upper and lower Otsu limits.[211] No specific range for the contrast is defined for each region because the contrast value depends on the acquired conditions (Appendix 4). However, the contrast *order* in the histogram is the criterium to be considered rather than the contrast values.

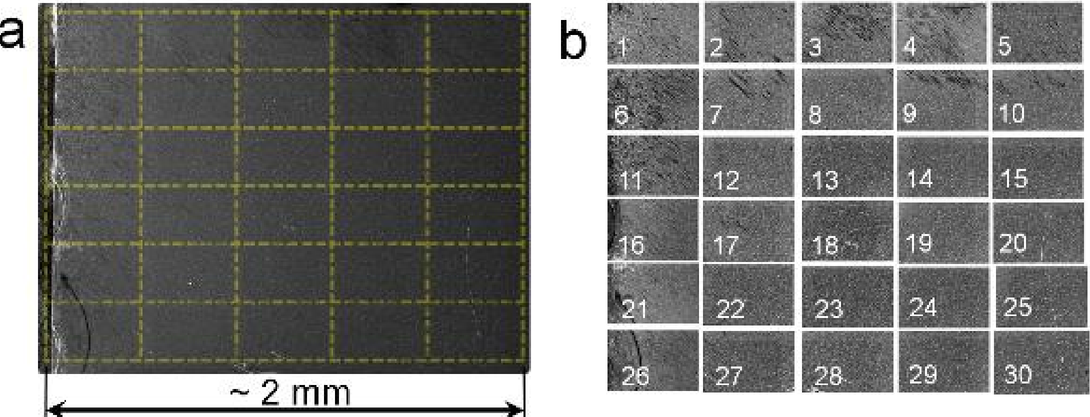

Figure 62. SEM montage covers a scalable area of 1.5 × 2 mm² area. (a) Low magnification SEM image covers 1.5 × 2 mm². The yellow matrix represents 30 positions where dense-pixelated images are acquired in (b). An overlap of 10-15% is maintained for all images in both the horizontal and vertical directions.

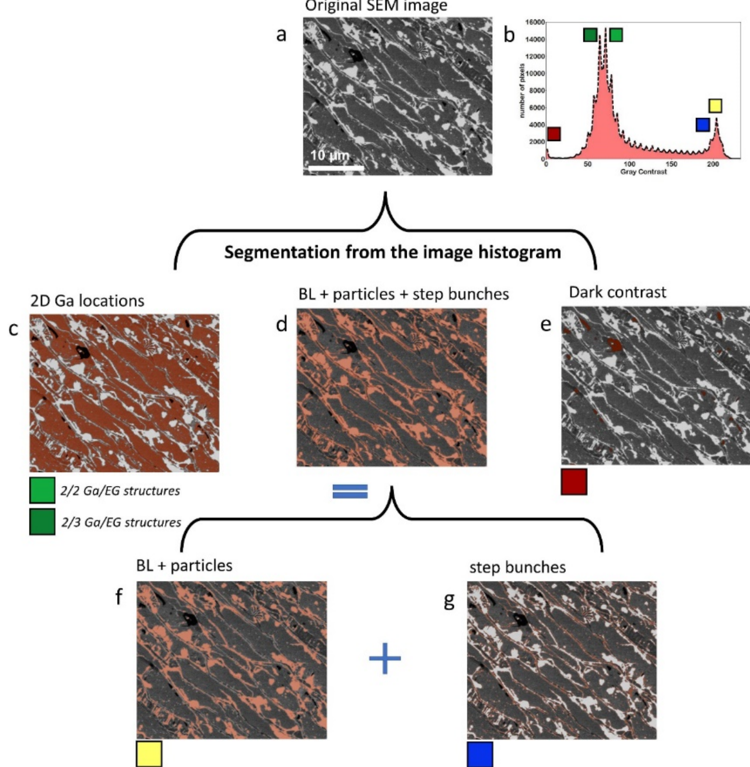

Figure 63. SEM segmentation from the image histogram. (a and b) are the SEM image and the corresponding histogram on a linear scale. (c) marking of the

gray contrast that represents gallium intercalation into monolayer and thicker regions. (d and e) segmentations of the bright and dark contrast, respectively. The histogram segmentation of the white contrast is sensitive to differentiate between the edges of the buffer layer (BL) or damaged areas and particles on the surface.

4.9.1.3. Calculating gallium coverage over 2 × 1.5 mm area

The Ga coverage is calculated based on the gray SEM contrast, representing the successfully intercalated regions as understood from the correlative characterization. SEM contrast of the 2D-Ga surface represents mainly 5 peaks in the image histogram, discussed in Figure 54 and Table 1. The medium-gray (III) and light-gray (IV) contrast represent the intercalated Ga of monolayer and thicker EG, respectively. These two contrasts can be segmented by identifying the corresponding range in the image histogram, as shown in Figure 63c. Both the bright and dark regions in the image can also easily be identified from the histogram, which is considered non-intercalated regions, as seen in Figure 63d-e. This segmentation process is performed for a total of 30 SEM frames. Figure 64 shows one of the 30 frames before and after the segmentation.

Calculating the Ga coverage starting from the substrate edge, the SEM images reveal that the 2D-Ga covers ~64% on average of the SiC surface within the outer 2 mm of the substrate. Additionally, the ga coverage trends to higher values as one moves away from the edge - up to ~74% at 2 mm far from the edge (Figure 65f). The coverage variation combines edge effects during the growth of the EG and how the sample is mounted for the CHet fabrication in front of the ga source. This results in a nonuniform Ga exposure on the outer 1.5 mm of the sample, and hence nonuniform intercalation. It is expected, based on trending, that the Ga coverage may reach >90% at the center of the wafer.

Every 2D-Ga region can also be identified and quantified from the stitching process. Figure 65c and d show the distribution of the width and length of the 2D-Ga regions. In this sample, the 2D-Ga appears as disconnected patches along the SiC terraces. The width of these patches is limited by the width of the SiC terraces (2–5 μm in this sample), which may be engineered by changing the SiC wafer miscut angle. However, the 2D-Ga patch length is more variable and can reach a few tens of micrometers in some places.

4.9.1.4. How SEM contrast analysis pushes the microscopy limits

The donut graphs in Figure 65f result from the segmentations of the SEM contrast that represents the 2D-Ga heterostructure. The SEM contrast is sensitive to the number of layers of EG and the presence of atomically thin gallium layers, similar to what can be seen in STEM images. Here, TEM techniques have a limited field of view when reaching the atomic scale. Experimentally, a typical STEM-HAADF image at ~1,000,000X magnification that just resolves the layers of EG and Ga has a field of view about 60 nm only. However, the segmentation of the SEM contrast in Figure 65f provides the same information of the heterostructure thickness (EG and presence of Ga) over a 2 × 1.5 mm^2 area. This is about 20,000,000-increase of the field of view, compared with a typical STEM or other microscopy technique, as illustrated in Figure 65g. This work leverages the SEM's spectroscopic imaging capabilities that allow high-spatial-resolution imaging for tracking intercalants, identifying relative surface potentials, determining the number of 2D layers, and further employed to characterize the scalability and uniformity of low dimensional materials.

Another benefit of the spatially resolved understanding of 2D vdW layers is establishing a higher-resolution interpretation of optical probes (like Raman, spectroscopic ellipsometry, XPS, and second harmonic generation) which provide micrometer-to-millimeter spatial resolution. This limited resolution means the optical response comes from multiple heterostructure features at the same time, confounding their interpretation. An example of this is a recent report of ellipsometry data for a 2D indium heterostructure[181] in which the 2D indium thickness varies between 2 and 3 layers within the same SiC terrace. This makes the ellipsometry probe measure both thicknesses at once because the probe is the same size as the terrace. To develop 2D-Ga for scalable devices, we recommend using SEM to identify the most extended and most uniform 2D-Ga strips. Site-specific devices could be printed based on online and unsupervised segmentation of the SEM contrast.

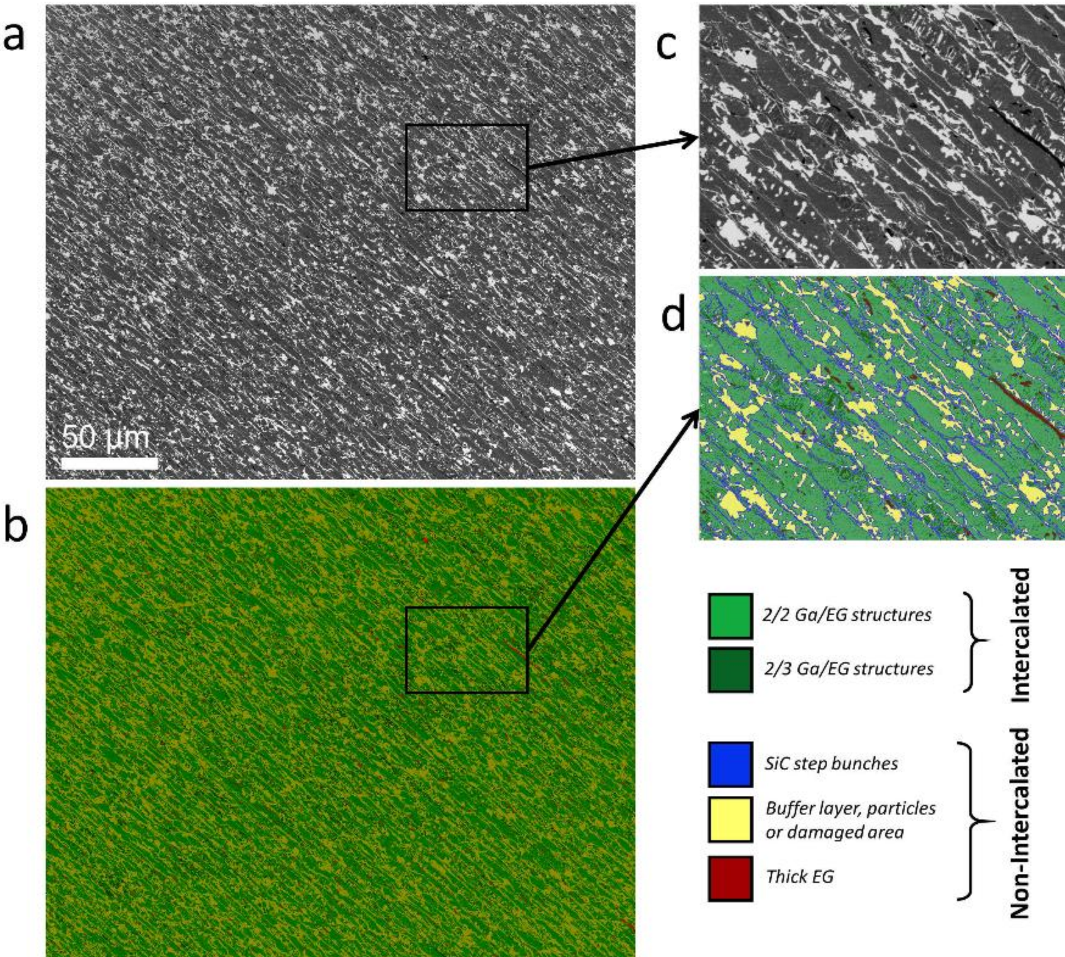

Figure 64. Segmentation of a large field dense-pixelated SEM frame. (a) SEM image. (b) segmentation of (a) with the same color codes in Figure 63 and on the bottom right. (c and d) zoom of the regions indicated in (a and b), respectively.

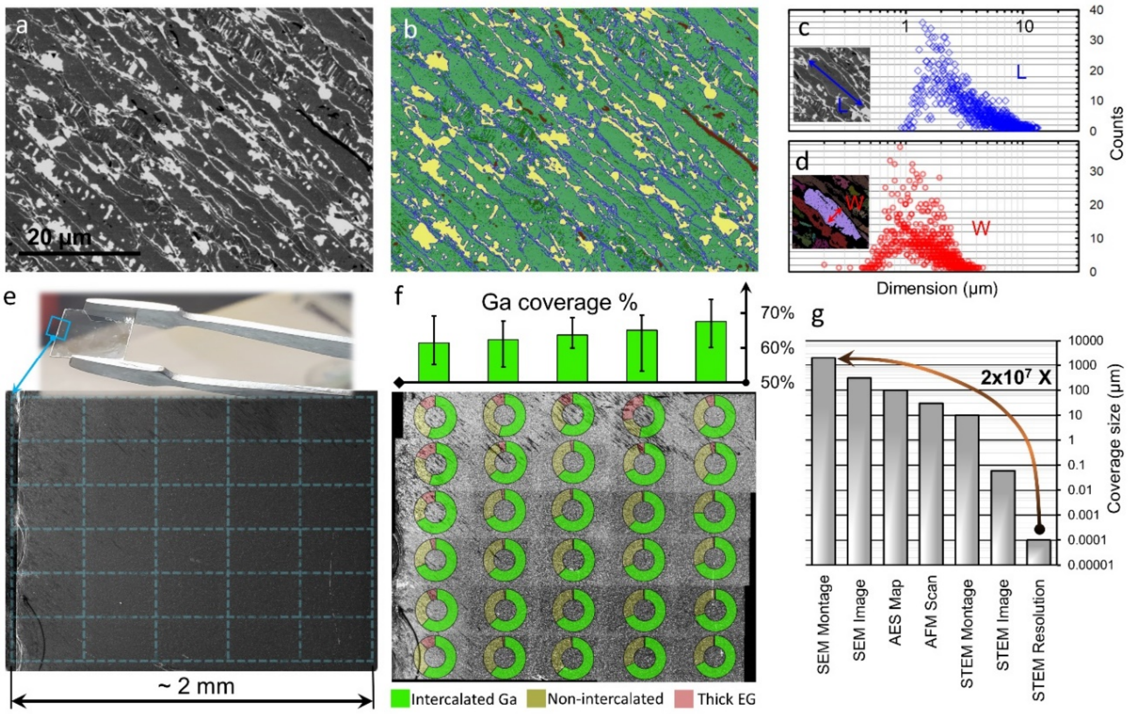

Figure 65. Scaled-up characterization of the 2D-Ga over 1.5 × 2 mm² areas. (a) a region from the SEM frame of the 2D-Ga surface. (b) segmentation of (a) based on threshold identification of five contrast regions, see Figure 64 for the color-coding. (c–d) Distributions of length (L) and widths (W) of the uniform Ga intercalated regions at the middle of the terraces. The inserts in (c–d) are SEM images (in c) and the corresponding terrace identification (in d) as determined by the segmentation process. (e) low magnification SEM images acquired near the wafer edge over a ~2 × 1.5 mm area. The top insert is a photograph of the actual substrate (10 × 10 mm), where the blue box indicates the position of the SEM image. The blue matrix represents the positions where 30 low-magnification and dense-pixelated SEM images (matrix of 5 × 6) are acquired, as illustrated in Figure 62. (f) 30 Donut charts of the intercalated Ga, non-intercalated regions, and thick EG of the same area in (e). The charts are overlayed on the stitched montage of the 30 images. The top inserted graph is the ga area coverage percentages starting from the wafer edge (left) towards the middle of the wafer (right). (g) Comparing the width from the stitched SEM montage in (f) with the average width determined by other techniques. The SEM montage maintains the in-plane feature information with the SEM resolutions (few nm) but combined with the 2D-Ga heterostructure thickness – a few Å –

similar to what can be achieved by STEM (resolution of 1 Å or less). The contrast information from the SEM montage is similar to that from STEM but with a scale-up of ~2×10^7 in linear dimension.

4.9.1.5. Automation of the segmentation process.

In recent work, different techniques of unsupervised segmentation of SEM images have been used to determine graphene locations on a copper surface.[212] The concept of unsupervised segmentation has also been introduced for classifying exfoliated graphene using optical contrast.[213] Here, a trial of unsupervised segmentation is presented in Appendix 8 performed by training a neural network for a texture-based segmentation using a random forest algorithm. Although our machine learning segmentation can identify the Ga heterostructures in the middle of the terraces, it has difficulty identifying the EG fingers near the step edges. This may be further improved by further training of different surface regions using additional models. The automation of SEM image segmentation may provide a direct calculation of the area coverage while imaging the 2D-Ga and other Chest materials. Another future automation opportunity lies with the recent invention of multibeam SEM.[214] This imaging technique allows up to 91 electron beams to acquire images simultaneously. Then, the images can be stitched to form a broad panorama of the sample. This can significantly benefit the 2D materials field by fast characterizing the heterostructures over large areas while preserving the SEM lateral resolution of a few nanometers.

There is always an error in calculating the coverage percentage, either the histogram method or the automated segmentation. Appendix 9 explained these errors at both the instrumentation and data analysis levels. The SEM contrast reproducibility should be sufficiently possible to minimize the errors in calculating the 2D-Ga coverage percentage. Further discussion of the SEM contrast reproducibility can be found in Appendix 10, where 3 different SEM machines at two different universities are used to reproduce the contrast of these samples.

4.9.2. Optimizing the electron transport

The segmentation analysis of the SEM image shows that the 2D-Ga in-plane morphology is a longitudinal stripe. This geometry and dimensions are adequate for building electronic devices that transport along the SiC terrace length to measure superconductivity. The superconductivity of 2D-Ga was previously reported and studied along and across the SiC terraces.[23] However, the effect of EG thickness variation on the superconductivity behavior is not well established yet.

Transport measurements were conducted in a Quantum Design physical property measurement system (PPMS). The superconductivity measurements were carried out on six point probe (6PP) devices fabricated on terraces of 2D-Ga heterostructure.[23] The probes (4 probes for voltage and 2 probes for current) were deposited with separation of the order of 5 μm by electron beam lithography at two regions, with different SEM contrast, to better explain the impact of EG thickness variation on electron transport. Based on the SEM contrast, only two voltages (out of four) and two current electrodes are used for each transport

measurement. These four used electrodes are highlighted by the asterisks in the SEM images in Figure 66.

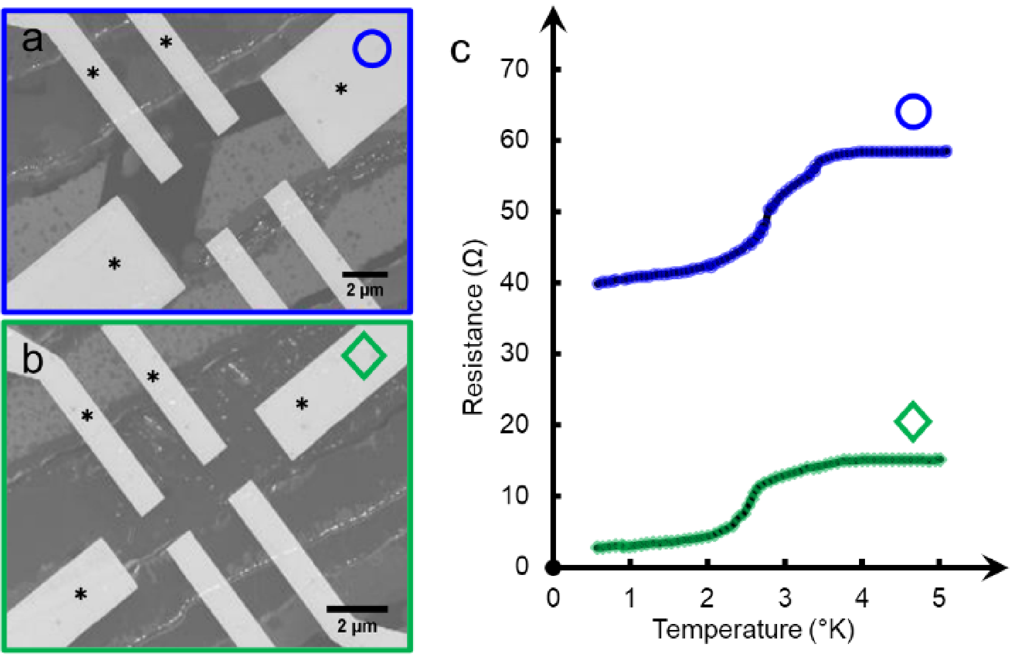

Figure 66. Superconductivity measurement of a 2D-Ga heterostructure. The sample in this figure was intercalated at 700 °C. (a) SEM images of the 2D-Ga surface show two contrasts (bright and dark-gray) in the measuring area between the device electrodes. (b) SEM image shows uniform contrast (medium gray) between the electrodes. (c) Superconductivity measurement acquired from the devices in (a and b) using the four electrodes highlighted by asterisks as the top or bottom voltage electrodes for the measurements. The uniform SEM contrast in (b) is correlated to a significant resistance drop in the superconductivity. This emphasizes the importance of SEM contrast in determining the correct locations for building devices on the 2D-Ga hetero-stacks.

It is evident that SEM contrast can be utilized to prescreen 2D-Ga uniformity prior to the development of 2D-metal-based devices. The resistance (in Figure 66c) drops to near zero only, including resistance of the electrodes and contacts, for heterostructure devices fabricated in areas of uniform SEM gray contrast, where

there is a uniform bilayer of Ga beneath a bilayer EG structure, as understood from the correlative multiscale microscopy. This suggests that there is a finite resistance related to the thickness and quality of the graphene cap, regardless of the superconductivity of the gallium, which is assumed to reach zero resistance around 4° K.[23] Despite introducing a tunneling barrier that affects the superconductivity, still, the graphene cap is essential to provide stability for this atomically thin metallic layer. The layer air stability is vital for employing 2D-Ga in devices.[176]

4.9.3. Optimizing the CHet fabrication

Another significance of SEM contrast is its sensitivity to graphene quality. Both EG and Ga layers may be exposed to high growth temperatures or harsh atmospheres during the growth steps, resulting in a nanocrystalline mixture of carbon and gallium. This mixture has no morphological fingerprint of EG thickness variation due to severe graphene damage (Figure 67i). Thus, SEM imaging is recommended for fast preliminary feedback of layer quality while optimizing the growth conditions. Figure 67 shows that the coverage of the gallium intercalation is optimized around 700–800 °C compared with lower and higher temperatures.

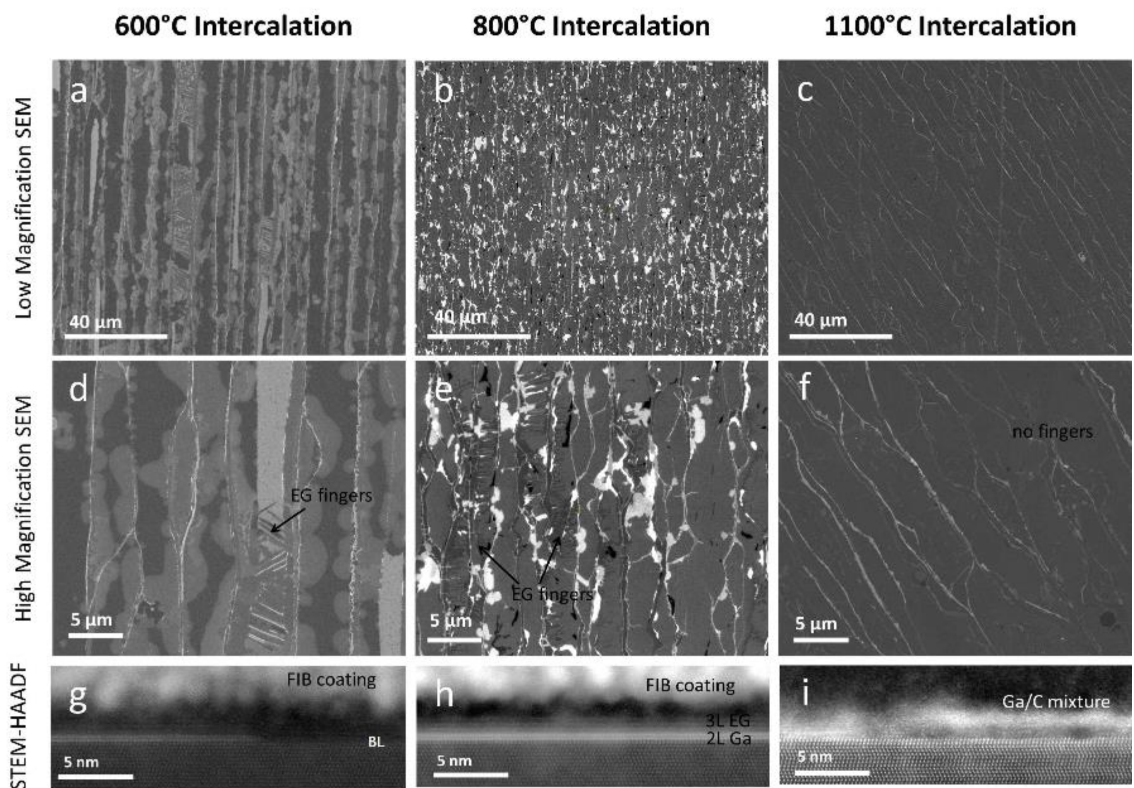

Figure 67. Tracking the successful Ga intercalation using the SEM contrast. (a-c) low-magnification SEM images for 2D Ga samples intercalated at 600, 800, and 1100 °C, respectively. (d-f) high magnification SEM images show the morphological surface features of graphene and intercalated EG at the corresponding growth temperatures. (g-f) cross-section STEM-HAADF images show partial intercalation of Ga, near-full intercalation, and interface damage, respectively. The SEM contrast can track the surface fingerprint of multilayer EG to indicate the quality of the 2D Ga heterostructure.

4.10. Si-Ga interface challenge

In this section, both imaging and spectroscopy STEM techniques are applied to investigate the interface challenges and instabilities between ga and, mainly, the topmost SiC layer. The investigations start with STEM imaging and STEM-EELS

of the SiC substrate after preparing the EG and applying the plasma process in order to assess the substrate and investigate possible surface reconstructions effects at the EG interface prior to the intercalation process. Then, other investigations of the 2D-Ga are discussed to demonstrate how the gallium atoms interact with pre-existing EG surfaces.

4.10.1. SiC-EG interface prior intercalation

Figure 68 shows STEM images of the substrate interface after applying both the Si-sublimation and the plasma treatment of the EG. This means that the interface seen in Figure 68a and b is the interface just before the intercalation process. Notably, the epitaxial graphene appears slightly damaged due to the oxygen plasma, but it still preserves the vdW spacing. The topmost SiC layer has lower HAADF intensity compared to the SiC rows of the SiC bulk. Additionally, there is a ***selvedge*** spacing between the first and second topmost SiC layers (~2.75 Å) compared to the bulk distance (~2.45 Å), as measured from the STEM-HAADF image in Figure 68c. This selvedge distance is an indication that there is a surface reconstruction at the EG-SiC interface before the intercalation process.

Remarkably, there is a variation of the HAADF intensity at the topmost SiC layer despite the SiC stacking order, as seen in Figure 68d-e. This means that the number of Si atoms in the column of atoms is varying. In other words, this is an indication of the preexistence of silicon vacancies at the topmost SiC layer. The density and location of these Si-vacancies seem random. Nevertheless, at least, an estimation of the Si-vacancy percentage (~19.2%) in the topmost layer may be calculated from the HAADF intensity ratio compared to the pristine SiC intensity. These

observations at the interface should affect the 2D-Ga heterostructure after the intercalation and the performance of the 2D-Ga as a device.

4.10.2. Existence of Si-vacancies prior to intercalation

A controlled electron beam damage experiment (Figure 69) was conducted to test the assumption of preexisted Si-vacancies in the EG substrate. The position is selected from the plasma-treated EG sample, which shows the topmost layer with the same HAADF intensity similar to the bulk SiC, see frame#1 in Figure 69. In this experiment, the electron beam current is adjusted at a 60 e/Å^2/second electron dose rate at 300 keV. Then, a set of 60 images (frames) are acquired at 2048 × 2048 frame size and 0.11Å pixel size at the same electron dose. The beam current is assumed to introduce minimal damage recorded in the images as changes in the atomic structure. The beam damage is accumulated, and its effects on the atomic structure are simultaneously recorded at every frame by both HAADF and BF detectors, as seen in Figure 69. After acquiring all 60 images, Digital micrograph software is used to correct the stage drift and crop an area of interest at the interface.

Mainly, the focus of this study of the beam damage is to look at the structural changes at the topmost SiC layer due to the accumulated beam damage. After acquiring 10 frames, a slight change of the HAADF intensity appears at the topmost SiC layer. This HAADF contrast fading increased when recording frame#28 and beyond. At the end of the experiment, Frame #60 shows an entirely damaged topmost SiC layer and the graphene layer. It is expected that the graphene is damaged at 300 keV because its threshold imaging is around 80 keV in plan view imaging. It is more likely that graphene in cross-section view can survive longer under voltages of more than 80 keV, as noticed in the first 20 frames

in this study. However, the noticeable damage at the topmost SiC layer is unexpected.

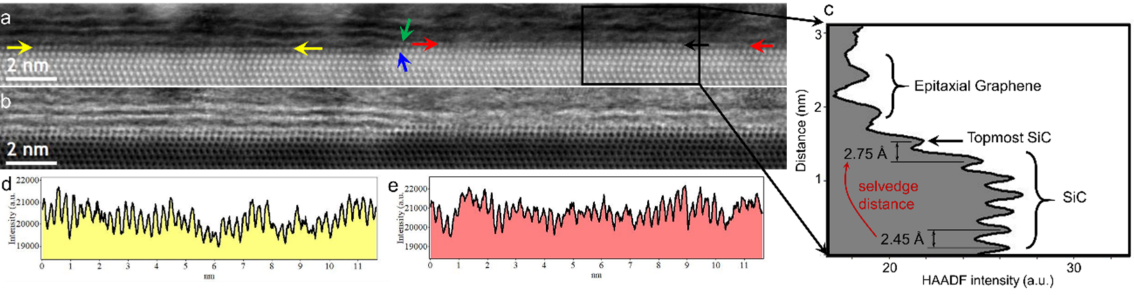

Figure 68. Reconstruction appears on the EG interface before intercalation. (a) Co-located STEM-HAADF, and (b) STEM-BF images of a SiC substrate just before the intercalation process. FIB cross-section is prepared from a sample after both Si-sublimation and plasma treatment processes of the EG. The EG appears in (a and b) to be damaged because of the plasma treatment process. Minor damage may also be introduced because of the electron beam current during imaging. Remarkably, the topmost SiC layer shows lower HAADF intensity than the bulk SiC (c), which indicates a lower number of Si/C atoms/column. Moreover, higher spacing (~2.75 Å) at the topmost layer compared to the deeper SiC spacing (~2.45 Å) indicates a selvedge due to a surface reconstruction at the topmost SiC layer. (d and e) show HAADF intensity profiles from the region indicated between the yellow and red arrows. The number of Si/C atoms/column at the topmost SiC layer is changing from one column of atoms to another.

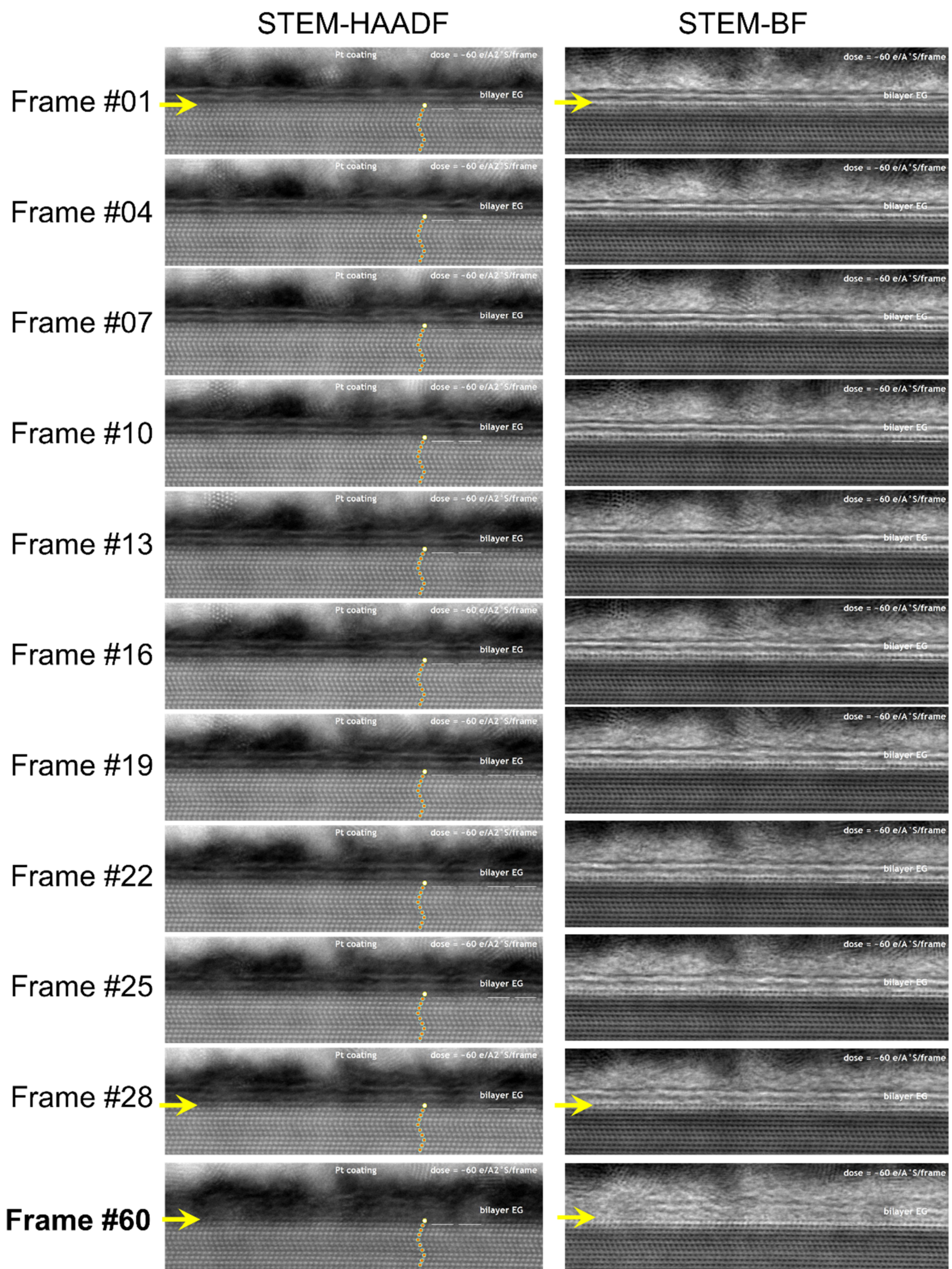

Figure 69. Electron beam damage study of the topmost SiC of EG sample. STEM-HAADF (left) and STEM-BF (right) images were taken at a fixed dose rate of 60 e/Å^2/second at 300 keV at the topmost layer. Minor HAADF intensity changes are present in the first ten frames (see frames #1, 4, 7, and

10). Then, a diminishing of HAADF intensity appears at the topmost SiC layer. This intensity fading incrementally increases until the topmost layer is wholly damaged in frame #60. In this figure, not all the frames are presented. Only ten frames (from #1 to #28) with an increment of 3 are shown, then the last frame is presented. The yellow arrow indicates the topmost SiC layer.

Here, the beam damage experiment informs, qualitatively, that the topmost SiC layer has weaker bonding strength than the bulk SiC row of atoms. This qualitative weaker bonding can be explained due to surface reconstructions, which usually occur at the topmost layers of a substrate. It seems that accumulating more electron dose at the interface leads to broken Si-C or/and Si-Si bonds, which progress to eject Si atoms from the topmost layer of the substrate. This ejection of the Si atoms, *similar to the Si-sublimation at high temperature*, gradually diminishes HAADF intensity because of losing more atoms from the atomic column. Note that the thickness of the sample is around 100 nm (or lower), which means every atom that appears in the cross-section view is about 1000 atoms (or less) in projection.

4.10.3. The reconstructed interface of the as-prepared EG

The STEM imaging and the electron beam damage experiment imply a surface reconstruction at the topmost SiC layer, which results in Si-vacancies before the intercalation process. However, to conclude this, the effect of the plasma process that deliberately damages the EG layers should be avoided. For this reason, another FIB cross-section is prepared from EG before the plasma treatment process. STEM-EELS analysis is conducted at the interface of this sample to understand the bonding at the topmost SiC layer.

In Figure 70, core-loss EELS mappings (acquired by a direct electron detector) of the C-K and Si-L edges are present in red and blue colors, respectively. Noticeably, the C-K edge integration at the topmost layer of the SiC shows higher integration (denser red in Figure 70b) than the bulk SiC layers, which indicates a change of the near-edge fine structure of the C-K edge. Moreover, the topmost SiC layer (and the 2nd topmost layer) showed higher carbon content than silicon Figure 70e. Figure 70f-g shows the spatially resolved EELS spectra of the C-K and Si-L edges to investigate these changes further. Every spectrum is resulted from the averaging of 4-pixel wide of the EELS spectrum (which is 84 pixels in total, each is 0.51 Å) and representing approximately the position of one atomic column. The blue, green, magenta and red highlighted spectra in Figure 70f-g represent the spatial location of the bulk SiC, the topmost SiC, the buffer layer, and the EG layer, respectively. Noticeably, the topmost SiC layer contains the fingerprint of the weakly vdW bonding of the C-K edge, Figure 70h, which means the Si-C covalent bonds at this layer are broken due to a Si-sublimation or a Si-vacancy. Moreover, Si-L at the topmost layer, Figure 70i, shows diminished L-edge peaks, indicating no covalent Si-C bonds compared to the bulk SiC. This EELS result confirms that the EG-SiC interface contains surface reconstruction prior to both plasma treatment and gallium intercalation.

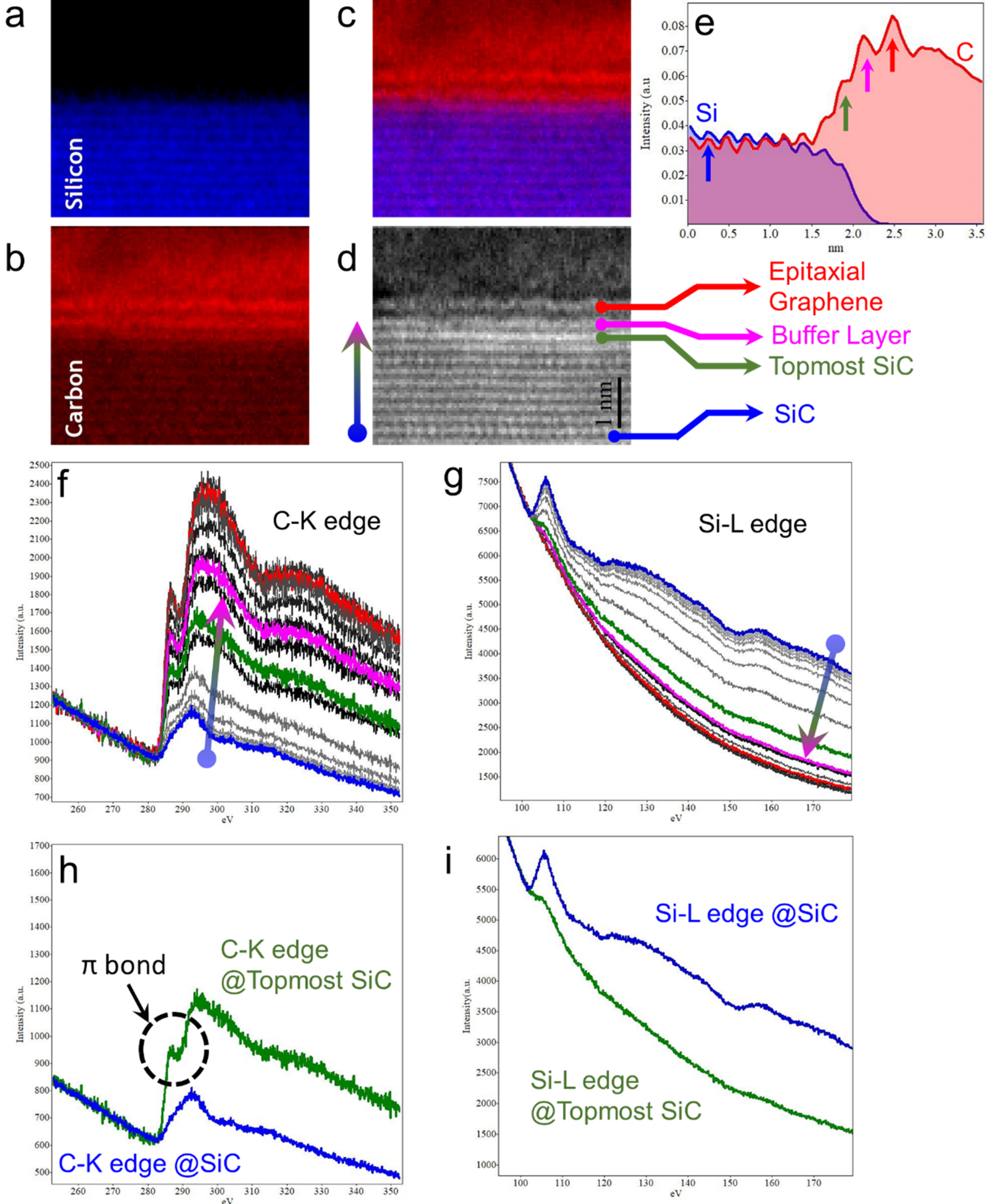

Figure 70. Core-loss EELS of EG shows the reconstructed topmost SiC layer. (a) Si-L and (b) C-K core-loss EELS mapping of the signal integral at the EG interface. (c) composite image of the Si and C maps. (d) EELS spectrum image shows enough atomic resolution to resolve the layers at the interface.

Every pixel in (d) contains an EELS spectrum. (e) Intensity profile, from the composite image in (c), normalized to the SiC regions. (f and g) cascade plots of the C-K and Si-L edges across the interface. Every cascade contains 21 profiles, and each profile results from the averaging of a 4-pixel wide area of the EELS spectrum image in (d). Note that the EELS spectrum image is 84 pixels wide. The blue, green, magenta and red highlighted spectra in (f and g) represent the spatial location of the bulk SiC, the topmost SiC, the buffer layer, and the EG layer, respectively. (h and i) C-K and Si-L edges from the bulk SiC (blue) compared to the topmost SiC (green) regions. Noticeably, the topmost SiC layer contains the C-K edge fingerprint of the weakly vdW bonding, which means the Si-C covalent bonds at this layer are broken, maybe due to a Si-sublimation. Moreover, Si-L at the topmost layer shows diminished L-edge peaks, indicating no covalent Si-C bonds compared to the bulk SiC.

4.10.4. Gallium-filling of Si-vacancies

Previous STEM analyses show that the SiC substrate more likely contains Si-vacancies at the topmost SiC layer. Moreover, the bonding at the SiC interface is more likely weaker than the bulk covalent SiC layer. Now the question is, what happens to this interface when gallium atoms are intercalated? Gallium atoms passivate the dangling bonds at the Si-face SiC interface between the SiC and the buffer layer. That is because the SiC-BL interface is the higher energy interface as previously studied. However, setting a gallium atom on top of a vacancy is not possible. This means the gallium atoms are more likely to fill all Si-vacancies before forming the first intercalated 2D-Ga layer.

Figure 71a-f shows a core-loss EELS investigation at the intercalated 2D-Ga interface. This spectrum image has a 52 x71 size in which each pixel is 0.46 Å. Since the sample is very thin (~ 70 nm thick), the plural scattering in EELS is neglectable. With the benefit of using a direct electron detector, it is remarkably possible to

map the C-K, Ga-L, and Si-K edges at 0.5 eV/channel electron dispersion (185 – 2040 eV window) with sufficient spatial resolution and signal count. Although the Si-K edge is acquired near the end of the spectrum window (at 1839 eV), the Si atom columns are present in the EELS map in Figure 71c as well as the composite profile in Figure 71e. This indicates the spatial precision of the EELS spectrum image. Surprisingly, the lower energy edges (Ga-L and C-K) do not show the exact spatial resolution as silicon in mapping. This may be because real-time electron beam damage and carbon contamination were introduced during the acquired EELS map. This EELS spectrum image is acquired at ~60 e/Å^2/second electron dose rate at 200 keV, which is the same dose rate of one frame in the previous study in Figure 69, which has no significant damage to the EG, SiC even at 300 keV. However, the rastering or imaging interface with a metallic layer seems to be more sensitive. To overcome these damaging effects, the EELS spectrum image is acquired very fast at a rate of 0.005 seconds/pixel, which means the whole spectrum image is only acquired in ~18 seconds. If severe damage is introduced during the acquisition, it should appear in the EELS spectrum image in Figure 71b. Therefore, it may be acceptable to neglect the beam damage at some point for the present data and assume that the damage is locally confined within the spatial size of the pixel (0.46 Å) of the EELS spectrum image.

With this analysis and assumptions, the profile of the composite image (Figure 71e) presents a fair gallium signal co-located with the topmost SiC layer and higher than the Ga-L noise level from the edge mapping. The comparison of the Ga-L edge from the topmost SiC layer and the 2D-Ga layers is shown in Figure 71f and referenced to the noise level in the edge from a deeper SiC bulk region. Besides the EELS mapping, STEM-HAADF intensity in Figure 71g-h may be a direct

investigation of possible gallium in the topmost SiC layer. The imaging current and dwell time are minimized intentionally to avoid introducing electron beam damage. Therefore far, the high-resolution analysis in Figure 71 implies that it is more like for the Si-vacancies to be filled by gallium during intercalation.

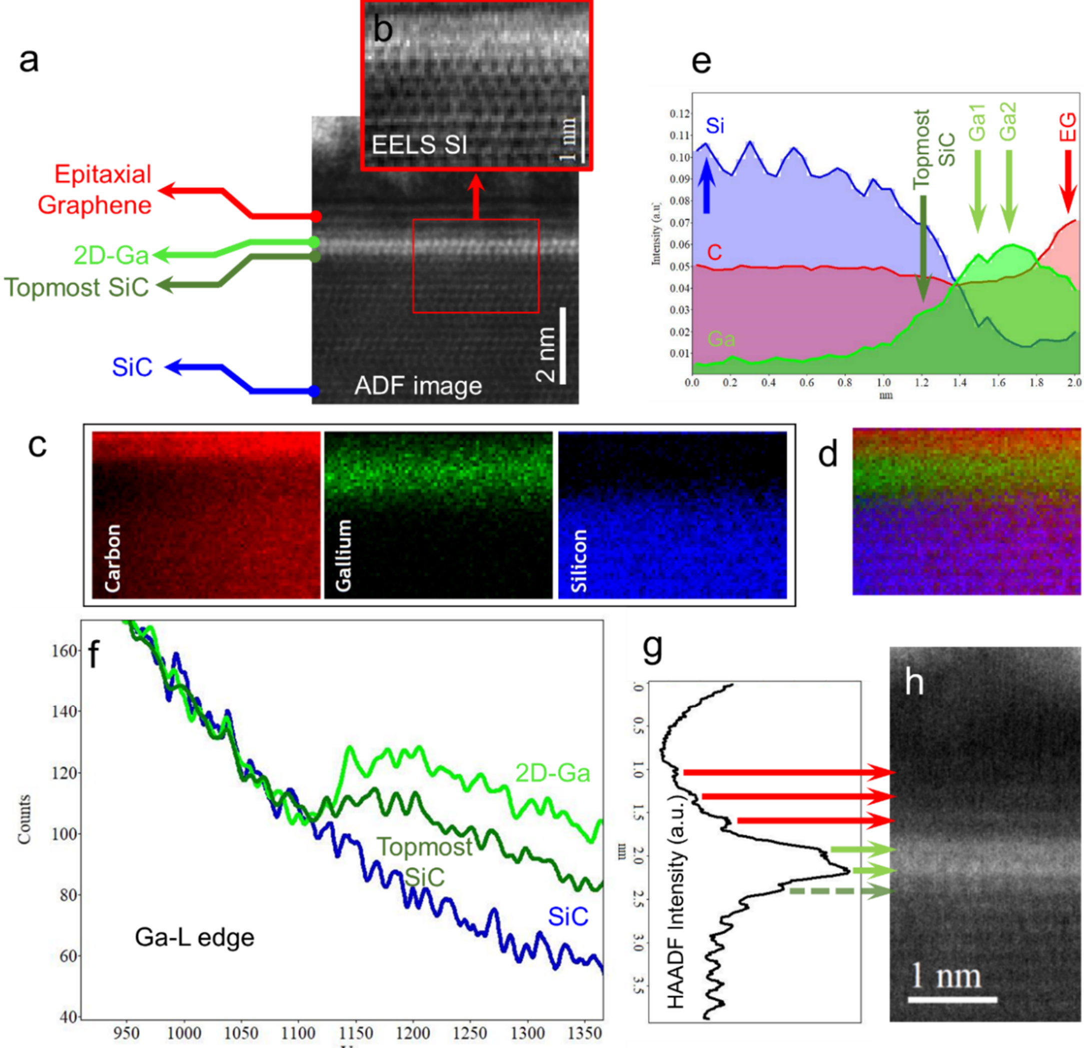

Figure 71. STEM imaging and spectroscopy of gallium filling Si-vacancies. (a) STEM-HAADF image shows the EG-Ga-SiC interface. The topmost SiC layer shows a little higher HAADF intensity than the bulk SiC. (b) EELS spectrum image from the indicated region in (a) by the red box. (c) C-K, Ga-L, and Si-K core-loss EELS maps. (d) composite image of the elemental

maps in (c). (e) intensity profile from (d). (f) focus on the Ga-L edge region at the bulk SiC, topmost SiC, and the 2D-Ga regions. Clearly, the topmost SiC layer contains a gallium signal but is lower than the 2D-Ga region. (g) HAADF intensity profile from (h) shows that the topmost SiC layer has a higher intensity profile compared to the bulk SiC region.

4.10.5. Gallium-discontinuity at 3C-6H stacking order

Another interface question occurs where the SiC-EG interface changes the stacking order, as noticed in the blue and green arrows in Figure 68a. In this sub-section, the stacking order of the SiC is discussed. Moreover, the gallium intercalation across this stacking order change is demonstrated.

4.10.5.1. 6H-SiC versus 3C-SiC stacking order

All SiC samples used in studies of this thesis have a 6H-SiC stacking order. This stacking order is a repeated unit cell of 6 rows of Si-C atoms. In the 6H-SiC stacking, the first 3-layers (named as A^*, B^*, and C^*) of silicon atoms of Si-C facing towards the right direction, then the second 3-layers (named as A, B, and C) have silicon facing to the opposite direction. This combination of polarity shifts produces the remarkable zigzag shape of the 6H-SiC stacking order in the $(11\bar{2}0)$ zone axis view, as seen in Figure 72a. However, it is noticed from STEM investigations of many FIB cross-sections that the EG formation occurs with an inverted stacking when the topmost layer ends with a single (A or B*) layer.

4.10.5.2. Relation of 3C-stacking with the EG growth mechanism

The density of carbon atoms in one graphene layer is approximately equal to the carbon atoms in 3 SiC layers. This ratio is calculated from the relaxed structure provided by our collaborators in Pennsylvania State University to be 3.58, not a

perfect 3, see Figure 72c. This means that the three topmost SiC layers produce only 84% of the total carbon density of one free-standing epitaxial graphene layer. The extra needed carbon atoms may be injected for further Si-sublimation from deeper SiC layers. This may explain why topmost SiC layers are seen in the previous STEM analysis, with Si-vacancies and reconstructed weaker Si-C bonding.

Another interesting point is detecting Si-L EELS signal at the buffer layer; see magenta color in Figure 70g. This may indicate that the 16% of missing carbon atoms are probably filled with Si-dopants during the sublimation process. Ironically, the buffer layer is usually identified in the literature as a carbon-rich layer that is partially attached covalently to the topmost SiC layer. Here, this work may indicate that the origin of the covalent bonds at the SiC-BL interface is from Si-doped atoms in the BL. This doping may explain the unique properties that are tested at the EG/BL/SiC interface, such as ferromagnetism and superconductivity. Still, further EELS and imaging analysis at cryogenic conditions (which is not the current scope of this thesis) are needed to confirm the nature of the BL and topmost SiC layers.

As a result of the mechanism of EG formation (which is a decades-long debate in the literature)[80, 185, 215-217], it seems from this work that a SiC topmost layer ends with the A or B* stacking is more likely to invert to the 3C-SiC stacking (see Figure 72b) as a part of the EG formation itself. Interestingly, the coordinated FIB cross-section with SEM contrast in this thesis enables us to link the 3C-6H transformation to the spatially resolved SEM contrast. Luckily, this transformation results in a new formation of the graphene layer, which can be easily identified as

an extra potential barrier in the SEM image, as dimmer regions than the monolayer EG in the terrace middle regions. Figure 73a shows that the 3C-6H transformation is co-located with the finger shapes inside the SiC terrace. It is understood from SEM images that these fingers represent the initiation of a nascent EG layer, where these fingers are connected later during the growth to form an EG layer.

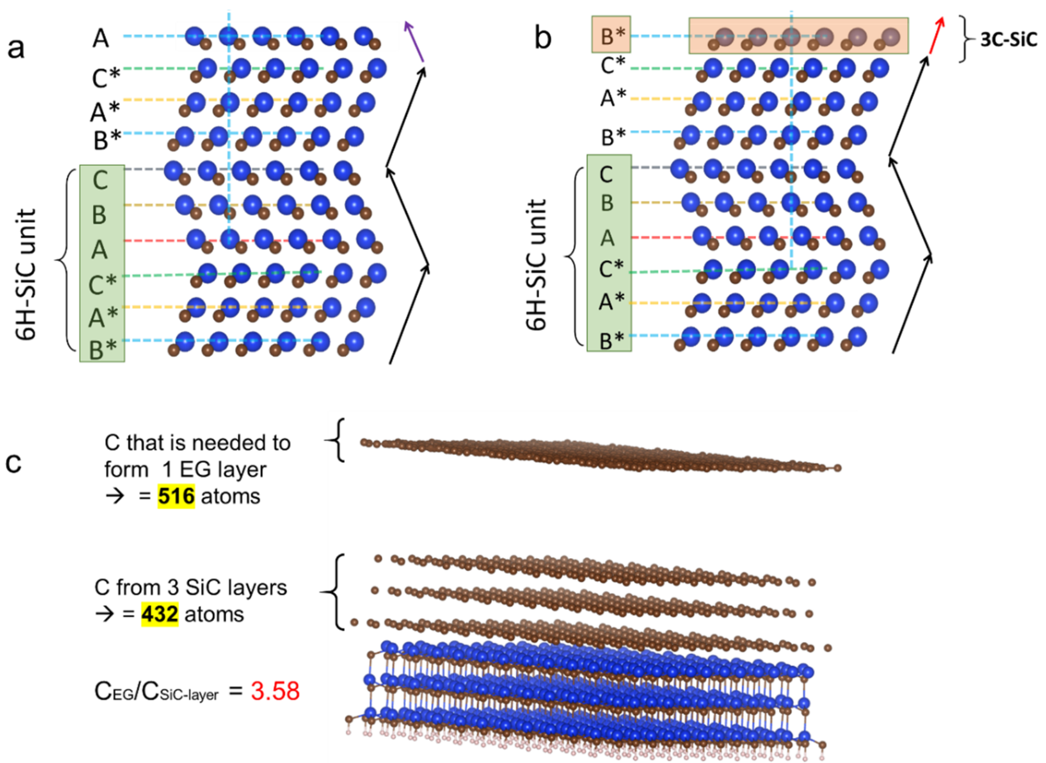

Figure 72. Topmost SiC transformation from 6H to 3C stacking order. (a) 6H-SiC stacking order ends with "A" layer. (b) 3C-SiC stacking transformation of the "A" layer to "B*" as both can be seen in the $(11\bar{2}0)$ zone axis. (c) a comparison of the number of carbon atoms in graphene and SiC layers from a large unit cell of EG/SiC structure. In this unit cell, monolayer graphene contains 516 carbon atoms, while one SiC layer with the same in-plane size contains 144 atoms. This makes the 3 SiC layers (a total of 432 carbon atoms) makes only ~86% of the carbon atoms needed for a fully carbonated graphene layer.

4.10.5.3. Growth of 2D-Ga across 3C-6H stacking order

Figure 73 shows that the pre-existing fingers at the EG terraces are the positions where the SiC stacking order has shifted from 6H to 3C. The 3C-SiC layer in Figure 73b (left) at the EG-SiC interface is connected to the buffer layer (right). Figure 73d shows the same SiC structure after gallium intercalation. The gallium is intercalated below the buffer layer, but it is disconnected at the 3C-6H stacking order transformed position. This means that the intercalated gallium is disconnected from the finger shapes in Figure 73c because of this stacking order transformation. Moreover, a preliminary measurement of stacking angle between the two gallium layers (Ga1-Ga2) shows around ~5° difference across the 3C-6H transformed position, which may be a direct structural impact on the gallium layer because of the stacking order change.

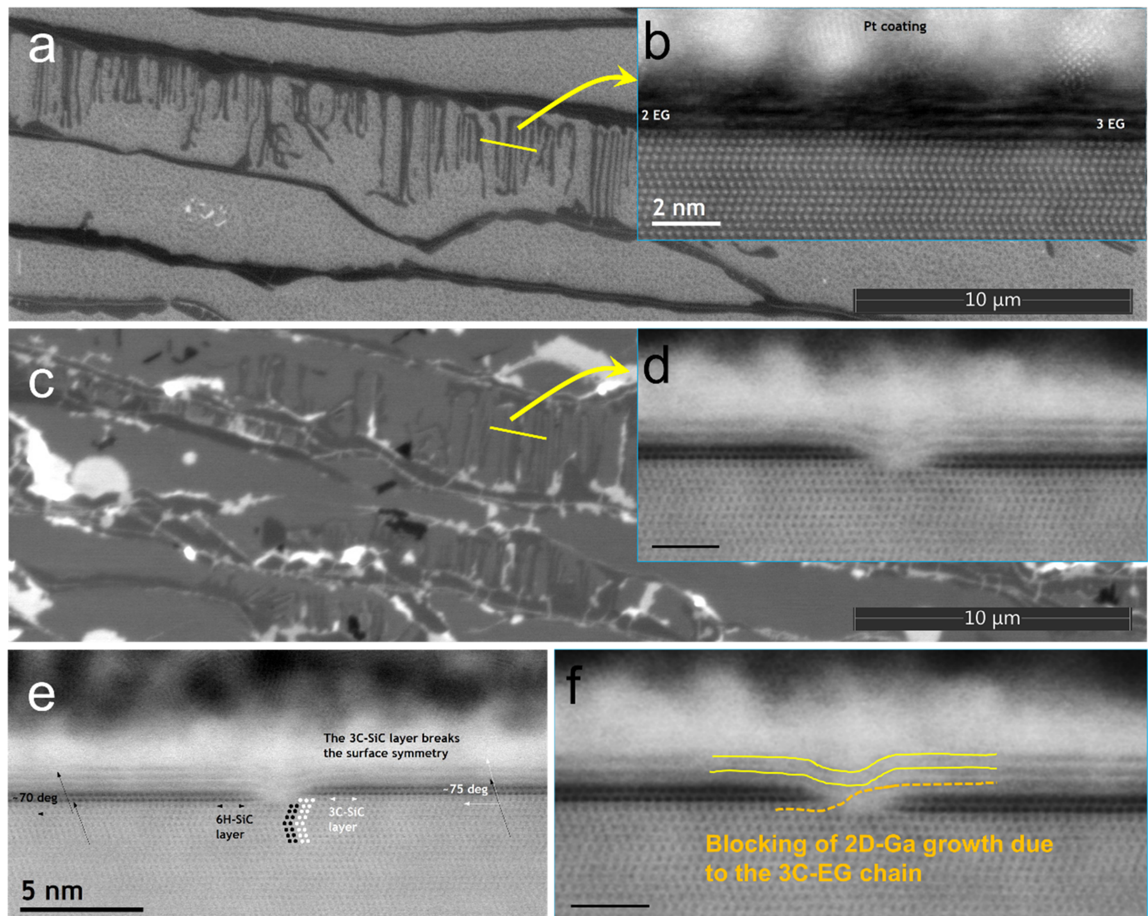

Figure 73. Gallium-discontinuity at 3C-6H stacking order transformation. (a and c) SEM of epitaxial graphene and 2D-Ga samples, respectively. (b and d) STEM-HAADF, and STEM-BF images – taken parallel to the SiC step edges and across the fingers within the terraces – from the epitaxial graphene surface and 2D-Ga sample, respectively. (e) low-magnification image of the Ga intercalation across the 6H-3C stacking order transformation. Preliminary measurements of the Ga1-Ga2 stacking angle show a ~5° (from ~70° to ~75°) difference across the 6H-3C stacking transformation, which adds to the symmetry breaking of the structure at the top gallium layer. (f) higher magnification of the position in (d and e) shows a connection of the 3C layer (left) to the detached BL (right) as indicated with the orange color. This connection blocks the growth of the 2D-Ga along the SiC terrace because it is related to the fingers perpendicular to the step edge. Scale bar in (a and c) is 10 µm. (b), (d and f) have a scale bar of 2 nm. (e) has a scale bar of 5 nm.

4.11. Summary

In summary, the confined gallium layers at the epitaxial graphene on the SiC interface are characterized at different length scales from sub-angstrom surface reconstruction to a few millimeters bulk in densely pixelated SEM. The multi-scale characterization in this chapter establishes the basic understanding of the 2D-Ga coverage percentage, uniformity, and air stability across the SiC terraces. Scanning electron microscopy is sensitive to local surface potential variations, thicknesses of the heterostructures, and their quality, and therefore able to elucidate the scalability and uniformity of 2D-metal heterostructures. Understanding SEM image contrast through correlative electron methods firmly establishes a reliable and fast SEM characterization of 2D-Ga heterostructures. Stitching STEM images over several micrometers demonstrates that the 2D-Ga heterostructure is mostly uniform bilayer Ga covered by bilayer graphene along the middle of the SiC terraces. Moreover, it is shown that, with the method used to prepare our samples, the intercalated Ga covers around 64% over a ~1.5 × 2 mm^2 area near the wafer edge. The surface quality and intercalation percentage increase towards the middle of the wafer. SEM is an affordable, non-destructive, easy-to-use technique for characterizing CHet surfaces.

Using aberration-corrected STEM and many FIB cross-section samples, it is noted that the 2D-Ga structure is not superficial bilayer gallium with a perfect 6H-SiC stacking. The SiC surface terminations vary from terrace to terrace and within the same terrace, including a significant 3C-SiC stacking order transformation on the topmost SiC layer. Accordingly, Si-vacancies are detected in the substrate prior to the intercalation. These vacancies are filled by gallium at the intercalation process.

These interface investigations are essential for any future wafer-scale applications, such as measuring the superconductivity, which can be affected by local variations.

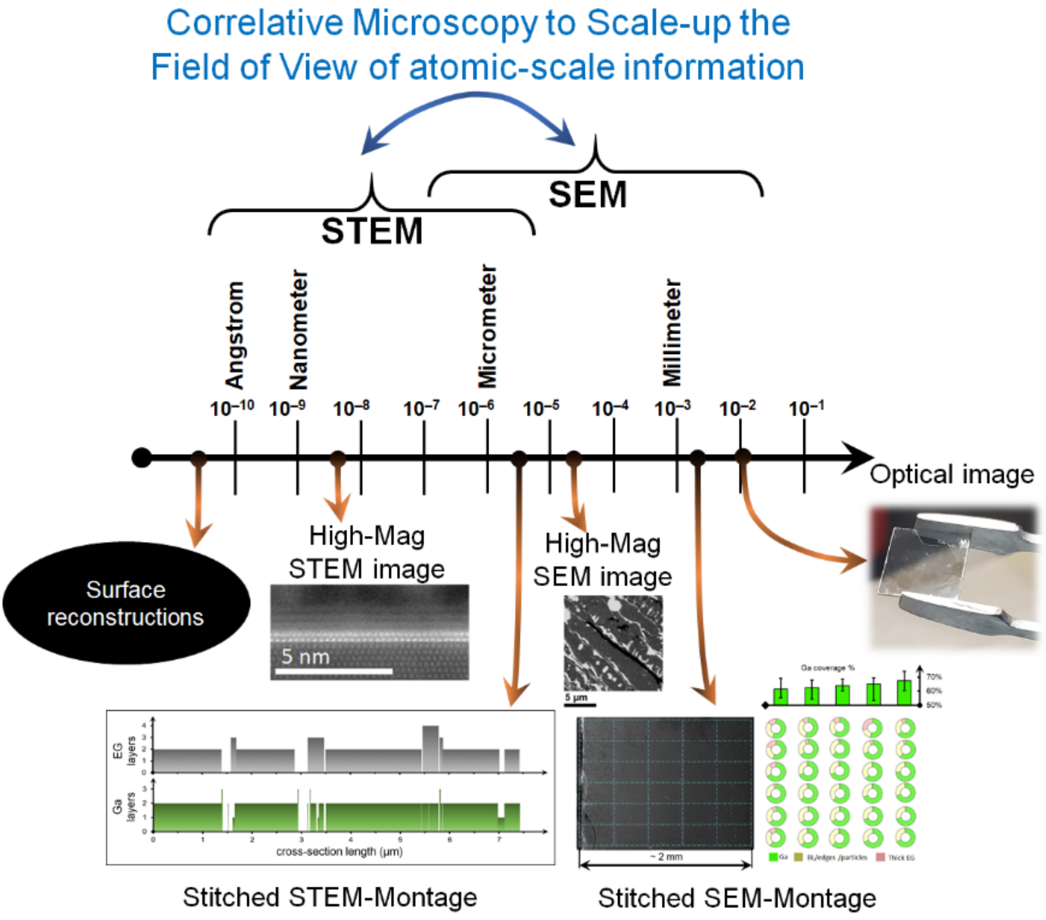

Figure 74. Summary of the multi-scale characterization of 2D Gallium. The STEM and SEM techniques are correlated with multiple correlative microscopy techniques to bring the coverage of gallium and layer thicknesses from the atomic scale to a few millimeters scale. Moreover, SEM imaging and spectroscopy reveal surface reconstruction effects that are linked to stacking order variation, which is also detectable in SEM images.

Chapter 5 Conclusions and Outlook

5.1. Multiscale characterization of CdTe/sapphire interface

Main conclusions

- High-quality CdTe thin film is grown in its (111) direction on the Sapphire (0001) c-plane using a one-step PLD fabrication at 300 °C.
- The relatively low-temperature growth enables a stable, relaxed surface reconstruction at the topmost sapphire layer. These growth conditions allow a unique tellurium buffer layer that is weakly bonded to the sapphire substrate.
- The presence of atomically thin tellurium at the CdTe/sapphire interface allows universal delamination of a few centimeters of CdTe film. Furthermore, the sapphire substrate can be used as a copying machine for further growth after delamination.
- The CdTe film grows with a mismatch-free interface due to the vdW-like bonding thanks to the atomically thin tellurium buffer.
- The tellurium buffer is mainly a monolayer, but thicker layers of bi- and tri-layers are also observed. The tri-layer tellurium may be a stable structure of tellurene which is the 2D form of tellurium.
- The co-located microscopy correlation between SEM and EBSD with STEM techniques enables identifying twin regions from the SEM contrast over a large area.

Future work

- It is more likely that CdTe/sapphire interface generates second harmonic generation (SHG) because the CdTe film grows with a cubic structure over the hexagonal sapphire structure, which breaks the crystal symmetry at the interface.
- Further STEM investigations of the tri-layer tellurium at the interface are highly recommended. The PLD growth system may inject more tellurium at the interface before the cadmium to ensure the formation of a thick tellurium buffer layer. This may lead to a one-step direct growth of the 3D/2D/3D system of CdTe/Tellurene/Sapphire, with confined Tellurene at the interface.
- Fabrication of other chalcogenide-based thin films (such as InSe or InSb) with the same PLD technique will be a recognizable replication of the compliant sapphire-terminated chalcogenide interface.

5.2. Multiscale characterization of 2D-Ga

Main conclusions

- The gallium intercalation of epitaxial graphene results in an epitaxial, air-stable, atomically thin gallium confined at the SiC-epitaxial graphene interface
- Understanding SEM contrast through correlative microscopy methods firmly establishes a reliable and fast characterization of the 2D-Ga heterostructure.

- Utilizing the SEM sensitive to the local surface potential variations, the quality, and thicknesses of this heterostructure can be determined.
- Stitching STEM images over several micrometers demonstrates that the 2D-Ga heterostructure is mostly uniform bilayer Ga covered by bilayer graphene within the middle of the SiC terraces.
- The intercalation of Ga covers 64% on average over a three mm^2 area near the SiC wafer edge. This percentage increases towards the middle of the wafer.

Future works

- Construction of a reliable automated segmentation of SEM images using machine learning algorithms. This will help in the fast identification of the 2D-Ga or other intercalated metals at the SiC-BL interface. Moreover, testing the electron emission from helium ion imaging technique in correlation with the 2D-Ga thicknesses.
- Cryogenic STEM, using a double tilted cryo-TEM holder, can record the local structural changes of SiC reconstructions and the 2D-Ga. Moreover, a cryogenic STEM analysis of the EG interface could lead to a new experimental explanation of the growth mechanism of the EG and the doping/defect nature of the buffer layer. The cryo-STEM could be significantly promising for these delicate interfaces because it significantly avoids the damage contributions from the electron beam.

- Investigating the effect of filling Si-vacancies with gallium atoms on the optical and electronic properties, such as the nonlinear optical response, superconductivity, and epsilon-near-zero behavior.
- The replacement of the SiC substrate with a Si substrate coated with a SiC thin film is future practical work. This integration of the Si/SiC can be implemented in the Si-based industry in which the SiC thin film is further used for growing EG and intercalating gallium (or other metals).

5.3. Common properties of the studied materials

Chapter 3 and Chapter 4 presented two different material systems prepared by two different techniques. We conclude with a summary of the similarities between both systems and interfaces. These similarities raise analogies and significant points, whatever the material systems.

Surface reconstruction effects.
Both CdTe/sapphire and 2D-Ga interfaces show substrate surface reconstruction effects regardless of the growth temperature. These reconstructions result from changing the atomic spacing, weakening the atomic bonds at the topmost layer. This reconstructed spacing is beyond the STEM resolution (for example, 0.1 Å in case of sapphire) of aberration-corrected STEM; however, the impact of this reconstruction on the EELS signal is still detectable with atomically resolved (around 0.5 Å) STEM-EELS mapping. The atomically resolved STEM-EELS edges (such as O-K and C-K) provide the identification peaks of the bonding broken-symmetry at the interface co-located with the atomic layer.

On another thread, surface reconstructions are usually studied with LEED and Xray synchrotron facilities. These studies provide a holistic average signal from a large area, which is sufficient with a homogenous sample. However, non-homogenous surfaces such as SiC may be challenging for these techniques when resolving a few nanometers' reconstructed features with different selvedge depths. This raises the importance of the aberration-corrected STEM-EELS of the cross-section view of these samples that provides direct co-located and atomically-resolved spatial signal correlated to the reconstructed feature.

Tracking local-surface quality by SEM contrast.

SEM sensitivity of local surface potentials enables the identification of the surface quality and visualization of defects in both CdTe/sapphire and 2D-Ga systems. SEM can look at the homogeneity and quality of the CdTe film in a scalable (bulk) manner by identifying the twin boundaries and pits at the surface. Also, the SEM establishes a scalable method to calculate coverage percentage in the bulk of the intercalated gallium at the interface of SiC-EG, thanks to the detachment of the buffer layer. This raises the significance of automation, and metrology is an unexplored area in the manufacture of electronics-grade thin films and 2D materials. This is important for any future wafer-scale conditions with local variations, such as choosing a location to deposit electrodes for superconductivity measurements. Moreover, the understanding of SEM contrast through correlative microcopy is a way to bridge both resolutions- and span length gaps between characterization techniques.

Materials for future electronic applications

Both CdTe film and 2D-Ga are candidates for novel spintronic and topological insulator applications. CdTe can be integrated with other thin films or used as a

substrate for growing films. For example, using CdTe as a substrate for growing HgTe provides a HgTe/CdTe interface that functions as a topological insulator, a heterostructure for low energy computational applications. Such devices may be applied in wearable device applications by transferring the HgTe/CdTe heterostructure to flexible substates.

In the case of 2D-Ga, the controlled oxidation of the metallic gallium to form a structured gallium oxide will provide a 2D dielectric layer confined at the SiC-EG interface. The healed graphene cap may be used as a substrate to grow a 2D transition metal dichalcogenide (TMD), such as tungsten diselenide. These heterostacks may work as a hot-electron transistor. The gallium oxide layer functions as the gate to tune the electron transport through graphene from the source (n-doped SiC) to the collector (a deposited 2D TMD layer).

Appendixes

Appendix 1. Notes on the FIB cross-section preparation.

The commercial Focused Ion beam (FIB) microscopes are dual-beam configuration systems with both the electron beam and ion, see Figure S1. The system is also accompanied by a gas nozzle for depositing purposes in addition to a Tungsten manipulator for lifting out samples. When the sample is at the coincidence height of the ion and electron beams cross-over, the system can provide co-located images of the same size. Moreover, and most importantly, the ion beam can be utilized to mill shapes or trenches deliberately. The dual-beam FIB is a system that can be used for many applications in the fields of materials science and biology. For example, the FIB tomography technique can be used to reconstruct a 3D-tomograph of material heterostructure or complicated biological organisms. Moreover, it can be used to pattern shapes on the surface of a wafer for electronic or optical testing. Nevertheless, here in this thesis work, the FIB is utilized for preparing samples for TEM and STEM characterization following the standard FIB cross-section preparation method.[218]

The standard FIB cross-section preparation steps (Figure S2) are widely used for preparing cross-section samples for TEM and STEM investigations. The advantage of this method is the ability to choose the cross-section in specific orientation as well as specific position from an interesting feature. Before sectioning, a 100 nm protective layer of amorphous carbon is deposited on the regions of interest and direction using the electron beam at 5 keV followed by a 3micrometer Tungsten layer deposited by the ion beam. Then the samples were prepared by performing a standard lift-out procedure and were attached to TEM half grids for tungsten deposition. Then, both sides of the samples were thinned in multiple steps by

lowering the ion beam voltage gradually from 30 kV to 5 kV until the cross-section window appeared transparent in the electron beam image at 5 keV. The sample thickness was measured later in the TEM by low-loss EELS and found to be less than 100 nm.

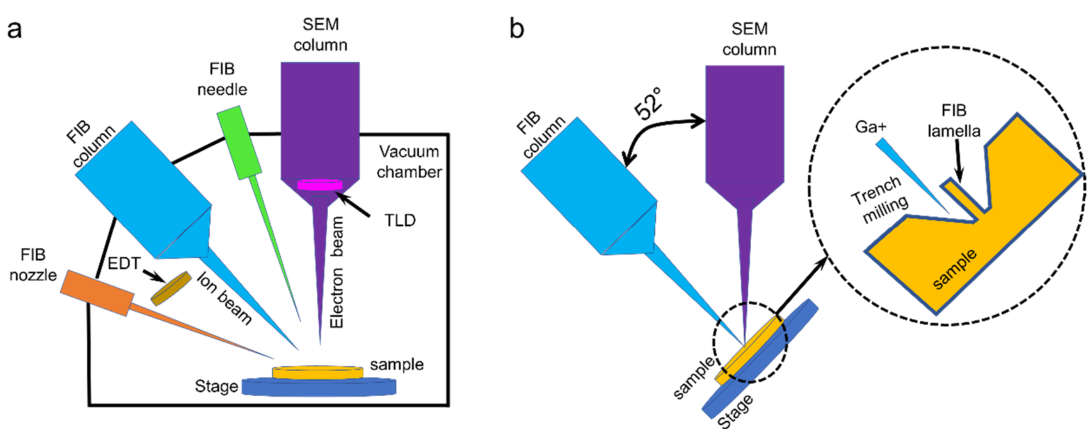

Figure S1. schematic of the FIB microscope. (a) the diagram shows the interaction of the main FIB components (Gas nozzle, manipulator, ion gun, and electron gun) with the sample. (b) the diagram shows the orientation of ion and electron guns related to the sample during the milling trench. The close-up view shows two trenches on both sides of the lamella before lifting it out.

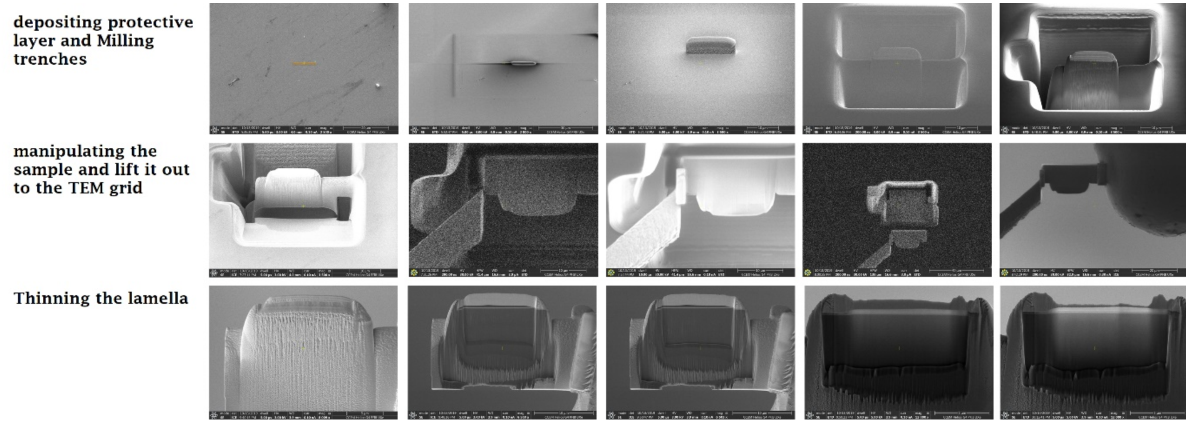

Figure S2. SEM images of the standardized FIB lift-out method. Images are arranged in 3 rows. The direction of the images is from left to right.

Appendix 2. Metamorphic 3D/3D heteroepitaxy interface.

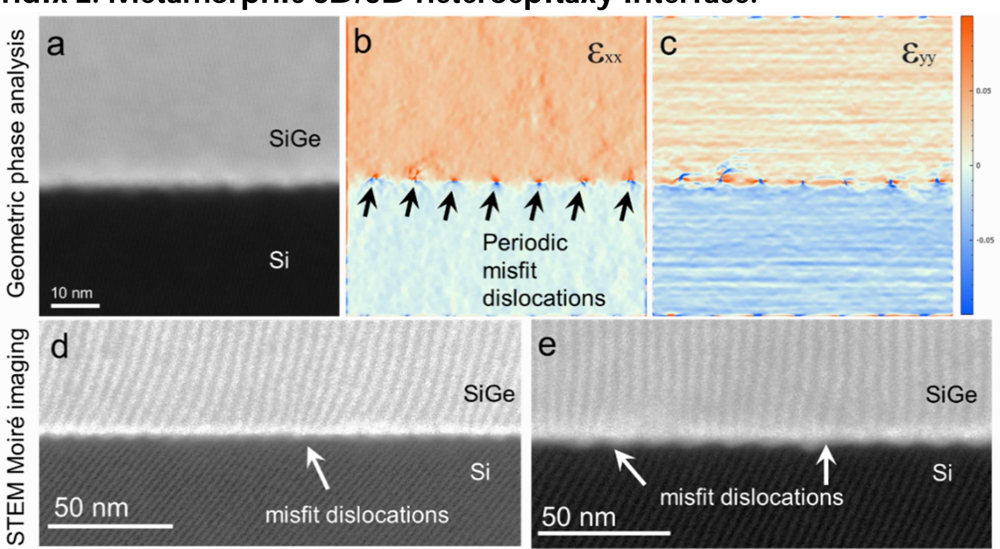

Figure S3. Strain mapping at metamorphic heteroepitaxy interface. (a) STEM-HAADF image of SiGe/Si interface. (b and c) GPA strain mapping in the x and y directions, respectively. (d and e) STEM moiré imaging of the SiGe-Si interface showing a discontinuity of the moiré fringes indicated by the white arrows as an indication of misfit dislocations.

Appendix 3. Photoluminescence (PL) comparison of CdTe films prior and post layer-transfer.

Figure S4 shows PL spectra acquired at ~10 °K for the same CdTe film before and after the delamination from the sapphire substrate. An energy shift to the left and a significant increase of the PL intensity occurs after the CdTe layer transfer. The CdTe/sapphire signal (red curve) has a significantly skewed direction which may indicate an interface inhomogeneity.

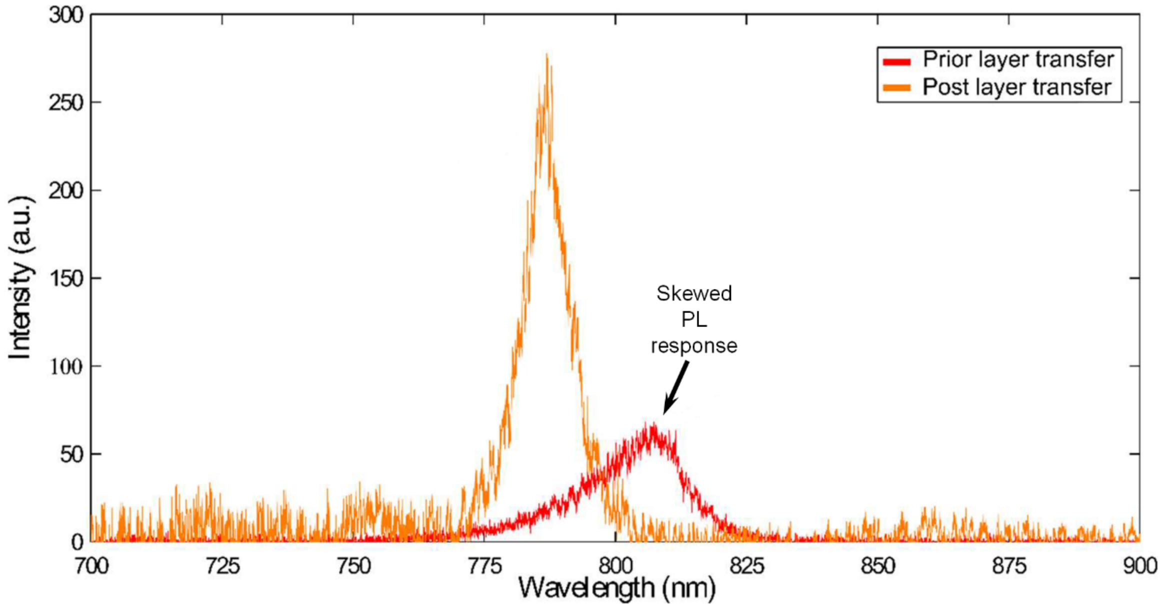

Figure S4. Photoluminescence (PL) comparison of CdTe films prior and post layer-transfer.

Appendix 4. Optimization of SEM acquisition parameters.

5KeV 3KeV 1KeV
0.2 nA
5 µm
0.4 nA
Hard to focus
0.8 nA
1.6 nA
3.2 nA
6.4 nA
Contrast flipping

Figure S5. Current and voltage study of EG. In this image matrix, the SEM images are acquired through lens detector (TLD) at a 3.1 mm working distance, stage at zero-tilt, same magnification of 5KX, and 5 µS dwell time. The low voltage imaging at 1 keV shows contrast flipping, similar to a

previous study conducted on graphene flakes with different dielectric substrates for imaging monolayer graphene.[107] Imaging at both low current and low voltage was challenging to focus. The optimized image contrast is achieved at 5keV and a moderate beam current around 1.6 nA. This result also matches previous results that suggest the optimum imaging voltage for graphene contrast is 5 keV.[107] Imaging at a voltage higher than 5 keV results in beam-induced carbon deposition resulting in contamination of the sample surface.

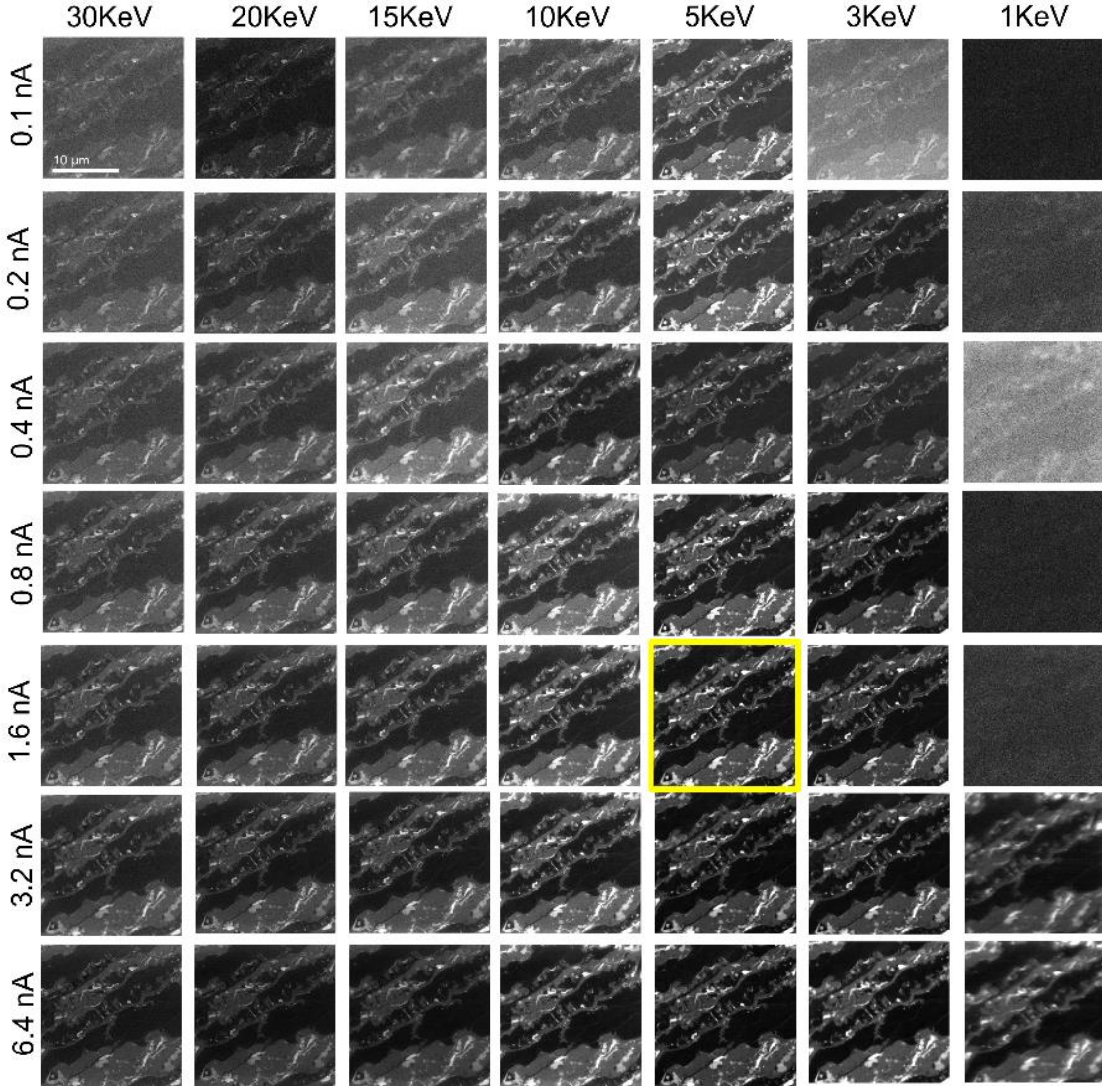

Figure S6. Current and voltage study of 2D Ga. All SEM images are acquired using a through lens detector (TLD) at 4 mm working distance, stage at

zero-tilt, same magnification of 5000X, and 5 μS dwell time. When imaging at 1 keV, it is hard to achieve focus at low currents. It also does not show contrast flipping in contrast to the EG imaging of monolayer EG. This suggests that the graphene on top of the 2D Ga is at least bilayer because the contrast flipping is associated with monolayer graphene. This supports the previous claims that metal intercalation results in detaching the buffer layer used to passivate the Si dangling bonds.[23, 191] We conclude that the optimum imaging conditions are 5 keV and 1.6 nA. Carbon deposition due to the electron beam was limited for the 2D Ga sample in contrast to the EG sample.

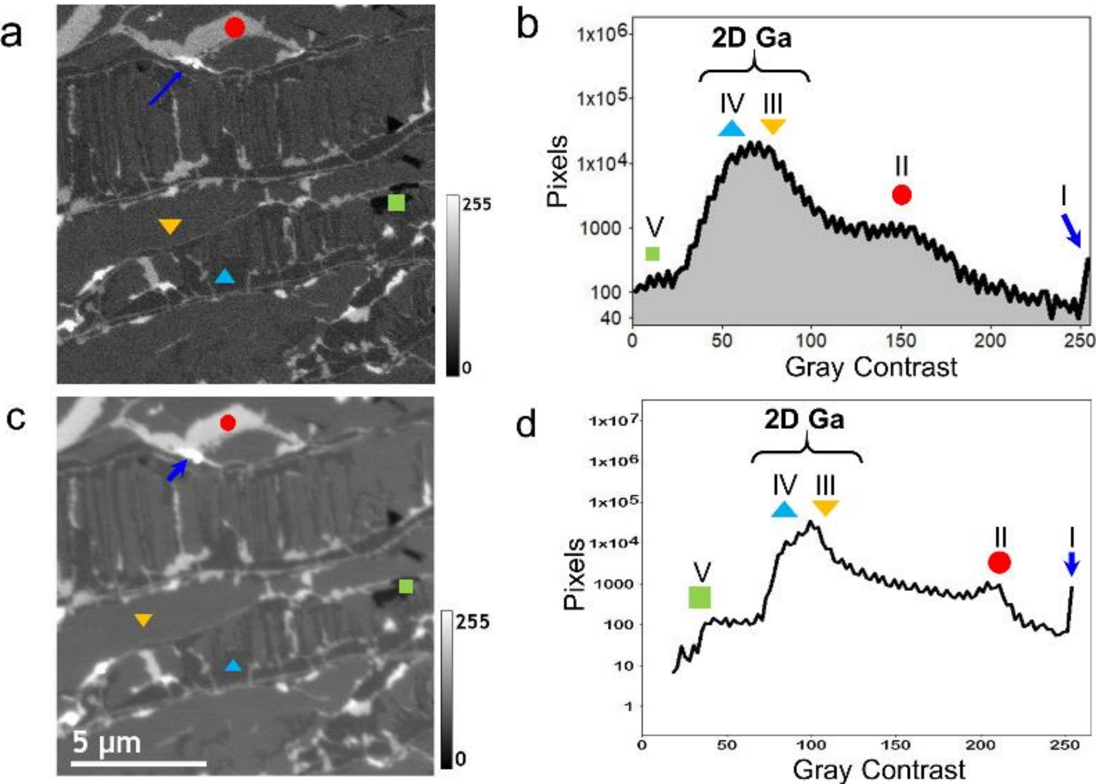

Figure S7. Current effect on histogram peaks. (a and c) images of 2D Ga surface are taken at the same conditions except for the beam current, which is 0.4 nA in (a) and 6.4 nA in (c). (b and d) are the corresponding histogram plots (in Log scale) for (a and c), respectively. The effect of increasing the current sharpens both the SEM image and the histogram peaks (i.e., improving the

signal to noise). Increasing current helps in identifying the peaks in the histogram and thus the image segmentation process.

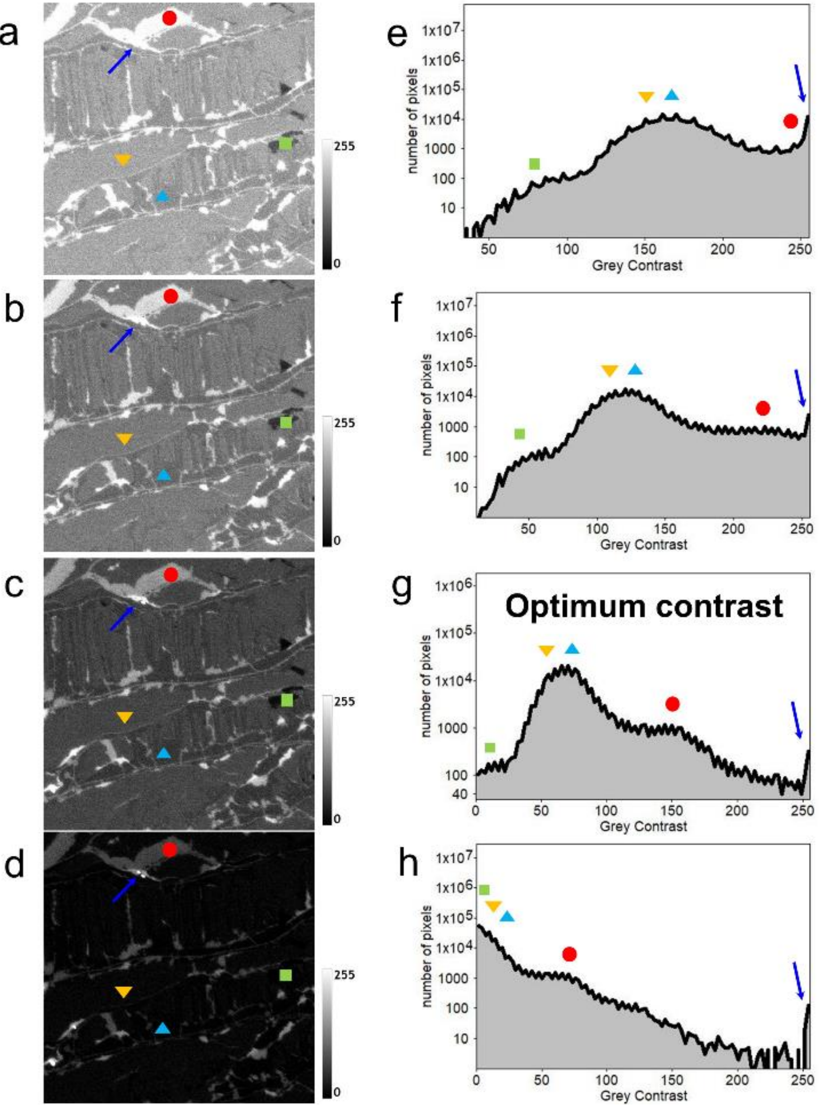

Figure S8. Effect of the contrast adjustment knob in the microscope. All these SEM images (a-d) are taken at 5 keV, 0.4 nA, zero-tilted stage, and 5 µS dwell time. The SEM images are adjusted to the same gray level (scale-bar at the right of the images). (e-h) The corresponding histogram plot of the SEM images in (a-d), respectively. The optimized image and histogram in (c and g) are acquired with the microscope's suggested settings of contrast and brightness. The contrast adjustment effect appears in shifting the histogram peaks to the right (in the case of higher contrast) or to the left (in

the case of lower contrast). To represent all possible peaks of the image, the contrast should be optimized like in the image (c). However, the best visualization of the Ga particles can be achieved at low contrast only. For facilitating easier segmentation of the SEM images, the particle contrast can be merged to the buffer/non-intercalated regions, which both appear bright, as shown in (b).

Appendix 5. DFT calculations of the surface potential of EG and 2D-Ga heterostructures.

A primary unit cell is built based on the 6H-SiC structure plus a buffer layer, EG, or bilayer gallium on the (0001) Si-face. Then, the structures are relaxed to make a self-consistent field (SCF) calculation to generate wave functions. After then, the SCF results are used to calculate the average potential along the z-direction (calculated in a 10,000 grid) for the SiC substrate and the four structures in Figure S9 using the NORM-conservating pseudopotentials software and the PBE function. The average potential is calculated to present the potential at different substrate terminations, which are (i) SiC, (ii) carbon buffer layer, and (iii) bilayer Ga. These calculations present the vdW graphene potential, which influences the SEM contrast as a function of both the substrate and graphene thickness.[107]

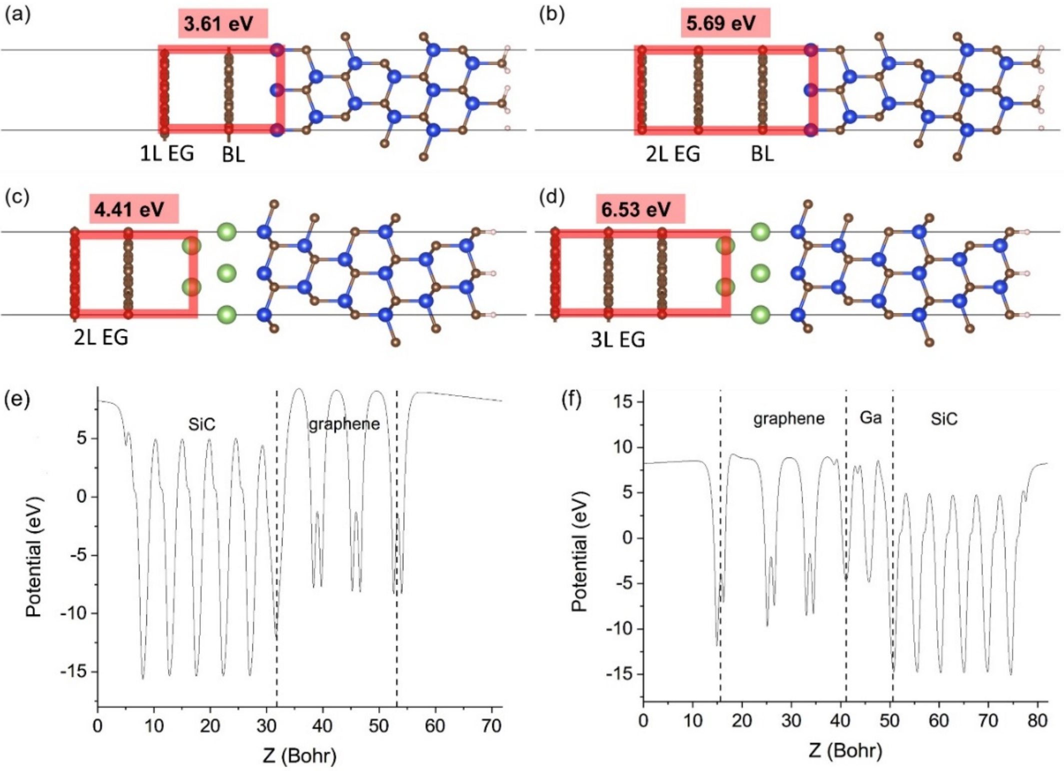

Figure S9. Density functional theory (DFT) calculations of surface potential. (a-d) ball-and-stick model of (a) monolayer EG covers SiC with BL, (b) bilayer EG covers SiC with BL, (c) bilayer EG covers SiC with bilayer Ga, and (d) trilayer EG covers SiC with bilayer Ga. the potential values in (a-d) are calculated using the corresponding averaging windows in red. (e and f) are the as-calculated potential (eV) versus the hetero-stack cross-section (Bohr) for structures in (b and d). Introducing Ga at the interface increases the graphene potentials.

Appendix 6. Thick graphene location correlated to the wafer-scale positions.

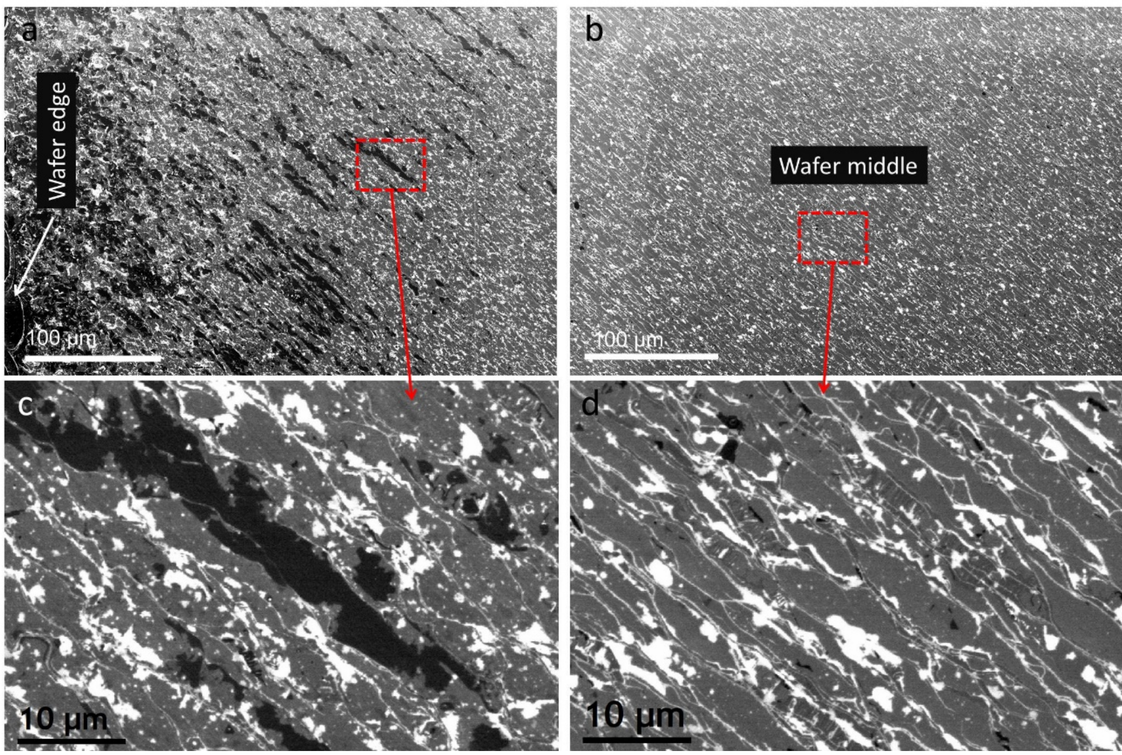

Figure S10. Thick graphene location correlated to the Wafer-scale position. (a and b) low magnification SEM images are taken near the wafer edge and the wafer middle, respectively. (c and d) are close-up views from the indicated red rectangles in (a and b), respectively. Edges of the wafer contain large thick graphene patches that can dominate several SiC terraces. In contrast, the middle of the wafer contains small patches of thick graphene that can be observed only in higher magnification SEM images.

Appendix 7. Correlation between SEM, KPFM, and AES maps.

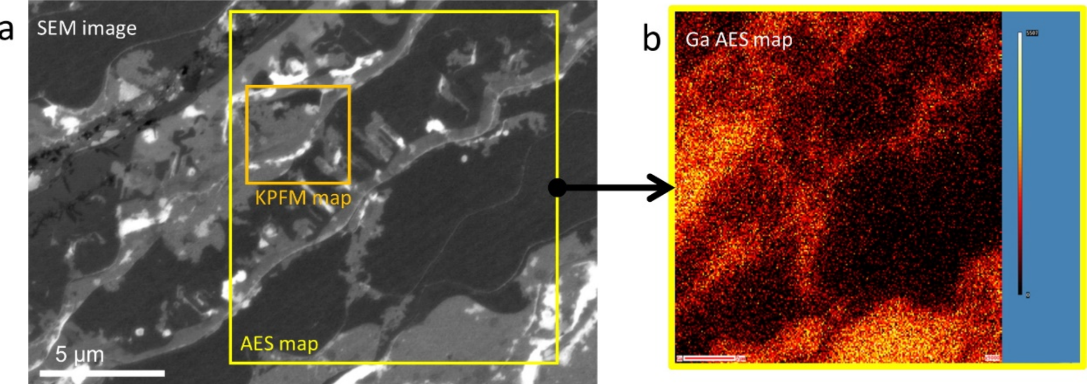

Figure S11. Correlation between SEM, KPFM, and AES maps. (a) SEM image is taken from the position where the KPFM was firstly conducted. The thick graphene patches appear in SEM are because the KPFM is conducted relatively near the wafer edge. Orange and yellow boxes in the SEM image represent the positons the KPFM and AES maps are acquired from, respectively. (b) raw AES map of Ga. The AES map shows a strong correlation with the gray color in the SEM image, which indicates the intercalation positions. In the SEM image, it seems that the intercalation of these areas with thick graphene regions starts from the step bunches towards the middle of the terrace. The saturated dark and bright regions represent contaminations at this particular region of the wafer.

Appendix 8. Deep learning segmentation of CHet 2D-Ga surface.

The SEM segmentation of graphene locations on a copper surface is has been determined unsupervised segmentation with different techniques.[212] The concept of unsupervised segmentation is also introduced for classifying the exfoliated graphene using optical contrast.[213] Here, we test the CHet surface for segmentation by training a neural network for texture-based segmentation using

a random forest algorithm (Figure S12). Although our machine-learned segmentation can identify the Ga heterostructure in the middle of the terraces, it is still challenging to identify the EG fingers near the step edges. This may be further improved by training more extra models at different surface regions.

Segmentation of SEM images in Figure S12 is performed using a random forest method utilizing the segmentation wizard in DragonFly Software 2020.[210, 219] Before the automated segmentation be applied to The 4K images, random three windows of 3:5% of the total area are painted with four label colors representing the main five structures as understood from correlative electron microscopy results. Then, the Labeled windows are used to train a neural network as a backpropagation to improve the weights and biases of the network until the loss function is dropped under 0.1 through at least five epochs. The result in Figure S12 presents poor identification of the EG fingers across the SiC terraces, which may be improved by training more models.

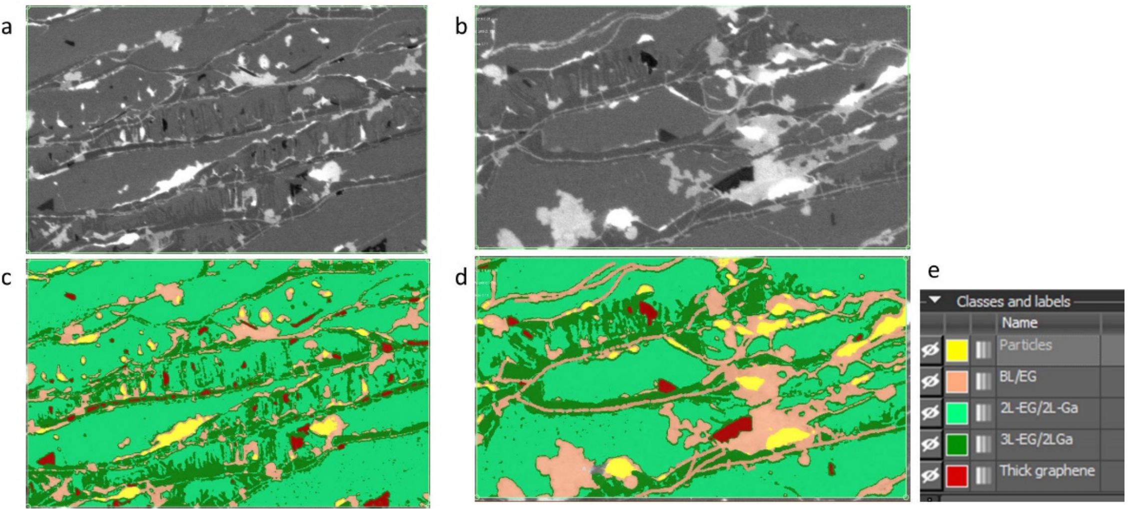

Figure S12. Deep learning segmentation of the 2D ga surface. (a and b) TLD SEM images. (c and d) are the segmentation result after running the

machine learning algorithm with two models. (e) color code for (c and d). The segmentation is performed by DragonFly software.

Appendix 9. Source of possible errors in calculating the gallium coverage.

Although the ga coverage is calculated from the SEM image segmentation, there are some errors associated with the coverage percentage. The following points summarize the sources of error in calculating the ga coverage percentage.

- ***Pixel size limit***: In our work, we used 67.4 nm to reduce the acquisition time to 1 hour approximately for covering ~2×1.5 mm^2 areas near the wafer edge. This reduces the accuracy of the coverage percentage down to the pixel size limit. However, this can be further improved by lowering the pixel size down to the SEM beam size (1-10 nm) at the cost of increased acquisition time.
- ***SEM beam size***: SEM beam size (typically 1-10 nm) varies depending on the instrument and the manufacturer. The size and shape of the beam also depend on the focus and astigmatism, which can be controlled and corrected in any SEM. Recent aberration-corrected SEM microscopes can even reach below 1 nm resolution.
- ***Segmentation limits:*** The segmentation process may significantly affect the calculations of the Ga coverage. This includes the method used for segmentation, threshold identification, and step edge identification. We think that the following two factors can improve the accuracy of the segmentation process:
  a) First, try to increase the SEM image quality itself by increasing the dwell time or the current or the number of pixels per frame.
  b) Second, try to reduce the effect of SEM contamination (carbon deposition) during the acquisition, which needs a fast scan (opposite to the first-mentioned factor a). This effect can be treated

by leveling the SEM contrast by mean plane subtraction, as described in the method section. Moreover, a high chamber vacuum (< 10^{-6} mbar) helps to reduce carbon deposition.

- ***Graphene proximity***: The vdW planar spacing distance between two graphene sheets is about 0.334 nm. This spacing may vary within a specific range of sub-Angstrom orders of magnitude without significantly affecting the SEM contrast. However, in severely reduced graphene quality at some positions, this inter-planar spacing may be changed, which will change the gray levels of the SEM contrast, which could lead to misidentification.
- ***Charging of large particles on the surface***: The nanometer-scale particles are usually particles on the surface associated with the intercalation process (typically Ga and GaO particles). However, some micrometer-scale particles may be formed on the surface due to direct contact with the precursor source. These micrometer-scale particles significantly charge in the SEM and can affect the SEM image quality for segmentation. We recorded one of these particles in the top of frame #4 in Figure 62b. Manual segmentation helps overcome this artifact, but these charging features challenge automated segmentation.
- ***Scratches on the surface***: This could happen during wafer handling with tweezers. We recorded a few scratches in frames #20, #25, and #30 in Figure 62b. These scratches appear as bright contrast and are excluded from the ga coverage calculations.
- ***Wafer edges***: edges of the wafer are usually damaged and exhibit inadequate intercalation coverage depending on this edge's quality.

Appendix 10. Consideration for SEM contrast reproducibility.

SEM contrast for EG or 2D Ga surfaces can be reproduced with different detectors (EDT and TLD) and different SEM instruments from different manufacturers, which is discussed in the experimental section.

For example, SEM images in Figure 47, Figure 60, Figure 54, and Figure 57 are taken with the TLD in an FEI Helios G4 PFIB microscope at 5 keV and 1.6 nA. The SEM image in Figure 50 is taken by the EDT in the JEOL JAMP-9500F AES system. The SEM images in Figure 66 are taken using a Zeiss field-emission scanning electron microscope (SEM).

This reproducibility is essential for characterization by laboratories that can not afford expensive techniques like aberration-corrected TEM/STEM or AES microscopes. With SEM contrast analysis, the fabrication of the CHet 2D materials can be expanded to many labs across the world because SEM can be found in most universities and industrial laboratories.

To reproduce the SEM contrast of this work for the EG and 2D Ga surfaces, we recommend considering the following acquisition parameters

- Stage tilt: zero.
- Beam current of 0.8–1.6 nA, and voltage 3–5 keV.
- Dwell time of 5 microseconds or higher.
- Chamber vacuum in the 10^{-6} mbar order of magnitude.
- Adjust the working distance depending on the detector being used, as explained in Figure 52
- Use conductive carbon tape to hold the wafer on the SEM stub.

Microscopy art

Throughout hundreds of microscopy hours to explore the nanoscale features, the author recognized many features that may have an artistic scene besides science.

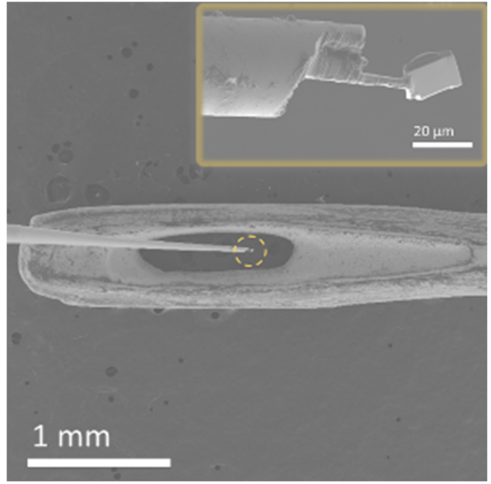

FIB sample in a sewing needle

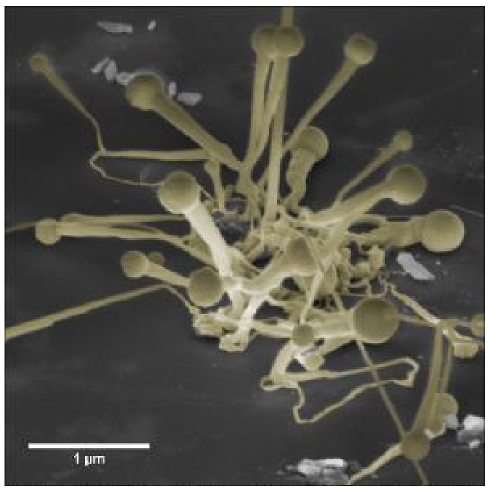

Enoki Mushroom

Ferrier Roche

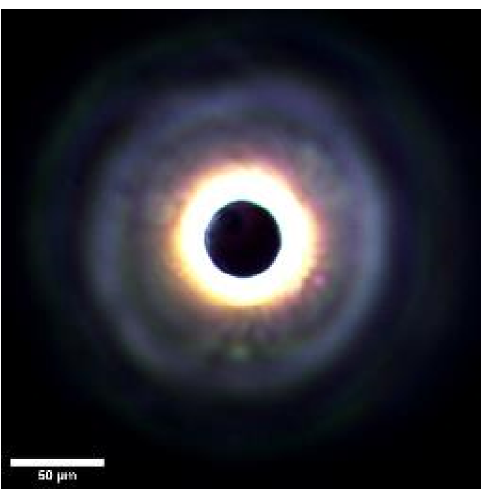

Blackhole

Bibliography

1. Jovanovic, S. M.; El-Sherif, H. M.; Bassim, N. D.; Preston, J. S., Spontaneous Relaxation of Heteroepitaxial Thin Films by van der Waals-Like Bonding on Te-Terminated Sapphire Substrates. *Small* **2020,** 16, (45), e2004437.

2. El-Sherif, H.; Jovanovic, S.; Preston, J.; Basim, N., Electron Microscopy and Interface Plasmons Characterization of Cadmium Telluride Thin Film Grown Incommensurately with Weak Bonding on Sapphire. *Microsc. microanal.* **2020,** 26, (S2), 3116-3118.

3. El-Sherif, H.; Briggs, N.; Robinson, J.; Bassim, N., Correlative Electron Microscopy Enables Scalable Characterization of 2D half-van der Waals Heterostructures. *Microsc. microanal.* **2021,** 27, (S1), 636-638.

4. Splendiani, A.; Sun, L.; Zhang, Y.; Li, T.; Kim, J.; Chim, C.-Y.; Galli, G.; Wang, F., Emerging photoluminescence in monolayer MoS2. *Nano Lett.* **2010,** 10, (4), 1271-1275.

5. Novoselov, K.; Mishchenko, A.; Carvalho, A.; Neto, A. C., 2D materials and van der Waals heterostructures. *Science* **2016,** 353, (6298), aac9439.

6. Cavin, R. K.; Lugli, P.; Zhirnov, V. V., Science and Engineering Beyond Moore's Law. *Proceedings of the IEEE* **2012,** 100, (Special Centenni), 1720-1749.

7. Collaert, N. In *1.3 Future Scaling: Where Systems and Technology Meet*, 2020 IEEE International Solid- State Circuits Conference - (ISSCC), 2020-02-01, 2020; IEEE: 2020.

8. Kozhakhmetov, A.; Nasr, J. R.; Zhang, F.; Xu, K.; Briggs, N. C.; Addou, R.; Wallace, R.; Fullerton-Shirey, S. K.; Terrones, M.; Das, S.; Robinson, J. A., Scalable BEOL compatible 2D tungsten diselenide. *2D Mater.* **2020,** 7, (1), 8.

9. Novoselov, K. S.; Geim, A. K.; Morozov, S. V.; Jiang, D.; Zhang, Y.; Dubonos, S. V.; Grigorieva, I. V.; Firsov, A. A., Electric Field Effect in Atomically Thin Carbon Films. *Science* **2004,** 306, (5696), 666-669.

10. Capasso, A.; Del Rio Castillo, A. E.; Sun, H.; Ansaldo, A.; Pellegrini, V.; Bonaccorso, F., Ink-jet printing of graphene for flexible electronics: An

environmentally-friendly approach. *Solid State Communications* **2015,** 224, 53-63.

11. Low, C. T. J.; Walsh, F. C.; Chakrabarti, M. H.; Hashim, M. A.; Hussain, M. A., Electrochemical approaches to the production of graphene flakes and their potential applications. *Carbon* **2013,** 54, 1-21.

12. Li, X.; Cai, W.; An, J.; Kim, S.; Nah, J.; Yang, D.; Piner, R.; Velamakanni, A.; Jung, I.; Tutuc, E.; Banerjee, S. K.; Colombo, L.; Ruoff, R. S., Large-Area Synthesis of High-Quality and Uniform Graphene Films on Copper Foils. *Science* **2009,** 324, (5932), 1312-1314.

13. Emtsev, K. V.; Speck, F.; Seyller, T.; Ley, L.; Riley, J. D., Interaction, growth, and ordering of epitaxial graphene on SiC{0001} surfaces: A comparative photoelectron spectroscopy study. *Physical Review B* **2008,** 77, (15).

14. Riedl, C.; Starke, U.; Bernhardt, J.; Franke, M.; Heinz, K., Structural properties of the graphene-SiC(0001) interface as a key for the preparation of homogeneous large-terrace graphene surfaces. *Physical Review B* **2007,** 76, (24), 8.

15. Mounet, N.; Gibertini, M.; Schwaller, P.; Campi, D.; Merkys, A.; Marrazzo, A.; Sohier, T.; Castelli, I. E.; Cepellotti, A.; Pizzi, G.; Marzari, N., Two-dimensional materials from high-throughput computational exfoliation of experimentally known compounds. *Nat Nanotechnol* **2018,** 13, (3), 246-252.

16. Stehle, Y.; Meyer, H. M.; Unocic, R. R.; Kidder, M.; Polizos, G.; Datskos, P. G.; Jackson, R.; Smirnov, S. N.; Vlassiouk, I. V., Synthesis of Hexagonal Boron Nitride Monolayer: Control of Nucleation and Crystal Morphology. *Chemistry of Materials* **2015,** 27, (23), 8041-8047.

17. Herrmann, C.; Omelchenko, P.; Kavanagh, K. L., Growth of h-BN on copper (110) in a LEEM. *Surface Science* **2018,** 669, 133-139.

18. Li, L.; Yu, Y.; Ye, G. J.; Ge, Q.; Ou, X.; Wu, H.; Feng, D.; Chen, X. H.; Zhang, Y., Black phosphorus field-effect transistors. *Nature Nanotechnology* **2014,** 9, (5), 372-377.

19. Kou, L.; Chen, C.; Smith, S. C., Phosphorene: Fabrication, Properties, and Applications. *The Journal of Physical Chemistry Letters* **2015,** 6, (14), 2794-2805.

20. Huang, X.; Guan, J.; Lin, Z.; Liu, B.; Xing, S.; Wang, W.; Guo, J., Epitaxial Growth and Band Structure of Te Film on Graphene. *Nano Letters* **2017,** 17, (8), 4619-4623.

21. Shi, Z.; Cao, R.; Khan, K.; Tareen, A. K.; Liu, X.; Liang, W.; Zhang, Y.; Ma, C.; Guo, Z.; Luo, X.; Zhang, H., Two-Dimensional Tellurium: Progress, Challenges, and Prospects. *Nano-Micro Letters* **2020,** 12, (1).

22. Yoon, Y.; Ganapathi, K.; Salahuddin, S., How Good Can Monolayer MoS2Transistors Be? *Nano Letters* **2011,** 11, (9), 3768-3773.

23. Briggs, N.; Bersch, B.; Wang, Y.; Jiang, J.; Koch, R. J.; Nayir, N.; Wang, K.; Kolmer, M.; Ko, W.; De La Fuente Duran, A.; Subramanian, S.; Dong, C.; Shallenberger, J.; Fu, M.; Zou, Q.; Chuang, Y. W.; Gai, Z.; Li, A. P.; Bostwick, A.; Jozwiak, C.; Chang, C. Z.; Rotenberg, E.; Zhu, J.; van Duin, A. C. T.; Crespi, V.; Robinson, J. A., Atomically thin half-van der Waals metals enabled by confinement heteroepitaxy. *Nature Materials* **2020,** 19, (6), 637-643.

24. Al Balushi, Z. Y.; Wang, K.; Ghosh, R. K.; Vila, R. A.; Eichfeld, S. M.; Caldwell, J. D.; Qin, X. Y.; Lin, Y. C.; DeSario, P. A.; Stone, G.; Subramanian, S.; Paul, D. F.; Wallace, R. M.; Datta, S.; Redwing, J. M.; Robinson, J. A., Two-dimensional gallium nitride realized via graphene encapsulation. *Nature Materials* **2016,** 15, (11), 1166-1171.

25. Guo, H. W.; Hu, Z.; Liu, Z. B.; Tian, J. G., Stacking of 2D Materials. *Advanced Functional Materials* **2021,** 31, (4), 2007810.

26. Novoselov, K. S.; Mishchenko, A.; Carvalho, A.; Castro Neto, A. H., 2D materials and van der Waals heterostructures. *Science* **2016,** 353, (6298), aac9439.

27. Onodera, M.; Masubuchi, S.; Moriya, R.; Machida, T., Assembly of van der Waals heterostructures: exfoliation, searching, and stacking of 2D materials. *Japanese Journal of Applied Physics* **2020,** 59, (1), 010101.

28. Novoselov, K. S.; Mishchenko, A.; Carvalho, A.; Neto, A. H. C., 2D materials and van der Waals heterostructures. *Science* **2016,** 353, (6298).

29. Deng, D. H.; Novoselov, K. S.; Fu, Q.; Zheng, N. F.; Tian, Z. Q.; Bao, X. H., Catalysis with two-dimensional materials and their heterostructures. *Nature Nanotechnology* **2016,** 11, (3), 218-230.

30. Geim, A. K.; Grigorieva, I. V., Van der Waals heterostructures. *Nature* **2013,** 499, (7459), 419-425.

31. Duan, X.; Wang, C.; Pan, A.; Yu, R.; Duan, X., Two-dimensional transition metal dichalcogenides as atomically thin semiconductors: opportunities and challenges. *Chemical Society Reviews* **2015,** 44, (24), 8859-8876.

32. Liu, Y.; Weiss, N. O.; Duan, X.; Cheng, H.-C.; Huang, Y.; Duan, X., Van der Waals heterostructures and devices. *Nature Reviews Materials* **2016,** 1, (9), 16042.

33. Biro, L. P.; Lambin, P., Grain boundaries in graphene grown by chemical vapor deposition. *New J Phys* **2013,** 15.

34. Huang, P. Y.; Ruiz-Vargas, C. S.; van der Zande, A. M.; Whitney, W. S.; Levendorf, M. P.; Kevek, J. W.; Garg, S.; Alden, J. S.; Hustedt, C. J.; Zhu, Y.; Park, J.; McEuen, P. L.; Muller, D. A., Grains and grain boundaries in single-layer graphene atomic patchwork quilts. *Nature* **2011,** 469, (7330), 389-+.

35. Nie, C. B.; Yu, L. Y.; Wei, X. Z.; Shen, J.; Lu, W. Q.; Chen, W. M.; Feng, S. L.; Shi, H. F., Ultrafast growth of large-area monolayer MoS2. film via gold foil assistant CVD for a. highly. sensitive photodetector. *Nanotechnology* **2017,** 28, (27).

36. Jeon, J.; Jang, S. K.; Jeon, S. M.; Yoo, G.; Jang, Y. H.; Park, J. H.; Lee, S., Layer-controlled CVD growth of large-area two-dimensional MoS2 films. *Nanoscale* **2015,** 7, (5), 1688-1695.

37. Ghosh, S.; Najmaei, S.; Kar, S.; Vajtai, R.; Lou, J.; Pradhan, N. R.; Balicas, L.; Ajayan, P. M.; Talapatra, S., Universal ac conduction in large area atomic layers of CVD-grown MoS2. *Phys Rev B* **2014,** 89, (12).

38. Shi, T.; Walker, R. C.; Jovanovic, I.; Robinson, J. A., Effects of energetic ion irradiation on WSe2/SiC heterostructures. *Sci Rep* **2017,** 7, 9.

39. Eichfeld, S. M.; Colon, V. O.; Nie, Y. F.; Cho, K.; Robinson, J. A., Controlling nucleation of monolayer WSe2 during metal-organic chemical vapor deposition growth. *2D Mater.* **2016,** 3, (2), 6.

40. de la Barrera, S. C.; Lin, Y. C.; Eichfeld, S. M.; Robinson, J. A.; Gao, Q.; Widom, M.; Feenstra, R. M., Thickness characterization of atomically thin WSe2 on

epitaxial graphene by low-energy electron reflectivity oscillations. *J. Vac. Sci. Technol. B* **2016,** 34, (4), 8.

41. Bhimanapati, G. R.; Hankins, T.; Lei, Y.; Vila, R. A.; Fuller, I.; Terrones, M.; Robinson, J. A., Growth and Tunable Surface Wettability of Vertical MoS2 Layers for Improved Hydrogen Evolution Reactions. *ACS Appl. Mater. Interfaces* **2016,** 8, (34), 22190-22195.

42. Vogel, E. M.; Robinson, J. A., Two-dimensional layered transition-metal dichalcogenides for versatile properties and applications. *MRS Bull.* **2015,** 40, (7), 558-563.

43. Davies, A.; Albar, J. D.; Summerfield, A.; Thomas, J. C.; Cheng, T. S.; Korolkov, V. V.; Stapleton, E.; Wrigley, J.; Goodey, N. L.; Mellor, C. J.; Khlobystov, A. N.; Watanabe, K.; Taniguchi, T.; Foxon, C. T.; Eaves, L.; Novikov, S. V.; Beton, P. H., Lattice-Matched Epitaxial Graphene Grown on Boron Nitride. *Nano Letters* **2018,** 18, (1), 498-504.

44. Liu, H. F.; Chi, D. Z., Dispersive growth and laser-induced rippling of large-area singlelayer MoS2 nanosheets by CVD on c-plane sapphire substrate. *Sci Rep-Uk* **2015,** 5.

45. Ohring, M., Chapter 8-Epitaxy. *Materials Science of Thin Films* **2002**, 417-494.

46. Bae, S.-H.; Kum, H.; Kong, W.; Kim, Y.; Choi, C.; Lee, B.; Lin, P.; Park, Y.; Kim, J., Integration of bulk materials with two-dimensional materials for physical coupling and applications. *Nature Materials* **2019,** 18, (6), 550-560.

47. Al Balushi, Z. Y.; Miyagi, T.; Lin, Y. C.; Wang, K.; Calderin, L.; Bhimanapati, G.; Redwing, J. M.; Robinson, J. A., The impact of graphene properties on GaN and AlN nucleation. *Surf. Sci.* **2015,** 634, 81-88.

48. Hull, R.; Bean, J. C., Misfit dislocations in lattice-mismatched epitaxial films. *Critical Reviews in Solid State and Materials Sciences* **1992,** 17, (6), 507-546.

49. Azizi, A.; Eichfeld, S.; Geschwind, G.; Zhang, K. H.; Jiang, B.; Mukherjee, D.; Hossain, L.; Piasecki, A. F.; Kabius, B.; Robinson, J. A.; Alem, N., Freestanding van der Waals Heterostructures of Graphene and Transition Metal Dichalcogenides. *ACS Nano* **2015,** 9, (5), 4882-4890.

50. Kim, Y.; Cruz, S. S.; Lee, K.; Alawode, B. O.; Choi, C.; Song, Y.; Johnson, J. M.; Heidelberger, C.; Kong, W.; Choi, S.; Qiao, K.; Almansouri, I.; Fitzgerald, E. A.; Kong, J.; Kolpak, A. M.; Hwang, J.; Kim, J., Remote epitaxy through graphene enables two-dimensional material-based layer transfer. *Nature* **2017,** 544, (7650), 340-343.

51. Wang, X.; Weng, Q. H.; Yang, Y. J.; Bando, Y.; Gotberg, D., Hybrid two-dimensional materials in rechargeable battery applications and their microscopic mechanisms. *Chem Soc Rev* **2016,** 45, (15), 4042-4073.

52. Ohring, M., Substrate surfaces and thin-film nucleation. *Materials Science of Thin Films: Deposition & Structure* **2002,** 2, 357-415.

53. Riedl, C.; Bernhardt, J.; Heinz, K.; Starke, U., Evolution and Structure of Graphene Layers on SiC(0001). In *Silicon Carbide and Related Materials 2007, Pts 1 and 2*, Suzuki, A.; Okumura, H.; Kimoto, T.; Fuyuki, T.; Fukuda, K.; Nishizawa, S., Eds. Trans Tech Publications Ltd: Durnten-Zurich, 2009; Vol. 600-603, pp 563-566.

54. Riedl, C.; Coletti, C.; Starke, U., Structural and electronic properties of epitaxial graphene on SiC(0 0 0 1): a review of growth, characterization, transfer doping and hydrogen intercalation. *J. Phys. D-Appl. Phys.* **2010,** 43, (37), 17.

55. Kim, H.; Lu, K.; Liu, Y.; Kum, H. S.; Kim, K. S.; Qiao, K.; Bae, S.-H.; Lee, S.; Ji, Y. J.; Kim, K. H.; Paik, H.; Xie, S.; Shin, H.; Choi, C.; Lee, J. H.; Dong, C.; Robinson, J. A.; Lee, J.-H.; Ahn, J.-H.; Yeom, G. Y.; Schlom, D. G.; Kim, J., Impact of 2D–3D Heterointerface on Remote Epitaxial Interaction through Graphene. *ACS Nano* **2021,** 15, (6), 10587-10596.

56. Lee, S.; Lee, S. K.; Kang, C. G.; Cho, C.; Lee, Y. G.; Jung, U.; Lee, B. H., Graphene transfer in vacuum yielding a high quality graphene. *Carbon* **2015,** 93, 286-294.

57. Shivayogimath, A.; Whelan, P. R.; Mackenzie, D. M. A.; Luo, B.; Huang, D.; Luo, D.; Wang, M.; Gammelgaard, L.; Shi, H.; Ruoff, R. S.; Bøggild, P.; Booth, T. J., Do-It-Yourself Transfer of Large-Area Graphene Using an Office Laminator and Water. *Chemistry of Materials* **2019,** 31, (7), 2328-2336.

58. Bean, J. C.; Sheng, T. T.; Feldman, L. C.; Fiory, A. T.; Lynch, R. T., Pseudomorphic growth of GexSi1−xon silicon by molecular beam epitaxy. *Applied Physics Letters* **1984,** 44, (1), 102-104.

59. Fitzgerald, E. A.; Xie, Y. H.; Green, M. L.; Brasen, D.; Kortan, A. R.; Michel, J.; Mii, Y. J.; Weir, B. E., Totally relaxed GexSi1−xlayers with low threading dislocation densities grown on Si substrates. *Applied Physics Letters* **1991,** 59, (7), 811-813.

60. Lee, M. L.; Fitzgerald, E. A.; Bulsara, M. T.; Currie, M. T.; Lochtefeld, A., Strained Si, SiGe, and Ge channels for high-mobility metal-oxide-semiconductor field-effect transistors. *Journal of Applied Physics* **2005,** 97, (1), 011101.

61. Bae, S.-H.; Lu, K.; Han, Y.; Kim, S.; Qiao, K.; Choi, C.; Nie, Y.; Kim, H.; Kum, H. S.; Chen, P.; Kong, W.; Kang, B.-S.; Kim, C.; Lee, J.; Baek, Y.; Shim, J.; Park, J.; Joo, M.; Muller, D. A.; Lee, K.; Kim, J., Graphene-assisted spontaneous relaxation towards dislocation-free heteroepitaxy. *Nature Nanotechnology* **2020,** 15, (4), 272-276.

62. Bae, S.-H.; Zhou, X.; Kim, S.; Lee, Y. S.; Cruz, S. S.; Kim, Y.; Hannon, J. B.; Yang, Y.; Sadana, D. K.; Ross, F. M.; Park, H.; Kim, J., Unveiling the carrier transport mechanism in epitaxial graphene for forming wafer-scale, single-domain graphene. *Proceedings of the National Academy of Sciences* **2017,** 114, (16), 4082-4086.

63. Liang, D. D.; Wei, T. B.; Wang, J. X.; Li, J. M., Quasi van der Waals epitaxy nitride materials and devices on two dimension materials. *Nano Energy* **2020,** 69, 23.

64. Fan, S.; Vu, Q. A.; Tran, M. D.; Adhikari, S.; Lee, Y. H., Transfer assembly for two-dimensional van der Waals heterostructures. *2D Materials* **2020,** 7, (2), 022005.

65. Caldwell, J. D.; Anderson, T. J.; Culbertson, J. C.; Jernigan, G. G.; Hobart, K. D.; Kub, F. J.; Tadjer, M. J.; Tedesco, J. L.; Hite, J. K.; Mastro, M. A.; Myers-Ward, R. L.; Eddy, C. R.; Campbell, P. M.; Gaskill, D. K., Technique for the Dry Transfer of Epitaxial Graphene onto Arbitrary Substrates. *ACS Nano* **2010,** 4, (2), 1108-1114.

66. Chen, Y.; Gong, X. L.; Gai, J. G., Progress and Challenges in Transfer of Large-Area Graphene Films. *Advanced Science* **2016,** 3, (8), 1500343.

67. Hwang, J.-Y.; Kim, Y.-M.; Lee, K. H.; Ohta, H.; Kim, S. W., Te Monolayer-Driven Spontaneous van der Waals Epitaxy of Two-dimensional Pnictogen Chalcogenide Film on Sapphire. *Nano Letters* **2017,** 17, (10), 6140-6145.

68. Ferro, G.; Chaussende, D., A new model for in situ nitrogen incorporation into 4H-SiC during epitaxy. *Sci Rep* **2017,** 7, (1), 43069.

69. Xu, X.; Hu, X.; Chen, X., SiC Single Crystal Growth and Substrate Processing. In *Light-Emitting Diodes*, Springer International Publishing: 2019; pp 41-92.

70. Panchal, V. Epitaxial graphene nanodevices and their applications for electronic and magnetic sensing. Royal Holloway, University of London, 2014.

71. Robinson, J.; Weng, X. J.; Trumbull, K.; Cavalero, R.; Wetherington, M.; Frantz, E.; LaBella, M.; Hughes, Z.; Fanton, M.; Snyder, D., Nucleation of Epitaxial Graphene on SiC(0001). *ACS Nano* **2010,** 4, (1), 153-158.

72. Weng, X. J.; Robinson, J. A.; Trumbull, K.; Cavalero, R.; Fanton, M. A.; Snyder, D., Structure of few-layer epitaxial graphene on 6H-SiC(0001) at atomic resolution. *Appl. Phys. Lett.* **2010,** 97, (20), 3.

73. Weng, X. J.; Robinson, J. A.; Trumbull, K.; Cavalero, R.; Fanton, M. A.; Snyder, D., Epitaxial graphene on SiC(000(1)over-bar): Stacking order and interfacial structure. *Appl. Phys. Lett.* **2012,** 100, (3), 4.

74. Sforzini, J.; Telychko, M.; Krejčí, O.; Vondráček, M.; Švec, M.; Bocquet, F.; Tautz, F., Transformation of metallic boron into substitutional dopants in graphene on 6 H– SiC (0001). *Physical Review B* **2016,** 93, (4), 041302.

75. Yazdi, G. R.; Iakimov, T.; Yakimova, R., Epitaxial graphene on SiC: a review of growth and characterization. *Crystals* **2016,** 6, (5), 53.

76. Oliveira, M. H.; Lopes, J. M. J.; Schumann, T.; Galves, L. A.; Ramsteiner, M.; Berlin, K.; Trampert, A.; Riechert, H., Synthesis of quasi-free-standing bilayer graphene nanoribbons on SiC surfaces. *Nat. Commun.* **2015,** 6, (1), 7632.

77. Brodie, B. C., XIII. On the atomic weight of graphite. *Philosophical Transactions of the Royal Society of London* **1859**, (149), 249-259.

78. Boersma, M. A. M., CATALYTIC PROPERTIES OF ALKALI METAL-GRAPHITE INTERCALATION COMPOUNDS. *Catalysis Reviews* **1974,** 10, (1), 243-280.

79. De Heer, W. A.; Berger, C.; Wu, X.; Sprinkle, M.; Hu, Y.; Ruan, M.; Stroscio, J. A.; First, P. N.; Haddon, R.; Piot, B.; Faugeras, C.; Potemski, M.; Moon, J.-S., Epitaxial graphene electronic structure and transport. *Journal of Physics D: Applied Physics* **2010,** 43, (37), 374007.

80. Kim, S.; Ihm, J.; Choi, H. J.; Son, Y.-W., Origin of Anomalous Electronic Structures of Epitaxial Graphene on Silicon Carbide. *Phys. Rev. Lett.* **2008,** 100, (17).

81. Daniels, K. M.; Shetu, S.; Staser, J.; Weidner, J.; Williams, C.; Sudarshan, T. S.; Chandrashekhar, M. V. S., Mechanism of Electrochemical Hydrogenation of Epitaxial Graphene. *J Electrochem Soc* **2015,** 162, (4), E37-E42.

82. Puls, C. P.; Staley, N. E.; Moon, J. S.; Robinson, J. A.; Campbell, P. M.; Tedesco, J. L.; Myers-Ward, R. L.; Eddy, C. R.; Gaskill, D. K.; Liu, Y., Top-gate dielectric induced doping and scattering of charge carriers in epitaxial graphene. *Appl. Phys. Lett.* **2011,** 99, (1), 3.

83. Robinson, J. A.; Hollander, M.; LaBella, M.; Trumbull, K. A.; Cavalero, R.; Snyder, D. W., Epitaxial Graphene Transistors: Enhancing Performance via Hydrogen Intercalation. *Nano Letters* **2011,** 11, (9), 3875-3880.

84. Bresnehan, M. S.; Hollander, M. J.; Wetherington, M.; LaBella, M.; Trumbull, K. A.; Cavalero, R.; Snyder, D. W.; Robinson, J. A., Integration of Hexagonal Boron Nitride with Quasi-freestanding Epitaxial Graphene: Toward Wafer-Scale, High-Performance Devices. *ACS Nano* **2012,** 6, (6), 5234-5241.

85. Hollander, M. J.; Agrawal, A.; Bresnehan, M. S.; LaBella, M.; Trumbull, K. A.; Cavalero, R.; Snyder, D. W.; Datta, S.; Robinson, J. A., Heterogeneous integration of hexagonal boron nitride on bilayer quasi-free-standing epitaxial graphene and its impact on electrical transport properties. *Phys. Status Solidi A-Appl. Mat.* **2013,** 210, (6), 1062-1070.

86. Rajabpour, S.; Vera, A.; He, W.; Katz, B. N.; Koch, R. J.; Lassauni\`ere, M.; Chen, X.; Li, C.; Nisi, K.; El-Sherif, H.; Wetherington, M. T.; Dong, C.; Bostwick, A.; Jozwiak, C.; Duin, A. C. T. v.; Bassim, N.; Zhu, J.; Wang, G.-C.;

Wurstbauer, U.; Rotenberg, E.; Crespi, V.; Quek, S. Y.; Robinson, J. A., Tunable Two-Dimensional Group-III Metal Alloys. *arXiv:2106.00117* **2021**.

87. Bersch, B. M. Electronic Transport in Synthetic Transition Metal Dichalcogenides and Novel Graphene/metal Heterostructures. The Pennsylvania State University, 2019.

88. Briggs, N. C. Novel Synthesis of 2-Dimensional Group III and IV Metals and Binary Compounds. The Pennsylvania State University, 2020.

89. Steves, M. A.; Wang, Y.; Briggs, N.; Zhao, T.; El-Sherif, H.; Bersch, B. M.; Subramanian, S.; Dong, C.; Bowen, T.; Fuente Duran, A.; Nisi, K.; Lassauniere, M.; Wurstbauer, U.; Bassim, N. D.; Fonseca, J.; Robinson, J. T.; Crespi, V. H.; Robinson, J.; Knappenberger, K. L., Jr., Unexpected Near-Infrared to Visible Nonlinear Optical Properties from 2-D Polar Metals. *Nano Letters* **2020,** 20, (11), 8312-8318.

90. Hiura, H.; Lee, M. V.; Tyurnina, A. V.; Tsukagoshi, K., Liquid phase growth of graphene on silicon carbide. *Carbon* **2012,** 50, (14), 5076-5084.

91. Fujita, J. I.; Hiyama, T.; Hirukawa, A.; Kondo, T.; Nakamura, J.; Ito, S. I.; Araki, R.; Ito, Y.; Takeguchi, M.; Pai, W. W., Near room temperature chemical vapor deposition of graphene with diluted methane and molten gallium catalyst. *Sci Rep* **2017,** 7, (1), 12371.

92. Kotsakidis, J. C.; Grubišić-Čabo, A.; Yin, Y.; Tadich, A.; Myers-Ward, R. L.; DeJarld, M.; Pavunny, S. P.; Currie, M.; Daniels, K. M.; Liu, C., Freestanding n-Doped Graphene via Intercalation of Calcium and Magnesium Into the Buffer Layer-SiC (0001) Interface. *arXiv preprint arXiv:2004.01383* **2020**.

93. Knoll, M.; Ruska, E., Das elektronenmikroskop. *Zeitschrift für physik* **1932,** 78, (5-6), 318-339.

94. Ernst Ruska, The Development of the Electron Microscope and of Electron Microscopy(Nobel Lecture). *Angewandte Chemie International Edition in English* **1987,** 26, (7), 595-605.

95. Van Ngo, V.; Hernandez, M.; Roth, B.; Joy, D. C., STEM imaging of lattice fringes and beyond in a UHR in-lens field-emission SEM. *Microscopy Today* **2007,** 15, (2), 12-16.

96. O'Keefe, M. A.; Hetherington, C. J. D.; Wang, Y. C.; Nelson, E. C.; Turner, J. H.; Kisielowski, C.; Malm, J. O.; Mueller, R.; Ringnalda, J.; Pan, M.; Thust, A., Sub-Ångstrom high-resolution transmission electron microscopy at 300keV. *Ultramicroscopy* **2001,** 89, (4), 215-241.

97. Ul-Hamid, A., A Beginners' Guide to Scanning Electron Microscopy. Springer: 2018.

98. Nellist, P. D., The principles of STEM imaging. In *Scanning Transmission Electron Microscopy*, Springer: 2011; pp 91-115.

99. Mohamed, A.; Taha, O.; El-Sherif, H. M.; Connerton, P. L.; Hooton, S. P. T.; Bassim, N. D.; Connerton, I. F.; El-Shibiny, A., Bacteriophage ZCSE2 is a Potent Antimicrobial Against Salmonella enterica Serovars: Ultrastructure, Genomics and Efficacy. *Viruses* **2020,** 12, (4), 424.

100. Egerton, R. F., *Electron energy-loss spectroscopy in the electron microscope*. Springer Science & Business Media: 2011.

101. Hart, J. L.; Lang, A. C.; Leff, A. C.; Longo, P.; Trevor, C.; Twesten, R. D.; Taheri, M. L., Direct Detection Electron Energy-Loss Spectroscopy: A Method to Push the Limits of Resolution and Sensitivity. *Sci Rep* **2017,** 7, (1).

102. Hofmann, S., Auger-and X-ray photoelectron spectroscopy in materials science: a user-oriented guide. Springer Science & Business Media: 2012; Vol. 49.

103. Reimer, L., Image formation in low-voltage scanning electron microscopy. SPIE press: 1993; Vol. 12.

104. Brintlinger, T.; Chen, Y.-F.; Dürkop, T.; Cobas, E.; Fuhrer, M. S.; Barry, J. D.; Melngailis, J., Rapid imaging of nanotubes on insulating substrates. *Applied Physics Letters* **2002,** 81, (13), 2454-2456.

105. Homma, Y.; Suzuki, S.; Kobayashi, Y.; Nagase, M.; Takagi, D., Mechanism of bright selective imaging of single-walled carbon nanotubes on insulators by scanning electron microscopy. *Applied Physics Letters* **2004,** 84, (10), 1750-1752.

106. Hiura, H.; Miyazaki, H.; Tsukagoshi, K., Determination of the Number of Graphene Layers: Discrete Distribution of the Secondary Electron Intensity

Stemming from Individual Graphene Layers. *Applied Physics Express* **2010,** 3, (9), 095101.

107. Kochat, V.; Nath Pal, A.; Sneha, E. S.; Sampathkumar, A.; Gairola, A.; Shivashankar, S. A.; Raghavan, S.; Ghosh, A., High contrast imaging and thickness determination of graphene with in-column secondary electron microscopy. *Journal of Applied Physics* **2011,** 110, (1), 014315.

108. Zhou, Y.; Fox, D. S.; Maguire, P.; O'Connell, R.; Masters, R.; Rodenburg, C.; Wu, H.; Dapor, M.; Chen, Y.; Zhang, H., Quantitative secondary electron imaging for work function extraction at atomic level and layer identification of graphene. *Scientific Reports* **2016,** 6, (1), 21045.

109. Ferrari, A. C.; Basko, D. M., Raman spectroscopy as a versatile tool for studying the properties of graphene. *Nature Nanotechnology* **2013,** 8, (4), 235-246.

110. Bing, D.; Wang, Y.; Bai, J.; Du, R.; Wu, G.; Liu, L., Optical contrast for identifying the thickness of two-dimensional materials. *Opt. Commun.* **2018,** 406, 128-138.

111. Shearer, C. J.; Slattery, A. D.; Stapleton, A. J.; Shapter, J. G.; Gibson, C. T., Accurate thickness measurement of graphene. *Nanotechnology* **2016,** 27, (12), 125704.

112. Albrektsen, O.; Eriksen, R. L.; Novikov, S. M.; Schall, D.; Karl, M.; Bozhevolnyi, S. I.; Simonsen, A. C., High resolution imaging of few-layer graphene. *Journal of Applied Physics* **2012,** 111, (6), 064305.

113. Grodecki, K.; Jozwik, I.; Baranowski, J. M.; Teklinska, D.; Strupinski, W., SEM and Raman analysis of graphene on SiC(0001). *Micron* **2016,** 80, 20-23.

114. De Luca, O.; Grillo, R.; Castriota, M.; Policicchio, A.; De Santo, M. P.; Desiderio, G.; Fasanella, A.; Agostino, R. G.; Cazzanelli, E.; Giarola, M.; Mariotto, G., Different spectroscopic behavior of coupled and freestanding monolayer graphene deposited by CVD on Cu foil. *Applied Surface Science* **2018,** 458, 580-585.

115. Fariah Hayee; Leo Yu; Linda Zhang, J.; J. Ciccarino, C.; Minh Nguyen; F. Marshall, A.; Igor Aharonovich; Jelena Vučković; Prineha Narang; F. Heinz, T.; A. Dionne, J., Revealing multiple classes of stable quantum

emitters in hexagonal boron nitride with correlated optical and electron microscopy. *Nature Materials* **2020,** 19, (5), 534-539.

116. Robinson, J.; Weng, X.; Trumbull, K.; Cavalero, R.; Wetherington, M.; Frantz, E.; Labella, M.; Hughes, Z.; Fanton, M.; Snyder, D., Nucleation of epitaxial graphene on SiC(0001). *ACS Nano* **2010,** 4, (1), 153-8.

117. S. Eswara; A. Pshenova; L. Yedra; H. Hoang, Q.; J. Lovric; P. Philipp; T. Wirtz, Correlative microscopy combining transmission electron microscopy and secondary ion mass spectrometry: A general review on the state-of-the-art, recent developments, and prospects. *Applied Physics Reviews* **2019,** 6, (2), 021312.

118. Hauser, M.; Wojcik, M.; Kim, D.; Mahmoudi, M.; Li, W.; Xu, K., Correlative Super-Resolution Microscopy: New Dimensions and New Opportunities. *Chem Rev* **2017,** 117, (11), 7428-7456.

119. Burnett, T. L.; Withers, P. J., Completing the picture through correlative characterization. *Nature Materials* **2019,** 18, (10), 1041-1049.

120. Herbig, M., Spatially correlated electron microscopy and atom probe tomography: Current possibilities and future perspectives. *Scr. Mater.* **2018,** 148, 98-105.

121. Kang, K.; Lee, K.-H.; Han, Y.; Gao, H.; Xie, S.; Muller, D. A.; Park, J., Layer-by-layer assembly of two-dimensional materials into wafer-scale heterostructures. *Nature* **2017,** 550, (7675), 229-233.

122. Lu, A.-Y.; Zhu, H.; Xiao, J.; Chuu, C.-P.; Han, Y.; Chiu, M.-H.; Cheng, C.-C.; Yang, C.-W.; Wei, K.-H.; Yang, Y.; Wang, Y.; Sokaras, D.; Nordlund, D.; Yang, P.; Muller, D. A.; Chou, M.-Y.; Zhang, X.; Li, L.-J., Janus monolayers of transition metal dichalcogenides. *Nature Nanotechnology* **2017,** 12, (8), 744-749.

123. Huang, L.; Zhang, D.; Zhang, F.-H.; Feng, Z.-H.; Huang, Y.-D.; Gan, Y., High-Contrast SEM Imaging of Supported Few-Layer Graphene for Differentiating Distinct Layers and Resolving Fine Features: There is Plenty of Room at the Bottom. *Small* **2018,** 14, (22), 1704190.

124. Filleter, T.; Bennewitz, R., Structural and frictional properties of graphene films on SiC(0001) studied by atomic force microscopy. *Phys. Rev. B* **2010,** 81, (15), 7.

125. Filleter, T.; Emtsev, K. V.; Seyller, T.; Bennewitz, R., Local work function measurements of epitaxial graphene. *Applied Physics Letters* **2008,** 93, (13), 3.

126. Robinson, J. A.; Puls, C. P.; Staley, N. E.; Stitt, J. P.; Fanton, M. A.; Emtsev, K. V.; Seyller, T.; Liu, Y., Raman Topography and Strain Uniformity of Large-Area Epitaxial Graphene. *Nano Letters* **2009,** 9, (3), 964-968.

127. Robinson, J. A.; Wetherington, M.; Tedesco, J. L.; Campbell, P. M.; Weng, X.; Stitt, J.; Fanton, M. A.; Frantz, E.; Snyder, D.; VanMil, B. L.; Jernigan, G. G.; Myers-Ward, R. L.; Eddy, C. R.; Gaskill, D. K., Correlating Raman Spectral Signatures with Carrier Mobility in Epitaxial Graphene: A Guide to Achieving High Mobility on the Wafer Scale. *Nano Letters* **2009,** 9, (8), 2873-2876.

128. Yamada, Y.; Haruyama, T.; Shimabukuro, K.; Konno, H., Correlative Atomic Force and Transmission Electron Microscopy toward Applications of Atomic Force Microscopy to Heterogeneous Systems. *Microsc. microanal.* **2016,** 22, (S5), 44-45.

129. Polishchuk, R. S.; Polishchuk, E. V.; Marra, P.; Alberti, S.; Buccione, R.; Luini, A.; Mironov, A. A., Correlative Light-Electron Microscopy Reveals the Tubular-Saccular Ultrastructure of Carriers Operating between Golgi Apparatus and Plasma Membrane. *The Journal of Cell Biology* **2000,** 148, (1), 45-58.

130. Van Rijnsoever, C.; Oorschot, V.; Klumperman, J., Correlative light-electron microscopy (CLEM) combining live-cell imaging and immunolabeling of ultrathin cryosections. *Nature Methods* **2008,** 5, (11), 973-980.

131. Rühle, S., Tabulated values of the Shockley–Queisser limit for single junction solar cells. *Solar Energy* **2016,** 130, 139-147.

132. Ehrler, B.; Alarcón-Lladó, E.; Tabernig, S. W.; Veeken, T.; Garnett, E. C.; Polman, A., Photovoltaics Reaching for the Shockley–Queisser Limit. *ACS Energy Letters* **2020,** 5, (9), 3029-3033.

133. Green, M. A.; Dunlop, E. D.; Levi, D. H.; Hohl-Ebinger, J.; Yoshita, M.; Ho-Baillie, A. W. Y., Solar cell efficiency tables (version 54). *Progress in Photovoltaics: Research and Applications* **2019,** 27, (7), 565-575.

134. Benson, J. D.; Bubulac, L. O.; Jaime-Vasquez, M.; Arias, J. M.; Smith, P. J.; Jacobs, R. N.; Markunas, J. K.; Almeida, L. A.; Stoltz, A.; Wijewarnasuriya, P. S.; Peterson, J.; Reddy, M.; Jones, K.; Johnson, S. M.; Lofgreen, D. D., Impact of CdZnTe Substrates on MBE HgCdTe Deposition. *Journal of Electronic Materials* **2017,** 46, (9), 5418-5423.

135. Johnson, S. M.; De Lyon, T. J.; Cockrum, C. A.; Hamilton, W. J.; Tung, T.; Gesswein, F. I.; Baumgratz, B. A.; Ruzicka, L. M.; Wu, O. K.; Roth, J. A., Direct growth of CdZnTe/Si substrates for large-area HgCdTe infrared focal plane arrays. *Journal of Electronic Materials* **1995,** 24, (5), 467-473.

136. Glass, H. L.; Appleby Woods, M. R.; Buehnerkemper, M. L.; Varnum, D. L.; Weismuller, T. P., Control of microtwins in MOCVD of CdTe on sapphire. *J Cryst Growth* **1993,** 128, (1-4), 617-621.

137. Yang, J.-H.; Yin, W.-J.; Park, J.-S.; Ma, J.; Wei, S.-H., Review on first-principles study of defect properties of CdTe as a solar cell absorber. *Semiconductor Science and Technology* **2016,** 31, (8), 083002.

138. Ueda, O.; Maruyama, K.; Hobbs, A.; Shinohara, K., Transmission electron microscopic evaluation of metalorganic chemical vapor deposition-grown CdTe crystals on sapphire substrates. *J Cryst Growth* **1992,** 117, (1-4), 266-270.

139. Li, C.; Poplawsky, J.; Yan, Y.; Pennycook, S. J., Understanding individual defects in CdTe thin-film solar cells via STEM: From atomic structure to electrical activity. *Materials Science in Semiconductor Processing* **2017,** 65, 64-76.

140. Zúñiga-Pérez, J.; Tena-Zaera, R.; Muñoz-Sanjosé, V., Structural characterization of CdTe layers grown on (0001) sapphire by MOCVD. *J Cryst Growth* **2004,** 270, (3-4), 309-315.

141. Glass, H. L.; Appleby Woods, M. R., Variation of microtwin content with thickness in cadmium telluride films grown on sapphire by metalorganic chemical vapor deposition. *Applied Physics Letters* **1992,** 60, (21), 2619-2621.

142. Myers, T. H.; Giles-Taylor, N. C.; Yanka, R. W.; Bicknell, R. N.; Cook, J. W.; Schetzina, J. F.; Jost, S. R.; Cole, H. S.; Woodbury, H. H., Properties and applications of CdTe/sapphire epilayers grown by molecular beam epitaxy. *Journal of Vacuum Science & Technology A: Vacuum, Surfaces, and Films* **1985,** 3, (1), 71-75.

143. Major, J. D., Grain boundaries in CdTe thin film solar cells: a review. *Semiconductor Science and Technology* **2016,** 31, (9), 093001.

144. Li, C.; Wu, Y.; Poplawsky, J.; Pennycook, T. J.; Paudel, N.; Yin, W.; Haigh, S. J.; Oxley, M. P.; Lupini, A. R.; Al-Jassim, M.; Pennycook, S. J.; Yan, Y., Grain-Boundary-Enhanced Carrier Collection in CdTe Solar Cells. *Phys. Rev. Lett.* **2014,** 112, (15).

145. Romeo, A.; Bätzner, D. L.; Zogg, H.; Vignali, C.; Tiwari, A. N., Influence of CdS growth process on structural and photovoltaic properties of CdTe/CdS solar cells. *Solar Energy Materials and Solar Cells* **2001,** 67, (1-4), 311-321.

146. Salavei, A.; Rimmaudo, I.; Piccinelli, F.; Romeo, A., Influence of CdTe thickness on structural and electrical properties of CdTe/CdS solar cells. *Thin Solid Films* **2013,** 535, 257-260.

147. Woodcock, J. M.; Turner, A. K.; Ozsan, M. E.; Summers, J. G. In *Thin film solar cells based on electrodeposited CdTe*, The Conference Record of the Twenty-Second IEEE Photovoltaic Specialists Conference - 1991, IEEE.

148. Mikhailov, V. I.; Butashin, A. V.; Kanevsky, V. M.; Polyak, L. E.; Rakova, E. V.; Moslemov, A. E.; Kvartalov, V. B., Study of molecular beam epitaxy of cadmium telluride on sapphire. *Journal of Surface Investigation. X-ray, Synchrotron and Neutron Techniques* **2011,** 5, (3), 595-600.

149. Muslimov, A. E.; Butashin, A. V.; Kanevsky, V. M.; Babaev, V. A.; Alikhanov, N. M.-R., Epitaxy of CdTe on sapphire substrates with titanium buffer layers. *Crystallography Reports* **2017,** 62, (3), 455-459.

150. Neretina, S.; Hughes, R. A.; Britten, J. F.; Sochinskii, N. V.; Preston, J. S.; Mascher, P., The role of substrate surface termination in the deposition of (111) CdTe on (0001) sapphire. *Applied Physics A* **2009,** 96, (2), 429-433.

151. Eason, R., Pulsed laser deposition of thin films: applications-led growth of functional materials. John Wiley & Sons: 2007.

152. Krebs, H.-U.; Weisheit, M.; Faupel, J.; Süske, E.; Scharf, T.; Fuhse, C.; Störmer, M.; Sturm, K.; Seibt, M.; Kijewski, H., Pulsed laser deposition (PLD)--a versatile thin film technique. In *Advances in Solid State Physics*, Springer: 2003; pp 505-518.

153. Meinander, K.; Preston, J. S., A DFT study on the effect of surface termination in CdTe (111)/α-Al2O3 (0001) heteroepitaxy. *Surface Science* **2015,** 632, 93-97.

154. Brooks, L. S., The Vapor Pressures of Tellurium and Selenium. *J. Am. Chem. Soc.* **1952,** 74, (1), 227-229.

155. Egerton, A. C.; Raleigh, F. V., CCCLX.—The vapour pressure of cadmium and its alloys wtih zinc. *J. Chem. Soc., Trans.* **1923,** 123, (0), 3024-3032.

156. Bangert, U.; Eberlein, T.; Nair, R. R.; Jones, R.; Gass, M.; Bleloch, A. L.; Novoselov, K. S.; Geim, A.; Briddon, P. R., STEM plasmon spectroscopy of free standing graphene. *physica status solidi (a)* **2008,** 205, (9), 2265-2269.

157. Eberlein, T.; Bangert, U.; Nair, R. R.; Jones, R.; Gass, M.; Bleloch, A. L.; Novoselov, K. S.; Geim, A.; Briddon, P. R., Plasmon spectroscopy of free-standing graphene films. *Physical Review B* **2008,** 77, (23).

158. Sodeck, H.; Mikler, H.; Komarek, K. L., Transition metal-chalcogen systems, VI: The zirconium-tellurium phase diagram. *Monatshefte fur Chemie* **1979,** 110, (1), 1-8.

159. Chang, C. C., LEED Studies of the (0001) Face of α-Alumina. *Journal of Applied Physics* **1968,** 39, (12), 5570-5573.

160. Godin, T. J.; Lafemina, J. P., Atomic and electronic structure of the corundum (α-alumina) (0001) surface. *Physical Review B* **1994,** 49, (11), 7691-7696.

161. Yoshimoto, M.; Maeda, T.; Ohnishi, T.; Koinuma, H.; Ishiyama, O.; Shinohara, M.; Kubo, M.; Miura, R.; Miyamoto, A., Atomic-scale formation of ultrasmooth surfaces on sapphire substrates for high-quality thin-film fabrication. *Applied Physics Letters* **1995,** 67, (18), 2615-2617.

162. Avanesian, T.; Dai, S.; Kale, M. J.; Graham, G. W.; Pan, X.; Christopher, P., Quantitative and Atomic-Scale View of CO-Induced Pt Nanoparticle Surface Reconstruction at Saturation Coverage via DFT Calculations Coupled with in Situ TEM and IR. *J. Am. Chem. Soc.* **2017,** 139, (12), 4551-4558.

163. Sun, J. T.; Gao, L.; He, X. B.; Cheng, Z. H.; Deng, Z. T.; Lin, X.; Hu, H.; Du, S. X.; Liu, F.; Gao, H.-J., Surface reconstruction transition of metals induced by molecular adsorption. *Physical Review B* **2011,** 83, (11).

164. Kvashnin, A. G.; Kvashnin, D. G.; Oganov, A. R., Novel Unexpected Reconstructions of (100) and (111) Surfaces of NaCl: Theoretical Prediction. *Scientific Reports* **2019,** 9, (1).

165. Hÿtch, M.; Snoeck, E.; Kilaas, R., Quantitative measurement of displacement and strain fields from HREM micrographs. *Ultramicroscopy* **1998,** 74, (3), 131-146.

166. Kim, S.; Lee, S.; Oshima, Y.; Kondo, Y.; Okunishi, E.; Endo, N.; Jung, J.; Byun, G.; Lee, S.; Lee, K., Scanning moiré fringe imaging for quantitative strain mapping in semiconductor devices. *Applied Physics Letters* **2013,** 102, (16), 161604.

167. Su, D.; Zhu, Y., Scanning moiré fringe imaging by scanning transmission electron microscopy. *Ultramicroscopy* **2010,** 110, (3), 229-233.

168. Apte, A.; Bianco, E.; Krishnamoorthy, A.; Yazdi, S.; Rao, R.; Glavin, N.; Kumazoe, H.; Varshney, V.; Roy, A.; Shimojo, F.; Ringe, E.; Kalia, R. K.; Nakano, A.; Tiwary, C. S.; Vashishta, P.; Kochat, V.; Ajayan, P. M., Polytypism in ultrathin tellurium. *2D Materials* **2018,** 6, (1), 015013.

169. Wang, Y.; Xiao, C.; Chen, M.; Hua, C.; Zou, J.; Wu, C.; Jiang, J.; Yang, S. A.; Lu, Y.; Ji, W., Two-dimensional ferroelectricity and switchable spin-textures in ultra-thin elemental Te multilayers. *Materials Horizons* **2018,** 5, (3), 521-528.

170. Cai, X.; Han, X.; Zhao, C.; Niu, C.; Jia, Y., Tellurene: An elemental 2D monolayer material beyond its bulk phases without van der Waals layered structures. *Journal of Semiconductors* **2020,** 41, (8), 081002.

171. Pécz, B.; Nicotra, G.; Giannazzo, F.; Yakimova, R.; Koos, A.; Kakanakova-Georgieva, A., Indium Nitride at the 2D Limit. *Advanced Materials* **2021,** 33, (1), 2006660.

172. Kakanakova-Georgieva, A.; Giannazzo, F.; Nicotra, G.; Cora, I.; Gueorguiev, G. K.; Persson, P. O. Å.; Pécz, B., Material proposal for 2D indium oxide. *Applied Surface Science* **2021,** 548, 149275.

173. Watcharinyanon, S.; Johansson, L. I.; Xia, C.; Virojanadara, C., Ytterbium oxide formation at the graphene–SiC interface studied by photoemission. *Journal of Vacuum Science & Technology A: Vacuum, Surfaces, and Films* **2013,** 31, (2), 020606.

174. Baringhaus, J.; Stöhr, A.; Forti, S.; Krasnikov, S. A.; Zakharov, A. A.; Starke, U.; Tegenkamp, C., Bipolar gating of epitaxial graphene by intercalation of Ge. *Applied Physics Letters* **2014,** 104, (26), 261602.

175. Kim, H.; Dugerjav, O.; Lkhagvasuren, A.; Seo, J. M., Doping modulation of quasi-free-standing monolayer graphene formed on SiC(0001) through Sn1-Ge intercalation. *Carbon* **2019,** 144, 549-556.

176. Tokura, Y.; Kawasaki, M.; Nagaosa, N., Emergent functions of quantum materials. *Nature Physics* **2017,** 13, (11), 1056-1068.

177. Wang, W.; Li, Y.; Zheng, Y.; Li, X.; Huang, L.; Li, G., Lattice structure and bandgap control of 2D GaN grown on graphene/Si heterostructures. *Small* **2019,** 15, (14), 1802995.

178. Wang, W.; Zheng, Y.; Li, X.; Li, Y.; Zhao, H.; Huang, L.; Yang, Z.; Zhang, X.; Li, G., 2D AlN Layers Sandwiched Between Graphene and Si Substrates. *Advanced Materials* **2019,** 31, (2), 1803448.

179. Wundrack, S.; Momeni, D.; Dempwolf, W.; Schmidt, N.; Pierz, K.; Michaliszyn, L.; Spende, H.; Schmidt, A.; Schumacher, H. W.; Stosch, R.; Bakin, A., Liquid metal intercalation of epitaxial graphene: Large-area gallenene layer fabrication through gallium self-propagation at ambient conditions. *Phys. Rev. Mater.* **2021,** 5, (2).

180. Kochat, V.; Samanta, A.; Zhang, Y.; Bhowmick, S.; Manimunda, P.; Asif, S. A. S.; Stender, A. S.; Vajtai, R.; Singh, A. K.; Tiwary, C. S.; Ajayan, P. M., Atomically thin gallium layers from solid-melt exfoliation. *Science Advances* **2018,** 4, (3), e1701373.

181. Nisi, K.; Subramanian, S.; He, W.; Ulman, K. A.; El-Sherif, H.; Sigger, F.; Lassaunière, M.; Wetherington, M. T.; Briggs, N.; Gray, J.; Holleitner, A. W.; Bassim, N.; Quek, S. Y.; Robinson, J. A.; Wurstbauer, U., Light–Matter Interaction in Quantum Confined 2D Polar Metals. *Advanced Functional Materials* **2020**, 2005977.

182. Berger, C.; Song, Z.; Li, T.; Li, X.; Ogbazghi, A. Y.; Feng, R.; Dai, Z.; Marchenkov, A. N.; Conrad, E. H.; First, P. N.; De Heer, W. A., Ultrathin Epitaxial Graphite: 2D Electron Gas Properties and a Route toward

Graphene-based Nanoelectronics. *The Journal of Physical Chemistry B* **2004,** 108, (52), 19912-19916.

183. Berger, C., Electronic Confinement and Coherence in Patterned Epitaxial Graphene. *Science* **2006,** 312, (5777), 1191-1196.

184. Riedl, C.; Zakharov, A. A.; Starke, U., Precise in situ thickness analysis of epitaxial graphene layers on SiC(0001) using low-energy electron diffraction and angle resolved ultraviolet photoelectron spectroscopy. *Applied Physics Letters* **2008,** 93, (3), 3.

185. Cavallucci, T.; Tozzini, V., Intrinsic structural and electronic properties of the Buffer Layer on Silicon Carbide unraveled by Density Functional Theory. *Scientific Reports* **2018,** 8, (1).

186. Emtsev, K. V.; Zakharov, A. A.; Coletti, C.; Forti, S.; Starke, U., Ambipolar doping in quasifree epitaxial graphene on SiC(0001) controlled by Ge intercalation. *Physical Review B* **2011,** 84, (12).

187. Syed, N.; Zavabeti, A.; Messalea, K. A.; Della Gaspera, E.; Elbourne, A.; Jannat, A.; Mohiuddin, M.; Zhang, B. Y.; Zheng, G. L.; Wang, L.; Russo, S. P.; Esrafilzadeh, D.; McConville, C. F.; Kalantar-Zadeh, K.; Daeneke, T., Wafer-Sized Ultrathin Gallium and Indium Nitride Nanosheets through the Ammonolysis of Liquid Metal Derived Oxides. *J. Am. Chem. Soc.* **2019,** 141, (1), 104-108.

188. Fujita, J.-I.; Hiyama, T.; Hirukawa, A.; Kondo, T.; Nakamura, J.; Ito, S.-I.; Araki, R.; Ito, Y.; Takeguchi, M.; Pai, W. W., Near room temperature chemical vapor deposition of graphene with diluted methane and molten gallium catalyst. *Scientific Reports* **2017,** 7, (1).

189. Hibino, H.; Tanabe, S.; Mizuno, S.; Kageshima, H., Growth and electronic transport properties of epitaxial graphene on SiC. *Journal of physics D: Applied physics* **2012,** 45, (15), 154008.

190. Kruskopf, M.; Pierz, K.; Pakdehi, D. M.; Wundrack, S.; Stosch, R.; Bakin, A.; Schumacher, H. W., A morphology study on the epitaxial growth of graphene and its buffer layer. *Thin Solid Films* **2018,** 659, 7-15.

191. Kotsakidis, J. C.; Grubišić-Čabo, A.; Yin, Y.; Tadich, A.; Myers-Ward, R. L.; DeJarld, M.; Pavunny, S. P.; Currie, M.; Daniels, K. M.; Liu, C.; Edmonds, M.

T.; Medhekar, N. V.; Gaskill, D. K.; Vázquez De Parga, A. L.; Fuhrer, M. S., Freestanding n-Doped Graphene via Intercalation of Calcium and Magnesium into the Buffer Layer–SiC(0001) Interface. *Chemistry of Materials* **2020,** 32, (15), 6464-6482.

192. Xu, M.; Fujita, D.; Gao, J.; Hanagata, N., Auger Electron Spectroscopy: A Rational Method for Determining Thickness of Graphene Films. *ACS Nano* **2010,** 4, (5), 2937-2945.

193. Shima, M.; Kato, H.; Shihommatsu, K.; Homma, Y., Determination of absolute number of graphene layers on nickel substrate with scanning Auger microprobe. *Applied Physics Express* **2020,** 13, (1), 015502.

194. Li, L.; Li, Z.; Yoshimura, A.; Sun, C.; Wang, T.; Chen, Y.; Chen, Z.; Littlejohn, A.; Xiang, Y.; Hundekar, P.; Bartolucci, S. F.; Shi, J.; Shi, S.-F.; Meunier, V.; Wang, G.-C.; Koratkar, N., Vanadium disulfide flakes with nanolayered titanium disulfide coating as cathode materials in lithium-ion batteries. *Nature Communications* **2019,** 10, (1).

195. Quellmalz, A.; Wang, X.; Sawallich, S.; Uzlu, B.; Otto, M.; Wagner, S.; Wang, Z.; Prechtl, M.; Hartwig, O.; Luo, S.; Duesberg, G. S.; Lemme, M. C.; Gylfason, K. B.; Roxhed, N.; Stemme, G.; Niklaus, F., Large-area integration of two-dimensional materials and their heterostructures by wafer bonding. *Nature Communications* **2021,** 12, (1).

196. Katsnelson, M. I.; Novoselov, K. S.; Geim, A. K., Chiral tunnelling and the Klein paradox in graphene. *Nature Physics* **2006,** 2, (9), 620-625.

197. Jung, S.; Rutter, G. M.; Klimov, N. N.; Newell, D. B.; Calizo, I.; Hight-Walker, A. R.; Zhitenev, N. B.; Stroscio, J. A., Evolution of microscopic localization in graphene in a magnetic field from scattering resonances to quantum dots. *Nature Physics* **2011,** 7, (3), 245-251.

198. Yang, H., Graphene traps. *Nature Physics* **2016,** 12, (11), 994-995.

199. Yang, H.; Baffou, G.; Mayne, A. J.; Comtet, G.; Dujardin, G.; Kuk, Y., Topology and electron scattering properties of the electronic interfaces in epitaxial graphene probed by resonant tunneling spectroscopy. *Physical Review B* **2008,** 78, (4).

200. Lane, R.; Vos, Y.; Wolters, A. H. G.; Kessel, L. V.; Chen, S. E.; Liv, N.; Klumperman, J.; Giepmans, B. N. G.; Hoogenboom, J. P., Optimization of negative stage bias potential for faster imaging in large-scale electron microscopy. *Journal of Structural Biology: X* **2021,** 5, 100046.

201. Michael, J.; Joy, D.; Griffin, B., Use of Sample Bias Voltage for Low-Energy High-Resolution Imaging in the SEM. *Microsc. microanal.* **2010,** 16, (S2), 614-615.

202. Lee, J.; Wong, D.; Velasco Jr, J.; Rodriguez-Nieva, J. F.; Kahn, S.; Tsai, H.-Z.; Taniguchi, T.; Watanabe, K.; Zettl, A.; Wang, F.; Levitov, L. S.; Crommie, M. F., Imaging electrostatically confined Dirac fermions in graphene quantum dots. *Nature Physics* **2016,** 12, (11), 1032-1036.

203. Gutiérrez, C.; Brown, L.; Kim, C.-J.; Park, J.; Pasupathy, A. N., Klein tunnelling and electron trapping in nanometre-scale graphene quantum dots. *Nature Physics* **2016,** 12, (11), 1069-1075.

204. Rafiee, J.; Mi, X.; Gullapalli, H.; Thomas, A. V.; Yavari, F.; Shi, Y.; Ajayan, P. M.; Koratkar, N. A., Wetting transparency of graphene. *Nature Materials* **2012,** 11, (3), 217-222.

205. Sader, J. E.; Lu, J.; Mulvaney, P., Effect of cantilever geometry on the optical lever sensitivities and thermal noise method of the atomic force microscope. *Review of Scientific Instruments* **2014,** 85, (11), 113702.

206. Utama, M. I. B.; Kleemann, H.; Zhao, W.; Ong, C. S.; Da Jornada, F. H.; Qiu, D. Y.; Cai, H.; Li, H.; Kou, R.; Zhao, S.; Wang, S.; Watanabe, K.; Taniguchi, T.; Tongay, S.; Zettl, A.; Louie, S. G.; Wang, F., A dielectric-defined lateral heterojunction in a monolayer semiconductor. *Nature Electronics* **2019,** 2, (2), 60-65.

207. Mammadov, S.; Ristein, J.; Krone, J.; Raidel, C.; Wanke, M.; Wiesmann, V.; Speck, F.; Seyller, T., Work function of graphene multilayers on SiC (0001). *2D Materials* **2017,** 4, (1), 015043.

208. Ochedowski, O.; Kleine Bussmann, B.; Ban D'Etat, B.; Lebius, H.; Schleberger, M., Manipulation of the graphene surface potential by ion irradiation. *Applied Physics Letters* **2013,** 102, (15), 153103.

209. Momeni Pakdehi, D.; Schädlich, P.; Nguyen, T. T. N.; Zakharov, A. A.; Wundrack, S.; Najafidehaghani, E.; Speck, F.; Pierz, K.; Seyller, T.; Tegenkamp, C.; Schumacher, H. W., Silicon Carbide Stacking-Order-Induced Doping Variation in Epitaxial Graphene. *Advanced Functional Materials* **2020**, 2004695.

210. Makovetsky, R.; Piche, N.; Marsh, M., Dragonfly as a Platform for Easy Image-based Deep Learning Applications. *Microsc. microanal.* **2018,** 24, (S1), 532-533.

211. Otsu, N., A Threshold Selection Method from Gray-Level Histograms. *IEEE Transactions on Systems, Man, and Cybernetics* **1979,** 9, (1), 62-66.

212. Schiller, J. A.; Toro, R.; Shah, A.; Surana, M.; Zhang, K.; Robertson, M.; Miller, K.; Cruse, K.; Liu, K.; Seong, B.; Seol, C.; Foster, I. T.; Blaiszik, B. J.; Galewsky, B.; Adams, D.; Katz, D. S.; Ferreira, P.; Ertekin, E.; Tawfick, S., Crowd-Sourced Data and Analysis Tools for Advancing the Chemical Vapor Deposition of Graphene: Implications for Manufacturing. *ACS Appl. Nano Mater.* **2020,** 3, (10), 10144-10155.

213. Masubuchi, S.; Machida, T., Classifying optical microscope images of exfoliated graphene flakes by data-driven machine learning. *npj 2D Materials and Applications* **2019,** 3, (1).

214. Lena Eberle, A.; Schalek, R.; Lichtman, J. W.; Malloy, M.; Thiel, B.; Zeidler, D., Multiple-Beam Scanning Electron Microscopy. *Microscopy Today* **2015,** 23, (2), 12-19.

215. Mallet, P.; Varchon, F.; Naud, C.; Magaud, L.; Berger, C.; Veuillen, J.-Y., Electron states of mono- and bilayer graphene on SiC probed by scanning-tunneling microscopy. *Physical Review B* **2007,** 76, (4).

216. Varchon, F.; Mallet, P.; Veuillen, J.-Y.; Magaud, L., Ripples in epitaxial graphene on the Si-terminated SiC(0001) surface. *Physical Review B* **2008,** 77, (23).

217. Wang, D.; Liu, L.; Chen, W.; Chen, X.; Huang, H.; He, J.; Feng, Y.-P.; Wee, A. T. S.; Shen, D. Z., Optimized growth of graphene on SiC: from the dynamic flip mechanism. *Nanoscale* **2015,** 7, (10), 4522-4528.

218. Giannuzzi, L. A., Introduction to focused ion beams: instrumentation, theory, techniques and practice. Springer Science & Business Media: 2004.

219. Badran, A.; Marshall, D.; Legault, Z.; Makovetsky, R.; Provencher, B.; Piché, N.; Marsh, M., Automated segmentation of computed tomography images of fiber-reinforced composites by deep learning. *Journal of Materials Science* **2020,** 55, (34), 16273-16289.